Turbulent Flame Microstructure, Dynamics, and Thermoacoustic Instability in Swirl-Stabilized Premixed Combustion: Measurements, Statistics, and Analysis

by

Zachary Alexander LaBry

S.B., Massachusetts Institute of Technology (2008)
S.M., Massachusetts Institute of Technology (2010)

Submitted to the Department of Mechanical Engineering
in partial fulfillment of the requirements for the degree of
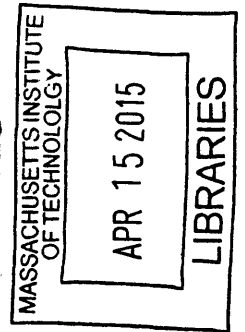
Doctor of Philosophy in Mechanical Engineering

at the

MASSACHUSETTS INSTITUTE OF TECHNOLOGY

February 2015

© Zachary Alexander LaBry, MMXV. All rights reserved.
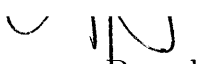
Signature redacted

Author . . . .
Department of Mechanical Engineering
Signature redacted   October 22, 2014

Certified by . . . .
Ahmed F. Ghoniem
Ronald C. Crane (1972) Professor
Thesis Supervisor

Accepted by . . . . Signature redacted . . . .
David E. Hardt
Ralph E. and Eloise F. Cross Professor in Manufacturing
Chairman, Department Committee on Graduate Students

Turbulent Flame Microstructure, Dynamics, and Thermoacoustic Instability in Swirl-Stabilized Premixed Combustion: Measurements, Statistics, and Analysis

by

Zachary Alexander LaBry

Abstract

One of the most difficult challenges facing the development of modern gas turbines–for power generation, and propulsion–is the mitigation of dynamic instabilities in the presence of efficiency and emissions constraints. Dynamic instabilities–self-excited, self-sustaining oscillations which link the combustor acoustics to the combustion process–can result in significant levels of thermal and mechanical stress on combustion systems, leading to reduced operational lifetime, potentially dangerous failure modes, and significant deviations from the desired operating conditions. Due to the complexity of the problem, with the relevant time and length scales of the system–from the chemistry to the acoustics–spanning several orders of magnitude, even sophisticated numerical techniques have been severely limited in their ability to make reliable predictions, leaving the task of finding and eliminating modes of instability to a lengthy and expensive trial-and-error process.

Lean-premixed combustion, one of the leading technologies for low emission combustors, is particularly susceptible to these types of instabilities. The sealed systems that are necessary to maintain a reaction in a lean mixture do not attenuate acoustics well, which often results in high-amplitude pressure fluctuations. In this thesis, we focus on developing a better predictive framework for the onset of combustion instabilities in a swirl-stabilized, lean-premixed combustor. We correlate the self-excited acoustic behavior with quantifiable system properties that can be generalized across different fuel blends.

This work is predicated on the idea that self-excited combustion instability arises from the selective amplification of the noise inherent in a turbulent combustion system, and that the frequency-based response of the flame is a function of the flame geometry. In the first part of the thesis, we focus on the flame geometry, identifying several discrete transitions that take place in the swirl-stabilized flame as we adjust the equivalence ratio. By comparing the transitions across several CH_4/H_2 fuel blends, and using statistical techniques to interrogate the global effect of the

small-scale flow-flame interactions, we find that the extinction strain rate–the flow-driven rate of change in flame surface area at which the chemistry is no longer sufficiently fast to maintain the reaction–is directly linked to the flame transitions. The swirl-stabilized flow features several critical regions with large and unsteady velocity derivatives, particularly, a pair of shear layers that divide the incoming flow of reactants from an inner and an outer recirculation zone. As the extinction strain rate increases with increasing equivalence ratio, the flame transitions through these critical regions, manifesting as discrete changes in the flame geometry.

In the second part, we address the correlation between self-excited instability and the forced acoustic response. By modifying the pressure boundary conditions, we decouple the flame from the acoustics over a domain of interest (defined by a range of equivalence ratios that correspond to the onset of dynamic instability in the coupled system). We then apply external acoustic forcing at a single frequency to ascertain the response of the flame to each particular forcing frequency by means of a flame transfer function. This enables us to consider the frequency-by-frequency response of the flame to its own internally generated noise. We show that the onset of instability is well-predicted by the overlap of the natural acoustic frequencies of the combustor (predicted using a non-linear flame response model) with those frequencies for which the phase of the flame transfer function satisfies the well-known Rayleigh criterion, which is a necessary condition for the presence of self-excited combustion instability.

By examining both the forced response and the self-excited instability across several different fuel blends, we go on to show that both behaviors correlate well with the flame geometry, which we have already shown to be dictated by the extinction strain rate of the particular fuel blend. We go on to collapse both sets of data on the strained flame consumption speed taken at the limit of the extinction strain rate, and in doing so, present a framework for predicting the operating conditions under which the combustor in the coupled configuration will go unstable based on measurements and correlations from the uncoupled configuration. Furthermore by taking the consumption speed at the extinction limit, we are correlating the geometry and dynamics with a parameter that is solely a function of mixture properties. This provides the basis for a framework for predicting instability from properties that are more readily measured or simulated, and provides and explicit means of converting these results to different fuel mixtures.

Thesis Supervisor: Ahmed F. Ghoniem
Title: Ronald C. Crane (1972) Professor

Acknowledgments

If you are reading this, then I suspect that there is a fair chance that you are one of the people who has made the last ten years that I have spent in Boston and at MIT worthwhile, and for that I would like to thank you. There are far too many of you to name, from MIT and outside, but I would like to call out a few people in particular.

First among them, I would like to thank Kate Wymbs, who has supported me unwaveringly through the protracted endgame of this thesis, and always knows just how to pull me through the Nth late night in a row with a smile on my face. I would also like to thank Chris "AZ" Birch, for being an invaluable friend and a fantastic training and Madison partner on those occasions when we could escape lab onto our bikes, and I wish her a swift conclusion to her own PhD and good luck when she races her first World Championship, whenever and in whichever discipline that may be. I would like to thank David Singerman for his exceptional humor in the face of nearly everything, as well as his exquisite taste in coffee and hard cheese, and Nick Loomis, one of the gentlest people who I have ever met, and the person who originally introduced me to track racing and cyclocross. And of course, I must call out Mike "Grandpa" Garrett. Ad astra.

I owe a great deal to many of my Reacting Gas Dynamics labmates as well, and none more so than John Hong. Good luck as you move on from MIT, and my best wishes for your whole family. I am not sure if I am more or less sane because of Nwike Iloeje and Katherine Ong, but either way it has been a fun few years, and just remember: you're late! I wish Ray Speth the best of luck with his continuing research, and thank him for getting me started down my own path of research.

I would like to thank the MIT Cycling Team for making the last many years fun, and while I have seen many generations of the team come and go, I will always associate myself primarily with those first few years on the team with Jason Sears, Caitlin Bever, Paul Nerenberg, Eric Edlund, Ilana Brito, Kenny Cheung, Ariel Herrmann, Tony Sagneri, and everyone else. The New England track cycling contingent also deserves a special mention, in particular, Tom Worster, Eva Papp, and Kurt

Begemann. I wish Kim Blair the best of luck with the Wright Brothers Wind Tunnel and continuing forward with STE@M.

I would like to thank my thesis advisor, Professor Ahmed Ghoniem for his support and guidance through both my Masters and PhD research. I would also like to thank Professor Darmofal, not only for his guidance while serving on my thesis committee, but also for the guidance and encouragement which he gave me as an undergraduate. There are two final members of the MIT faculty, who stand out in particular during my time here who I would like to acknowledge. First, I would like to say thank you to Professor Ian Waitz for his inspiration and encouragement. And also, I wish the best of luck to Professor Woody Hoburg.

James and Allison Houghton have been fantastic friends throughout my time at MIT, and it is fair to say that I would likely have finished my thesis living in a tent without them. And finally, I would like to thank my parents, Leslie and John LaBry, for there support, as none of this would have been possible without them.

Contents

List of Figures

11

13

15

17

List of Tables

Chapter 1

Introduction

One of the great challenges facing the design of practical combustion systems–ranging from industrial burners, power plants, and aircraft engines to rocket motors–is the prediction and mitigation of combustion instability [1, 2]. This is particularly challenging for modern, high-efficiency, low-emission systems, wherein the design constraints limit the applicability of traditional mitigation strategies. While the term "stability" has several different meanings in the context of combustion systems, we are particularly focused on those dynamic instabilities that are known as thermoacoustic instabilities.

These instabilities manifest themselves as coupled oscillations in the heat release rate and acoustic field, which can arise spontaneously in response to quasi-steady changes in the operating conditions of the combustion system. For high-pressure, high-power combustors such as those that are used for stationary power generation, the magnitude of these oscillations can induce such high levels of thermal and mechanical stress as to render the operation of these systems unsafe or lead to greatly accelerated wear and reduced component lifetimes and efficiencies. The present state of understanding of the origin of these instabilities is such that the conditions at which an instability arises are often not discovered until late in the design process, at which point design modifications become very costly in terms of both time and resources. The difficulty in modeling, and even simulating, combustion instability arises from the wide range of length and time scales over which important physical processes take place.

In this thesis, we develop a framework for predicting the onset of instability in a turbulent, swirl-stabilized combustor, which captures many important elements of the flow physics that are pertinent to practical gas turbine combustors. In §1.1, we review the physics of combustion instability, particularly as it pertains to swirl-stabilized systems, before summarizing the critical points of our model in §1.2. Finally, we will provide an outline of the rest of this thesis in §1.3.

1.1   Combustion instability

Although a broad range of research on diffusion combustors over the past sixty years has led to a substantial body of knowledge and sets of guidelines for designing around the problems of combustion instability [3], the drive toward higher efficiency, lower emission combustion systems, particularly for power generation applications, has led to the development of new technologies and the deprecation of the many of these old guidelines. One of the most promising technologies to have arisen is lean-premixed combustion (LPM), sometimes known as lean-premixed pre-vaporized combustion (LPP) when liquid fuels are used. In these systems, the fuel and oxidizer are well mixed upstream of the combustion chamber so that the reaction takes place in a nearly homogenous mixture at a prescribed equivalence ratio. By choosing an appropriate equivalence ratio, the peak temperatures in the combstor may be limited, significantly reducing thermal NO_x produced through the Zeldovich mechanism when air is used as the oxidizer [4, 5, 6].

Thermoacoustic noise is particularly prevalent in modern, high-efficiency, low-emission systems such as premixed combustors, which are more susceptible to these types of instabilities than more traditional diffusion combustors. For gas turbine applications the combination of high energy density, an aerodynamically stabilized flame, and weak internal attenuation of resonant processes can easily admit large amplitude oscillations [7, 8].

A positive feedback loop between chamber acoustics and oscillations in the combustion process lead to the resonant phenomenon known as thermoacoustic combus-

24

tion instability. When the acoustic pressure and heat release rate oscillations are nearly in phase, there is a net increase in the energy transferred into the acoustic field, leading to an amplification of the oscillations, a fact that was first described by Lord Rayleigh [9], and later quantified by Chu [10, 11] in what is known as the Rayleigh criterion. Succinctly, the Rayleigh criterion can be expressed as:

$$\int_0^T \int_{\mathcal{V}} q'(\mathbf{x}, t) p'(\mathbf{x}, t) \, dV \, dt > \Phi \tag{1.1}$$

where $q'(\mathbf{x}, t)$ is the volumetric heat release rate, $p'(\mathbf{x}, t)$ is the fluctuating component of the pressure, and Φ represents system losses. The integral is taken over the flow domain, $\mathcal{V}$, and must be positive (and exceed the system losses) over a cycle of the oscillation, T. Although this criterion may be extended to include more details of the system losses, it remains a necessary condition for instability [12], but is not sufficient, nor does it, in itself address the mechanisms by which small-scale interactions lead to this integrated, global behavior.

A variety of mechanisms by which small-scale interactions can lead to fluctuations of the heat release rate have been identified and studied, including mixture effects, flame-vortex interactions, and flame-wall interactions [1]. The most straightforward mechanism is the modulation of the inlet equivalence ratio by coupling the injector flow rates with the back-pressure provided by the combustion chamber. For self-sustaining instabilities to arise from such a coupling, the convective time delay need only match with the acoustic frequency in such a manner that high pressure corresponds with a high equivalence ratio mixture entering the reaction zone [13, 14, 15, 16]. Physically, this mechanism is of little interest, and practically, it is relatively straightforward to design around by accounting for convective time delays or decoupling the injection flow rate from acoustic oscillations. More interestingly, however, dynamic instability arises even in the presence of a homogenous reactant mixture. Heat release oscillations arise from instantaneous changes in the total reacting mass flow rate which can be quantified through changes in the flame surface density.

In addition to local flame wrinkling effects, which lead to variations in the rate at

which reactants are consumed, pressure oscillations can lead to periodic surges in the mass flow rate of the reactants into the combustion chamber [17]. Fundamentally, the instantaneous global heat release rate, $q(t)$ can be expressed as:

$$q(t) = \rho_u S_f A_f \tag{1.2}$$

where ρ_u is the density of the unburned reactants, S_f is the flame speed, and A_f is the flame surface area, measured along the contours of an identifiable point normal to the flame structure. Some useful reference points are the point of greatest heat release rate along the flame, or a point of constant concentration or constant consumption/production rate for an appropriate species. While the inlet density remains fairly constant for a given operating point, the changes in the total flame area, either through large-scale changes in the flame geometry or small-scale wrinkling provide a clear mechanism modulating the global heat release rate, the flame speed also responds to changes in the flow environment, providing a secondary mechanism of heat release oscillation in a homogenous mixture [18, 19, 20, 21]. These changes are particularly significant where the turbulent wrinkling yields locally high curvatures in the flame front.

Swirl stabilization provides a complex turbulent environment in which these interactions can take place. The central component of a swirling columnar flow is the axial vortex tube. This vortex tube is unstable, and spontaneously undergoes tilting and stretching, rapidly turning perpendicular to the axis of the tube, which generates the recirculation bubble [22, 23, 24]. While such transitions of the primary vortex, known as vortex breakdown, are robust, the precise location cannot readily be predicted or controlled, and is sensitive to very small and poorly understood changes in the inlet parameters [25, 26]. Although this vortex breakdown would happen spontaneously in a constant area duct, rapid expansion of the cross-sectional area may be used to setup an adverse pressure gradient and force the transition to happen at a particular axial location. This is turn makes the flow behavior more predictable, and creates addition pockets of low speed flow. Vortex breakdown is desirable for

combustion applications. The recirculation of combustion products within the vortex breakdown bubble transports heat upstream toward the reactants, aiding in static flame stabilization and ignition, enhancing flame speed, and creating an axially short (or compact) reaction zone.

Although this particular technique, and variants upon it, are widely used in practical combustion systems precisely because the vortex breakdown creates aerodynamically-anchored recirculation zones, the inherent instability of the flow leads to very complex dynamics [27, 28, 29]. These dynamics are further complicated through their interaction with the resonant acoustics under thermoacoustically unstable conditions [30, 31, 32].

In this thesis, we examine a swirl-stabilized combustor, and extract statistical patterns from the small-scale flow interactions, particularly those related to the flame strain, and correlate them with the larger-scale behavior of the flame in regards to its stabilization, and its spatial relationship with the recirculation zones created by the vortex breakdown and the sudden expansion. We show how these interactions influence the shape of the flame brush, which in turn, alters the response of the flame to acoustic perturbations–both of external and internal origin–thereby determining under what conditions dynamic instabilities arise and what form they take.

1.2   A model of combustion instability

The goal of this thesis is to present a mechanistic description of the onset of dynamic instability in a swirl-stabilized, premixed combustor. The model we present is one in which the the broad spectrum, background combustion noise is amplified, turning into an instability when a natural acoustic frequency of the combustor overlaps with the resonant frequencies of the flame, at a phase angle that satisfies the Rayleigh criterion. Turbulent combustion noise is broad spectrum and generally low in amplitude. However, acoustic perturbations induce a response by the flame in the form of a heat release oscillation at the same frequency, due to the small acoustic velocity perturbations. If the phase difference between the pressure and heat release satisfies

the Rayleigh criterion, then the amplification of the pressure leads to additional amplification of the heat release oscillation, and so forth. Instability is the result of this positive feedback loop. If the phase difference does not satisfy the Rayleigh criterion, then the amplified pressure serves to dampen the heat release oscillations, stopping the runaway feedback. Over the next several chapters of this thesis, we will break this proposed mechanism down into its constituent components and provide evidence for the plausibility of this mechanism.

Network acoustic models have long shown promise in the search for predictive tools for combustion instability. Fundamentally, we know that in order for an oscillation to arise and become self-sustaining, it must do so at one of the natural frequencies of the combustion chamber, otherwise the interference from reflected acoustic waves will serve to dampen the acoustic response, and thus, the driven flame response [33, 34, 35]. One critical piece of the problem, therefore, is determining exactly at which frequencies a combustor *can* go unstable. For large aspect ratio combustors, the longitudinal acoustics can be approximated to a high order of accuracy as plane waves. Determining the resonant modes then becomes a matter of determining the approximate impedance conditions at each boundary and junction, including the combustor inlet, outlet, cross-sectional area changes, and most critically, across the flame. Many successful approaches have shown that for practical and laboratory-scale systems, the flame can be modeled as an acoustically compact element, which means that one need not consider the acoustic pressure gradient across the flame. The behavior of the flame, however, turns out to be an important element, which we discuss in greater depth in chapter 2.

This thesis is predicated on the idea that a network acoustic model can be used as a predictive tool for a turbulent, swirl-stabilized combustor. By first identifying the conditions that lead to changes in the global flame geometry, we can put forth an analytical model for, at a minimum, the phase relationship between the acoustic pressure fluctuations and the response of the flame as a function of frequency. In effect, we create a transfer function that is a function of the flame geometry (which we show depends primarily on the extinction characteristics in the presence of a turbulent flow

field). In the presence of broad spectrum turbulent noise, those frequencies which are both resonant frequencies of the chamber acoustics and satisfy the Rayleigh criterion at a particular operating point will be selectively amplified (so long as there is a sufficiently large flame response to overcome any system losses, although these are not directly addressed in this work). This framework provides a means of predicting the self-excited instability from a network acoustic model coupled with a measured or simulated flame transfer function, and furthermore, extends the relationship to the other fuel compositions by identifying the extinction behavior as the governing physical parameter of the flame geometry.

1.3   Summary and overview

The remainder of this thesis has been divided into material presenting evidence for the model described in the previous section and supporting material. Beginning in chapter 2, we look at the details of the experimental facility and the diagnostics that we use throughout the remainder of the thesis. We also look at the acoustic characteristics of the system. We examine both the frequency predictions made by a network acoustics model, and the self-excited instabilities that arise in the "coupled" configuration (and the lack of such instabilities in the "uncoupled" configuration for the operating conditions in which we are most interested). In chapter 3, we look at the properties of the $CH_4/H_2/air$ flames under investigation, and the dependence of the various parameters on the composition, equivalence ratio, and strain rate.

The next two chapters are divided up into the two logical units of the framework:

- Chapter 4 looks at the turbulent combustion aspect related to flame geometry and the interplay between the flow field and the flame brush as a function of combustion parameters.

- Chapter 5 focuses first on the forced acoustic response, and then uses the findings of the previous chapter to collapse both the forced response and the self-excited thermoacoustic behavior on the strained flame consumption speed.

Chapter 4 explores the flame geometry. We begin by showing that the flame geometry is primarily a function of the combustor geometry and operating point, by observing the same flame structures both under quiet conditions and in the presence of dynamic instability, and across several different fuel compositions, which are created by varying the molar ratio of CH_4 and H_2. We show that the flame geometry undergoes several distinct transitions, correlated with transitions in the large-scale flow structures. Further, we show that the progression of the flame through the various geometries is bounded by the high strain rates encountered in the shear layers. For a given fuel composition, as the equivalence ratio increases, the extinction strain rate of the flame increases, allowing it to persist in increasingly unsteady environments. At low equivalence ratios, the flame remains confined to the inner recirculation zone, transitioning to a conical flame in the inner shear layer, and finally developing an appendage, which extends into the outer shear layer where the highest strain rates are observed.

In chapter 5, we explore the response of these flame to acoustic forcing. We show that for a given fuel composition, as the equivalence ratio increases, the amplitude of the unsteady heat release increases for low frequency oscillations, and the phase difference between the pressure and heat release also increases. Further, we show that both the gain and phase of the flame transfer functions are quantitatively similar for a given flame geometry across different fuel compositions. By examining the phase relationship of the flame transfer function, we show that the onset of combustion instability corresponds to the phase between the pressure and the heat release rate closing to within $\pi/2$, the maximum phase difference permissible by the Rayleigh criterion. An observed drop off in the sound pressure level, and loss of a coherent low frequency mode, is explained by the increase in amplitude and phase of the flame transfer function. The quasi one-dimensional acoustics model predicts the existence of a low frequency acoustic mode only if the flame response does not exceed a certain threshold. We then go on to show that, since that based on the findings of chapter 4, we can collapse both the thermoacoustic behavior, as described by the curves of overall sound pressure level, and the forced acoustic response, as measured by

the relationship between the forcing frequency and the phase difference between the pressure and heat release rate oscillations, on a single variable: the consumption speed taken in the limit of the extinction strain rate for the particular fuel composition and equivalence ratio.

In chapter 6, we wrap up the discussion of this model, summarizing the major results of chapters 4 and 5, and make suggestions for future explorations of this model. In addition, we briefly discuss how this model relates to the swirl-counter-swirl microjets, a passive control device that was shown to eliminate the lowest frequency dynamic mode by modifying the flame geometry and flow structures, which provided the impetus for this work [36].

Chapter 2

Swirl-Stabilized Combustor

2.1   Experimental setup

Experiments were conducted in an atmospheric pressure, laboratory scale combustor, exposed to a room temperature environment. A schematic of two combustor configurations is shown in figure 2-1. The upstream section of the combustor consists of a 38 mm diameter cylindrical steel inlet pipe. The inlet pipe is divided into two sections by a choke plate. Fuel mixing occurs upstream of the choke plate. Main air is supplied by an Atlas Copco GA 30 FF air compressor capable of delivering up to 110 g/s at 883 kPa. The air flow rate is set by a Sierra Instruments 780S Flat-Trak flow controller. Methane is supplied by a Sierra C100M Smart-Trak2 digital mass flow controller, and hydrogen is supplied by a Sierra C100L Smart-Trak2 digital mass flow controller. The system is capable of delivering up to 0.3 g/s of hydrogen and 2.3 g/s of methane in arbitrary ratios. The uncertainty in the mass flow rates is ±1% of full scale. Upstream mixing eliminates coupling of the fuel mass flow with acoustic pressure oscillations in the combustion chamber.

The combustion chamber lies downstream of the choke plate. Premixed reactants flow through the 38 mm inlet pipe for 44 cm downstream of the choke plate, where the mixture is passed through an axial swirler producing a swirling flow with an estimated swirl number of 0.7. Flow expands into a 40 cm long, 76 mm diameter quartz combustion chamber 54 cm downstream of the choke plate. The rapid expansion induces
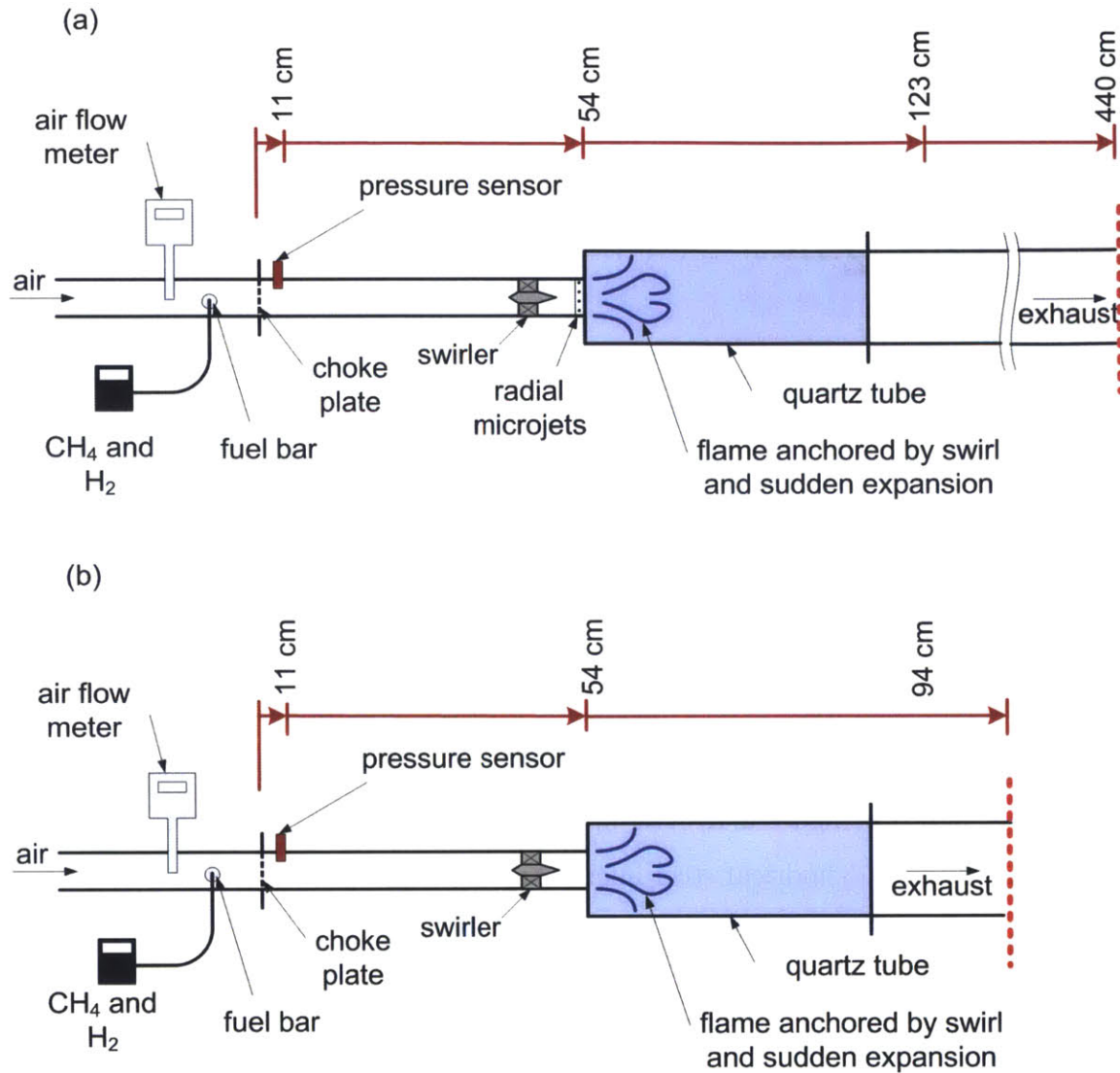
Figure 2-1: The laboratory scale combustor used for experiments in shown schematically in two configurations, the "long-wave" configuration (a), and the "short-wave" configuration (b), differing in the downstream acoustic boundary condition, and named for the relative wavelength of the first admitted acoustic mode.

vortex breakdown in the swirling flow, creating a robust flame anchoring zone.

There are two configurations of the combustor, shown in figures 2-1(a) and 2-1(b). The "long-wave" combustor admits lower frequency acoustic oscillations than the "short-wave" combustor. In the long-wave configuration, the quartz combustion chamber is connected to a 50 cm steel pipe of the same diameter, beyond which flow enters a corrugated steel duct and is directed into a vented exhaust trench with a
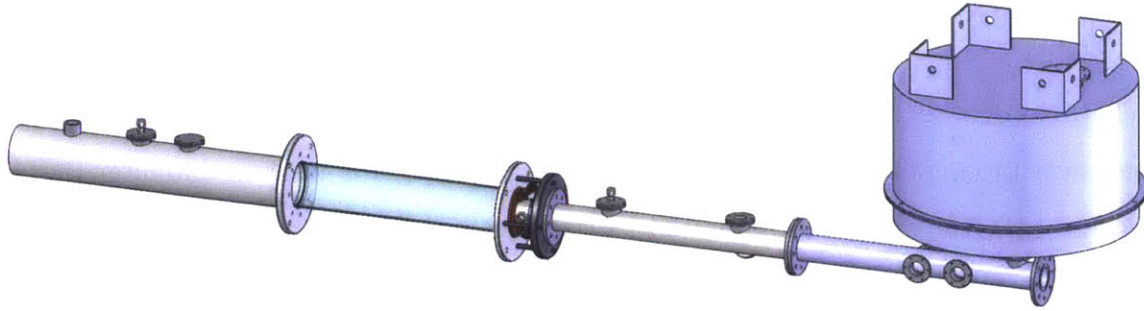
Figure 2-2: Schematic drawing of the combustor inlet (downstream of the choke plate), with the acoustic driver and mounting ports for pressor sensors for the two-microphone method. Flow is from right to left.

cross-sectional area of more than 1 m². In the short-wave configuration, the quartz tube is opened to atmospheric conditions at the downstream end. The corrugated duct is moved directly behind the quartz chamber to direct exhaust gases into the trench, but the pressure boundary is set by atmospheric conditions.

Pressure measurements are taken 11 cm downstream of the choke plate using a Kulite MIC-093 high-intensity microphone mounted in a semi-infinite line configuration. High-speed chemiluminescence and flame images are captured using a NAC GX-1 CMOS camera with a 50 mm Nikon $f/1.8$ lens. The camera has a resolution of 1280x1024 px and a 12 bit/px monochrome bit depth. Spatially integrated chemiluminescence measurements are made using a Hamamatsu H930602 photomultiplier tube (PMT).

Analog signals are sampled using a National Instruments PCIe-6259 data acquisition card. A custom Matlab program using the Matlab Data Acquisition Toolbox is used to control experimental inputs and collect data from various instruments. Separate acquisition systems are used for PIV and PLIF imaging, which will be discussed in the following sections.

2.1.1 Acoustic forcing

In chapter 5, we examine the forced acoustic response of several flame geometries. These measurements were conducted by driving the flow with an 18 in diameter B&C Speakers 18PS100 subwoofer mounted to the inlet pipe immediately downstream of the choke plate as shown in figure 2-2. Power to the subwoofer (acoustic driver) was amplified using a Crown XS2500 audio amplifier, and sinusoidal inputs were generated using an Agilent 33220A function generator capable of fine control of output frequency and amplitude. The acoustic driver was selected for its low frequency range, from 30-1000 Hz, encompassing the range of resonant frequencies observed in the long-wave combustor.

These experiments required measurement of the acoustic perturbation velocity (relative to the bulk flow velocity) upstream of the swirler and perturbations from the expansion and the flame. This region is not optically accessible, making PIV impossible. Additionally, as bulk measurements are necessary, the detail provided by any optical measurement is unnecessary. Instead, we compute the acoustic velocity using the two microphone method [37, 38]. Two Kulite MIC-093 microphones were places at a distance of $\Delta l = 8.5$ cm apart from each other, inline and downstream of the acoustic driver inlet, as shown in figure 2-2. Prior to use for the two-microphone method, the two Kulite pressure sensors were placed inline at the same longitudinal coordinate and their relative calibration was verified.

The two-microphone method is based on the incompressible Euler equation at a fixed location, given by

$$\frac{\partial u}{\partial t} = -\frac{1}{\rho}\frac{\partial p}{\partial x} \tag{2.1}$$

where u is the axial (x) component of velocity and ρ is the fluid density. The pressure term can be expressed as a function of time by noting that small amplitude pressure waves travel at the speed of sound, c, giving us the expression

$$\frac{\partial u}{\partial t} = -\frac{1}{\rho}\frac{\partial p}{\partial t}\frac{\partial t}{\partial x} = -\frac{1}{\rho c}\frac{\partial p}{\partial t} \tag{2.2}$$

36

Within a region of homogeneous gas composition and uniform duct cross section, the pressure must satisfy the planar wave equation. The pressure amplitude at a given point is the sum of forward and backward propagating pressure waves, given by the expression:

$$\hat{p}(x, f) = \hat{p}_f(x, f)e^{-ik_f x} + \hat{p}_b(x, f)e^{ik_b x} \tag{2.3}$$

where the corresponding wave numbers are given by:

$$k_f = \frac{2\pi f}{c + \bar{u}} \tag{2.4}$$

for the forward propagating wave and:

$$k_b = \frac{2\pi f}{c - \bar{u}} \tag{2.5}$$

for the backward propagating wave. The quantity $\bar{u}$ is the mean axial velocity and c is the speed of sound in the fluid. The inlet velocity of the combustor as a function of fuel properties (due to slight differences in the kinematic viscosity of the constituent mixtures) changes negligibly, so these variations where ignored.

    With zero mean velocity, a mapping between input voltage and acoustic particle velocity was created between 32 Hz and 80 Hz using the two-microphone method. Although rated to 30 Hz, the response of the subwoofer to a sinusoidal input voltage at 30 Hz was unacceptably intermittent. Acoustic velocity was mapped at 1.0 V intervals, and linear interpolation was used to calculate the input voltage corresponding to a 1% of nominal mean velocity perturbation (or 0.085 m/s absolute velocity perturbation). A persistent, low amplitude electrical noise signal was detected on one of the pressure sensors at 60 Hz. The two-microphone method calculations were conducted after passing the pressure data through a notch filter to eliminate the 60 Hz noise. The input voltages for 58, 60, and 62 Hz were not directly calculated, but interpolated using a cubic spline curve fit.
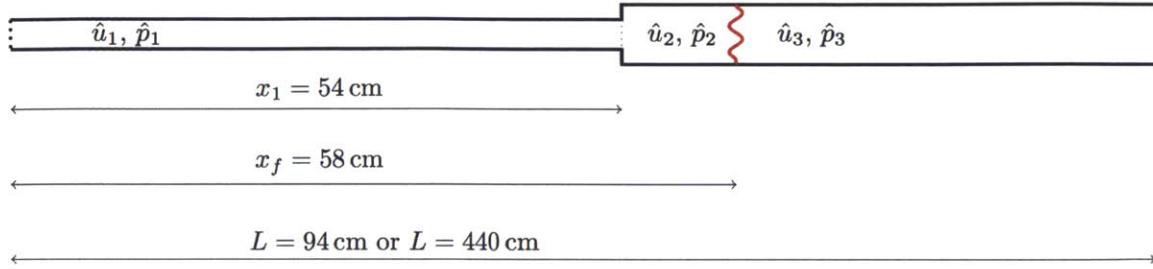
Figure 2-3: Simplified geometry for the acoustic mode calculations include a flame downstream of a single area expansion.

2.2 Combustor acoustics

As an inherently acoustical phenomenon, combustion dynamics present itself as high-amplitude, narrow-bandwidth acoustic pressure oscillations. From a simple quasi one-dimensional acoustics model we are able to predict with reasonable accuracy which frequencies are resonant frequencies of the system. Such models have been successfully applied to many systems with greater geometric complexity than the combustor used for these experiments [34]. The model is derived from energy and momentum conservation equations.

The derivation of the model is based on the same equations presented in §2.1.1, applied piecewise to regions of the combustor with both homogeneous speed of sound and area. The flame is considered to be a step-discontinuity in the speed of sound, due to the temperature relationship:

$$c = (\gamma R T)^{1/2} \tag{2.6}$$

where γ is the ratio of specific heats at constant pressure and volume, R is the gas constant, and T is the fluid temperature. An appropriate boundary condition is applied at every discontinuity. What follows is a brief derivation of the model created by Speth [39], and applied to the combustor in the two configurations that are shown in figure 2-1.

38

We let the pressure perturbation be expressed as:

$$p(x,t) = \text{Re}\left[\hat{p}(x)e^{i\omega t}\right] \tag{2.7}$$

and the acoustic velocity perturbation be expressed as:

$$u(x,t) = \text{Re}\left[\hat{u}(x)e^{i\omega t}\right] \tag{2.8}$$

where the pressure and velocity coefficients are given by:

$$\hat{p}(x) = \hat{f}e^{-i\omega x/c} + \hat{g}e^{i\omega x/c} \tag{2.9}$$

$$\hat{u}(x) = \frac{1}{\rho c}\left[\hat{f}e^{-i\omega x/c} - \hat{g}e^{i\omega x/c}\right] \tag{2.10}$$

which is a relation that was derived in a slightly different form in §2.1.1, and the quantities $\hat{f}$ and $\hat{g}$ are complex coefficients.

The upstream boundary condition is set by the choke plate, where the acoustic perturbation velocity must be zero, and we can state this boundary condition as:

$$\hat{u}(x = 0) = 0 \tag{2.11}$$

The downstream pressure is set by the opening of the combustion exhaust to the atmosphere. In the case of the long-wave combustor configuration, the exhaust runs into a large area trench with a slightly lower than atmospheric pressure to clear exhaust gases. In the short-wave combustor configuration, the combustion chamber is exposed directly to the atmosphere, however the exhaust gases are directed into the long exhaust pipe leading to the exhaust trench. In both scenarios, we can assume for the sake of this model that the exhaust is at atmospheric pressure and exposed to an infinite plenum and so no pressure perturbations are admitted at the downstream boundary. This boundary condition can be expressed as:

$$\hat{p}(x = L) = 0 \tag{2.12}$$

39

Cross-sectional area changes can be accounted for through the conservation of mass. If we imagine a discontinuity in the cross-sectional area in the duct with an area of A_1 on the upstream side and A_2 on the downstream side, located at $x = x_1$, then the appropriate velocity matching condition is given by:

$$\hat{u}_1(x = x_1)A_1 = \hat{u}_2(x = x_1)A_2 \tag{2.13}$$

and conservation of momentum would require the pressure to be matched across the jump, which can be expressed by:

$$\hat{p}_1(x = x_1) = \hat{p}_2(x = x_1) \tag{2.14}$$

keeping in mind that $\hat{u}_1$ and $\hat{u}_2$, just like $\hat{p}_1$ and $\hat{p}_2$, are continuous functions of x defined within their particular domain. These conditions can be applied across all such area expansions.

The final matching condition that must be considered is the jump across the flame. We consider the flame to be infinitely thin (with respect to the acoustics) at $x = x_f$. The heat release rate per unit area can be modeled as:

$$q(t) = \Lambda e^{-i\theta}p(x = x_f, t) \tag{2.15}$$

where $q(t)$ is the time-dependent heat release rate, θ is the phase between the heat release rate and the pressure at the flame location, and Λ is the scaling between heat release rate and pressure.

We consider the case of a flame being located at x_f with equal duct area on both sides of the flame so that $A_2 = A_3$. The pressure must be continuous across the flame, giving us:

$$\hat{p}_2(x = x_f) = \hat{p}_3(x = x_f) \tag{2.16}$$
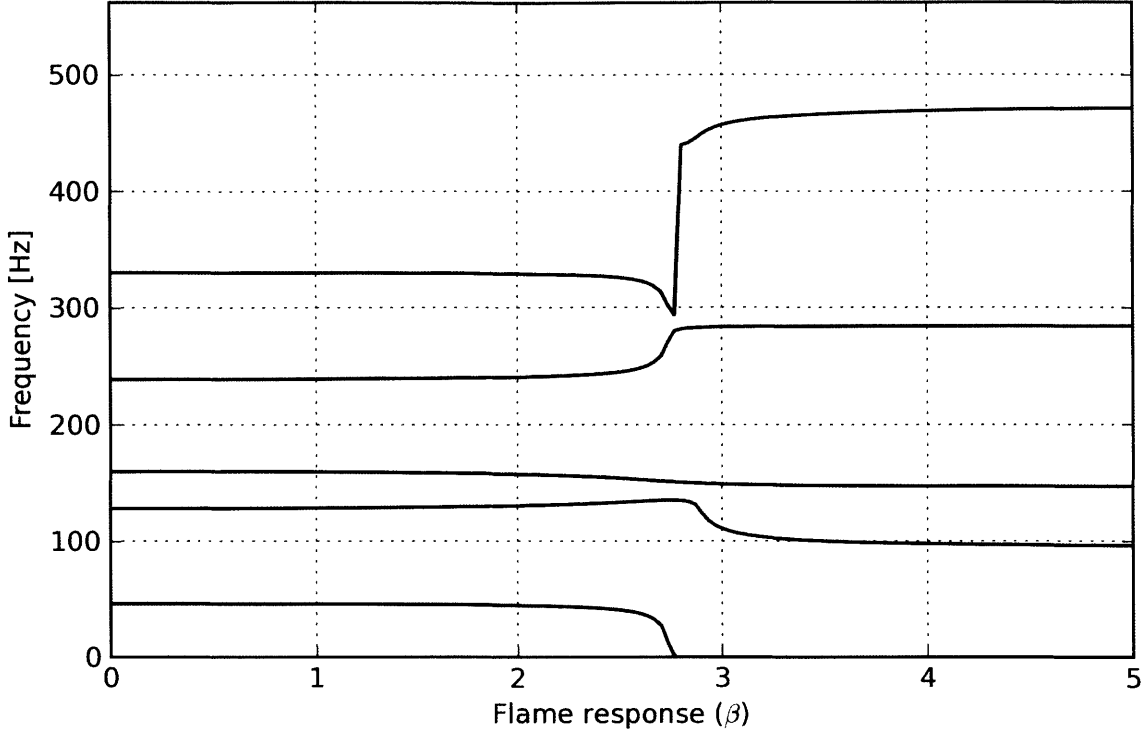
Figure 2-4: Nominal standing wave frequencies for the long-wave combustor with an acoustic length of 440 cm as a function of the heat release rate parameter.

Conservation of mass across the rapid dilatation is given by:

$$\hat{u}_3(x = x_f) = \hat{u}_2(x = x_f) + \frac{\beta e^{-i\theta}}{\rho c} \hat{p}_2(x = x_f) \tag{2.17}$$

where the normalized heat release rate is given by:

$$\beta = \frac{\gamma_u - 1}{c_u} \Lambda \tag{2.18}$$

where γ_u is the ratio of specific heats of the unburned gas, and c_u is the speed of sound in the unburned gases. Physically, this is a normalized parameter for the heat release oscillation, and we would expect this value to change across operating conditions, dependent on the final amplitude of the oscillation, which is not a quantity that we model, but the quantity $\beta e^{-i\theta}$ is proportional to the flame transfer function. Speth showed that values of β between 0.5 and 3.0 are appropriate for syngas/air flames in

41
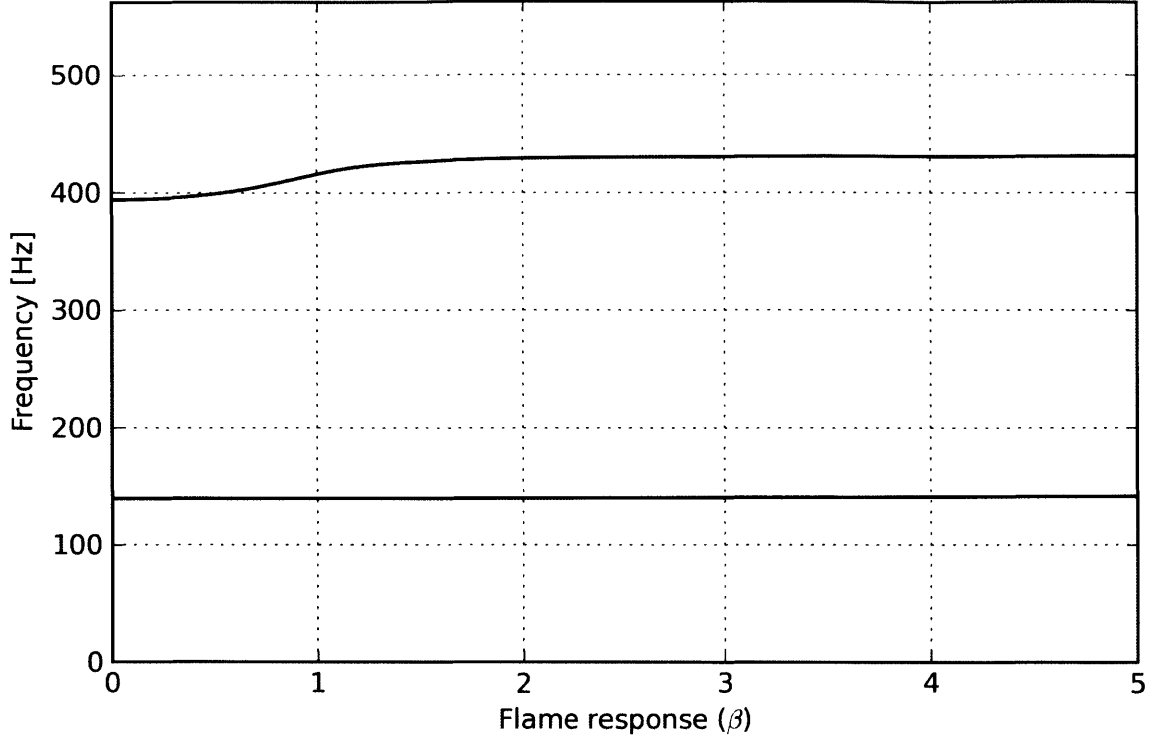
Figure 2-5: Nominal standing wave frequencies for the long-wave combustor with an acoustic length of 94 cm as a function of the heat release rate parameter.

this combustor. Chemiluminescence data has shown us that a similar range of values is appropriate for methane/air combustion. As this section is meant to illustrate the range of resonant frequencies that we might observe, we do not conduct a detailed analysis to measure β throughout the operating regime, and we assume that the pressure and heat release rate are in phase so that $\theta = 0$. The simplified geometry for both combustors is shown in figure 2-3.

For both cases, we divide the interval up into three distinct sections, and from the equations derived above, we are left with seven unknowns ($\hat{f}_1$, $\hat{f}_2$, $\hat{f}_3$, $\hat{g}_1$, $\hat{g}_2$, $\hat{g}_3$, and ω) and six equations (two boundary conditions and four matching conditions). As we are unconcerned with the amplitude, we arbitrarily set $\hat{f}_1 = 1$, and proceed with six unknowns in six equations. These equations are linear in the $\hat{f}$ and $\hat{g}$ parameters, and can be solved numerically for ω.

The acoustic modes, shown as a function of β with no phase lag, are shown in figure

2-4 for the long-wave combustor configuration. For $\beta < 2.8$ we see a low frequency mode in the long wave combustor with a frequency at 45 Hz, and a second mode at 117 Hz for the steady flame case of $\beta = 0$. Subsequent higher frequency modes are observed. As β increases, we have successively higher amplitude heat release rate oscillations. A critical point exists (for perfectly in-phase oscillations) beyond which the lowest frequency mode is no longer available.

The acoustic modes of the short wave combustor configuration are shown in figure 2-5. The acoustic boundary conditions applied over a shorter geometry eliminate the lower frequency modes, and we only observe two resonant modes below 500 Hz, one at 126 Hz and a second one at 398 Hz for the steady flame condition.

The model described above predicts the frequency at which an instability may be observed. As we will see later, the shift in the frequency of the first resonant acoustic frequency is an important piece in the idea of "decoupling" the flame from the acoustics for an in-depth study of the flame geometry. This is based on the hypothesis that the resonant frequencies of the combustion process are a function of the flame geometry, which itself, is a function of the inlet properties of the combustor. As we we observe later, eliminating the overlap between the resonance frequencies of the combustion process and the acoustics allow us to view the system in isolation from combustion dynamics. This relationship is explored further in chapter 5.

The model does not predict the operating conditions under which certain resonant frequencies will be observed (which is the subject of this thesis), nor the amplitude of each resonance (which is limited by non-linear processes that are beyond the scope of this thesis). Next, we show the acoustic spectra and regimes of (in)stability as a function of the operating parameters. The overall sound pressure level (OASPL), defined as:

$$\text{OASPL} = 10 \cdot \log_{10} \overline{\left[\frac{p(t) - \overline{p(t)}}{p_0}\right]^2} \tag{2.19}$$

where $p_0 = 2 \cdot 10^5$ is the reference pressure and the overbars denote time-averaged quantities, is a measure of the amplitude of acoustic noise. In general, a background noise on the order of 120 dBa is observed, even for stable (or "quiet") reacting flows.
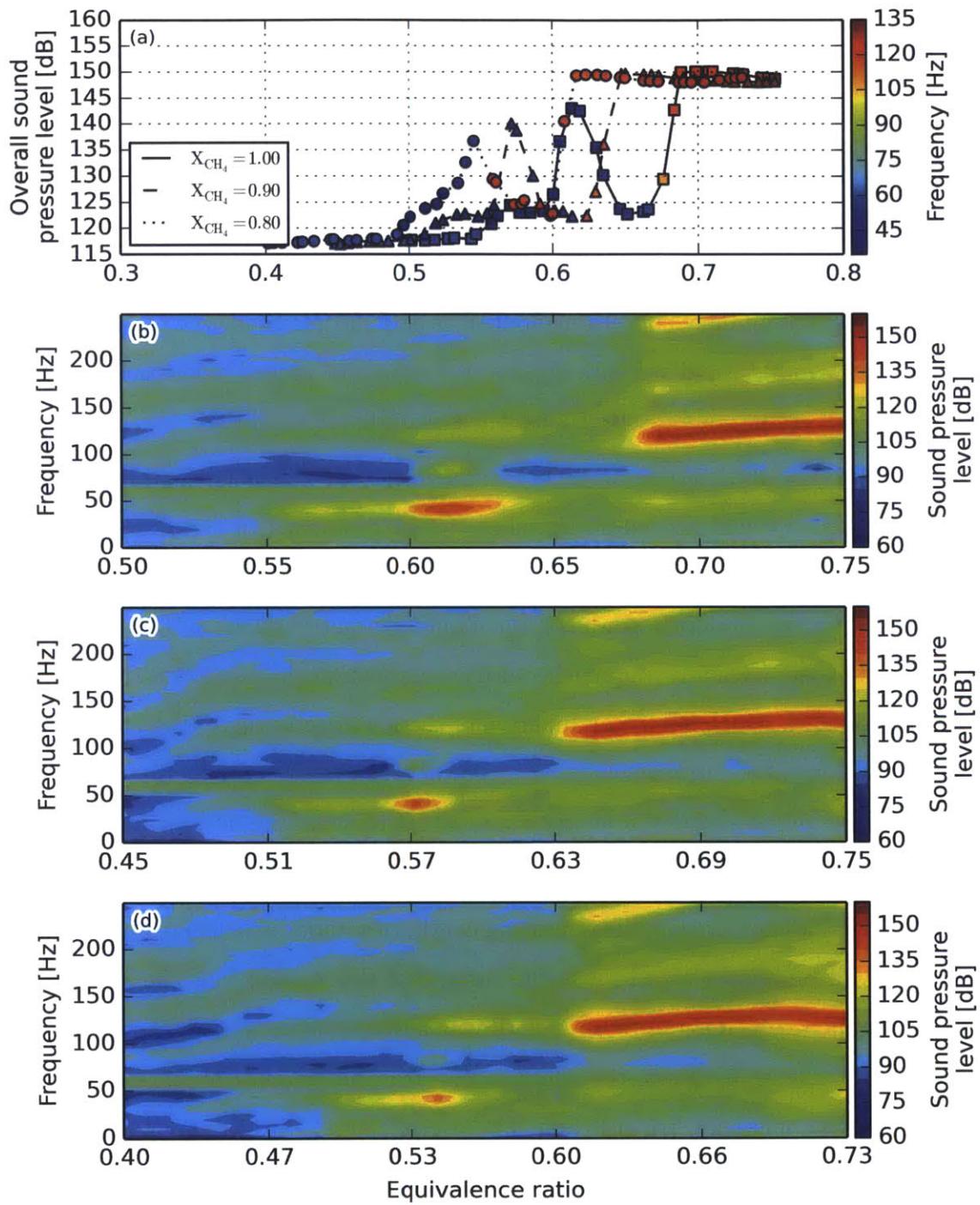
Figure 2-6: The overall sound pressure level (OASPL) (a) and sound pressure level (SPL) spectra as a function of equivalence ratio in the long-wave combustor for volumetric CH_4/H_2 fuel mixtures of 0% (b), 10% (c), and 20% (d).
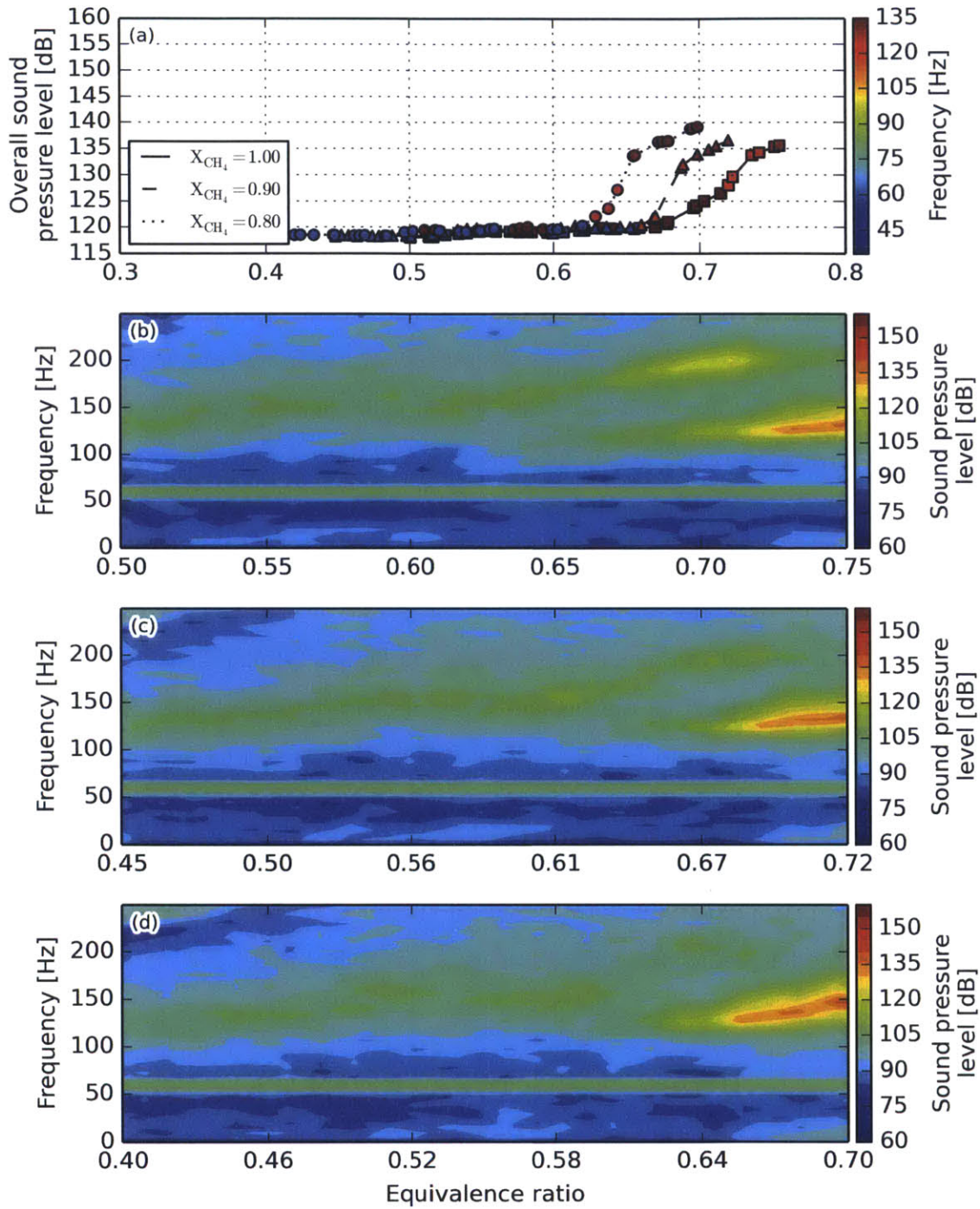
Figure 2-7: The overall sound pressure level (OASPL) (a), and sound pressure level (SPL) spectra as a function of equivalence ratio in the short-wave combustor for volumetric CH_4/H_2 fuel mixtures of 0% (b), 10% (c), and 20% (d).

This background noise is broad spectrum. Figure 2-6(a) shows the overall sound pressure level in the long-wave combustor, and 2-7(a) shows the OASPL in the short-wave combustor as a function of the equivalence ratio across fuel mixtures. Data points in both plots are colored by the dominant frequency at the corresponding operating condition. Both combustors are quiet at low equivalence ratios just above the lean blow off limit, across all fuel mixtures. As a general, and robust trend, we observe that as the equivalence ratio increases, the we eventually encounter a condition at which a rapid increase in the OASPL occurs, which is considered to be the onset of instability. While we do observe small regions in which the OASPL drops to "quiet" levels, instability is reestablished at higher equivalence ratios. The dominant frequency however, is a non-decreasing function of equivalence ratio of all mixtures, and changes in discrete jumps.

Combustion instability, is not simply the presence of large amplitude pressure oscillations, but of resonant acoustic oscillations, which necessarily have a sharply peaked spectrum around the resonant frequency. In figures 2-6 and 2-7, we show the overall sound pressure level as well as the frequency-filtered sound pressure level as a function of equivalence ratio in the long-wave and short-wave combustor configurations, respectively. We show spectra for 0%, 10%, and 20% H_2 fuel blends.

Comparing the observed frequencies in figure 2-6 to 2-4, and in figure 2-7 to 2-5, we see that the predicted frequencies based on the quasi one-dimensional, standing wave acoustic model predict the actual modes of instability well.

2.3   Particle image velocimetry (PIV)

Particle image velocimetry (PIV) is an optical diagnostic technique for measuring the velocity field in a fluid flow. Nominally neutrally-buoyant particles with low inertia are introduced into the flow, and the illuminated in a thin region of the flow by a laser sheet. Images are captured in pairs with the time delay between successive images being based on the flow velocity.

PIV images were captured by an unfiltered 1280x1024 px NAC GX-1 CMOS cam-

era. A Photonics Nd:YLF 532 nm laser illuminated Al_2O_3 seeding particles ranging in size from 1-3 μm. Aluminum oxide seeding particles were chosen based on their high melting temperature and consistent scattering cross-section across the broad range of temperatures encountered in a reacting flow. The seeding images were processed in LaVision DaVis 7.2 software using a multi-pass approach. The final window size was 16x16 px with 50% overlap. PIV vector fields were captured at 1 ms time intervals.

2.3.1 Dynamic mode decomposition (DMD)

Dynamic mode decomposition (DMD) is a data-based post-processing technique that is used to extract dynamic information from both experimental and numerical data. DMD is superficially similar to eigenvalue decomposition, in that the ultimate goal of the technique is to decompose a linearized system matrix into components with discrete complex frequencies. Eigenvalue decomposition may be practical for some numerical applications, in which the system matrix is known, however, such information is usually unavailable for experimental data. DMD creates an approximation to the eigenvalues and eigenvectors of the system matrix based solely on a series of snapshots of the data to produce a decomposition of the form:

$$
\begin{aligned}
\mathbf{u}(\mathbf{x}, t) &= \mathrm{Re}\left[\sum_{j=1}^{N-1} \Psi_j(\mathbf{x})\lambda_j^t\right] \\
&= \mathrm{Re}\left[\sum_{j=1}^{N-1} \Psi_j(\mathbf{x})e^{(\sigma_j+i\omega_j)t}\right]
\end{aligned}
\tag{2.20}
$$

where the *Ritz vectors*, $\Psi_j(\mathbf{x})$, are approximations to the system eigenvectors and the *Ritz values*, λ_j, are approximations to the system eigenvalues based on N observations of the system, each separated by a fixed time step of Δt.

The Ritz vectors are, in general, complex valued, and can be expressed as $\Psi_j(\mathbf{x}) = \Psi_j^r(\mathbf{x}) + i\Psi_j^i(\mathbf{x})$, the sum of two real-valued scalar fields. We can expand the each term on the right hand side of equation (2.20) into:

$$
\mathrm{Re}\left[\Psi_j(\mathbf{x})e^{(\sigma_j+i\omega_j)t}\right] = e^{\sigma_j t}\left(\Psi_j^r(\mathbf{x})\cos\omega_j t - \Psi_j^i(\mathbf{x})\sin\omega_j t\right)
\tag{2.21}
$$

wherein we are able to see the interplay between these two components of the Ritz vectors. The two components of Ψ_j represent two orthogonal snapshots of a cyclic structure where Ψ_j^r leads Ψ_j^i by a phase of $\pi/2$. The cyclic pattern of the Ritz vectors are scaled by a growth or decay coefficient, where σ_j is the growth rate. A value of $\sigma_j \approx 0$ indicates a neutral mode, and is the expected value of all truly cyclic flow processes. Negative growth rates indicate transient modes, often related to stochastic behavior of a turbulent flow field or noise in the measurements. These modes are dependent upon the exact conditions at the time of measurement, and are very sensitive to the precise initial conditions. Transient modes are of little interest to the present research. Substantially positive growth rates indicate that either the flow itself is not steady state, or insufficiently many snapshots have been captured to create a proper DMD representation.

For an in-depth discussion of the mathematics and principles that underly DMD, we refer the reader to the literature [40, 41, 42], however we will present a simple overview of the algorithm and the mathematics involved below.

We begin by assuming that we have a series $\mathbf{u}_i$ of N snapshots of the flow field, with subsequent snapshots being separated by a constant time step ($t_{i+1} - t_i = \Delta t$). We denote a matrix formed by a sequence of snapshots beginning with i and ending with j, with $i < j$ as:

$$\mathbf{U}_i^j = \{\mathbf{u}_i, \mathbf{u}_{i+1}, \ldots, \mathbf{u}_{j-1}, \mathbf{u}_j\} \tag{2.22}$$

where $\mathbf{U}_1^N$ is the full matrix of snapshots.

Although each snapshot is generated by a non-linear process, we assume that there is a linear operator, $\mathbf{A}$, such that $\mathbf{u}_{i+1} \approx \mathbf{A}\mathbf{u}_i$, which constitutes a local linearization of the flow field dynamics. The goal of DMD is to extract dynamic information about the system described by $\mathbf{A}$ based solely on the observed snapshots of the system.

Beyond a critical number of snapshots, it becomes reasonable to assume that the snapshots become linearly dependent. That is, the dominant physical processes are captured by a finite number of snapshots, and no further information is gained by

increasing the number of snapshots. If this condition is met, then:

$$\mathbf{u}_N = c_1\mathbf{u}_1 + c_2\mathbf{u}_2 + \cdots + c_{N-1}\mathbf{u}_{N-1} + \mathbf{r} \qquad (2.23)$$

for sufficiently large N where $\mathbf{r}$ is the remainder (which is identically $\mathbf{0}$ for a truly linear system). The system can be rewritten as:

$$\mathbf{A}\mathbf{U}_1^{N-1} = \mathbf{U}_2^N = \mathbf{U}_1^{N-1}\mathbf{S} + \mathbf{r}\mathbf{e}_{N-1}^T \qquad (2.24)$$

where $\mathbf{e}_i$ is the ith unit vector, and $\mathbf{S}$ is a companion matrix with the final column created from the coefficients in equation (2.23). If λ_i and $\mathbf{y}_i$ are the eigenvalues and eigenvectors of $\mathbf{S}$, then we can show that λ_i and $\Psi_i = \mathbf{V}\mathbf{y}_i$ approximate the eigenvalues and eigenvectors of $\mathbf{A}$, where $\mathbf{V}$ is the matrix formed by the right singular values of $\mathbf{U}_1^{N-1}$.

Although the algorithm presented above is mathematically correct, additional preprocessing is done to compute the an equivalent matrix to $\mathbf{S}$ from the singular value decomposition of $\mathbf{U}_1^{N-1}$, to increase the stability of the algorithm. Additional details are provided in the references, particularly [40].

2.4   Planar laser-induced fluorescence (PLIF)

Planar laser-induced fluorescence (PLIF) is a optical diagnostic tool capable of capturing instantaneous chemical species profiles by illuminating a thin region of the flow with a high energy, narrow bandwidth laser. The frequency of the dye laser is tuned to a precise wavelength corresponding to a resonant optical transition in the target species. Absorbed photons are reemitted at a different frequency, and are collected by a filtered, high-speed camera.

OH PLIF measurements were conducted by exciting the Q1(8) line of the $A^2\Sigma(\nu' = 1) \leftarrow X^2\Pi(\nu'' = 0)$ band at 283.56 nm. This was accomplished using a 220 mJ/pulse Nd:YAG pump beam at 355 nm from a Spectra-Physics LAB-170 laser routed into a Sirah Cobrastretch dye laser circulating Coumarin 153 dye dissolved in ethanol. The

resonator in the dye laser converts this beam to 567 nm, which is then frequency-doubled using a BBO crystal and compensator to a 283.56 nm beam with approximately 13 mJ/pulse. This beam is expanded into a plane in the horizontal plane using a 50 mm cylindrical lens and focused in the vertical axis using a 1 m spherical lens. The maximum repetition rate is 10 Hz.

The fluorescent emissions were collected by a 1280x1024 px LaVision Nanostar CCD camera fitted with a 308±10 nm filter. To improve the signal, pixels were binned in 2x2 px squares. An f/2.8 Cerco UV lens was used to focus the emission from the combustor onto the camera sensor. The calculations used throughout this thesis rely on the gradient field of the PLIF signal, and beam thickness corrections were not made during post-processing.

2.4.1   Microscale and flame structure identification

Raw PLIF measurements present a point-wise surrogate for the concentration of the target species on a plane. By carefully selecting a target species for its chemical kinetics in the context of combustion, we are able to extract a greater level of detail about the microstructure of the flame. OH is a transient species in the combustion of hydrocarbon flames that has a high production rate and is sharply peaked in the reaction zone, and decays slowly. The sharp peak allows the OH gradient to be used as a surrogate for the flame front, while a relatively slow decay rate (in comparison to the production rate) allows OH to be used to determine the orientation of the flame front. The species concentration profiles are discussed in greater depth in chapter 3.

We use edge detection techniques from image processing to identify the flame front. Fundamentally, edge detection algorithms define edges as steep, well-localized gradients, where the thresholds are parameterized for the input images. For the purposes of flame edges detection, the edge finding algorithm needs to have the following characteristics: a high probability of detecting true edges, a low probability of detecting false edges, and a narrow edge profile. The third characteristic is necessary in order to properly calculate the arc-length along a flame, as a thick edge (much more than 1 px on average) will artificially inflate the calculated distance along the curve

of the flame, which is subject to aliasing regardless of the edge width.

Each pixel in a PLIF image contains only intensity information corresponding to the strength of the signal at that point. As a grayscale image, derivatives and gradients within the image are well defined. The Canny edge detection algorithm satisfies these requirements, and is one of the most popular image detection algorithms due to its high performance [43]. There are four basic steps to the algorithm:

1. Smooth the image with a Gaussian filter to reduce high-frequency noise.

2. Determine the magnitude and direction of the image intensity gradient.

3. If the magnitude of the gradient at a pixel is larger than the magnitude of the surrounding pixels in the direction of the gradient, then the pixel is marked as an edge. Otherwise, it is marked as background.

4. Remove weak edges by hysteresis thresholding.

Once Gaussian smoothing is applied, the gradients are calculated by means of the Sobel operators in the principal image directions. The Sobel operators, $\mathbf{G}_x$ and $\mathbf{G}_y$, are discrete differentiation operators, acting in the x and y directions, respectively. The Sobel operators are each two-dimensional convolutions of a 3x3 kernel matrix with the signal matrix, $\mathbf{A}$. They are defined as:

$$\mathbf{G}_x = \begin{bmatrix} -1 & 0 & +1 \\ -2 & 0 & +2 \\ -1 & 0 & +1 \end{bmatrix} * \mathbf{A} \tag{2.25}$$

in the x direction, and:

$$\mathbf{G}_y = \begin{bmatrix} -1 & -2 & -1 \\ 0 & 0 & 0 \\ +1 & +2 & +1 \end{bmatrix} * \mathbf{A} \tag{2.26}$$

in the y direction, where $\mathbf{A}$ is the intensity map of the image. The magnitude of the gradient is simply the point-wise L_2-norm, $\mathbf{G} = \sqrt{\mathbf{G}_x^2 + \mathbf{G}_y^2}$. The angle of the gradient is given by the point-wise operation $\theta = \arctan(\mathbf{G}_y/\mathbf{G}_x)$, however, it is

51

important to note that for OH PLIF, the flame normal is actually $\theta_f = -\theta$. The direction of the gradient is rounded to the nearest of four lines: the horizontal, the vertical, or one of the two diagonals (however, we do *not* round the computed flame normals similarly). The next step in the Canny edge detection algorithm is known as *non-maximum suppression*. The value of the gradient at each pixel is compared to the value at the two pixels on either side of it, in the direction of the rounded gradient. Only if the value of the gradient is higher than at its two neighbor is the pixel marked as an edge. Otherwise, it is marked as background. This step ensures that the edge is 1 px in width (to within aliasing error), minimizing error in arc-length calculations, improving feature detection and providing greater localization. The final step in the Canny edge detection algorithm is *hysteresis thresholding*. An upper and lower threshold are selected. All points with gradient intensities greater than the upper threshold are automatically added to the locus of edge points. Points greater than the lower threshold, but less than the upper threshold, are recursively searched and added to the locus of edge points if they are attached to an edge. This step ensures greater continuity, and reduces the number of broken flamelets that are observed in the data.

Edge data is stored on a Boolean grid, where a value of 'true' indicates the presence of a detectable edge, while a value of 'false' indicates no detectable edge. This allows flame fronts to be individually identified and allows us to perform statistics over the entire grid. Following the Canny edge detection, each image is searched and divided into separate, identifiable flamelets.

Following the edge detection, the images are further processes to refine the flame edge estimates. Individual flamelets are identified based on a continuity criterion. The flamelet identification selects points based on a greedy selection of the nearest neighbors to the points in the set that are not already in the set, and are separated from another point by no more than a small cutoff distance. We then order the points, and determine the endpoints based on the two neighboring points in the list who are farthest apart (that is, their second neighbor is on the other side of the flamelet), and connect any flamelets whose endpoints are no farther apart than a fixed threshold.

This ensures that small breaks in the measured signal due either to noise or an edge detection artifact are not counted as true breaks in the flame. Flames with a total flame length less than 1 mm (approximately the flame thickness) are removed.

The procedure outlined above has shown excellent results for detecting distinct flamelets in a PLIF snapshot, and removing spurious noise. In a small number of cases (less than 1%), wrinkles with very high aspect ratios and a very small absolute width (on the order of the grid spacing) caused the algorithm to misidentify the tip of the wrinkle as the end of the flamelet, attached to one of the two sides, and the second side of the flamelet to be identified as a separate, intersecting flamelet. These cases were sufficiently rare as to cause no significant impact on the overall processing, and so no modifications were made to the algorithm to specifically identify these cases.

Chapter 3

Strained CH$_4$/H$_2$/Air Flames

Practical combustors, as well as the laboratory-scale swirl-stabilized combustor presented in this thesis, create complex turbulent environments in which the flames are subject to various aerodynamic forces. While some flow motions–translation and rotation–act to modify the microstructure by advecting flamelets, creating and destroying wrinkles, another component of the fluid motion–stretch–acts to modify the flame structure directly. Stretch alters the interactions between the species that participate in the combustion reaction, and therefore modifies the flame speed, temperature profile, and species profiles normal to the flame surface. The microscale interaction between the flow and flame that leads to flame stretch alters the combustion process on the level of the flame structure, which leads to large scale effects. These effects are particularly central to flames in turbulent flow environments, and so we take some time in this chapter to examine the consequences of strain on CH$_4$/H$_2$/air flames. We will refer back to these results in later chapters, as well as use the calculations presented here as basis for future calculations.

Flame stretch, is defined as the normalized rate of change of the flame surface area in the presence of a non-uniform flow, which is determined by those components of the flow field that act locally tangent to the surface of the flame and the curvature of the flame surface [44, 45]. Stretch is defined by the expression:

$$\kappa \equiv \frac{1}{\delta A}\frac{d\delta A}{dt} \tag{3.1}$$

where we are taking a Lagrangian derivative of a flame surface element, δA. Matalon and Matkowsky [46] derived a coordinate-free expression for the flame stretch, which has subsequently been simplified by Candel and Poinsot [47]. The expansion of the flame stretch expression yields:

$$\kappa = -\mathbf{n}\mathbf{n} : \nabla\mathbf{u} + \nabla \cdot \mathbf{u} + S_f \nabla \cdot \mathbf{n}$$
$$= -n_i n_j \frac{\partial u_i}{\partial x_j} - S_f(\delta_{ij} - n_i n_j)\frac{\partial n_i}{\partial x_j} \tag{3.2}$$

where $\mathbf{u}$ is the flow velocity, $S_f = \mathbf{v}_f \cdot \mathbf{n}$ is the displacement speed of the flame, $\mathbf{n}$ is the flame normal vector. The first term represents the steady stretch rate due to flame curvature and a non-uniform flow field, while the second term expresses the change in stretch rate due to the combined effects of unsteadiness and flame curvature. In much of the analysis that follows, we will be considering only the steady stretch that occurs in the xy-plane. Using equation (3.2), we can express this quantity as:

$$\kappa_{xy} = -n_x n_y \left(\frac{\partial u}{\partial y} + \frac{\partial v}{\partial x}\right) - n_x^2 \frac{\partial u}{\partial x} - n_y^2 \frac{\partial v}{\partial y} \tag{3.3}$$

where u and v are the x and y components of the flow field, and n_x and n_y are the x and y components of the flame normal vector. Through the remaining sections, we will be making the approximation that $\kappa \approx \kappa_{xy}$, thus neglecting the contributions of the third component of the velocity and gradients in the out of plane direction.

Before we proceed to discuss the impact of stretch on the properties and propagation of a flame, we will first discuss the magnitude of the error that we are committing by making the two-dimensional approximation. As we will show in chapter 4, the conical section of the flame, which constitutes the bulk of the reaction, and importantly, the critical region governing several important transitions, features a conical jet that is angled, to a reasonable approximation, to within 45°of the combustor axis. From this, we can define a length scale L, which is on the order of the cross-jet dimension, where:

$$L \sim O(\Delta x) \sim O(\Delta y) \tag{3.4}$$

and a velocity scale U where:

$$U \sim O(\Delta u) \sim O(\Delta v) \qquad (3.5)$$

which is a consequence of the angle of the jet, and pertains to the incoming reactants rather than the flow as a whole. As a consequence of the angle of the jet and the fact that $U \gg S_f$, which states that the flow speed is substantially greater than the displacement speed of the flame, the flame is angled, to first order, perpendicular to the flow, and so we can define another scale, N, such that:

$$N \sim O(n_x) \sim O(n_y) \qquad (3.6)$$

which quantifies the rough orientation of the flame in two dimensions.

We take the azimuthal velocity scale, $W \sim O(\Delta w)$ to be related to the axial velocity through the swirl number, S, by the equation $W/U = S$. We are left with defining the azimuthal length scale. Since the conical region of the flame is what is of primary interest, this length scale should be on the order of the circumference of the jet, so $\ell \sim O(\Delta z) \sim R$, where R is the radius of the combustion chamber. This order of magnitude analysis is not strictly in keeping with a divergence-free flow, however, we are dealing with the flame region where we *do* expect significant divergence as the flow accelerates through the flame. From the geometry under consideration, $S < 1$ and $\ell > L$. Likewise, since $W > S_f$, the azimuthal normal, M, is scaled by the swirl number, giving us $M \sim O(n_z) \sim SN$.

Accordingly, in the expansion of equation (3.2) any derivatives of the form $\partial(.)/\partial z$ are of $O(S/\ell)$ or smaller, and any terms of the form $\partial w/\partial(.)$ are of $O(S^2)$ or smaller. That is not to say that these terms are strictly negligible, but none are leading order terms. In general, we should predict that our spatially resolved statistics underestimate the actual flame strain.

3.1 Fundamental properties of strained flames

Before presenting numerical results for cases and properties of interest, we will briefly examine an analytical model so that we might gain some insight into the physical mechanisms underlying the microscale changes in the flame structure. Law [48] derived approximate analytical expressions for strained flame temperature and strained flame speed that elucidate the role of preferential diffusion (non-unity Lewis number effects) on the burning velocity and flame temperature. These linearized adjustments to the unstrained properties are given by:

$$\frac{T_b}{T_b^o} = 1 + \left(\frac{1}{\text{Le}} - 1\right)\text{Ka} \tag{3.7}$$

for the temperature of a strained flame relative to its unstrained counterpart and:

$$\frac{S_b}{S_b^o} = 1 - \frac{\text{Ka}}{\text{Le}} + \left(\frac{1}{\text{Le}} - 1\right)\frac{\text{Ka}}{2T_b^o/T_a} \tag{3.8}$$

for the strained laminar burning velocity. The unstrained values, T_b^o and S_b^o, are the adiabatic flame temperature and the laminar burning velocity, respectively.

The Karlovitz number, $\text{Ka} \equiv \kappa t_c = \kappa(\delta_T^o/S_b^o)$, is a non-dimensional parameter combining the stretch rate and the characteristic flow time within the flame, given as the unstrained thermal flame thickness divided by the laminar burning velocity. For unstrained flames, where $\kappa = 0$, Ka vanishes, and to first order, there are no effects on the flame temperature due to a non-unity Lewis number. Temperature and burning velocity remain identical to their unstrained values.

The Lewis number, $\text{Le} \equiv \alpha/D$, is the ratio of thermal diffusivity to mass diffusivity. Methane and the various constituents of air each have a Lewis number near unity. For pure CH_4/air flames we can see from equation (3.7) that the flame stretch, which is parameterized within the Karlovitz number has very little effect on the adiabatic flame temperature, while having a linear and negative effect on the flame speed. That is, from Law's model, we expect positively strained flames with near unity Lewis numbers to propagate more slowly than their unstrained counterparts. Hydrogen, however, has

a Lewis number significantly less than unity, leading to a more complicated variation in parameters.

For positive stretch rates, at Lewis numbers less than unity, the strained flame experiences an increase in the adiabatic flame temperature. This increase comes about from the preferential diffusion of the lighter species (such as hydrogen) into the hot part of the flame. From equation (3.8), we see that the effect of preferential diffusion on the flame speed is more complicated, but for positively stretched flames, we still expect an increase in the consumption speed. Mixed compositions of fuels with differing Lewis numbers lead to more complicated interactions, and the behavior of the governing properties must be determined either numerically or experimentally.

For strained or turbulent flames, there are many reasonable choices for defining the flame speed. We have elected to use the consumption speed, which is derived by integrating the energy equation across the flame, and can be expressed as:

$$S_c = \frac{\int_{-\infty}^{\infty} \frac{q'''}{c_p} \, dx}{\rho_u (T_b - T_u)} \tag{3.9}$$

where q''' is the volumetric heat release rate, c_p is the specific heat at constant pressure, ρ_u is the density of the unburned mixture, and T_b and T_u are the temperature of the burned and unburned gases, respectively. This choice of definition remains consistent across fuel compositions since it is based on the heat release rate rather than the rate of fuel consumption. In the limit of an unstrained flame, the consumption speed reduces to the laminar burning speed. Since unstrained flames are difficult to stabilize either numerically or physically, we can calculate the laminar burning speed by extrapolating the consumption speed at low strain rates.

Another concept central to the discussion of strain and its influence on larger scale properties of the combustion system is that of the *extinction strain rate*. This is the strain rate beyond which the reaction rate diminishes to the point where there is insufficient energy to maintain a continuous reaction, and the flame extinguishes. While we consider this parameter in the steady sense throughout much of this thesis, the system which we are focusing on is a turbulent combustion system, and flames

are therefore inherently subject to unsteady strain rates.

The extinction strain rate is very sensitive to fuel composition, and in particular, hydrogen enrichment of hydrocarbon fuels has been observed to substantially increase the extinction strain rate, effectively making the flames more robust to the effects of turbulence, especially at lean equivalence ratios [49, 50, 51]. This has an effect on the lean stability of the flame, however, these flames tend to be very low power and axial extent over which the combustion process takes place (the "flame length") tends to be exceedingly large, making these flames of little practical interest in the design of gas turbines for power production. As we will see later, however, as the equivalence ratio increases, the flame brush becomes more compact, and interact with various shear layers within the flow, each of which subjects the flame to very high unsteady strains. The preferential diffusion of hydrogen across positively stretched flames means that the presence of hydrogen allows flames to persist in higher strain areas than those in which they could otherwise be sustained.

Instead of relying on analytical models, we numerically calculate strained flame parameters using a code that simulates one-dimensional strained flames under a variety of boundary conditions. The code, Ember, was developed by Speth [39], based on numerical tools originally created by Marzouk *et al* [52, 53], however, substantial updates to the numerics have been made to the version that was used throughout this thesis [54].

Computations are done on a planar twin flame model. A potential flow field is created by directing two opposing jets toward the origin, creating a stagnation plane passing through the origin. The velocity of the potential flow is given by:

$$u = ay \tag{3.10}$$

$$v = -ax \tag{3.11}$$

where a is an independent parameter, quantifying the strain rate. From equation (3.3), for a planar flame, we can see that the stretch rate can be fully parameterized by the prescribed value of the strain rate, leaving us with $\kappa = a$.

Both jets are composed of premixed reactants. Flames are established symmetrically on both sides of the origin, propagating outward. The region in between the two flames is composed of combustion products, and since these products are computed from the actual flame chemistry, this allows for the simulated flames to reach extinction at high strain rates. Although Ember is capable of calculating flame properties in stagnation flows with different boundary conditions, the twin flame configuration was chosen as the most appropriate model for the flame in the presence of recirculation, where the flame is supported by hot combustion products.

3.2 Flame structure

Computations were carried out on premixed flames ranging in equivalence ratio from 0.400 to 0.700, for CH_4/H_2 mixtures ranging from 0% to 30% H_2. The lean limit of the calculations was adjusted by composition due to flame blow off for the low H_2 mixtures. Flames were subject to a steady strain rate, neglecting curvature. Simulations were carried out until a steady state solution was found. Calculations were performed in Ember using the full GRI-Mech 3.0 mechanism, designed for modeling natural gas combustion, and associated thermodynamic and transport coefficients [55].

Two typical flame profiles showing the major species are shown in figure 3-1. In 3-1(a), we show the profile of a CH_4/air flame at an equivalence ratio of $\phi = 0.650$. In addition to the major reactants and products, we also show the OH radical concentration, scaled by a factor of 10 for clarity. At atmospheric pressure and temperature, the range of fuel compositions under consideration produce a flame with an approximate thickness of 1 mm. These results are shown at a very moderate strain rate of 160 s^{-1}, low compared to the extinction strain rate at this equivalence ratio, which is in excess of 800 s^{-1} for both fuel compositions shown. For a given fuel composition, the results of the numerical simulation showed very similar profiles as a function of strain rate, which is consistent with literature on opposed-flow, CH_4/air flames [56].

In figure 3-2, we examine the OH profile of four different flames in relation to the
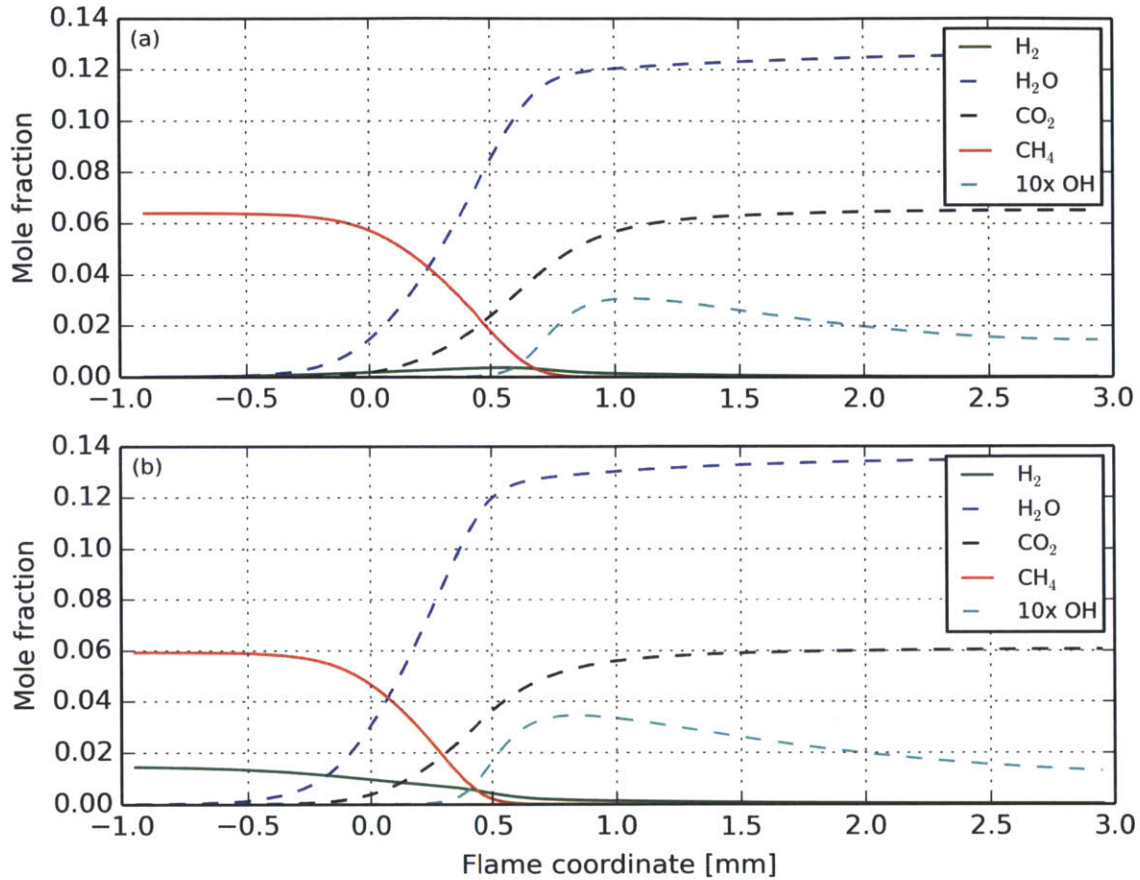
Figure 3-1: The major species of the flame are shown for a pure CH_4/air flame (a) and a CH_4/H_2/air flame with 20% H_2 by volume (b). The concentration of the OH radical has been scaled by a factor of 10x to be visible on the plot.

CH_4 consumption rate, $\dot{w}$, for two different fuel compositions at two different strain rates each. Figure 3-2(a) establishes that the OH is a good marker for the reaction zone across compositions, and thus is an appropriate species to select for illumination by the PLIF, capable of resolving the spatial location of the flame to within one flame width. The value of targeting OH with PLIF imaging is further illustrated by 3-2(b), which shows the flame normal gradient of the OH concentration under the same conditions. The gradient is sharply peaked on the leading edge, as the production of OH in the reaction zone is very rapid. The consumption of OH, however, is a much slower process, and the species persists in nontrivial concentrations well downstream of the reaction zone. When the OH PLIF data is post-processed to determine flame
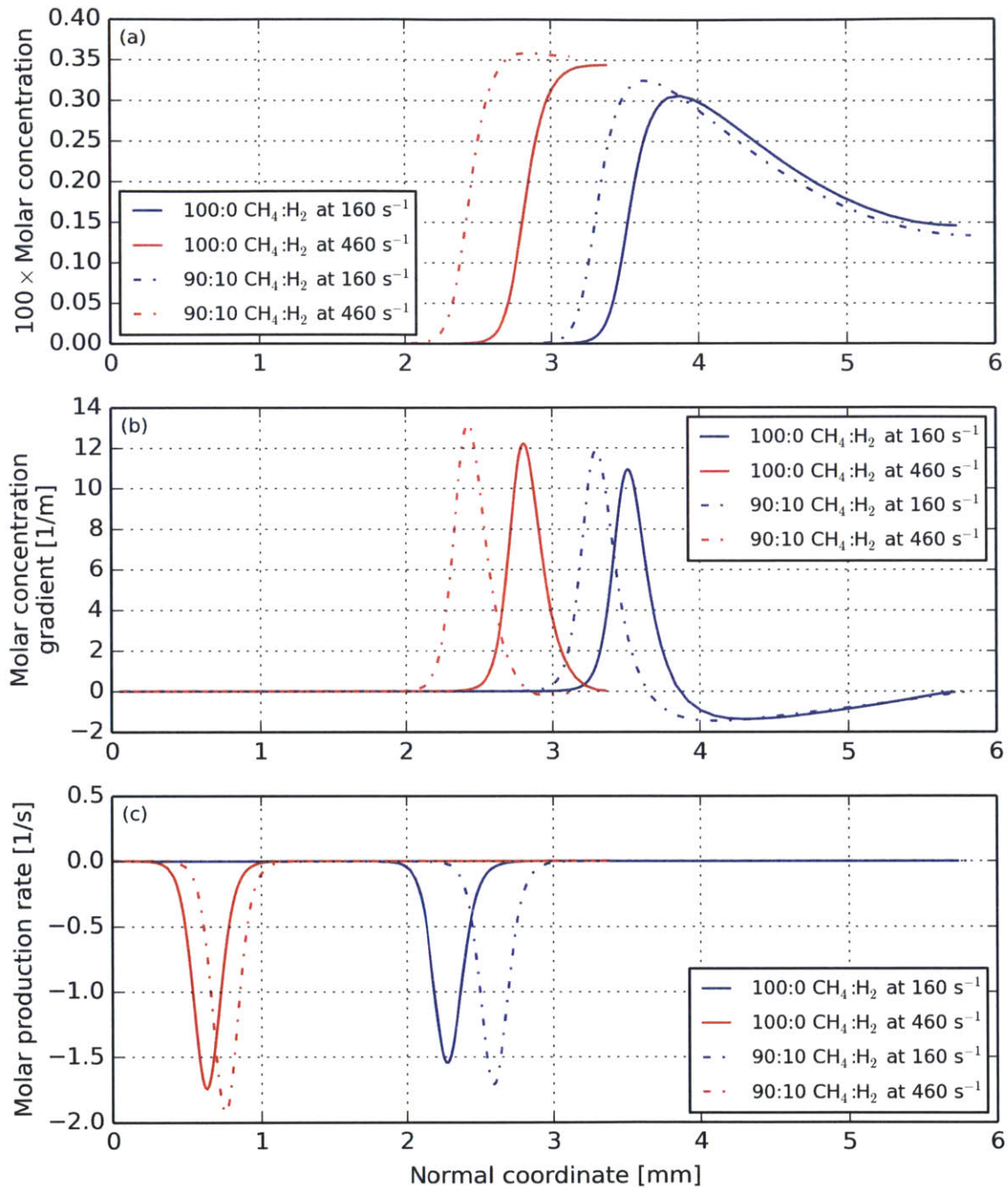
Figure 3-2: The OH profile is shown along the flame-normal coordinate (a), along with the flame-normal gradient of OH (b). OH concentration rises sharply in the reaction zone, but only gradually dissipates. The production rate of CH_4 is plotted in (c) as a marker of the flame position.

edges, the disparity between the production and consumption rates of OH allow us to orient the detected flame edges and determine the direction of propagation of the flames. Advection immediately downstream of the reaction zones further disperses the OH, reducing the local consumption rate, enhancing the contrast between leading and trailing edges of the flame. As a result of this advection, however, the downstream OH profiles are not directly comparable to the numerical profiles, and so it is impossible to determine quantities such as stretch rate directly from PLIF measurements.

3.3   Effects of flame strain and fuel composition

In order to understand the effects of equivalence ratio and strain on $CH_4/H_2/air$ flames, we ran a parametric numerical study for fuel compositions from 0% to 30% H_2 in 10% increments and at equivalence ratios from 0.400 to 0.700 in increments of 0.010. Inlet temperature was fixed at 300 K at a pressure of one atmosphere. The fuel compositions and parameter ranges were chosen to encompass the experimental conditions considered in the remaining chapters. Throughout this section, numerical results as a function of equivalence ratio are plotted at a fixed strain rate of $a = 160\,s^{-1}$ unless otherwise noted, and numerical results that are shown as a function of strain rate are plotted at an equivalence ratio of $\phi = 0.650$.

We begin our examination of the sensitivity of premixed laminar CH_4H_2/air flames to inlet parameters by looking at the peak temperature in figure 3-3 as a function of equivalence ratio at a fixed strain rate and as strain rate at a fixed equivalence ratio. As we expect, there is a substantial increase in the peak temperature as the equivalence ratio increases, as shown in 3-3(a), corresponding to the increase in available reactants per unit volume of the reactant mixture for oxygen-deficient flames. In 3-3(b), we show the dependence of the peak temperature on the strain rate. We see that after a very brief rise in the peak temperature, it rapidly drops off as the strain rate continues to increase, which corroborates prior measurements and calculations [19, 57].

By enriching the CH_4 with H_2, we see that there is a small, but distinct increase
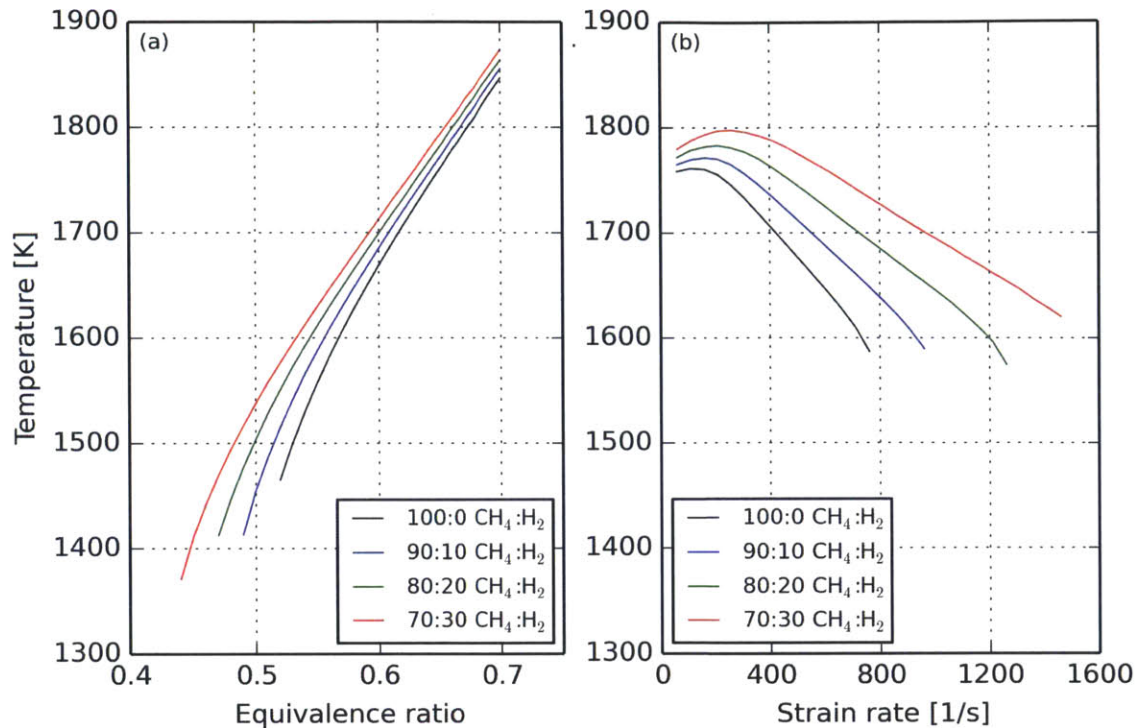
Figure 3-3: The adiabatic flame temperature is shown as a function of equivalence ratio (a) for a fixed strain rate of $a = 160\,\mathrm{s}^{-1}$ and as a function of strain rate (b) for a fixed equivalence ratio of $\phi = 0.650$.

in the peak temperature at low strains, which can be attributed to a change in enthalpy of the reacting mixture. For a given equivalence ratio, however, we see that at a fixed strain rate, increasing the H_2 fuel fraction has the effect of increasing the temperature, which is consistent with the concomitant decrease in Lewis number. The effect is more pronounced at higher strain rates, and we see that H_2 addition further serves to increase the strain rate beyond which we no longer have a viable flame (the extinction strain rate).

The laminar flame speed, shown in figure 3-4, was calculated by extrapolating the consumption speed (which will be discussed momentarily) to zero strain rate, to avoid the challenges of numerically stabilizing a flame in an unstrained flow field (in which a steady solution could only be obtained if the flow speed *exactly* matched the flame speed). The laminar flame speed is a monotonically increasing function of the
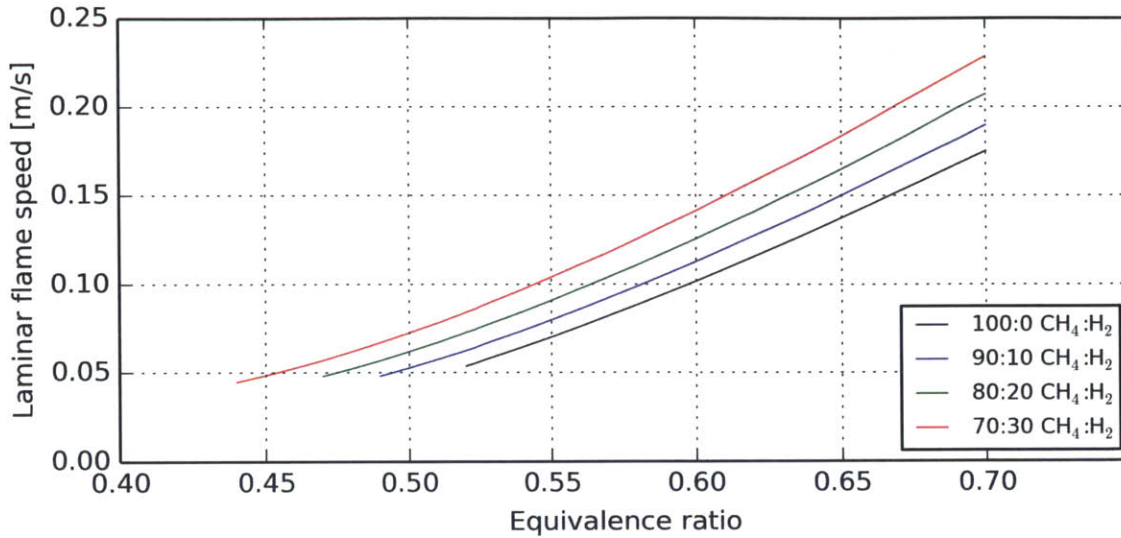
Figure 3-4: The laminar burning speed as shown as a function of equivalence ratio and fuel composition.

equivalence ratio for all fuel compositions. However, we observe that H_2-enrichment effectively enhances the laminar burning speed, and has a more pronounced effect as the equivalence ratio increases. A substantial body of work has shown the enriching hydrocarbon fuels, such as methane, with hydrogen increases the flame speed, which is often used to increase the static stability of the flame[58, 59, 60].

In the presence of non-zero stretch rates, the consumption speed may deviate substantially from the laminar flame speed, and a manner that is dependent on the particular composition of the flame, particularly accounting for Lewis number effects. In the consumption speed calculations shown in figure 3-5, the stretch rate has been quantified by the steady strain parameter, a, which was discussed at the beginning of this chapter. For a fixed strain rate, shown in 3-5(a), we observe much the same trend as we did with the laminar flame speed, with the consumption speed monotonically increasing as a function of the equivalence ratio. The consumption speed for a fixed equivalence ratio is shown in 3-5(b), however, and the we see a much different trend. We observe an initial decline in the consumption speed as the strain rate increases to 200 s^{-1} to 300 s^{-1}, followed by a gradual, monotonic increase until the extinction

66
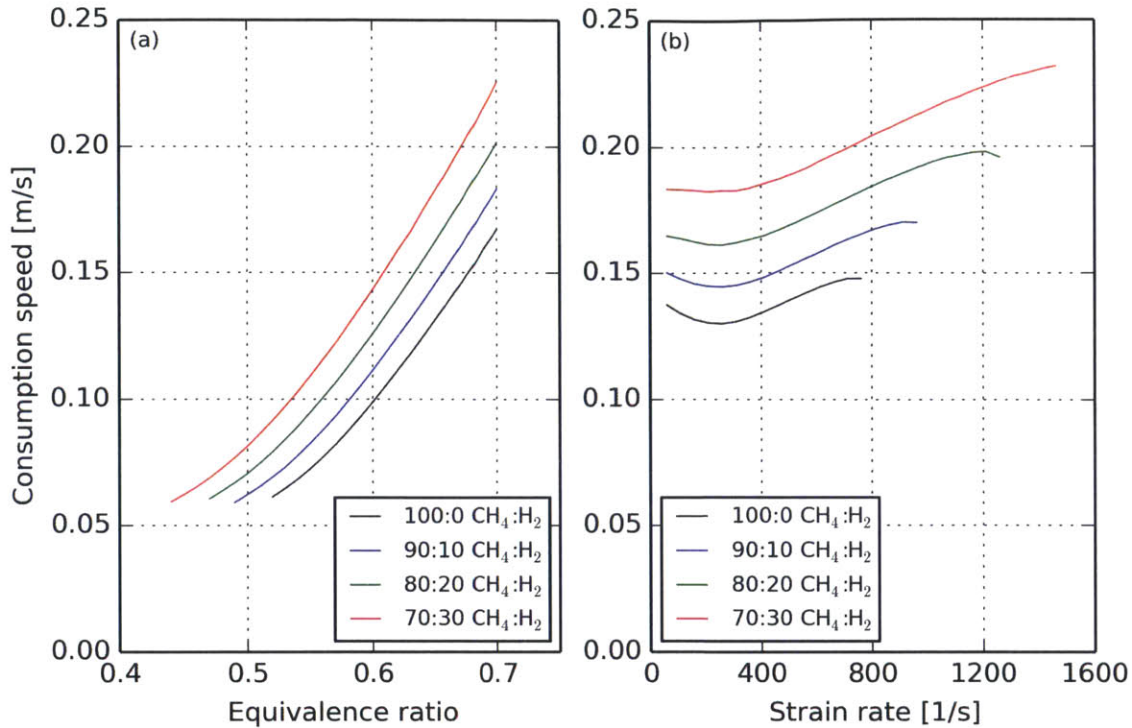
Figure 3-5: The consumption speed is shown as a function of equivalence ratio (a) for a fixed strain rate of $a = 160\,\mathrm{s}^{-1}$ and as a function of strain rate (b) for a fixed equivalence ratio of $\phi = 0.650$.

limit is reached. It is notable that as we enrich the flame with H_2, the flame speed, at a given strain rate, increases, which is what we should expect strictly from Lewis number considerations. At 20% H_2, the initial decrease in consumption speed is barely perceptible. Above this range, the consumption speed monotonically increases with increasing strain rate.

In figure 3-6, we show the ratio of the strained flame consumption speed to the laminar flame speed for comparison. At the fixed strain rate of 160 s^{-1}, we see that the ratio drops from about 1.3 to just below 1.0 as the equivalence ratio increases–a change that takes place as the chosen fixed strain rate sits at a decreasing fraction of the extinction limit of the particular flame. In 3-6(b), we see the ratio of the consumption speed to the laminar flame speed as a function of strain rate. We see that the effect of H_2-enrichment on this ratio, while changing the absolute value of
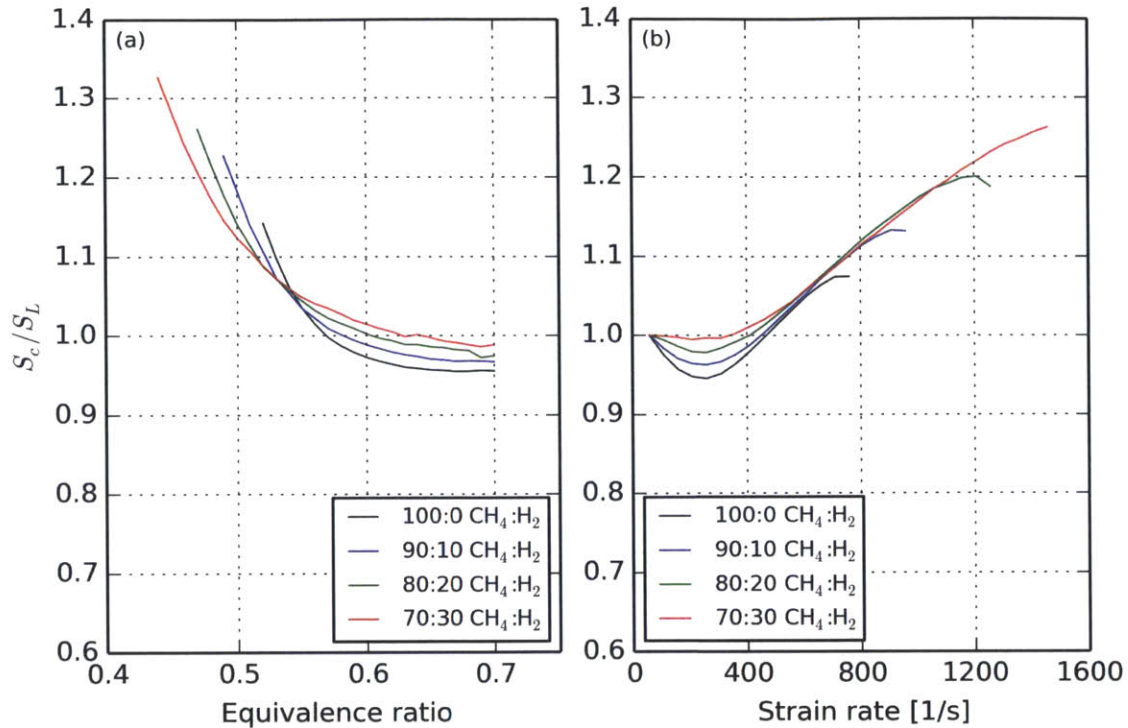
Figure 3-6: The ratio of the consumption speed to the laminar flame speed is shown as a function of equivalence ratio (a) for a fixed strain rate of $a = 160\,\mathrm{s}^{-1}$ and as a function of strain rate (b) for a fixed equivalence ratio of $\phi = 0.650$.

the laminar flame speed, is confined to the low-strain regime, where we observe the initial decline. Within this regime, the higher hydrogen fuels remain closer to the laminar flame speed. As the strain rate increases past $600\ \mathrm{s}^{-1}$, however, the curves coalesce (up until the extinction limits).

The density of the combustion products, shown in figure 3-7, at equilibrium primarily reflects the change in temperature with both equivalence ratio and strain rate, with compositional effects playing a very minor role. To a very good approximation, we can consider the combustion process as an isobaric increase in temperature. The concentration-weighted gas constant, which is a function of composition changes little compared to the temperature increase. As a result, we see the inverse relationship that we saw with peak temperature. The hydrogen-enriched fuels have a slightly lower equilibrium density than pure methane, however the effect is most pronounced

68
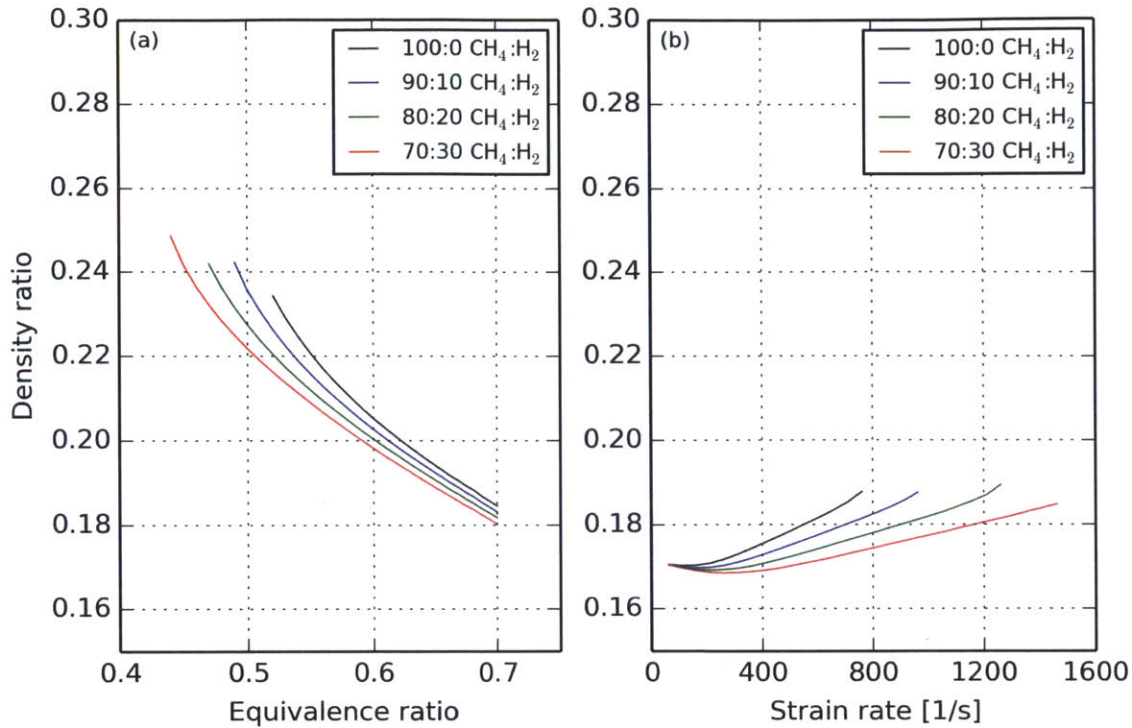
Figure 3-7: The equilibrium ratio of the product density to the reactant density is shown as a function of equivalence ratio (a) for a fixed strain rate of $a = 160\,\mathrm{s}^{-1}$ and as a function of strain rate (b) for a fixed equivalence ratio of $\phi = 0.650$.

at the lean end of the equivalence ratio range, and the curves run closer to parallel as stoichiometry is approached, as shown in 3-7(a).

The relationship between density and strain rate, shown in 3-7(b), follows a similar trend. A very brief reduction in density is observed, followed by a gradual increase as the post-reaction temperature decreases. However, as we should expect, the slope of the density decreases with the increase in hydrogen concentration due to preferential diffusion.

3.4   Extinction strain rate

In the chapters that follow, one of the critical aspects of strained flames that we will be discussing in the context of flame geometry is *flame extinction*, and how it changes with composition of the fuel and oxidizer. Flame extinction is an aerodynamically
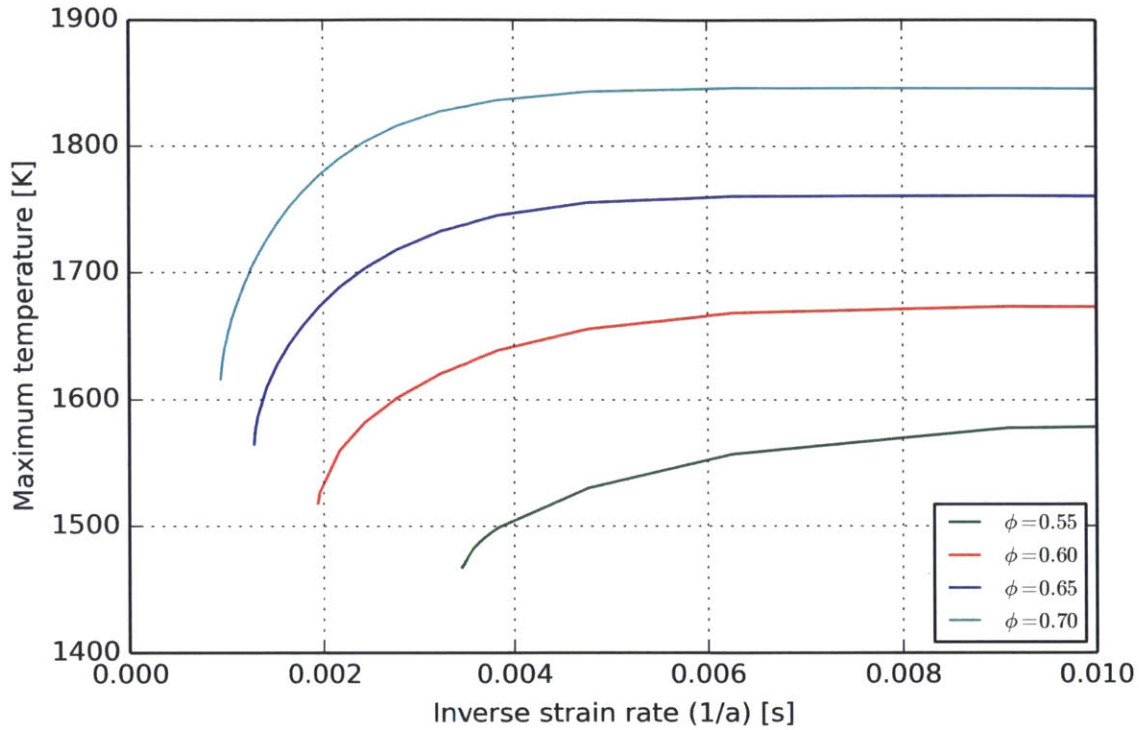
Figure 3-8: The maximum temperature is plotted versus the inverse strain rate for CH_4/air flame at several different equivalence ratios. The extinction limit is found where the gradient becomes vertical.

driven cessation of the reaction process that happens in the presence of high strain rates. For lean CH_4/air flames, this process is a result of flame stretch and the incomplete reaction [61, 62].

Classically, the extinction strain rate is computed by examining the relationship between the inverse strain rate and the peak temperature. Previous computational methods generated two solutions for the peak temperature for strain rates near the extinction limit, on either side of a Hopf bifurcation. The upper (higher temperature) branch of such computations corresponds to the physically realizable solution, while the lower branch corresponds to an non-physical solution. The extinction strain rate can be computed by following the curve, and locating the point where the derivative of the peak temperature with respect to the inverse strain rate becomes vertical.

Extinction then occurs where the following condition is satisfied:

$$\frac{dT_{max}}{d(1/a)} \to \infty \tag{3.12}$$

As we continue along the curve, the strain rate begins to decrease once again, and we find ourselves on a lower branch of the curve with lower values of T_{max}. Using Ember, a much more direct approach can be used. The flame is stabilized within the domain starting from a given initial profile. Attempting to stabilize a flame at high strain rate with poor initial conditions will lead to poor numerical behavior, and give an artificially low value for the extinction strain rate. However, beginning with a stable species profile at a relatively high strain rate, we can increase the strain rate in small steps, effectively feeding quasi-steady increments in the strain rate into the unsteady solver. A sharp drop in the peak calculated temperature (or volumetric heat release rate) is observed when the chemistry no longer allows a flame to stabilize. Before discussing the numerical results of the extinction strain rate calculations, we first turn your attention to figure 3-8, in which we plot the peak temperature against the inverse of the strain rate for CH_4/air flames at four different equivalence ratios. These points come from calculations made successively in increments of 5 s^{-1}, where the leftmost point of each curve is the last point calculated before the drop in the peak temperature. We see the expected behavior, wherein the derivative near the final strain rate (approximating the extinction strain rate) is approaching vertical. Confirming this observation, we calculate the extinction strain rate incrementally for each of the operating points of interest.

We turn our attention to figure 3-9, in which we show the calculated extinction strain rate as a function of equivalence ratio for the four fuel compositions of interest. We see two trends in the data. First, the resistance of the flame to extinction is strongly a function of the equivalence ratio. In the lean range over which we ran our calculations, the extinction strain rate increase by a factor of five to ten going from the leanest equivalence ratios (near the blowoff limit for our particular experiment) to the highest equivalence ratio of $\phi = 0.70$, which was chosen as an upper limit just

71
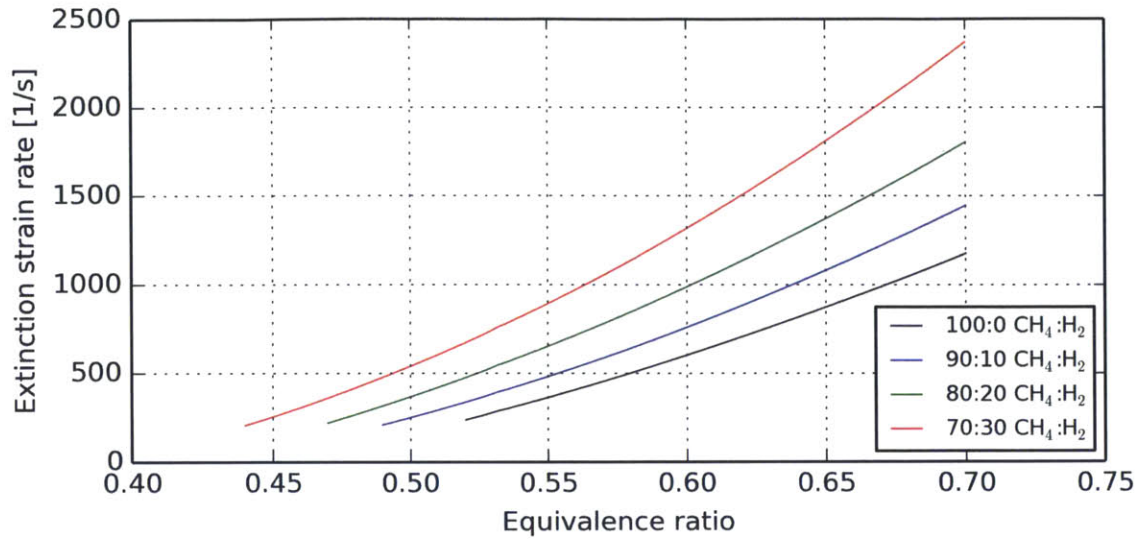
Figure 3-9: The extinction strain rate is shown as a function of equivalence ratio and composition for fuels H_2-enriched CH_4 ranging from 100% to 70% CH_4.

above the equivalence ratios that we will be considering in detail in the rest of this thesis. Second, H_2-enrichment has a non-linear effect, substantially enhancing the extinction strain rate as the equivalence ratio increases.

Chapter 4

Flame Geometry

In this chapter, we explore transitions in the flame geometry that take place under quasi-steady changes in the parameters of the combustion process. In particular, we will show that under identical inlet flow conditions, the flame stabilization is very strongly influenced by the chemistry, and particularly in a swirl-stabilized flow with numerous stationary flow structures and shear zones, the extinction limit of the strain rate. We undertake this investigation in anticipation of chapter 5, in which we will show that, irrespective of the particular fuel composition, the self-excited acoustic behavior of the system is determined by the coupling of the flame to the acoustic field, and that, in turn is very strongly a function of the flame geometry, rather than the finer details of the flame structure, which depend on the chemistry and transport properties.

The relationship between flame geometry and combustion instability is one that has been repeatedly observed, however, the mechanism linking the two remains open, particularly in the case of turbulent flames. Some studies, such as that of Kim *et al* [63] have looked to flame length, attempting to correlate this metric with the self-excited flame instabilities. Although some correlation can be drawn between a decrease in the flame length and an increase in the frequency of self-excited instability, the argument that this is more than an incidental correlation arising from the fact that flames that burn more vigorously in the conical section (consuming relatively more fuel in this region than downstream) also go unstable at higher frequencies is

not convincing. The flame length is short compared to the acoustic wavelength, yet very large compared to the diameter of any vortices that might be shed in response to the pressure oscillations. Likewise, the flame center of mass, the motion of which was discussed by Kim *et al* [64] while undergoing thermoacoustic oscillations, while implicitly accounting for more of the axial structure of the flame, fails to provide a clear physical connection between this virtual axial point and the physical processes that drive the oscillations. Nonetheless, this latter study does make note of an important property, which is the stabilization of the flame in the outer recirculation zone, which is observed under certain operating conditions.

In the domain of laminar flames, different flame geometries have been shown to have vastly different responses to acoustic forcing and consequently, very different thermoacoustic behaviors, with the differences of not being correlated to the upstream section of the flame that sits at an angle relative to the mean incoming flow direction. In particular, several studies [65] have investigated a series of different laminar flame shapes including the "V-flame" and "M-flame" which bear some relation to the flame geometries that we study here.

Turbulent flames, incorporating both a conical and outer flame, which undergo thermoacoustic oscillation have also been examined [66, 67, 68, 69]. Unlike their laminar counterparts, the M-flames, the flame front does not wrap around the entire jet in a steady manner, consuming all incoming reactants. Nonetheless, these flames do provide additional flame surface area in both the mean and instantaneous sense, and have been observed to vary substantially through the cycle of a thermoacoustic oscillation. Strong oscillations in the flame intensity near the boundary of the wall, the reactant jet, and the outer recirculation zone are often observed, and they frequently result in the extinction of the outer flame for some portion of the cycle.

In chapter 5, we focus on the influence of the flame shape on the forced acoustic response, and therefore, the self-excited acoustic behavior. In this chapter, we focus on the turbulent combustion aspect of how global combustion parameters affect the flame geometry. All of this work is predicated on the idea that the flame geometry can be described using a few parameters that are more fundamental to the combustion
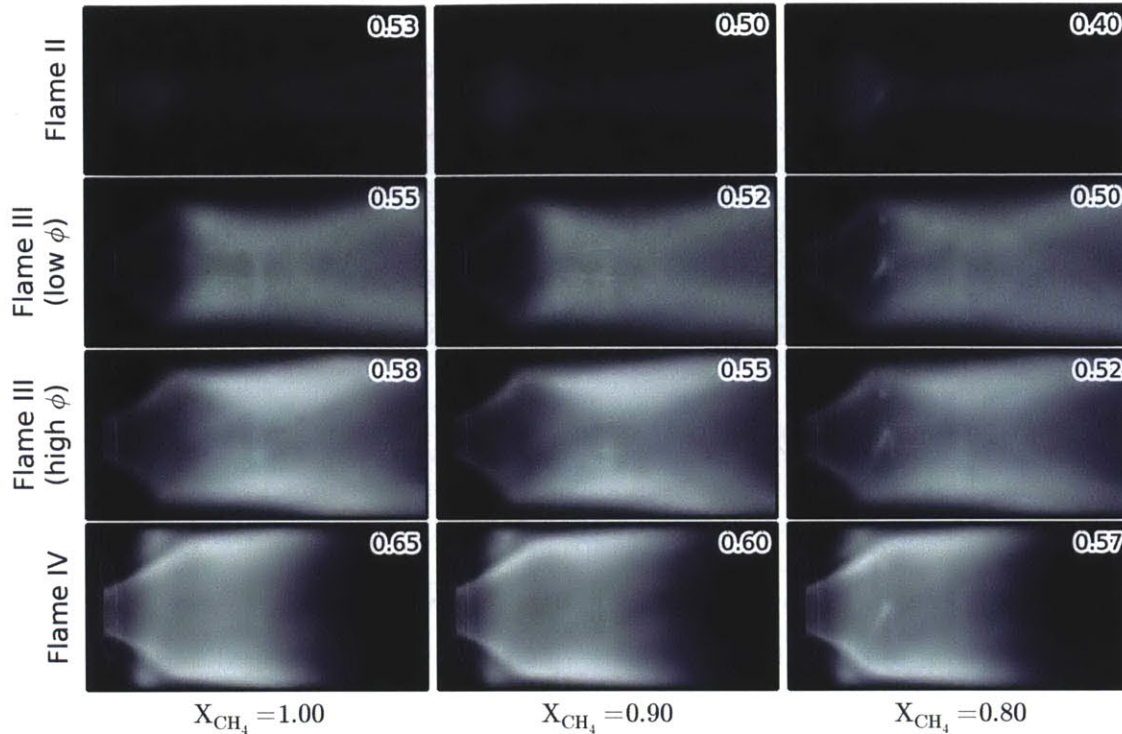
Figure 4-1: Visible light emission of the flame is shown for three different fuel compositions over a range of operating conditions that correspond to very similar flame shapes. The left column shows pure CH_4, the center column shows a blend of 90% CH_4 and 10% H_2, and the right column shows a blend of 80% CH_4 and 20% H_2. The equivalence ratio for each image is displayed in the upper right corner.

process than the particular details of the chemistry, and thus, that there is some hope of reducing the complexity of multiple fuels and fuel compositions. We begin by adding weight to this idea by showing the flame geometry for several different CH_4/H_2 fuel blends and several fuel compositions within each blend in figure 4-1. The figure shows IR-filtered flame images taken with an exposure time on the order of $O(10\,\mathrm{ms})$, and therefore, they represent ensemble averaged flames. All of these images were taken with the combustor in the short configuration, in the absence of acoustic coupling. Within each column, representing a particular fuel composition, we see a very similar progression as we go from low equivalence ratios, not far from the lean blowoff limit (top row), to sequentially higher equivalence ratios. We start off with a long bubble flame, which we have called flame II, and progressively advance into

a conical flame, which is eventually accompanied by a flame in the outer recirculation zone. Although the equivalence ratio at which we observe these different geometries changes with the fuel composition, we nevertheless see the same progression and the same geometries, suggesting that there a more fundamental parameter does exist.

4.1   Relationship to dynamic instability

Having found that the flame geometry is a function of combustion parameters that are more physically fundamental than fuel composition and equivalence ratio, we now look toward understanding the relationship, if one exists, between the geometry and self-excited acoustic instabilities. We previously observed a series of flame geometries that were common to three different blends of CH_4 and H_2, albeit at different equivalence ratios for each particular blend, and we showed images of three geometries that we will be paying particular attention to throughout the remainder of this thesis. These flame images were all shown under acoustically uncoupled conditions. That is, we took these images using the short combustor configuration and the equivalence ratios at which they were taken did not exhibit coupling at any particular frequency or set of frequencies. In order to study these geometries in detail over the next several sections, we wish to isolate them from potentially confounding oscillations that are not a direct result of the flame behavior, but of the weak coupling within the system. Nevertheless, we must first ensure that we are studying equivalent flames under uncoupled conditions as we would be under coupled conditions.

In figure 4-2, we show CH^* chemiluminescence images of CH_4 flames that have been deconvolved using a three point Abel inversion. In the left column, we show images of flames taken in the long combustor configuration, which do undergo self-induced acoustic oscillations, and in the right column we show images that were taken using the short combustor configuration, which do not undergo such oscillation save for at high equivalence ratios (and, in fact we do see coupling in both system at $\phi = 0.650$). At the top, we show an image of flame I, the leanest flame. This is a particularly weak flame with all of the reaction taking place very near the centerline.

76
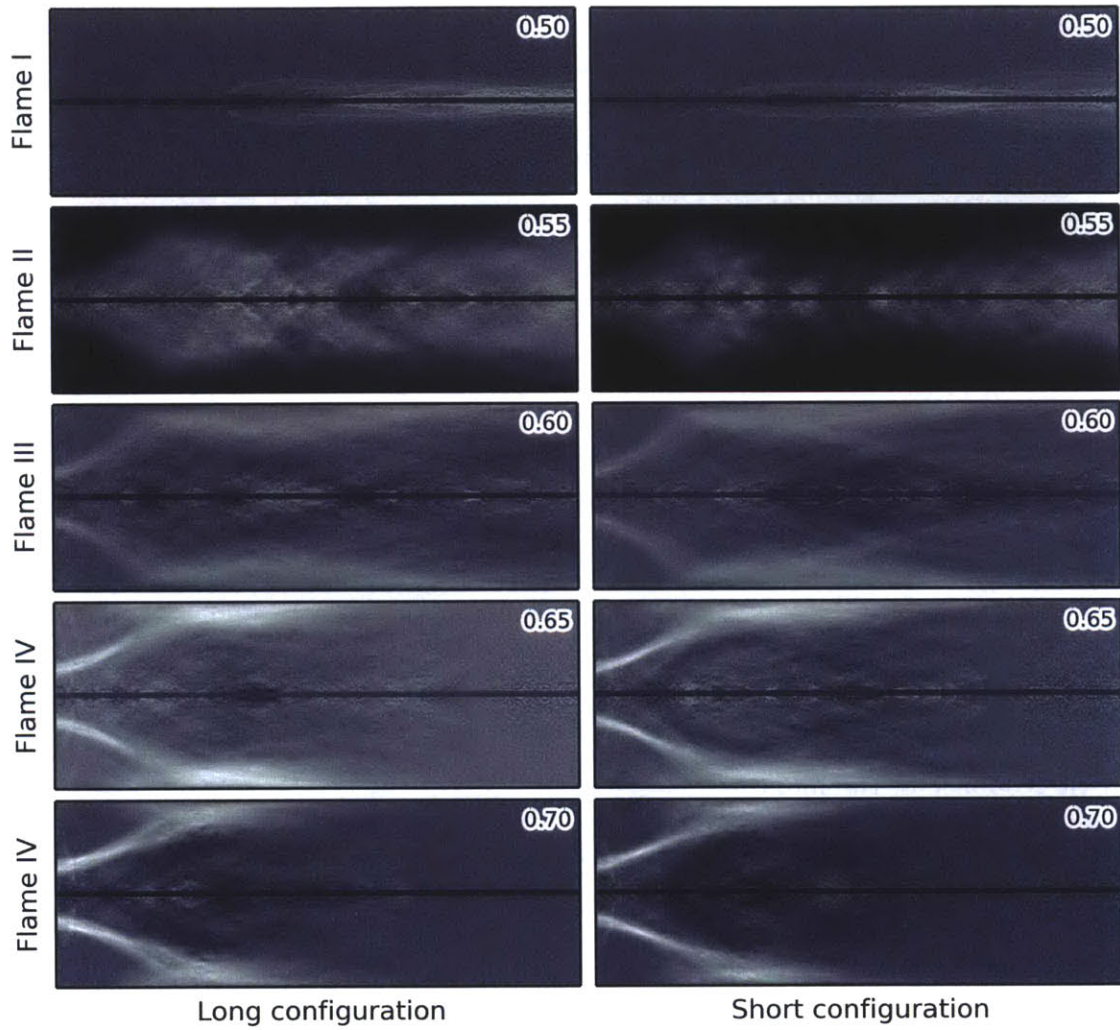
Figure 4-2: CH* filtered flame images for pure CH_4 flames from both the long and short combustor configurations have been deconvolved using an inverse Abel transform to show that the same structures are observed at the same operating points under both acoustic boundary conditions. The equivalence ratio of each image is shown in the top right.

The reactants are not completely consumed within the combustion chamber and the flame extends downstream into the exhaust. Flame II, shown below, is characterized by the confinement of the flame to the inner recirculation zone. Making note that these images are deconvolved, we can clearly see that the flames are confined to and distributed within the interior of the bubble, as well as downstream, ultimately extending into the exhaust.

Above $\phi = 0.560$, we see the flame enter the shear layers, and the devonvolutions of the flame III and flame IV show that while the interior of the inner recirculation zone is generally clear of any reaction, the CH* signal is concentrated near the edges of the image along the wall, in the conical region corresponding to the jet or inner shear layer, and in the case of flame IV, wrapping around through the jet, and into the outer recirculation zone. Critically, we see nearly identical structures with both acoustic boundary conditions, from which we can posit that the same flame stabilization mechanism are at play. This allows us to investigate the flame stabilization independent of the weak acoustic oscillations, or in the case of higher equivalence ratio, strong acoustic oscillations that do affect the stabilization in this chapter, and in chapter 5, it will allow us to consider the affect of flame geometry on the forced acoustic response of the flame.

To support the hypothesis that the flame geometry is a critical, if complex, parameter that governs dynamic coupling with the acoustic field, we show how the transitions in the geometry relate to the transitions in the dynamic behavior in figure 4-3. We map the sound pressure level as a function of frequency and equivalence ratio for three different CH_4/H_2 fuel combinations. These are the same maps that we have shown previously in chapter 2. In this figure, however, we have indicated, by dashed red lines, the transitions between different flame geometries and labeled each section by the name that we have assigned to each geometry. We see that flames I and II are very quite flames with no discernible signal above the broad spectrum turbulent noise. As the structure of the flame changes to that of flame III, we begin to detect a weak, self-excited oscillation at 40 Hz. Although the amplitude is too low for this oscillation to be classified as an instability under the guidelines that have previously
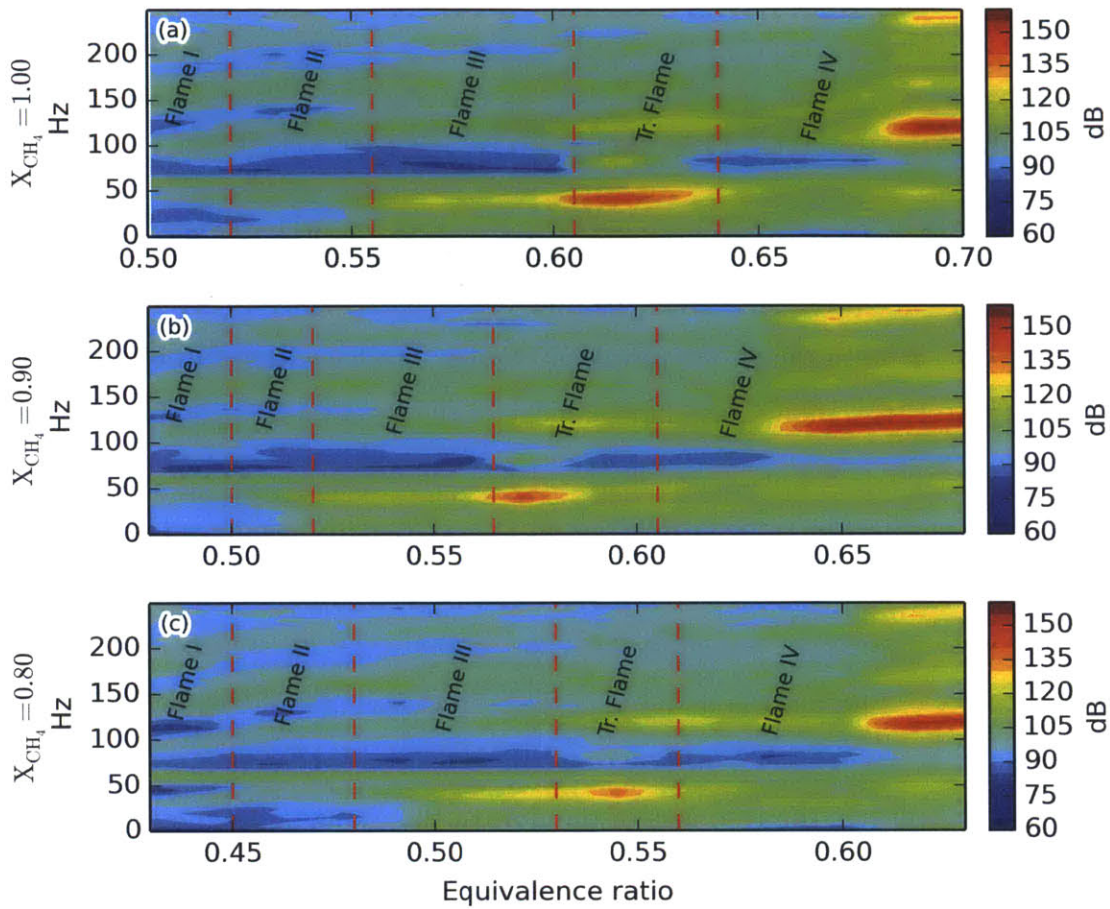
Figure 4-3: The transition points between different flame geometries, based on the uncoupled configuration, are marked on the sound pressure level maps, based on the coupled configuration, for three different fuel compositions from pure CH_4 to a mixture of 80% CH_4 and 20% H_2.

been used with this combustor, namely there is no appreciable increase in the overall sound pressure level, the sound pressure level map does show weak coupling in this regime. The onset of the transitional (or "flickering") flame corresponds to a sudden increase in the sound pressure level at 40 Hz and the overall sound pressure level in the combustor. There is a weaker correlation between the transition to flame IV geometry and the disappearance of the 40 Hz acoustic mode, however as we will show in chapter 5, this is most likely the result of a change in the stationary acoustic frequencies in the system with an increase in the response of the flame to acoustic

perturbations.

4.2 Flame geometry and flow structure

In this work, we focus our attention on four flame geometries: flame II, flame III, flame IV, as shown in figure 4-2, and the transitional state between flames III and IV that we observe over a finite range of equivalence ratios. We have already observed that the geometries of these flames are independent of the acoustic boundary conditions, allowing us to study their structure in the absence of acoustic velocity fluctuations, and we have seen that the same geometries are observed across a range of fuel compositions, suggesting that the geometry is dependent on a more fundamental parameter of the combustion process.

We begin by examining the underlying flow structures. All of the flames that we consider share the same basic flow structure, characteristic of columnar swirling flows, however, as we will see, the response of the flow to the changing geometry results in important quantitative and qualitative changes to the structure of the flow. Nonetheless, there are some features in common. As the flow passes through the inlet into the combustion chamber, it is subject to a rapid deceleration due to the sudden expansion into a chamber with four times the cross sectional area. The deceleration results in an adverse pressure gradient, which amplifies instability in a swirl flow, leading to the phenomena known as vortex breakdown [70]. Inducing vortex breakdown in this manner ensures that the bubble forms in a predictable location, as in the absence of such a pressure gradient, the position of the vortex breakdown is very sensitive to the inlet conditions [71]. When vortex breakdown occurs, the strong axial vortex lines tilt 90°, forming a strong recirculation zone, known as the inner recirculation zone, in the center of the flow, forcing the incoming jet to divert around this bubble [72]. Due to viscous effects at the boundaries, the jet propagates into the combustion chamber at an angle less than 90°, creating a secondary recirculation zone, known as the outer recirculation zone, bounded by the expansion plane, the combustor wall, and the jet itself.
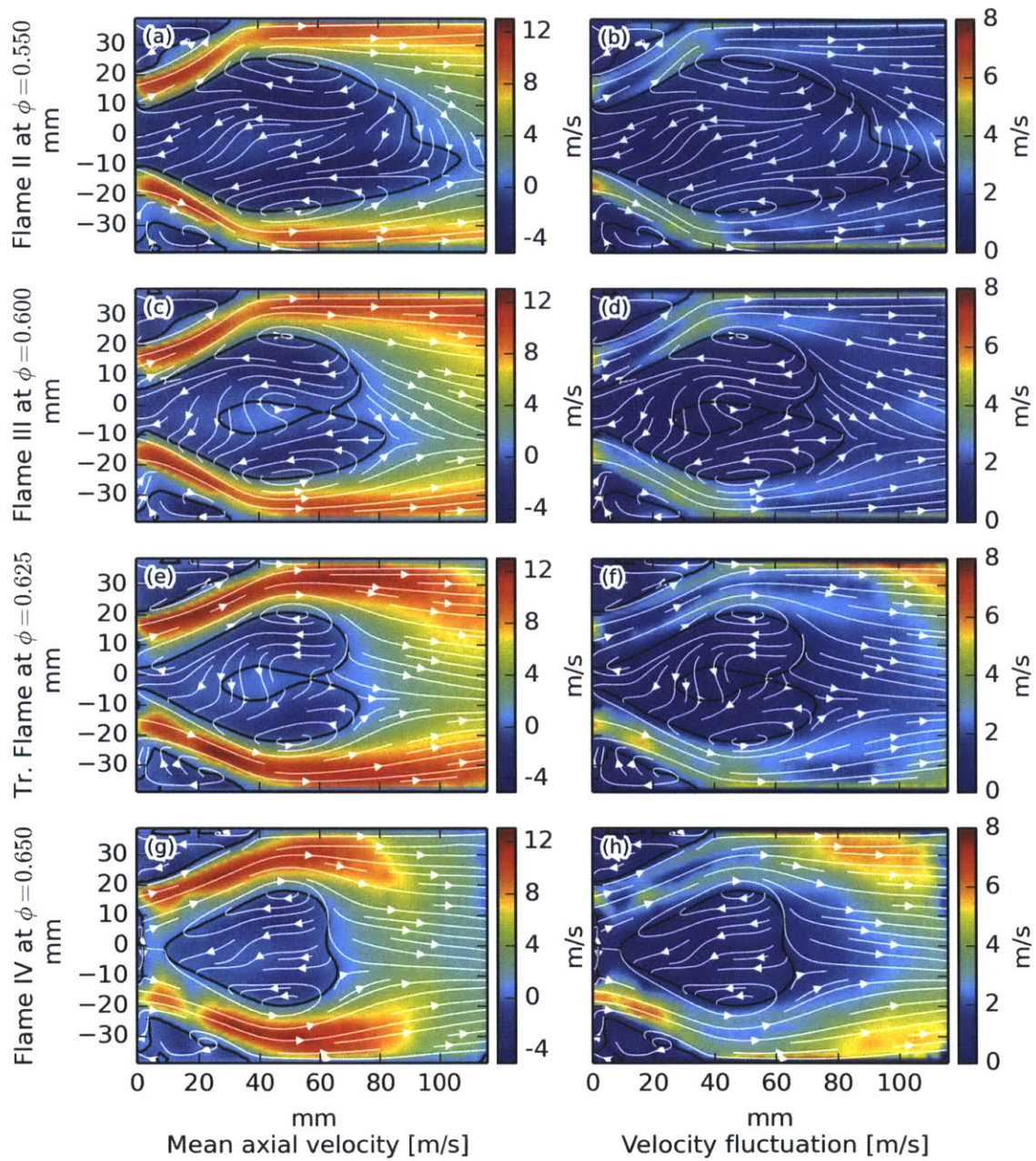
Figure 4-4: Mean axial velocity (left) and turbulent fluctuations (right) are shown for four flame geometries at different equivalence ratios in pure CH_4.

Vortex breakdown is a critical part of the design of swirl-stabilized combustors [73]. In a gas turbine combustor, the use of a swirling flow provides a convenient mechanism of recirculating hot combustion products into the recirculation zone. This brings the hot gases in contact with the fresh reactants, facilitating ignition. Vortex breakdown is inherent to swirling flows, although the particular form that the breakdown takes is dependent on such parameters as the Reynolds number and the swirl number–the ratio of axial momentum times the radius of confinement to the axial flux of tangential momentum.

As a consequence of the rapid flow reversal, a pair of shear layers is created between the annular jet of reactants and the two recirculation zones. These shear layers, however, can produce sufficiently high rates of strain on the flame such that they can cause flame extinction, which we will show evidence for later in this chapter.

As the flame geometry changes, via quasi steady changes in the operating parameters, and particularly for our purposes, the equivalence ratio, the flow field adjust to the new flame properties, including the burned gas temperature and the flame location. In figure 4-4, we show some basic statistics of the flow, and their evolution with the equivalence ratio. In the left column, we plot the mean axial velocity, with overlying mean streamlines. Black contours divide forward propagating flow from backward propagating flow, serving as surrogate markers for the location of the two recirculation zones. In the right column, we plot the turbulent velocity fluctuation throughout the interrogation window, along with the same mean contours of zero axial velocity and mean streamlines to serve as spatial references.

We begin by examining flame II, the long bubble flame that we observe in the interior of the inner recirculation zone. The mean flow field for this flame is shown in 4-4(a), and the turbulent fluctuations are shown in 4-4(b). The flow is dominated by a single, large inner recirculation zone that is composed of a single large vortex ring. The recirculation zone extends upstream past the expansion plane and to the swirler center body, and downstream approximately 110 mm downstream of the expansion plane. The incoming jet of reactants splits around the leading side of the recirculation bubble, coming in contact with the combustor wall 35 mm downstream

of the expansion plane, after which, it turns nearly parallel to the wall. Although the experiment is nearly radially symmetric, and those asymmetries that do exist in the inlet (the presence of an opposed pair of spark igniters to provide the initial ignition energy) have been carefully aligned to be symmetric with respect to the plane of measurement, we do observe slight asymmetry in the mean flow. The greatest axial extent of the recirculation zone lies approximately 5 mm off of the centerline, which could be due in part to the particular form of vortex breakdown as well as slight asymmetries in the surface boundary conditions in the inlet. Some measure of asymmetry should be expected. While the assumption of a perfectly symmetric vortex breakdown leads to many useful conclusions and remains a useful tool, experimental observations do not yield perfectly axisymmetric recirculation bubbles, and the details of these asymmetries may underly the transitions between various forms of vortex breakdown [74].

The turbulence is moderately strong in the conical section of jet, but is low elsewhere throughout the flow, particularly in the inner recirculation zone, which sees fluctuations on the order of the 50 cm/s or less, and in the downstream region, beyond the end of the recirculation zone. Although the jet velocities remain high, between 8 and 10 m/s in the downstream region, the gradual tapering of the downstream portion of the recirculation bubble slowly expands the jet back toward the centerline, likely keeping the downstream behavior of the jet more steady.

We show the mean axial and fluctuating corresponding to flame III in 4-4(c) and 4-4(d). Compared to the flow corresponding to flame II, the most striking difference that we observe is the change in the structure of the inner recirculation zone from a single vortex ring to a pair of counter-rotating vortex rings, the result of which is to create an inner recirculation zone with a small region of forward propagating flow in the center, similar to the structure reported by Faler and Leibovich [75]. As before, we notice a slight asymmetry in the mean flow. Novak and Sarpkaya [76] observed that the both spiral type bubbles and the double celled vortex breakdown bubbles could be observed in the flows with Reynolds numbers on the order of 10^4, however, they observed that the double cell structures were less robust and subject to additional

influences such as the local turbulence intensity. This is most clearly observed by looking at the contours that denote zero mean axial velocity. In conjunction with this structural shift, the recirculation zone contracts. Although it still extends upstream past the expansion plane, it only extends 85 mm downstream of the expansion plane. In conjunction with the decreasing extent of the recirculation bubble, the jet expands from the walls back to the centerline over a shorter distance, and we see a slight increase in the turbulence within the jet downstream of the impingement point. In addition to the contraction of the inner recirculation zone, we begin to see the neck of the bubble, which extends past the expansion plane, begin to pinch. Whereas the neck of the bubble was 20 mm in diameter at $\phi = 0.550$, at $\phi = 0.600$, it is only 15 mm in diameter.

The transitional flame represents a transitional case, in which we observe flickering of the flame in the outer recirculation zone, and as we will see in the next section, a intermittent transition between two different flow structures. However, in figure 4-4(e) and 4-4(f), we consider only the mean axial and fluctuating statistics of the flow. The mean recirculation zone is double-celled, similar to that which we observe in flame III, however the bubble continues to contract, now extending only 70 mm downstream, while the neck of the recirculation zone that extends upstream of the expansion plane has contracted to only 5 mm, and the maximum width of the recirculation bubble has decreased from 50 mm in flame II to 40 mm in the transitional flame. Notably, however, the mean flow corresponding to the transitional flame is much more symmetric than what we have observed with either of the previous cases.

The expansion of the jet in the downstream region occurs over yet a shorter distance. We begin to see an increase in turbulence in the downstream region, emanating from the wall and moving toward the centerline. We observe that the streamlines nearest the wall, downstream of the jet impingement point begin to angle inward rather than run parallel to the wall as in the previous two cases. Together, these two observations suggest that the flow separates from the wall downstream of the interrogation window. This may be expected when we consider the interaction between the jet and the recirculation bubble. The bubble forced the jet to contract, increasing speeds in

the jet. Downstream of the bubble, the jet expands and slows, setting up an adverse pressure gradient, which become stronger as the recirculation bubble contracts and the expansion becomes more rapid.

Finally, we examine the flow statistics corresponding to flame IV in 4-4(g) and 4-4(h). At this condition, the inner recirculation zone has transitioned to a symmetric, single-celled structure, however, it has undergone a series of other substantial changes as well, which lead to this structural change. As Novak and Sarpkaya note, the spiral type vortex breakdown bubble is apparently the most fundamental type of breakdown. Such spirals, rotating at extremely high frequencies create the characteristic bubble that is observed at high Reynolds numbers, however the prediction of how a vortex breakdown will manifest itself given the properties of circulation, Reynolds number, turbulence intensity, and so forth remains elusive, even in the absence of reacting flows. The neck of the recirculation zone has completely pinched off, and there is a free stagnation point 10 mm downstream of the expansion plane, while the recirculation zone now only extends 65 mm downstream of the expansion plane. The width of the inner recirculation zone has contracted to approximately 36 mm, and we see that the intersection of the zero axial velocity contour that separates the outer recirculation zone from the jet has suddenly shifted 5 mm downstream. The latter observation can be accounted for by noting that flame IV is characterized by a persistent flame in the outer zone, which means that the outer recirculation zone is now filling with low density products rather than high density reactants. Downstream of the inner recirculation zone, the jet expands very rapidly, as we see it effectively disappear approximately 90 mm downstream of the expansion plane, replaced by a zone of high intensity turbulence, due to the pressure gradients formed by the sudden expansion of the jet in the wake of the inner recirculation bubble.

As we increase the equivalence ratio, we have seen that the mean structure of the flow undergoes several very distinct changes. Furthermore, we have observed an increase in symmetry concomitant with this increase. The presence of the flame, and the increasing temperature of the burned gas products undoubtedly plays an intricate role in driving these changes. To first order, we might suggest that the

changes might be associated with changes in swirl number in the post-combustion region. The expansion of the flow through the flame in the axial direction (and the very low production of angular momentum through baroclinic torque) serves to decrease the swirl number, however, the still-controversial literature on the subject which we have discussed above does not provide much confidence that a change in a global parameter like the swirl number can so easily be causally linked to the observed changes. Rather, the answer is likely linked to much more subtle details of the flow.

In figure 4-5, we show the same flow structures in a a different light. Rather than plotting statistical quantities, we plot a pair of (uncorrelated) instantaneous flow fields at each of the equivalence ratios that we are examining. The vectors correspond to the instantaneous direction and magnitude of the velocity, while the colormap separates forward flowing from recirculating regions. The instantaneous flow fields of flame II show a very strong similarity to the mean flow field. In 4-5(a), we observe a particularly strong recirculation in the lower half of the snapshot, and a very small region of forward flow, within the center of the recirculation zone, although there is no coherent vortex associated with it, so this could simply be the result of turbulent fluctuations. In 4-5(b), the strongest recirculation is in the top of the snapshot. In both instances, the jet expands slowly downstream int he wake of the recirculation bubble.

Flow fields corresponding to flame III are shown in figures 4-5(c) and 4-5(d), and qualitatively very similar flow fields corresponding to the transitional flame are shown in figures 4-5(e) and 4-5(f). The two realizations of the flame III flow field show a transitory nature of the inner recirculation zone structure. In 4-5(c), we see the recirculation zone split by a region of forward flow along the centerline, whereas the axial extent of this forward flowing region is greatly reduced in 4-5(f). In all four of these realizations, the jet gradually expands as it progresses farther downstream. While we start to see some significant deviations from the parallel to the centerline near the wall at the downstream end of the interrogation window in 4-5(e) and 4-5(f), the deviations from parallel are gradual.

The contraction of the inner recirculation zone at $\phi = 0.650$, and the result of this
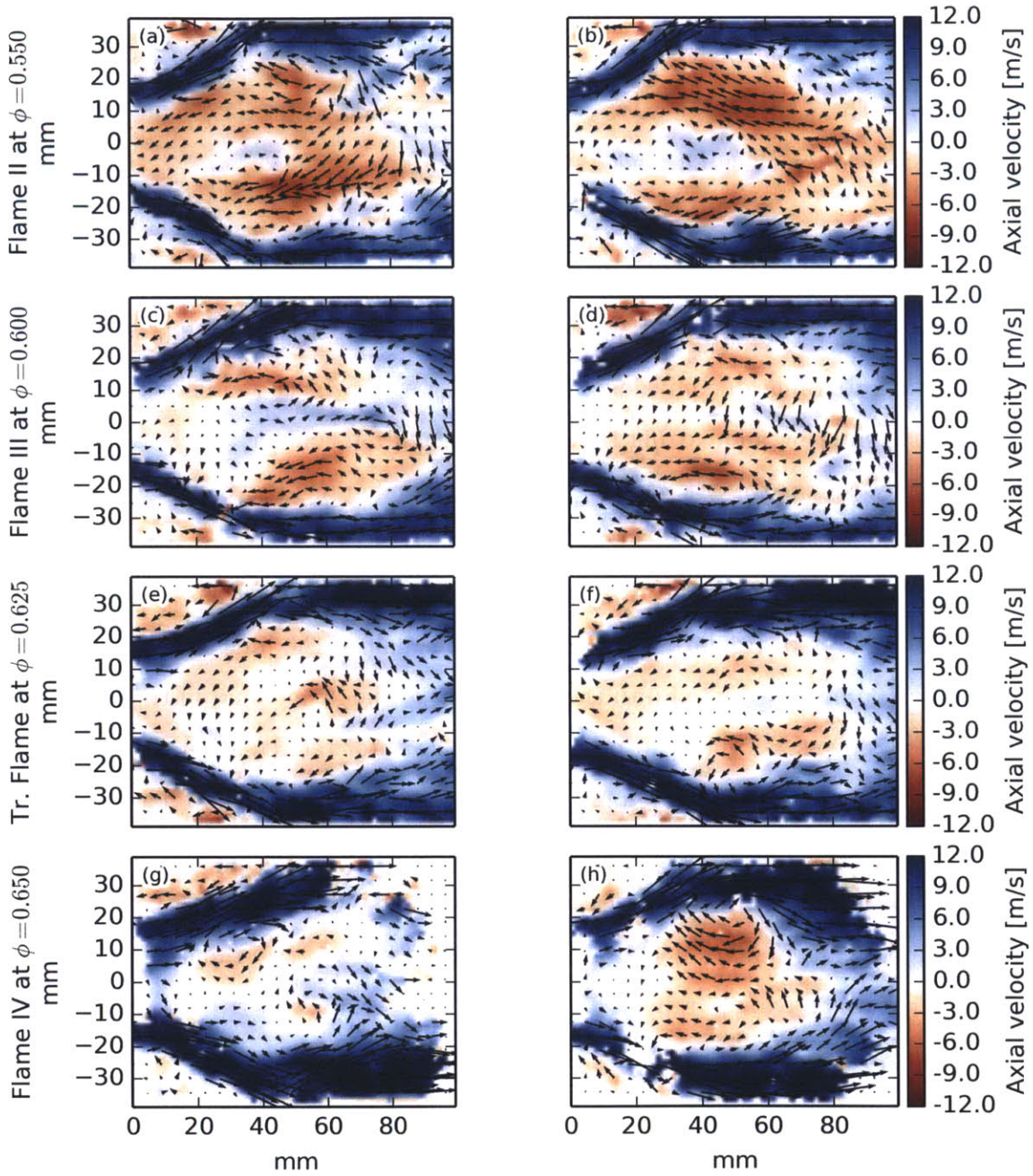
Figure 4-5: Two (uncorrelated) instantaneous realization of the flow field are shown for each flame geometry.

contraction on the jet is apparent in figures 4-5(g) and 4-5(h). In both snapshots, the inner recirculation zone has a free stagnation point in the upstream region, and terminates abruptly downstream, resulting in rapid expansion of the jet beyond this point. In the upper half of 4-5(g), we see that this results in complete separation of the jet from the wall, with low overall flow speeds and significant excursions from parallel to the wall, with small pockets of recirculation.

4.2.1 Outer zone intermittency

The transition between flames III and IV presents an interesting case. The transition occurs over a finite range of equivalence ratios, in between which, we observe the flame intermittently entering and exiting the outer recirculation zone or, "flickering." This is shown in the sequence of CH* filtered flame images in figure 4-6, which was captured at a fixed equivalence ratio of $\phi = 0.625$ in pure CH_4. In the first two snapshots, we see a conical flame, qualitatively similar to flame III. In the third snapshot, we see a flame in the outer recirculation zone in the lower half of the image. In the fourth snapshot, the flame has rotated into the upper half of the image, and in the fifth and sixth snapshots, we see a flame in both sides of the outer recirculation zone. In the seventh snapshot, the outer flame only exists in the lower half of the image, and by the eighth snapshot, the flame is completely extinguished in the outer recirculation zone. This flickering, which involves the intermittent ignition and extinction of a flame in the outer recirculation zone is a persistent feature of this range of operating points, and this behavior is repeated as long as the combustor is held within this range of equivalence ratios.

We can examine this phenomena by taking a more quantified look at the chemiluminescence. In figure 4-8, we have analyzed the chemiluminescence signal in the outer recirculation zone for three operating points, corresponding to flame III at $\phi = 0.600$, right before the onset of flickering, the transitional flame at $\phi = 0.625$ while we observe flickering, and flame IV at $\phi = 0.650$ once the flame in the outer recirculation zone becomes persistent and we observe no more flickering. For each case, we define the outer recirculation zone by calculating the sign of the mean flow from PIV mea-
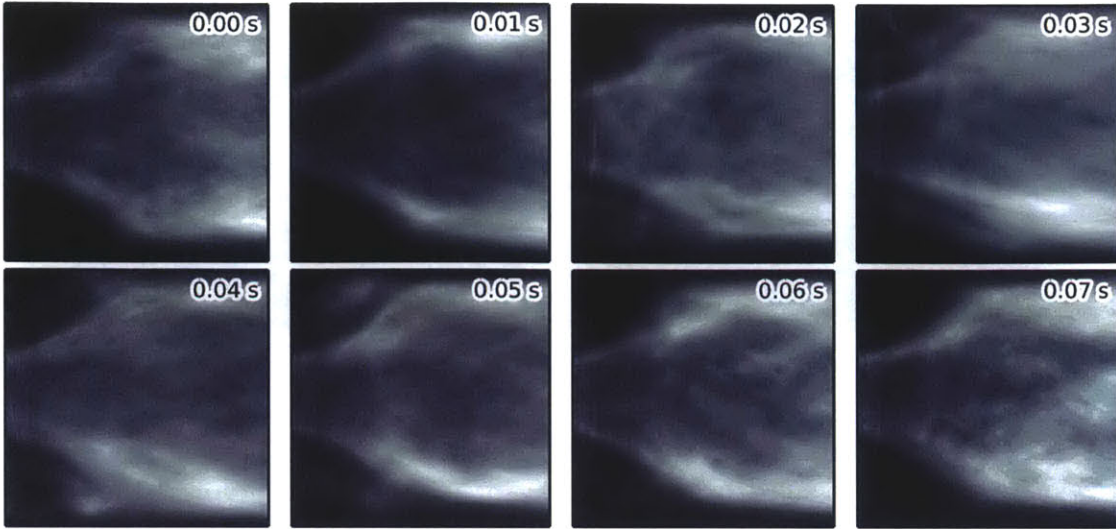
Figure 4-6: A sequence of CH* chemiluminescence images taken at 10 ms intervals show a flame entering the outer recirculation zone before being rapidly extinguished.

surements, and take the connected region of mean reverse flow in the upper corner of the flow field near the expansion plane as the spatial extent of the eddy.

We then apply this spatial mask to individual chemiluminescence images that were captured at a 100 Hz frame rate. The two spatial masks are shown in figure 4-7, corresponding to the upper and lower branches of the flame. We present results for the lower branch, but identical conclusions could be drawn from either. Under the assumption that the heat release rate in this region is proportional to the total intensity in this value, we create a single intensity value for each snapshot by summing up the intensity within the spatial mask. Since we are trying to measure the underlying motion of the flame in the outer zone, we do not correct for line-of-sight integration from the camera, and so we see local maxima in this signal when the flame either encompasses the entire outer recirculation zone, or otherwise rotates into the plane of the image. In the left column of figure 4-8, we show this raw intensity signal as a function of time for each of the operating points. The experiments were conducted using the same filters, camera aperture settings, and lighting conditions, allowing us to compare the absolute value of the intensity signal across conditions. The signal

89
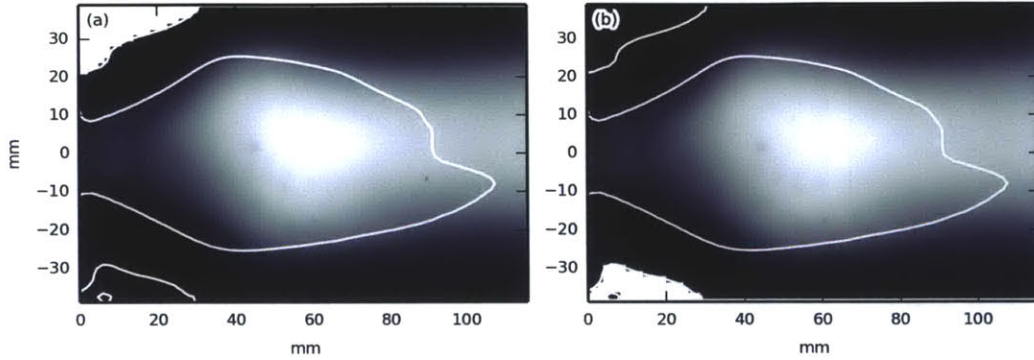
Figure 4-7: Masks for the outer recirculation zone are calculated based on the mean zero velocity contours derived from PIV data for each case and applied to chstar-chemiluminescence images. The masks, shown in white, for the upper (a) and lower (b) branches of the outer recirculation zone are applied to flame II at $\phi = 0.550$.

corresponding to flame III, shown in 4-8(a), gives us a low, and relatively flat signal, which, combined with the spatial information from the chemiluminescence, tells us there is very little CH* observed in the outer recirculation zone under these conditions. The signal for flame IV, shown in 4-8(e), however, shows a uniformly high signal, corresponding to a persistent flame in the outer recirculation zone, however, we do see some unsteadiness in the signal. The signal for the transitional flame, shown in 4-8(c) is more complicated. We see intermittent spikes in the CH* intensity, often followed by a short series of high frequency oscillations before the signal drops to a baseline value. This pattern is repeated many times throughout the full time signal.

Of the three frequencies that we have identified, the 28 Hz periodicity has a clear origin. In figure 4-9(a) we show the integrated intensity time signal for the upper and lower halves of the recirculation zone independently, and unsurprisingly, we see very similar waveforms. We take the Fourier transform of both of these signals and plot the phase angle between these signals as a function of frequency in 4-9(b). Most frequency components have a similar phase, within 90°, with one notable exception. We see a phase difference of nearly 180° at 28 Hz. Since the two signals come from two regions that are physically separated by 180° in a rotational flow, we can conclude that this is the frequency at which the flame is advected about the axis of symmetry
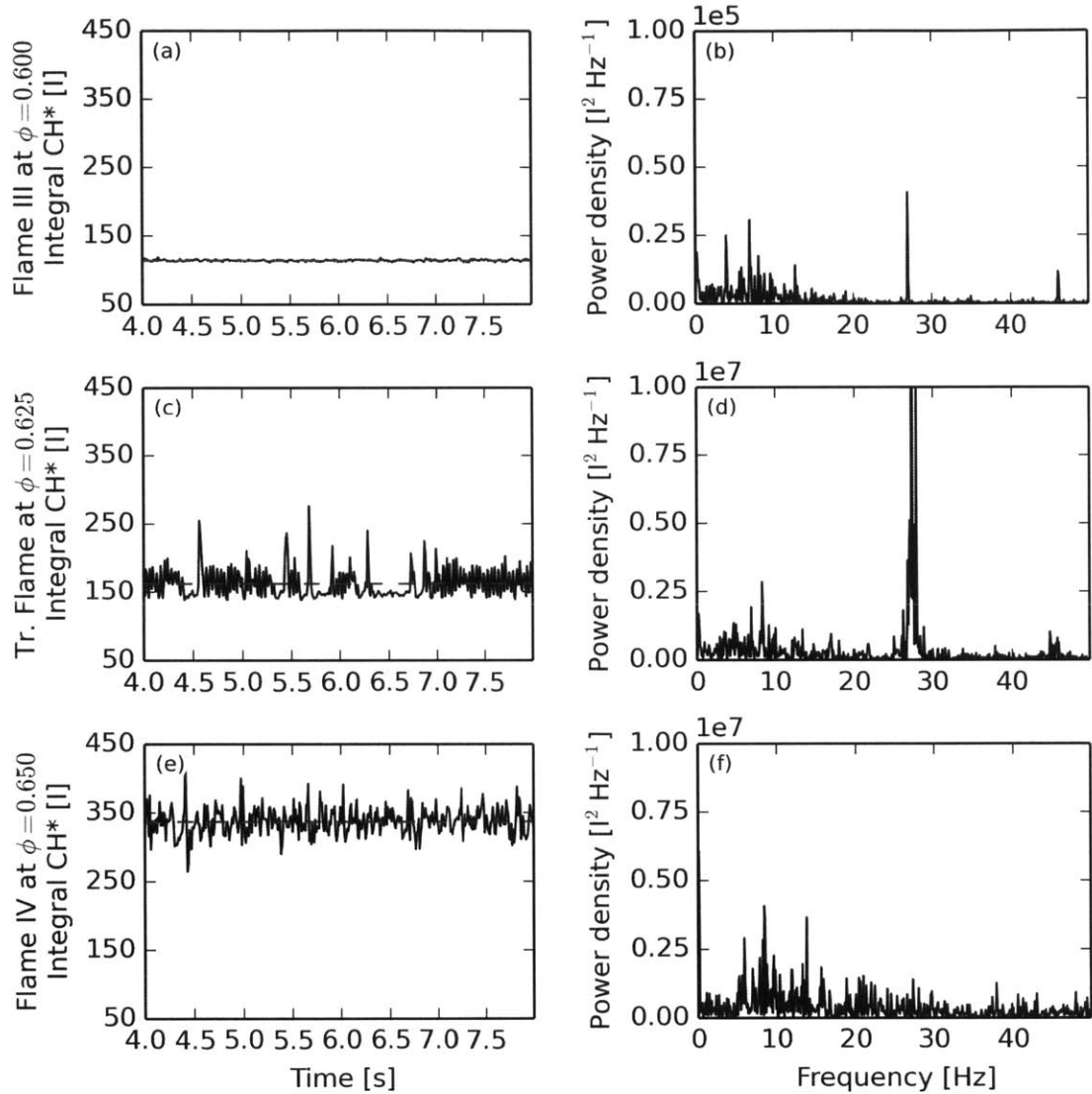
Figure 4-8: The integrated CH* signal in one branch of the outer recirculation zone is plotted as a function of time (left column) for flame III, the transitional flame, and flame IV. The power spectral density for these signals is plotted (right column) showing three distinct peaks at 4 Hz, 8 Hz, and 28 Hz.
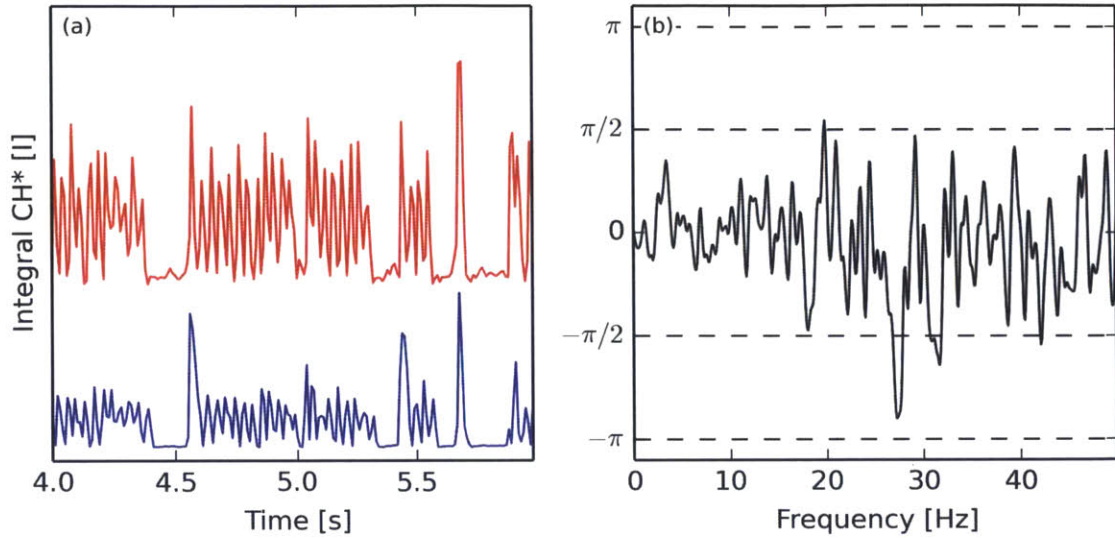
Figure 4-9: The time signal of CH* for both branches of the outer recirculation zone in the transitional flame are plotted as a function of time (left column). The relative phase between these two signals in plotted as a function of frequency (right column), showing a 180° phase shift at 28 Hz, indicating that this is the frequency of rotation.

in the outer recirculation zone. This signal is strongest in the transitional flame in which short-lived flames enter the outer recirculation zone and are advected around the axis before extinguishing without ever filling the outer recirculation zone, or said another way, the flames do not persist long enough to achieve symmetry about the axis of the combustor. The origin of the lower frequency peaks is less obvious, but on closer inspection of the dataset, corresponds to the peaks that occur when the CH* signal jumps between low and high mean values, and therefore, we can associate these frequencies with the flickering itself.

The CH* filtered flame images give us no more clue to either the nature or the origin of the low frequency oscillations. In order to gain further insight, we look at the dynamic mode decomposition of the flow field using PIV data. In order to perform the decomposition, each was composed of both axial and radial velocity components, ensuring that the decomposition would capture those modes with correlated motion in both components of the velocity field. In figure 4-10, we show the Ritz values of the top 20 most energetic modes from the three operating points that we interrogated. In
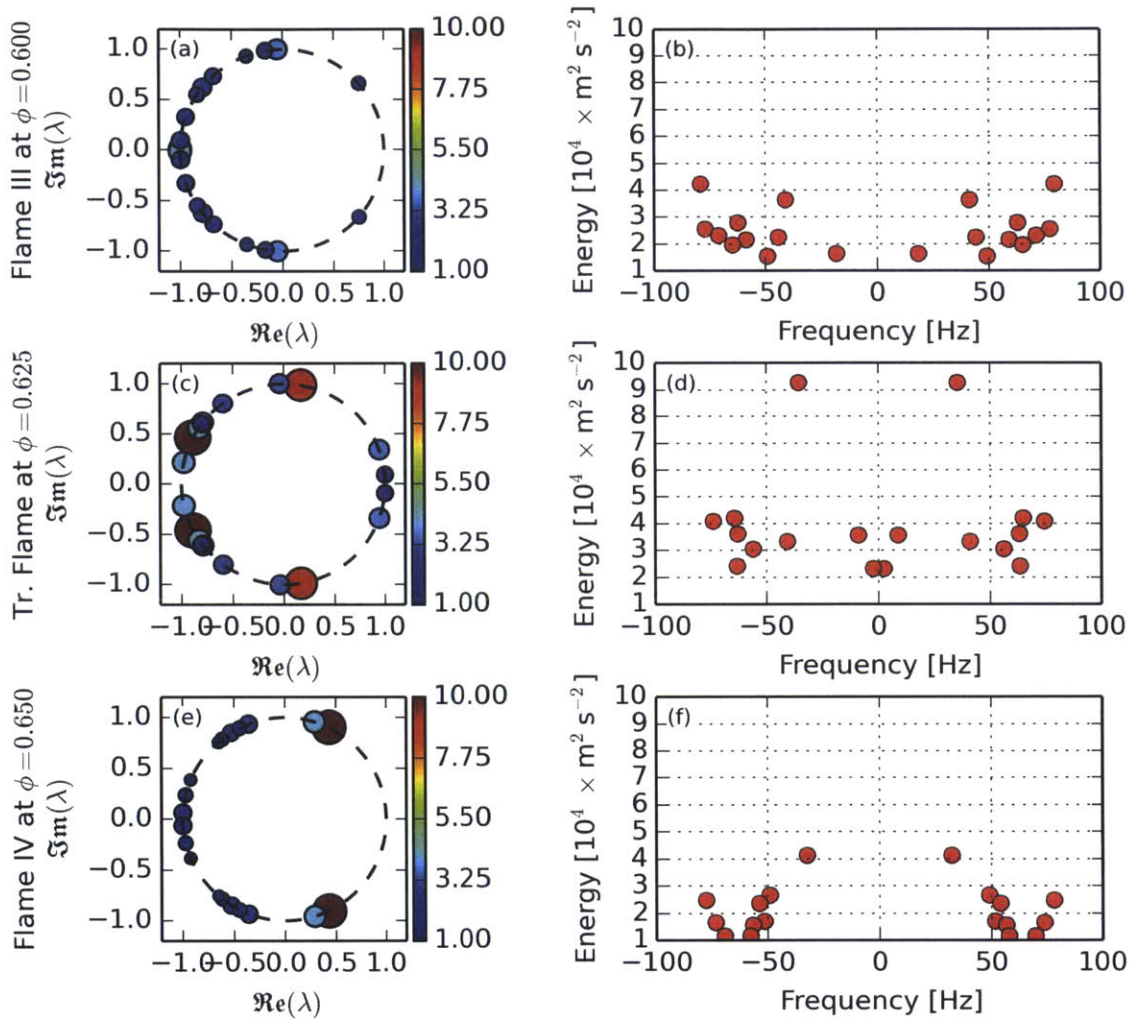
Figure 4-10: The real and imaginary components are plotted for the 20 most energetic, non-stationary Ritz values at three operating points (left column). The size and color scale of the values correspond to their relative energy values. Their proximity to the unit circle indicates that these are non-transient modes. Mode energy is plotted against frequency for the 20 most energetic modes at three operating points (right column).

93

the left column, we show real and imaginary components together, confirming that these are all persistent modes with nearly zero growth or decay. The right column plots the relative energy against the frequency. In the transitional flame, but absent from either flame III or flame IV, we find the signature of two low frequency modes at 4 Hz and 8 Hz (along with conjugate modes at -4 Hz and -8 Hz), the same frequency at which we observe flickering in the chemiluminescence signal, suggesting a relationship between flickering phenomena and these modes.

We show the flow field associated with each of these two modes as a function of phase angle in figure 4-11. In the left column, we show the 4 Hz mode, which is dominated by a vortex in the jet, centered near the impingement point on the combustor wall. Examining the upper half of each snapshot, we see that at zero phase, this is a positive vortex (counterclockwise in the coordinate system of the image), and a corresponding negative vortex is observed in the inner shear layer, centered a few mm downstream of the primary vortex. At 180° phase, the sign of these vortices has reversed, while 90° and 270° phase show very little activity. This pattern is mirrored in the lower half of each snapshot, suggesting that these are vortex rings. The absence of strong vortices farther upstream in the jet, which would be indicative of convective events, suggests that this particular instability may be related to the impingement of a jet on the combustor wall. In the right column, we examine the 8 Hz mode, in which we observe a very similar pattern with a phase lag of 90°.

Simply by examining what appears to be the production of a vortex pair near the jet impingement point in figure 4-11, we expect some modification to the jet and inner shear layer under the action of these two modes. We confirm this is figure 4-12 in which we have reconstructed the flow field using the stationary mode, as well as the 4 Hz and 8 Hz mode, and their conjugates. Although we noted a similarity in the structure of the two modes, they occur at different frequencies, so we reconstruct the flow field for a period of time spanning one half cycle of the 4 Hz mode and approximately one full cycle of the 8 Hz mode. Indeed, the action of these two modes changes the structure of the inner recirculation zone, jumping between single-celled and double-celled configurations with a small pocket of forward flow inside the
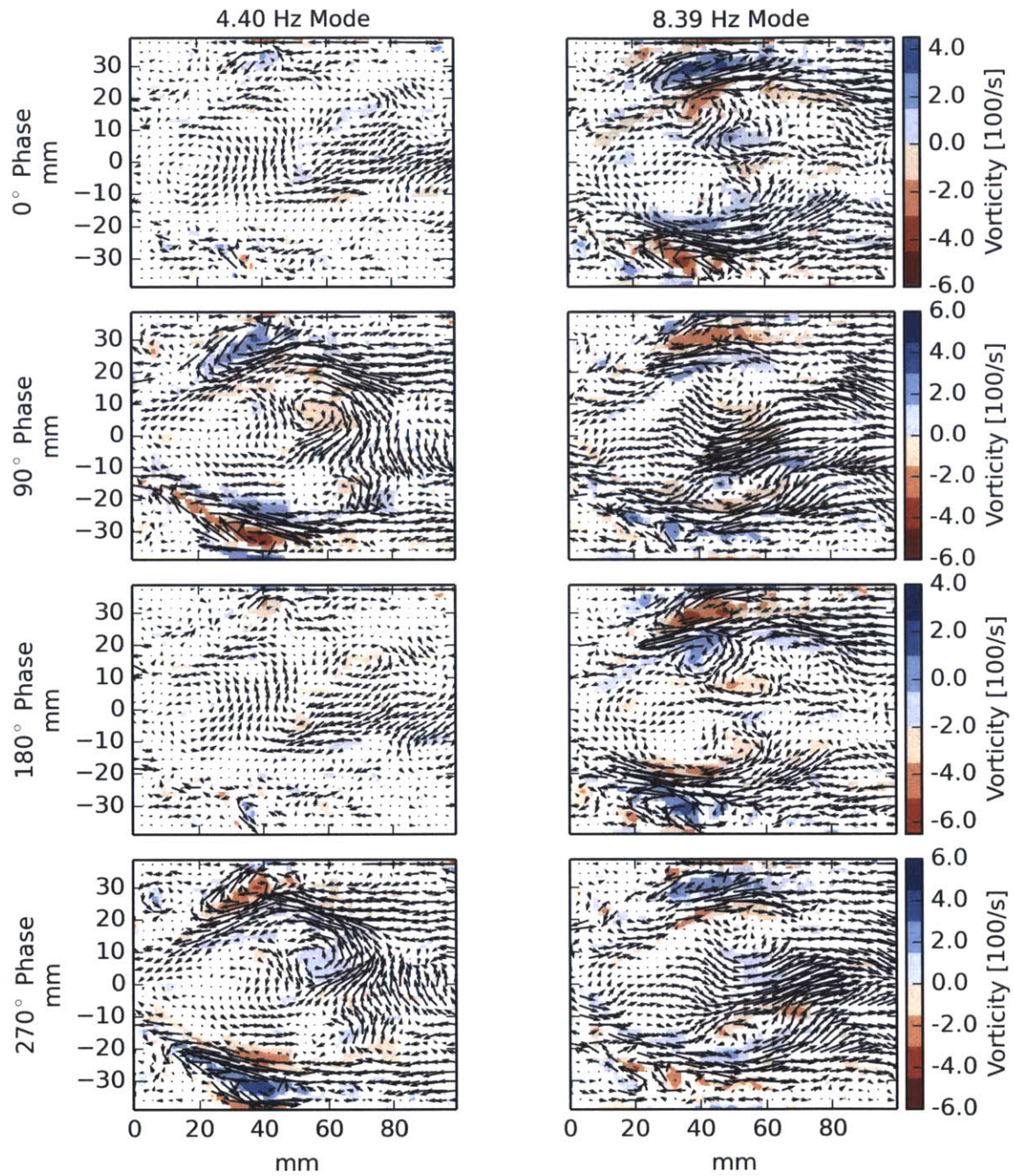
Figure 4-11: Snapshots of the 4 Hz mode (left column) and 8 Hz mode (right column) are shown at four different phase angles.
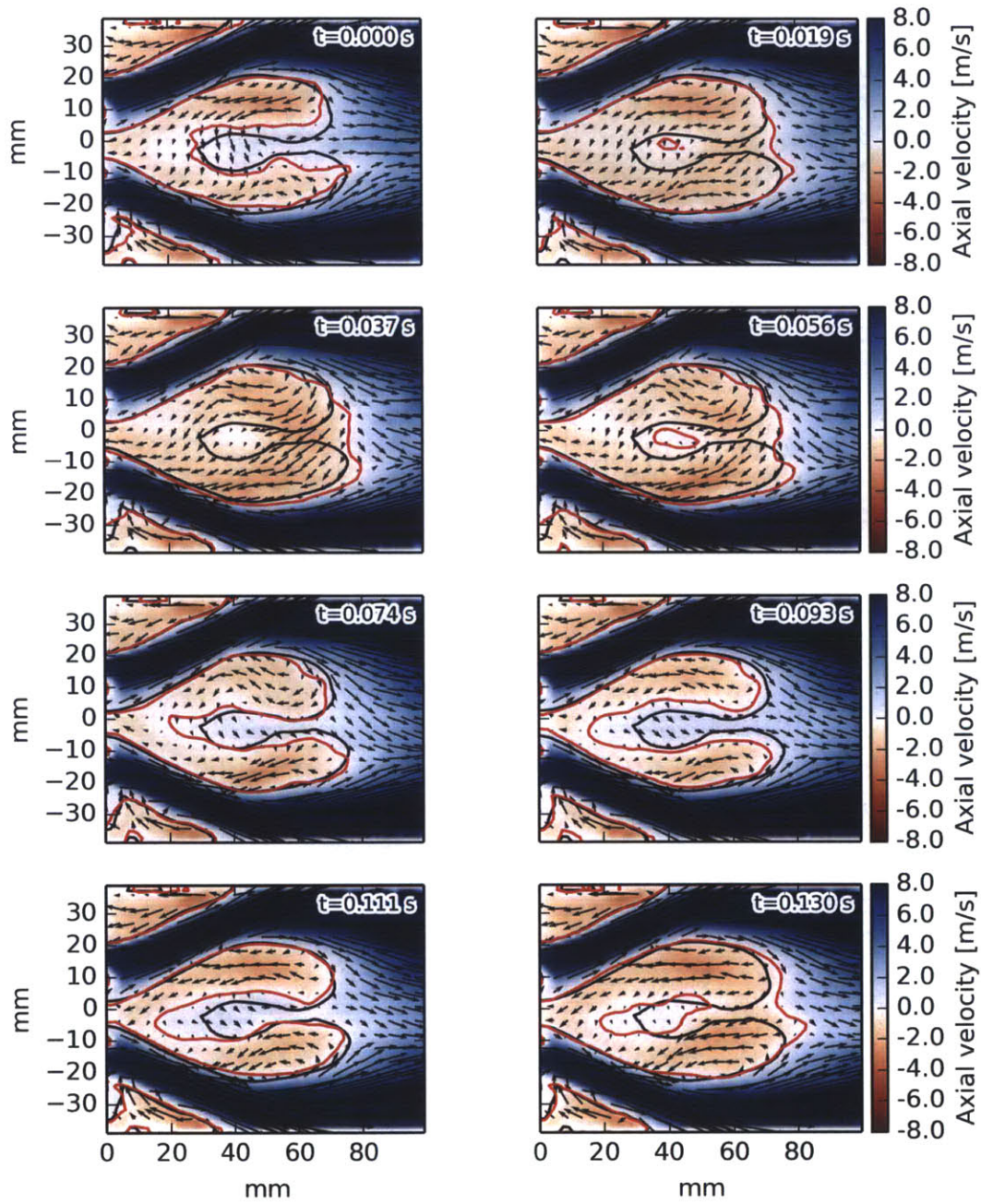
Figure 4-12: Reconstructed flow fields are plotted using the stationary, 4 Hz, and 8 Hz dynamic decomposition modes at a sequence of time intervals showing splitting and coalescing of the inner recirculation zone.

recirculation bubble. In conjunction, we see a subtle change in the mean direction of the jet over the course of this cycle.

This apparent "breathing" motion of the inner recirculation zone is an observed phenomena in vortex breakdown bubbles. Billant *et al* [77] observe similar oscillations in a non-reacting flow, observing that this periodic filling and emptying of the recirculation bubble, noting that as the opening angle of the enveloping cone increases, the diameter of the primary eddy increases. As noted by Bruücker and Althaus [78], this low frequency phenomenon corresponds with varying axial velocity as the interior of the recirculation bubble fills with fluid. This phenomenon is expected to happen on the order of $f \propto F/\mathcal{V}$ where f is the frequency, F is the characteristic volumetric flow rate, and $\mathcal{V}$ is the volume of the region being filled with fluid. Using values taken from our system, we find an approximate filling frequency on the order of $O(10\,\mathrm{Hz})$, which is in line with what we observe. This filling process is the result of the gyration of the toroidal vortex ring, the primary eddy, although there is some debate on whether the vortex bubble is filled with fluid from the upstream of downstream end of the bubble [79, 80].

As we will show in §4.3, the advancement of the flame into the outer shear layer is well correlated with increases in the extinction strain rate at higher equivalence ratios, however, there is evidence that the outer flame is unable to survive on its own, most likely due to heat loss to the combustor walls, and the conical flame in the jet and inner shear layer serves as its ignition source by bridging across to the outer zone. Even though the large vortices that comprise these modes are not sufficiently strong to advect the flame into the outer recirculation zone, it is very plausible that the slight shift in the jet, and in particular of the distance between the outer shear layer and the expansion plane increases the likelihood of flames bridging from the conical region into the outer region, providing an ignition source, and thereby resulting in the flickering that we see.
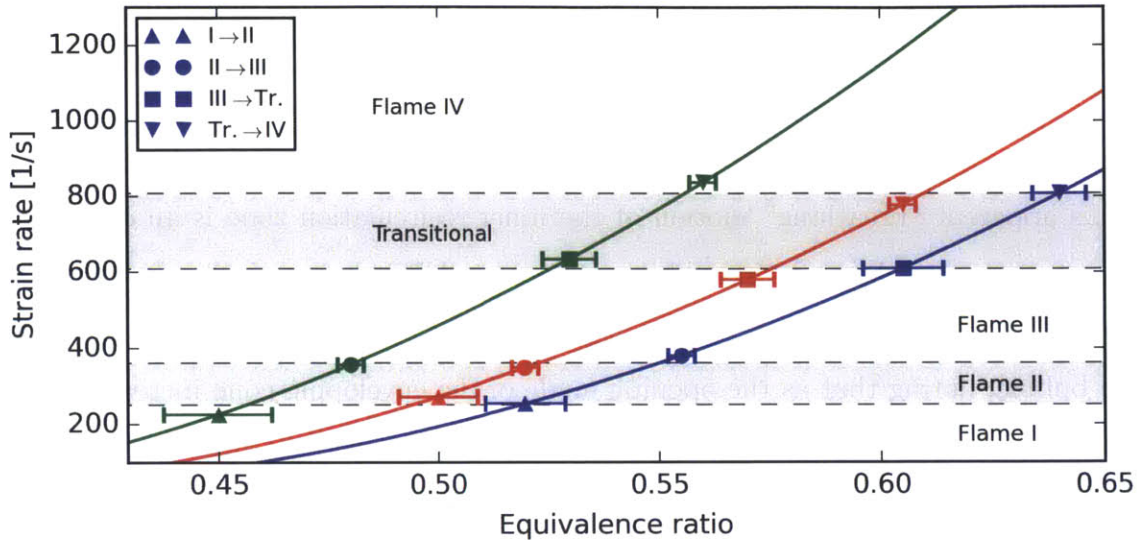
Figure 4-13: The extinction strain rate is plotted as a function of equivalence ratio for pure CH_4 (blue), 90% CH_4 enriched with 10% H_2 (red), and 80% CH_4 enriched with 20% H_2 (green). A marker is placed on each curve corresponding to the equivalence ratio for each transition in the flame geometry, and dashed black lines mark the average extinction strain rate at which each transition occurs.

4.3 Statistical flow-flame interactions

In the previous section, we made a series of observations showing that the macroscale flame geometry is well correlated both with the onset of instability and mode transitions, as well as transitions in the large-scale structure of the flow, particularly the structure of the inner recirculation zone. In this section, we argue that the flow field follows changes in the flow geometry, which in turn are driven by changes in the chemistry that limit the maximum strain rate in which the flame can survive. That is, we suggest that the changes that we observe in the flame geometry as the equivalence ratio increases in a quasi steady manner are primarily driven by the ability of the flame to persist in regions of higher and higher strain, and that the discrete transitions that we observe are a result of the extinction strain rate of the flame exceeding critical values, allowing the flame to persist in new regions of the flow: first the inner shear layer, and then the outer shear layer.

To motivate this, we begin by mapping our observations of the geometric tran-

sitions onto the extinction strain rate curve for the three different fuel compositions that we have been investigating. This mapping is shown in figure 4-13. Solid curves show the extinction strain rate for fuel compositions ranging from pure CH_4 to 80% CH_4 blended with 20% H_2. Dashed lines are drawn horizontally to the extinction strain rate curve at the mean equivalence ratios at which we observed each transition between two different flame geometries for each of the fuel compositions. The transition points were determined from visual observation of six separate runs for each case. After ignition, the equivalence ratio was brought to a low value near the lean blowoff limit and gradually increased in increments of 0.01. The system was allowed 10 s at each equivalence ratio to come to a stationary state, although in practice, it typically reached that state nearly instantaneously. The error bars indicate the uncertainty in the transition point based on these observations. Horizontal dashed lines are drawn from the points of intersection to the left. These horizontal lines cluster well around particular strain rate values. While not conclusive evidence, this figure strongly suggests a correlation between the extinction strain rate and the flame geometry. Through the remainder of this section, we will look at statistical flow-flame interactions, which provide further evidence that the flame preferentially will propagate upstream along both the inner and outer sides of the shear layer, but it is impeded by extinction due to high strain rates in the highest shear zones of the flow. As the chemistry becomes sufficiently robust, the flame advances.

4.3.1 Computing statistical flow-flame interactions from raw flow and flame data

In the turbulent environment in which the combustion takes place, unsteady effects are of clear importance to the overall behavior of the system. In the previous sections, we looked at the mean and RMS statistics of the flow field as measured by PIV, and the mean flame, as measured by CH^* chemiluminescence, for several cases of particular interest, and we went further to investigate the periodic behavior of the transitional case in which we see the flame intermittently jumping between geometries

that correspond to flame III and flame IV. Throughout this analysis, we saw that the instantaneous snapshots of the flow field may differ significantly from the mean in both direction and magnitude, and thus we cannot assume that first and second order, uncorrelated statistics are sufficient to describe the system. On the other hand, the robustness of the transitions at particular operating conditions tells us that there is a strong correlation between the small scale flow-flame interactions and the global system behavior, such that the examination of individual snapshots, without context of the ensemble, is not likely to yield appropriate conclusions. Rather, in order to begin understanding the influence of the small scale interactions on the global behavior, we must take a statistical approach.

As we have just shown, there is an apparent correlation between the operating points at which the transitions occur and the extinction strain rate. To refresh our memories, the two dimensional strain rate can be approximated as:

$$\kappa = -n_x n_y \left(\frac{\partial u}{\partial y} + \frac{\partial v}{\partial x} \right) - n_x^2 \frac{\partial u}{\partial x} - n_y^2 \frac{\partial v}{\partial y} \tag{4.1}$$

where we have neglected the curvature and time-dependent effects. The components of the flame normal vector, n_x and n_y come from performing edge detection on the PLIF measurements and the components of the flow velocity vector, u and v, come from the PIV measurements. The PIV and PLIF measurements are not simultaneous, nor are the correlations coefficients known, so we must be more clever in our processing of the independent datasets.

While we are examining the flame location, we should also interrogate the datasets to determine statistics with regard to the relative speed of the flow normal to the flame. While we know that the strained flame speeds are on the order of 10 cm/s to 20 cm/s, and the flow velocities reach up to 13 m/s, it is not immediately apparent from the PIV and chemiluminescence that we discussed earlier in this chapter if the flame stabilizes in the same manner we would expect a laminar flame to stabilize in (for which we would expect a high probability of finding the component of the flow normal to the flame on the order of 10 cm/s) or via another mechanism, so as continuous

ignition of the shear layer through the recirculation of hot products. Our assertion about the normal component of flow velocity is subtle, since as we have noted, the two datasets are not correlated, the flame is dynamic, and the flow is accelerated through the flame. What we have to consider is that when we observe a flame in a particular location, that means that it is either stabilized there, has propagated there, or has been advected back. In the first case, if the flame was stabilized, we would expect that the flow velocity normal to the direction of the flame either at our detected edge or in front of it would be near the laminar flame speed. In the second and third cases, we observe the flame in a particular location precisely because the normal flow component is not near the flame speed. This argument relies on some amount of smoothness of the flow transitions, both spatially and temporally, and although it does not yield very strong conclusions, it does allow us to accumulate additional evidence for or against a steady flame. This component of velocity, expressed as $-\mathbf{n}_f \cdot \mathbf{u}$, is also composed of combined PIV and PLIF data, and so we must treat the statistics in the same way. Through the remainder of this section, we will step through the calculation of the strain rate statistics for one case, however, the statistics of the normal component of velocity are computed in the same manner using the appropriate formula.

Before we step through the procedure, we will take a look at the datasets themselves, and show how some of characteristic instantaneous PLIF snapshots of the flame correlate with the mean PLIF signal and with our understanding of the flame geometry up to this point. The first point we must address is the interrogation window for the PLIF dataset that we use throughout the rest of this chapter. Due to the nanosecond timescales and the energy requirements to excite OH in order to capture PLIF data, there is a spatial limit to the axial extent of the usable interrogation window. The laser sheet forms a Gaussian profile, centered at a particular axial location, and decays as you move axially away from this line. As the beam decays, the signal to noise ratio decreases until we are no longer able to reliably detect flame edges using the Canny algorithm, which we outlined in §2.4.1. Two sets of data were taken, one targeted approximately 20 mm downstream of the expansion plane and one targeted approximately 40 mm downstream of the expansion plane. In figure 4-14, we show
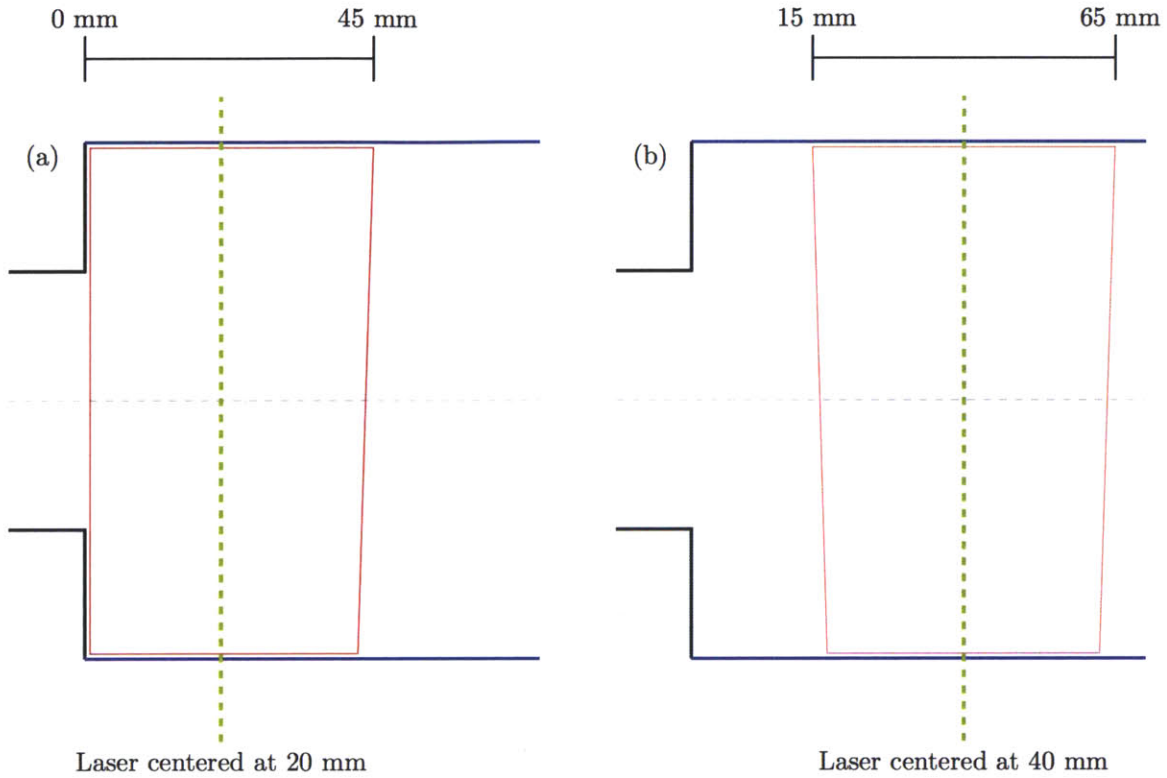
Figure 4-14: The interrogation windows for the two PLIF configurations are shown. The laser sheet was centered 20 mm downstream of the expansion plane in (a) and 40 mm downstream of the expansion plane in (b).

the approximate interrogation windows for these two configurations.

In figure 4-15, we show an instantaneous PLIF snapshot along with the mean captured with the sheet centered at 20 mm downstream of the expansion plane. We see that the flame extends upstream along the inner shear layer and into the inlet pipe, a feature which we observe for all flames considered in this analysis. The incoming reactant jet impinges on the wall between 30 mm and 40 mm downstream of the expansion plane, curving parallel to the wall by 50 mm downstream of the expansion. Despite the resolution of the upstream behavior of the flame, however, the poor signal to noise ratio means that we do not get good flame edge detection in a critical region of the flow: the region surrounding the impingement of the reactant jet on the combustor wall. To overcome this limitation, we focus our analysis of the data captured with the laser sheet targeted 40 mm downstream of the expansion plane.
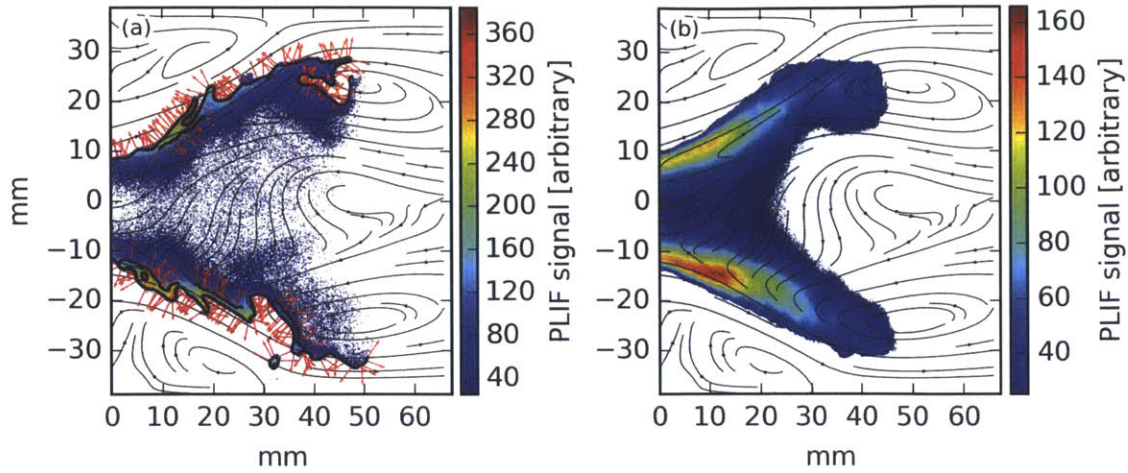
Figure 4-15: An instantaneous PLIF snapshot is plotted with the algorithmically detected edges overlaid (a) along with the mean PLIF signal averaged over the full ensemble of 128 snapshots (b). Data was captured at an equivalence ratio of $\phi = 0.600$ corresponding to flame III, with the PLIF laser sheet centered approximately 20 mm downstream of the expansion. Mean streamlines are plotted for reference.

In the next several figures, we will show mean and instantaneous PLIF data for each of the four configurations that we are focusing on, with the PLIF sheet centered downstream, 40 mm beyond the expansion plane, where we will see that we do resolve the region around the jet impingement point, at the expense of having information about the flame near the expansion itself. The conclusions that we draw make use of the data in the latter data set, however in appendix A, we run the same statistical calculations on the data that includes the expansion plane to show that the conclusions are not affected.

We begin with flame II, which we examine in figure 4-16. The mean PLIF signal, shown in 4-16(a), shows a fairly diffuse signal that is contained entirely within the mean inner recirculation zone. As we will show in appendix A, after following along the shear layer, the flame becomes highly contorted by the primary eddy of the recirculation zone. Using this interrogation window, we show that the strong advection of the flame by the primary eddy pushes the flame into the interior of the inner recircu-
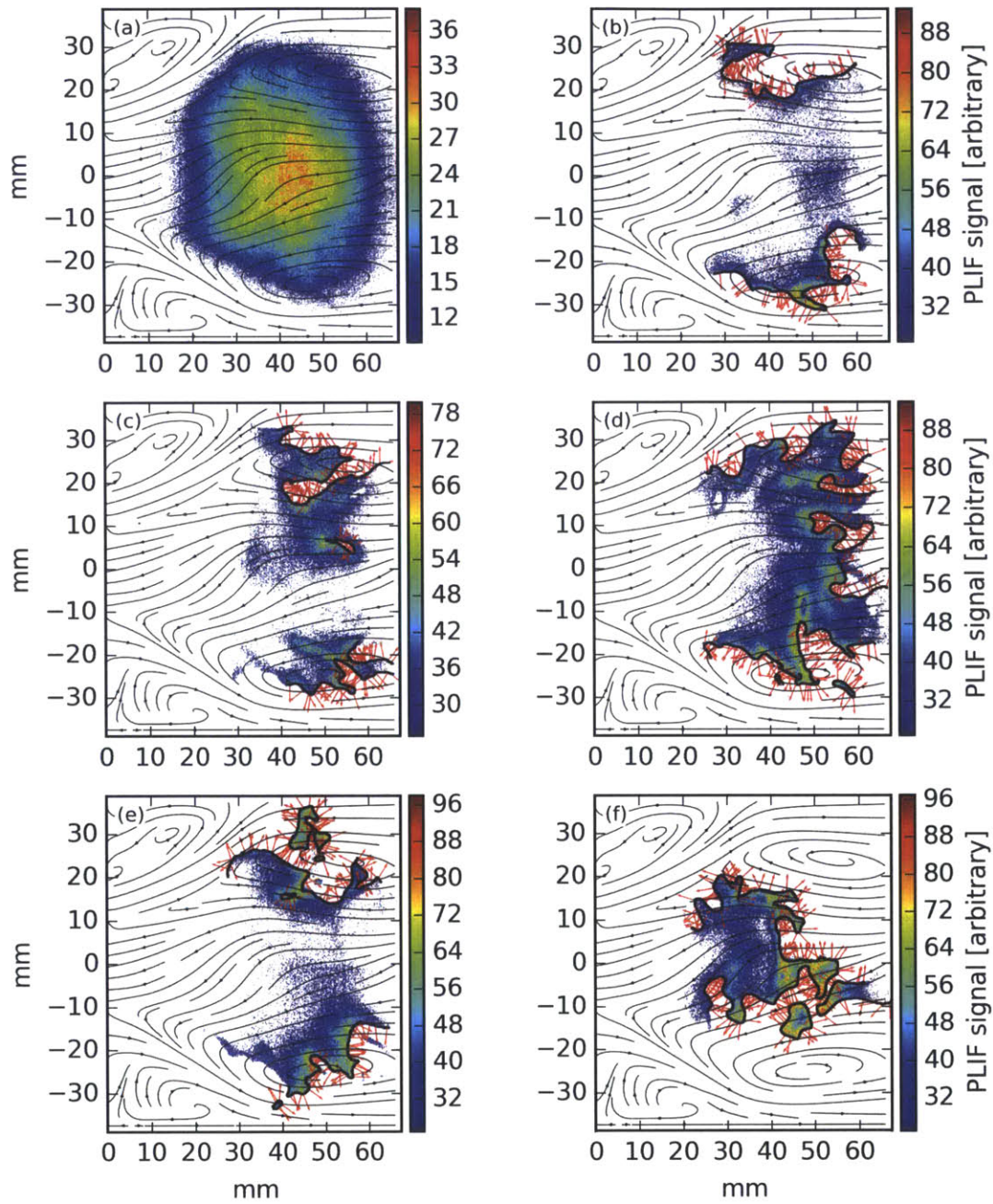
Figure 4-16: The mean PLIF signal (a) and several instantaneous snapshots (b-f) with corresponding flame edges and normals are superimposed on the mean streamlines for a CH$_4$/air flame at $\phi = 0.550$, corresponding to flame II.
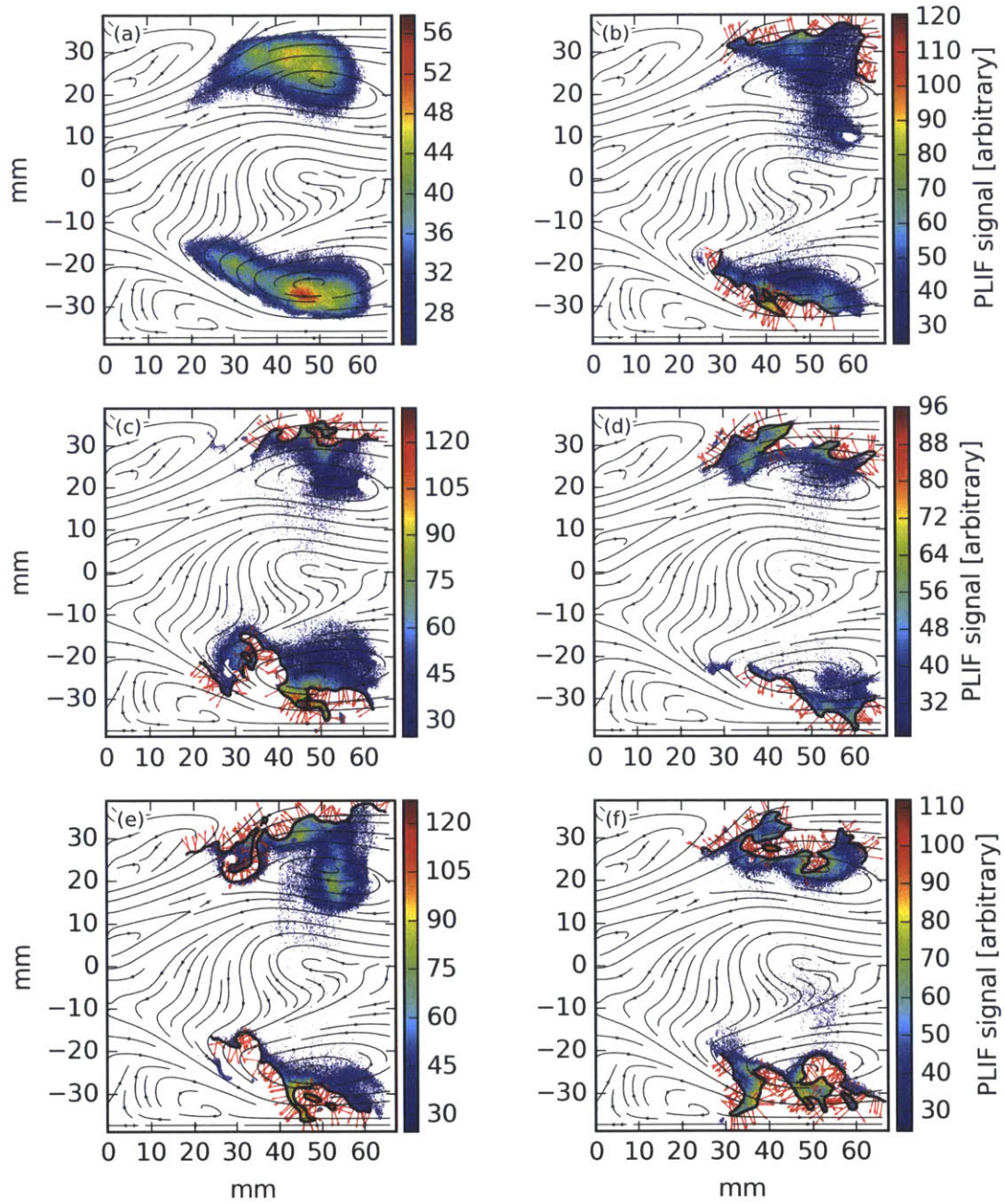
Figure 4-17: The mean PLIF signal (a) and several instantaneous snapshots (b-f) with corresponding flame edges and normals are superimposed on the mean streamlines for a CH_4/air flame at $\phi = 0.600$, corresponding to flame III.

lation zone, and as a result, it ends up propagating in the mean downstream direction into recirculating reactants. This is borne out by the instantaneous snapshots of the flame, shown in 4-16(b-f), where we see the flame interacting with the primary eddy, being pushed toward the combustor centerline, with some flame closing within the interior and some breaking. As a result, we expect that the inner recirculation zone is, in part, composed of reactants, and consequently should be at a lower temperature than it would otherwise achieve.

Flame III is examined in figure 4-17. Consistent with our observation that the geometry transitions to that of a conical flame, we see virtually no mean PLIF signal in the interior of the inner recirculation zone in 4-17(a). The instantaneous snapshots in 4-17(b-f) show some wrinkling of the flame along its length, but it remains confined to the inner shear layer, critically, it sits between the primary eddy and the combustor wall, consuming reactants as the jet turns parallel to the wall. As a result, the inner recirculation zone should be almost purely composed of hot combustion products which provide a more stable ignition source in the upstream region, when compared with flame II.

We show the transitional flame in figure 4-18. The transitional cases is characterized by intermittent flickering in the outer recirculation zone, in which the flame will briefly jump into the outer recirculation zone, and then rapidly extinguish at irregular intervals. Although the mean PLIF signal, shown in 4-18(a) is qualitatively very similar to the mean PLIF signal of flame III, we notice several important differences in the instantaneous snapshots. In 4-18(b-d), we see small but distinct flames in the outer recirculation zone, separate from the inner conical flame. These are the flames that we observe when we refer to flickering. There is a noticeable difference in the inner conical flame, however, when compared to flame III. We observe more wrinkling, but more critically, we see pockets of the inner flame extending into or toward the outer shear layer. Two particular examples of this are the lower branch of 4-18(e) and the upper branch of 4-18(f). While the wrinkles approach the outer shear layer, we do not see them fully wrapping around. As we will discuss later, this provides support for the notion that the ignition source for the outer flame is the inner flame wrapping
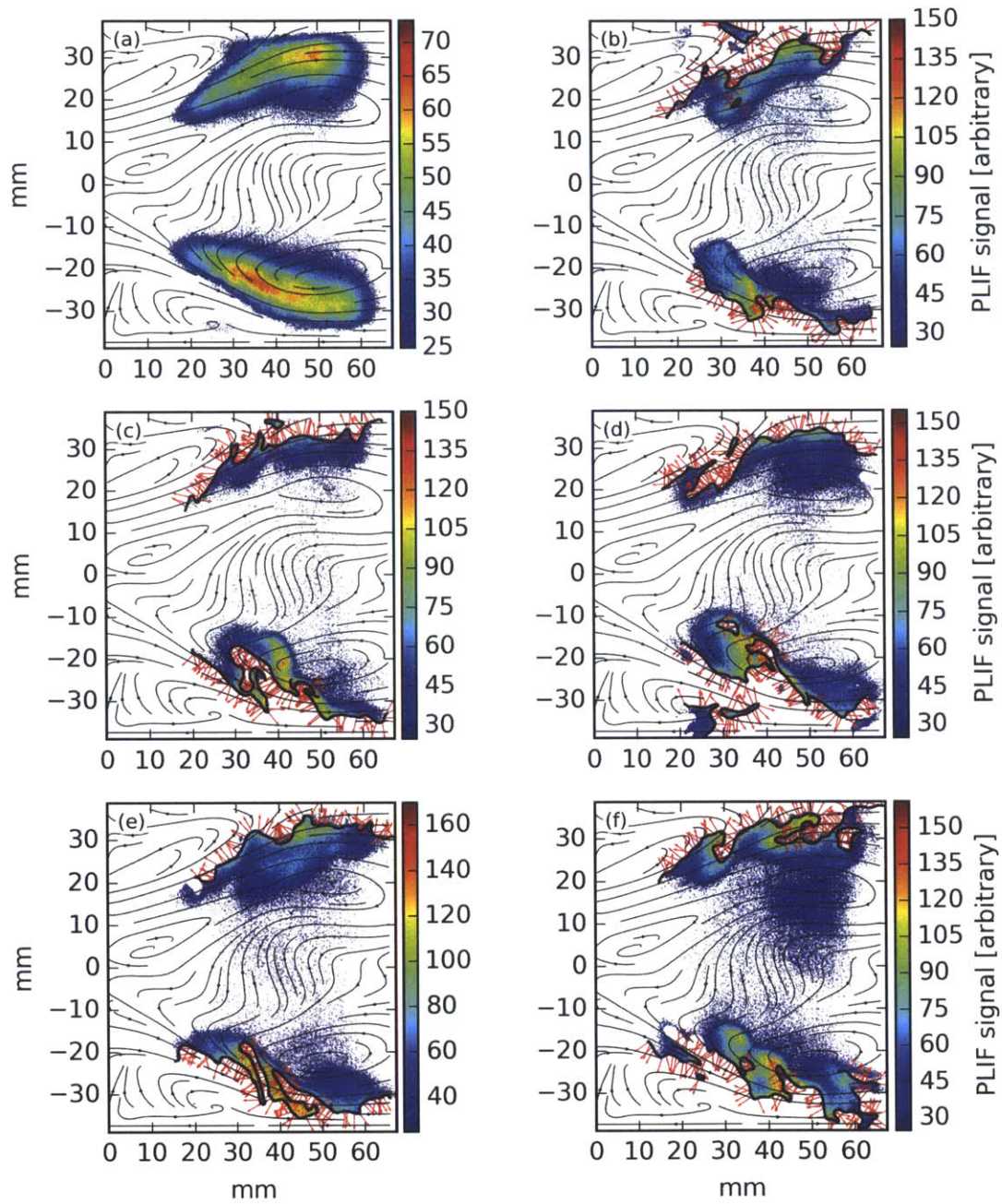
Figure 4-18: The mean PLIF signal (a) and several instantaneous snapshots (b-f) with corresponding flame edges and normals are superimposed on the mean streamlines for a CH_4/air flame at $\phi = 0.625$, corresponding to the transitional flame.
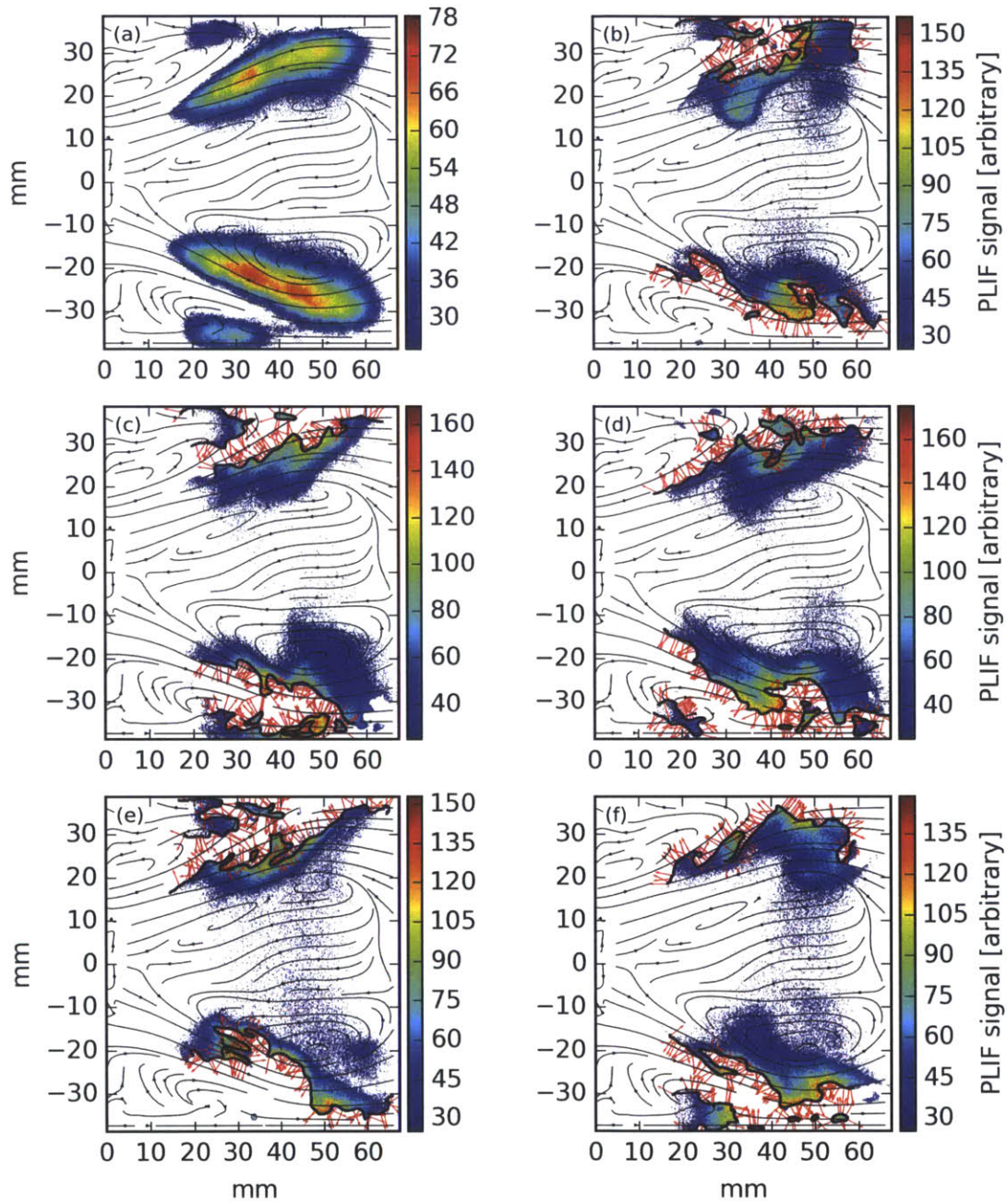
Figure 4-19: The mean PLIF signal (a) and several instantaneous snapshots (b-f) with corresponding flame edges and normals are superimposed on the mean streamlines for a CH$_4$/air flame at $\phi = 0.650$, corresponding to flame IV.

around the jet. In the transitional flame, although we do start to see this happen, it is a much more rare than the same phenomenon at higher equivalence ratios that correspond to flame IV.

Finally, we look at flame IV in 4-19. The mean PLIF signal in 4-19(a) shows a similar OH concentration of the flame in the conical region of the inner shear layer as we see in the previous two geometries, in addition to a nontrivial mean PLIF signal in both branches of the outer recirculation zone. The instantaneous snapshots are somewhat revealing, however. For those snapshots in which we observe a flame in the outer recirculation zone, we typically see the flame front propagating in two direction: into the reactant jet as a near mirror image of the inner conical flame, and toward the wall. As the jet impinges in the wall, most of the flow turns downstream parallel to the wall, however a small fraction turns parallel to the wall in, propagating back toward the expansion plane. Consequently, we have a small volume of reactants propagating backwards along the boundary layer of the combustor wall, and we see the outer flame propagating toward the wall, consuming these reactants. There is another key observation that we make in the upper flame branch in 4-19(b) and the lower flame branch in 4-19(c): at the impingement point, the inner flame wraps in toward the outer recirculation zone near the wall, connecting or nearly connecting with the outer flame. When we get into the statistical analysis of the flow-flame interaction, we will see that the data suggest that the inner flame provides an ignition source for the outer recirculation zone by bridging across like this, so finding examples of this happening is an important piece of evidence for this argument.

Back to the statistical calculations, we are left with two datasets–PLIF and PIV– which are correlated with an unknown correlations coefficient. In order to compute meaningful statistics, we start of with a conditional approach. We begin with two datasets. The PLIF datasets if processed to produce flame normal vectors, giving us $n_{x,i}(x_f, y_f)$ and $n_{y,i}(x_f, y_f)$ for $1 \leq i \leq N$, where N is the total number of PLIF snapshots, along with a boolean, $e_i(x_f, y_f)$ which tells us if each point $(x_f, y_f) \in \mathbb{X}_f^2$ within the PLIF domain lies on an edge or not. The PIV datasets give us flow components, $u_j(x_p, y_p)$ and $v_j(x_p, y_p)$ for $1 \leq j \leq M$, where M is the number of PIV
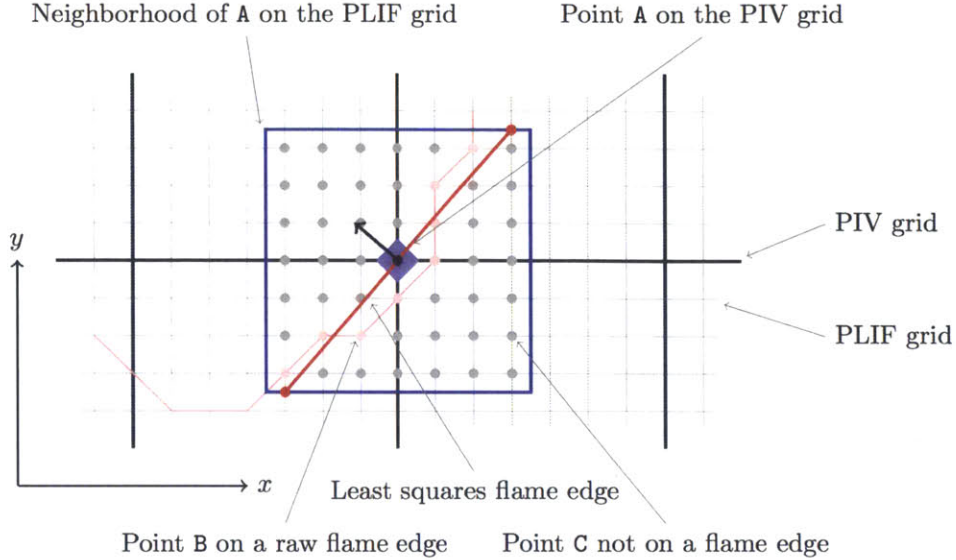
Figure 4-20: The raw PIV grid, $\mathbb{X}_p^2$ and PLIF grid, $\mathbb{X}_f^2$ are shown with a hypothetical flame edge passing through the central cell. The flame edge on $\mathbb{X}_f^2$ is shown in red, lightly faded out. The flame is remapped onto the statistics grid, $\mathbb{X}^2 = \mathbb{X}_p^2$, with a least-squares linear fit to the raw flame edge, which is shown as a bold red line traversing from the lower left to the upper right of the cell centered on point A.

snapshots. These variables are defined for all points $(x_p, y_p) \in \mathbb{X}_p^2$ on the PIV grid.

The PIV data is computed on a grid with 1.42 mm spatial resolution, while the PLIF, and consequently the flame edge is computed on a grid with 0.11 mm spatial resolution. As we have shown in chapter 3, the flame thickness is of the order of $\delta_f \approx 1\,\mathrm{mm}$, which is the approximate grid spacing for the domain, $\mathbb{X}^2$, on which we wish to calculate our statistics. Since the PIV grid spacing is on the order of the flame thickness, we can take $\mathbb{X}^2 = \mathbb{X}_p^2$, and use the PIV data without remapping it onto a new grid.

The flame edge data must be remapped, however, onto the coarser grid. In figure 4-20, we show typical flame data before and after remapping. For each snapshot i containing $n_{x,i}(x_f, y_f)$, $n_{y,i}(x_f, y_f)$, and $e_i(x_f, y_f)$, and we group those points, $(x_f, y_f) \in \mathbb{X}_f^2$ which are closer to point $A = (x, y)$ than any other point in $\mathbb{X}^2$, and consider this to be the neighborhood of point A. If $e_i(x_f, y_f)$ is true for any (x_f, y_f), then we set the value of $E_i(x, y)$ to true (or one) to indicate that there is a flame within that cell of the statistics grid. We then collect the set of points, (x_{f0}, y_{f0}) for

which $e_i(x_{f0}, y_{f0})$ is true, and fit a line through these, minimizing the square error to define the flame front in this cell, from which we can determine the flame normal on the cell, $N_{x,i}(x, y)$ and $N_{y,i}(x, y)$, choosing the sign of the normal based on the direction of the PLIF gradient.

Once we have completed this remapping, we are left with M instances of $u(x, y)$ and $v(x, y)$ from the PIV data and N instances of $N_x(x, f)$, $N_y(x, y)$, and $E_i(x, y)$ all mapped onto the same spatial grid, $\mathbb{X}^2$. From this data, we can calculate an ensemble of flame strain values. At each point, (x, y), we can calculate a particular strain rate for each flame edge and each velocity field:

$$
\begin{aligned}
\kappa_{i,j}(x, y) = &- N_{x,i}(x, y) N_{y,i}(x, y) \left(\frac{\partial u_j(x, y)}{\partial y} + \frac{\partial v_j(x, y)}{\partial x} \right) \\
&- N_{x,i}^2(x, y) \frac{\partial u_j(x, y)}{\partial x} \\
&- N_{y,i}(x, y) \frac{\partial v_j(x, y)}{\partial y}
\end{aligned}
\tag{4.2}
$$

$$
\text{for all} \quad i \ni E_i(x, y) = 1, \, j \in [1, M]
$$

where we see that $\kappa_{i,j}$ is not defined for snapshots, i, where there is no flame edge in the cell. In computing this ensemble, we are effectively creating a distribution of strain rates from the full ensemble of velocity fields for each particular flame edge, conditioned on its orientation. These values represent the strain not at a single time, but at a specific instant in each the sequence of PIV snapshots and PLIF snapshots. The resulting values are binned to create a distribution $\tilde{\kappa}(\kappa; x, y)$, representing the probability of the strain rate being between κ and $\kappa + d\kappa$ for each point in $\mathbb{X}^2$, conditioned on there being a flame there.

In a similar manner, we can compute the conditional values for the component of the flow field normal to the flame. These values can be expressed as:

$$
-(\mathbf{n}_f \cdot \mathbf{u})_{i,j}(x, y) = - N_{x,i}(x, y) u_j(x, y) - N_{y,i}(x, y) v_j(x, y)
$$

$$
\text{for all} \quad i \ni E_i(x, y) = 1, \, j \in [1, M]
\tag{4.3}
$$

where again, we omit those PLIF snapshots for which there is no flame edge at (x, y),

111

and we are left with a spatially resolved distribution of $\tilde{u}_n(u_n; x, y)$, which expresses the probability that $-(\mathbf{n}_f \cdot \mathbf{u})$ lies between u_n and $u_n + du_n$ for each point in $\mathbb{X}^2$, conditioned on a flame being present.

We are also interested in the spatially resolved statistics of the flame geometry, or more specifically, the flame angle. As this value is related only to the normals, we can compute exact values, expressed as:

$$\theta(x, y) = \arctan\left(\frac{N_{y,i}(x, y)}{N_{x,i}(x, y)}\right)$$

$$\text{for all} \quad i \ni E_i(x, y) = 1 \tag{4.4}$$

again omitting empty cells. This gives us a distribution, $\tilde{\theta}(\theta; x, y)$ expressing the probability that the flame angle lies between θ and $\theta + d\theta$ on the condition that a flame is found at (x, y).

In order to correlate the statistics of these distributions with the probability, P_{flame}, of finding a flame at each point, (x, y), we must compute this probability, which we can easily see is expressed as:

$$P_{flame}(x, y) = \frac{\sum_{i=1}^{N} E_i(x, y)}{N} \tag{4.5}$$

We can use these probability values to compute global distributions of the flame strain and normal component of the flow velocity by renormalizing the following weighed expressions:

$$\hat{\kappa}(\kappa) = k_\kappa \sum_{(x,y)\in\mathbb{X}^2} P_{flame}(x, y)\tilde{\kappa}(\kappa; x, y) \tag{4.6}$$

$$\hat{u}_n(u_n) = k_u \sum_{(x,y)\in\mathbb{X}^2} P_{flame}(x, y)\tilde{u}_n(u_n; x, y) \tag{4.7}$$

where k_κ and k_u are calculated such that $\int_{-\infty}^{\infty} \hat{\kappa}(\kappa)\, d\kappa = 1$ and $\int_{-\infty}^{\infty} \hat{u}_n(u_n)\, du_n = 1$. The value of $\hat{\kappa}(\kappa)$ represents the probability of the flame strain being between κ and $\kappa + d\kappa$ anywhere in the domain, conditioned on the existence of the flame, and $\hat{u}_n(u_n)$ takes on a similar meaning.

112

4.3.2 Flame II: Inner recirculation zone stabilization

We begin our statistical observations by looking at flame II, shown at $\phi = 0.550$ in pure CH_4. We recall that this flame geometry is characterized by the meandering flame that appears to be confined to the interior of the large inner recirculation zone. The flame stands well away from the wall, and we see the reaction taking place in the bubble, but also continuing well downstream of the expansion zone.

In figure 4-21, we plot the results of combining PLIF and PIV data to obtain statistics for the flame location, flame strain, and the flow velocity normal to the flame. The central component of this ensemble of images is the flame probability, shown in 4-21(a). The value at each point in the spatial domain is the probability of detecting a flame edge at that point. The probability of finding a flame at a given point in the domain is very low for flame two, in part due to the distributed nature of the flame both within and beyond the interrogation domain. Whereas in the higher equivalence cases that we will be examining, we will see the flame probability peak at or slightly higher than 0.50 in the conical regions, the peak flame probability in the flame II geometry does not exceed 0.25, and only right along the edge of the inner recirculation zone, inside the shear layer. The peak probabilities that we observe are at the upstream boundary of the inner recirculation zone and the jet. It should be noted that in these figures which map probabilities and distributions of flow-flame interactions, all of the mapping except the flame probability itself are conditioned on there actually being a flame observed in that region. In 4-21(b), we see the most probable value of the observed flame angle at that point. For flame II, this confirms the general observation that we saw earlier in the flame edges derived from instantaneous snapshots. The most probable flame angles near the centerline are predominantly oriented downstream. As we move radially outward, the most probable flame angle rotates toward the walls, and then upstream, always into the mean flow.

In figure 4-21(c), we see the most probable component of the flow velocity normal to the flame. Where the component of the flow velocity into the flame nearly matches
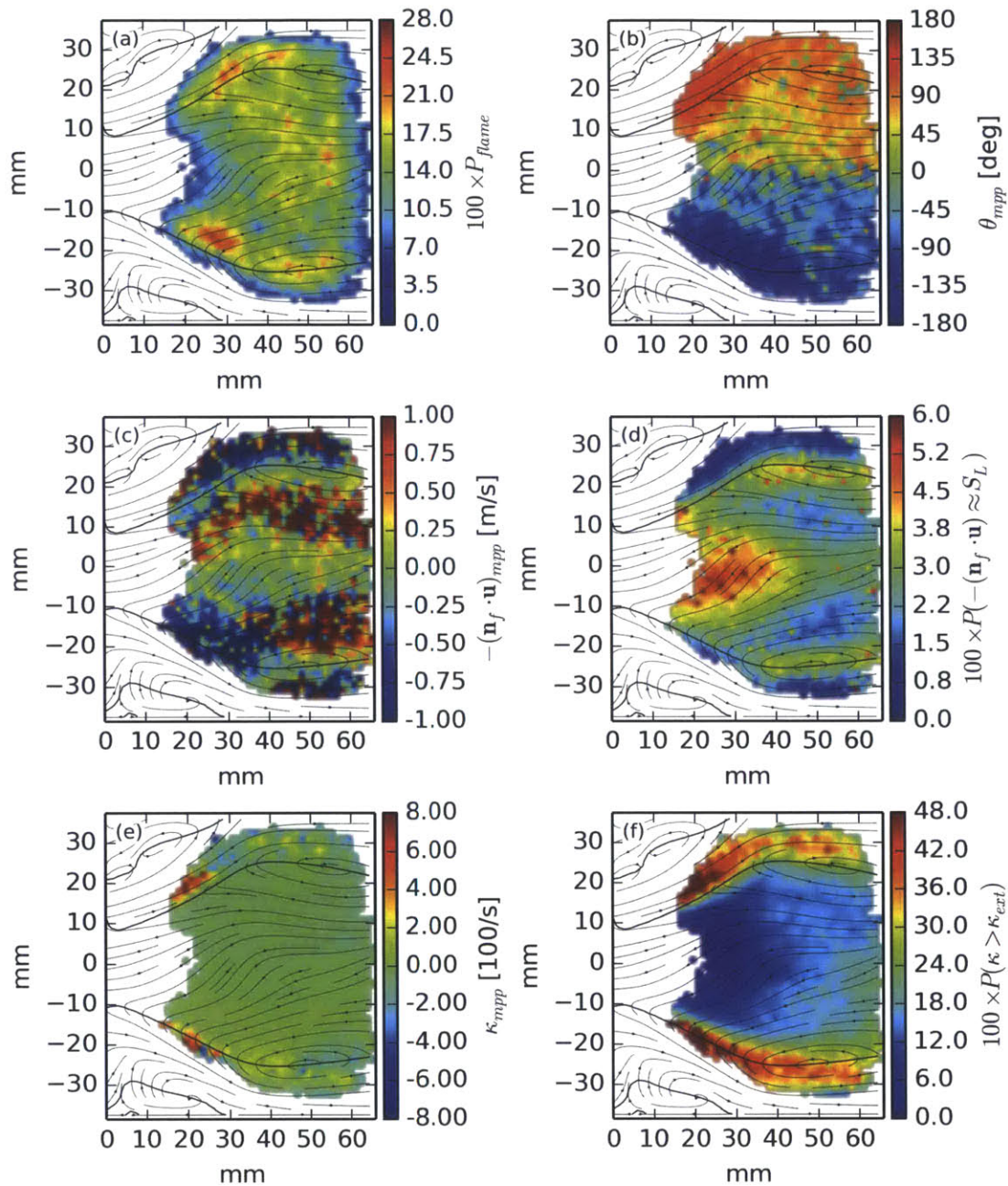
Figure 4-21: Spatially resolved maps show statistical flow-flame interactions for flame II at $\phi = 0.550$ in pure CH_4. The point-by-point probability of detecting a flame is shown in (a), and the most probable flame angle is shown in (b). The most probable velocity of the flow into the flame is shown in (c), and the probability of normal flow velocity being within 10 cm/s of the laminar flame speed (d). The most probable strain rate is shown in (e), and the probability of the strain rate exceeding the extinction limit is shown in (f).

114

the laminar flame speed, we can expect the flame to be nearly stationary. Essentially, these are the locations where we should be most likely to find an anchored flame. The figure gives us a picture of the structure of the flow. In the central region, the most probable normal flow component is nearly zero, so we should expect to observe flame slowly propagating in the downstream direction. This corresponds with the core of the recirculation bubble. Moving radially outward, we find a zone of high relative flow velocity into the flame, where the outwardly expanding flame fronts propagate into the inflow of the main eddy. In the center of the eddy, the most probable flow velocity drops to nearly zero. At the outermost, upstream edge of the inner recirculation zone, the most probable normal component of the velocity pushes the flame. Correlating the mean streamlines with the most probable flame angle in this region, we see that this flow pushes the flame into the shear layer at the leading edge of the recirculation zone. Comparing this observation to the most probable flame angle in the region, we see that the shift in sign of the most probable flow velocity corresponds not to a shift in the flow itself, which we can see from the mean streamlines, but from a shift in the flame angle outward and toward the expansion plane. This can be better seen in figure 4-22(a), where we plot the instantaneous flame from a single snapshot over the most probable normal flow component. As the flame propagates outward, it continues downstream along the centerline, but near the edges, it turns upstream into the recirculating reactants, and the recirculation zone pushes it into the shear layer.

In figure 4-21(d), we look at another metric of the normal flow distribution. We plot the spatially-resolved fraction of the flow velocity normal to the flame that lies within 10 cm/s of the laminar flame speed of 7.6 cm/s at his operating point. From this figure, we see a similar picture as we saw in 4-21(d). Near the combustor centerline, at the leading edge of the flame, and near the center of the primary eddy on both sides, we see a relatively high probability of the normal flow velocity nearly matching the laminar flame speed. Between the centerline and each of the two centers of the vortex ring, the probability of the normal flow velocity matching the laminar flame speed drops with respect to the rest of the inner recirculation zone. This corresponds
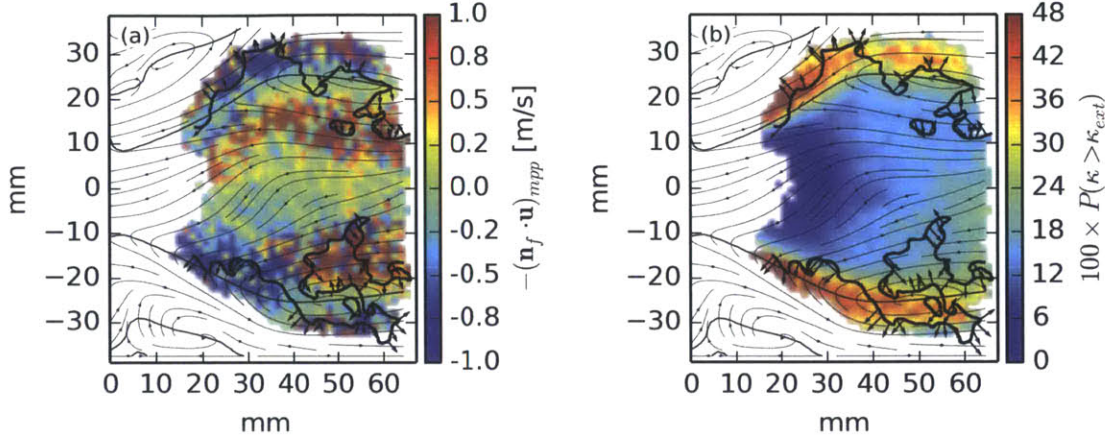
Figure 4-22: An instantaneous flame edge is overlaid on the most probable normal flow velocity (a) and the probability of exceeding the extinction strain rate (b) for flame II. Red arrows indicate the direction of flame propagation.

to a relatively high most probable normal flow component into the flame, a fact that is two be expected given the location of these regions with respect to the vortex centers. Nonetheless the probability of a stationary flame is relatively high throughout the entire inner recirculation zone, and only diminishes near the shear layer where, as we have already shown, the flow tends to push the flame away.

In figure 4-21(e), we examine the most probable strain rate along the flame. Save for the upstream edge of the conical flame, where the jet and recirculation zone meet, the most probable strain rate is nearly zero. In the initial part of the cone, however, we see this value jump up into the range of 450 s^{-1} to 600 s^{-1}, which is well is excess of the 360 s^{-1} static extinction strain rate, which begins to suggest that the farther upstream along the cone you look, the flow field begins to become more and more unfavorable for the propagation or persistence of at flame at this operating point. Hence, we do not see the flame propagating strongly up the inner shear layer.

We show a much more striking picture in the figure 4-21(f), where we plot the fraction of the strain rate distribution at each point that resides above the extinction limit. Within the mean boundaries of the recirculation zone, the shear is very low, and the flame strain distribution is almost entirely below the extinction limit. Coupled

116

with the relatively close match between the flame speed and flow velocity, this provides a very favorable location for the flame. The gradient of this property of the flame strain distribution is very sharp, however, and as soon as we move into the inner shear layer, nearly half of the distribution lies above the extinction limit. Upstream, in the inner boundary, over half of the distribution lies above the limit. As the flames are pushed into the shear layer in this area, we should not be surprised that they rapidly extinguish, given how hostile the flow is to flame survival.

A very critical point to understanding these results is to realize that although that in the presence of unsteady strains, flames do not immediately extinguish when the static extinction limit is reached, but that there is a time constant associated with the extinction event [81, 82, 52, 53]. In particular, for weak oscillations or strain rate excursions not far from the extinction limit, the time taken to extinguish a premixed flamelet increases nearly exponentially compared to higher strain rates or higher amplitude velocity oscillations. Egolfopoulos examined the mechanism of unsteady extinction in laminar premixed flames, and found that for sufficiently high frequency oscillations, extinction may be delayed or altogether suppressed [83]. During these high frequency oscillations, the flame begins to extinguish, but a hot radical pool remains. If the strain rate drops sufficiently quickly, the flame will reignite. If the period of the oscillation is too high, the flame may be permanently weakened by the loss of radicals, and eventually the chemical reaction is unable to restart. If the period is sufficiently low (or equivalently, the frequency is sufficiently high), the flame may not be permanently weakened, and may avoid extinction altogether. In our experiment, we can see that the time scale for straining is directly related to the turbulent velocity fluctuations that we presented in figure 4-4. If we take the flame thickness of approximately 1 mm as our length scale, the turbulent time scales are on the order of 1 ms to 4 ms in the inner recirculation zone and between 250 μs and 500 μs in the shear layers of the jet (and less in the downstream separation zone of flame IV). This timescale drops slightly as a function of increasing equivalence ratio in the conical region of the jet.

The important takeaway from these metrics is that flame II appears to be bounded

by a high strain region and high jet velocities. We do see outlying high values within fraction of observations which lie above the laminar flame speed, suggesting that flame stabilization is partially responsible for limiting the propagation of the flame. At the outer boundary of the inner recirculation zone, however, we see a sharp increase in the flame strain, and a subsequent decline in the flame probability. We can see a negative correlation between these two parameters, which lends support to the notion that the flame propagation is strain limited. Put another way, in the spatial regions where more of the observed flames exists at strain rates above those that they can sustain in steady state, we observe flames less often.

If we think about the physics of ignition, once we have established a flame in a flow with a recirculation zone, the hot combustion products become entrained in the recirculation zone, and ignite the fresh mixture of reactants in the shear layer between the jet and the recirculation zone. In the case of flame II, ignition must take place in the upstream zone of the shear layer. As the flame is unable to propagate into the shear layer, the jet contains a primarily unburned gas mixture, and as this mixture is entrained, the flame consumes it, propagating into the reverse flow and toward the outer edge of the recirculation zone. As much of jet bypasses the initial recirculation zone, reactants continue to propagate downstream around the outside of the bubble. Some of the flames propagating against the recirculating flow must reach the downstream end of the recirculation zone. In the previous section, we observed that the recirculation bubble is closed, and so flames propagating past this boundary will continue to burn, but in a flow that is on average oriented in the downstream direction. These flames will be rapidly advected downstream as if they were experiencing blow off, thereby producing the highly elongated flame that we see.

Focusing once more on the fact that the flame is observed with high probability throughout the inner recirculation zone, rather than being concentrated near the inner shear layer, we need to account for the effects of chemistry. In the presence of finite rate chemistry, when the hot products come into contact with the fresh reactants, there is an ignition delay, which has been shown to play a significant role in the stabilization of the flame [67, 84]. In chapter 3, we calculated the ignition delay

as a function of the equivalence ratio. A critical metric then is the ratio between the ignition delay, τ_{ig} from the reactants coming in contact with products, and the characteristic flow timescale, $\tau_{flow} = d/u$, where d is the characteristic eddy diameter, which we take to be one-half of the diameter of the combustion chamber, and u is the characteristic velocity of the flow in the outer eddy, which we take to be 3.0 m/s, and is fairly consistent across all of our tested operating points. Therefore, τ_{flow} is a characteristic turnover time for the eddy on the order of 6 ms. Calculations of ignition delays for CH_4/air flames by Meier *et al* [67] predict an ignition delay on the order of 5 ms at the lean equivalence ratios such as flame II, and reducing to approximately 0.1 ms by the time we reach flame IV. From this, we can see that not only are the flames unable to propagate past the inner shear layer in this flame configuration, but the ignition delay for reactants coming in contact with the recirculation zone is sufficiently long that ignition does not take place until the reactants have been propagated well into the center of the recirculation bubble.

4.3.3   Flame III: Inner shear layer stabilization

The next case we consider is flame III, the conical flame at $\phi = 0.600$ in pure CH_4. Once the flame transitioned into this configuration, we recall that the structure of the inner recirculation zone also underwent a significant qualitative change. The recirculation zone became shorter, such that its downstream edge (defined by the mean zero axial velocity contour) moved closer to the expansion plane, and a second, counter-rotating eddy joined the primary eddy, creating a small zone of positive flow buried within the inner recirculation zone. As for the flame geometry itself, we see a pronounced conical shape that appears preferentially along the inner shear layer, while the recirculation zone is flame-free. Unlike flame II, the axial extent of flame III is fairly well defined. We see the reaction continuing downstream of the conical section along the combustor wall for a finite distance, terminating within the field of view, due to complete consumption of the reactants.

The ensemble of pointwise statistical mappings for flame III is shown in figure 4-23. As before, the central component is the pointwise flame probability shown in

Figure 4-23: Spatially resolved maps show statistical flow-flame interactions for flame III at $\phi = 0.600$ in pure CH_4. The point-by-point probability of detecting a flame is shown in (a), and the most probable flame angle is shown in (b). The most probable velocity of the flow into the flame is shown in (c), and the probability of normal flow velocity being within 10 cm/s of the laminar flame speed (d). The most probable strain rate is shown in (e), and the probability of the strain rate exceeding the extinction limit is shown in (f).

4-23(a). Unlike flame II, and consistent with our observations from the filtered flame chemiluminescence and instantaneous PLIF snapshots, the interior of the recirculation zone is completely devoid of the flame. Instead, within the interrogation plane, we see the flame concentrated in two bands which extend from just inside the inner recirculation zone to near the centerline of the jet. The highest probability in these bands is concentrated in the center of the bands, which are bordered by thin regions of low flame probability. The most probable flame angle in each branch, shown in 4-23(b), is neatly divided into two regions: the conical section of the flame, and the flame downstream of the conical section. In the conical section of the flame, the most probable flame angles are clustered around 135°, which is just beyond the perpendicular to the mean angle of the jet, and correspondingly clustered around -135° in the lower branch. Downstream of the conical section, however, the flame angles cluster just above 90° and below -90° in the upper and lower branches, respectively. When the jet impinges on the combustor wall, there is a separation, with most of the remaining reactants continuing downstream along and parallel to the combustor wall, constrained to the outer region of the cylindrical volume by the inner recirculation zone, while the remaining reactants are diverted upstream and entrained in the outer recirculation zone. The reactants that continue downstream along the combustor wall are consumed by the flame we observe that propagates nearly directly into the wall. In both sections of the flame, the near perpendicularity of the flame to the mean flow is a result of the high jet velocity, on the order of 10 m/s to the laminar flame speed, which is approximately 10.6 cm/s for this fuel and operating point.

In a hypothetical stationary condition the flame would stabilize aerodynamically in the location where the flame speed matched the flow velocity normal to the flame, so long as the flow derivatives at that location did not exceed the static flame extinction strain rate. In figures 4-23(c) and 4-23(d), we examine the statistical relationship between the flow velocity normal to the flame and the laminar burning velocity. The most probable component of the flow velocity normal to the flame, shown in 4-23(c) shows us that throughout the interrogation region for this flame, the most probable flow speed often significantly exceeds the laminar burning velocity. We acknowledge

121

that the strained flame consumption speed *does* exceed the laminar flame speed for high strain rates, however in no case does the consumption speed exceed 20 cm/s, and the saturation values, red for positive and blue for negative, of figure 4-23(c) correspond to normal velocity components of 1.0 to over 10.0 m/s, exceeding the highest possible flame speed by a factor of at least five. These statistics for flame III betray some asymmetry in the experiment. In the upper branch, the most probable normal component of the flow is into the flame, while in the lower branch, it is away from the flame, as these values are situated just inside the recirculation zone, and so these velocities can be considered to be advocating the flame into the reactants in this situation. Comparing the spatial distribution of these values to the spatially resolved probability of finding a flame, we see that, as one would expect, the closer that this component of the flow velocity is to the ±20 cm/s, the higher the probability of finding a flame, however this is not an extremely strong correlation. A high most probable value for this velocity component could correlate with a relatively high flame probability in a very turbulent region, which we know the jet is from the observations of the RMS velocity component in the previous section.

We take a different perspective of the distribution of the normal flow velocity in figure 4-23(d). At each point in the flow, we integrate the distribution of the normal flow component from 10 cm/s below the laminar flame speed to 10 cm/s above the laminar flame speed, and therefore the color mapping corresponds to the spatially resolved fraction of the normal flow velocity distribution that lies within 10 cm/s laminar flame speed. We see that the normal flow velocity only has any significant probability of being near the laminar flame speed within a very thin region of the inner shear layer on both the upper and lower branches of the flame.

We should interpret this zone as the most likely zone in which we would find the flame, and this is the most likely place to find a stationary flame. The jet flow parallel to the combustor wall shows strong symmetry in this regard, but the conical portion of the flame betrays the slight asymmetry in this particular flame. In the lower brach, the flame is more often observed slightly inside the inner recirculation zone, a fact that results in a relatively high probability of realizing a stationary flame,

which is also evidence in the flame probability, which remains relatively high in the leading edge of the lower conical branch. The upper branch, however, is embedded more deeply in the jet, and consequently the zone in which we have any significant chance of observing a stationary flame is much lower, which is consistent with a low probability of observing the flame in the upper conical branch when compared to the lower conical branch. Thus, we see a negative correlation between the probability of observing a flame and the likelihood that the flow normal to an observed flame exceeds the laminar burning velocity, which is what we should expect from a flame stabilization perspective.

Next, we consider the flame strain, and plot similar statistics in figures 4-23(e) and 4-23(f). Downstream of the conical region, the most probable flame strain is very nearly zero in both branches of the flame. This value begins to increase as we enter the conical regions, however. While we observe a little bit of compression in the upper branch of the conical flame, on the outer edge near the wall, the main feature, shared by both branches of the flame is the very high most probable strain value as we move farther upstream along the flame. Between 20 mm and 25 mm (axially) downstream of the expansion (the farthest upstream that we are resolving), the most probable observed strain rate falls between 550 s^{-1} and 700 s^{-1}, which is comparable to slightly in excess of the calculated static extinction strain rate of 585 s^{-1}. While we know that flames can survive for a short period of time in at strain rates above their static extinction limit, these strain rates make flames less likely to survive and propagate through the fresh reactants. A more telling picture is shown in figure 4-23(f), which plots the fraction of the flame strain distribution that lies above the extinction limit as a function of spatial coordinate. Downstream, along the combustor wall, and approximately 10 mm upstream into the conical region on the outer edge of the flame, we see relatively low values falling between 0.30 and 0.50. In the interior of the conical region, extending 10-15 mm axially downstream, however, the fraction of strain rate observations in both branches exceeding the extinction limit falls between 0.55 and 0.70, increasing the farther upstream we look. Such frequent high strains mean that flame extinction events in this region should be very frequent,

123

and that flames propagating into this zone should extinguish before they are able to travel farther.

As we did with flame II, we can think about the physics of the ignition and fuel consumption process to help describe the overall geometry that we observe. As with the previous flame geometry, hot combustion products inside the inner recirculation zone are responsible for igniting the fresh mixture when they come in contact with the jet. Aside from the propagation of the flame into the shear layer that takes place in the transition between flame II and flame III, one feature, which has not directly been addressed yet, is the finite axial extent of flame III. In the previous section we noted that flames propagating against the reversed flow of the vortex breakdown bubble eventually reach the end of the recirculation zone, and enter a forward propagating flow of reactants which advect the flames rapidly downstream as they burn fresh mixture, resulting in a flame that propagates far into the exhaust section of the combustor. In flame III, in contrast, we see that the flame is able to propagate into the shear layer not only of the conical region, but along the combustor wall as well, consuming all or nearly all of the reactants before the jet progresses downstream.

4.3.4   Transitional flame: Intermittent stabilization

Next, we get into the transitional flame that intermittently transitions between two geometries: a conical flame similar to flame III, and a conical flame accompanied by a secondary burning zone in the outer shear layer, similar to flame IV. While we have a persistent flame in the conical region, we describe the outer flame as "flickering" insofar as any given realization of this flame geometry, there may or may not be a flame in the outer shear layer with comparable probabilities for both outcomes. In conjunction with the transition in the flame geometry, we see the flow undergoing a structural transition as the inner recirculation zone also jumps between two states–a double cell recirculation bubble similar to that observed with flame III, and a single cell recirculation bubble similar to that observed with flame IV. As the flame flickers into the outer recirculation zone, the instantaneous flame edges that we have extracted from the PLIF have shown us that the flame edge usually crosses from the inner to

the outer shear layer through the jet, and the connection between the two flames is likely a necessary condition for maintaining a reaction in the outer zone, which is more directly subject to heat loss to the combustor walls.

We show the ensemble of statistical calculations for the transitional flame in figure 4-24. We begin by examining the spatially resolved flame probability in 4-24(a), which shows us our first quantitative evidence of the flickering phenomenon. In the conical region of the flame, which has moved farther toward the jet centerline than we saw in flame III, the probability of observing a flame remains high, often as high as 50% or greater, however we now also see that there is a nontrivial probability of detecting a flame in the outer zone. In both branches of the flame, this zone extends outward from the jet centerline, immediately upstream of the impingement point, and spreads along the combustor wall and parallel to the jet along the outer shear layer. The outer flame is observed up to 20 mm upstream of the jet's impingement point on the combustor wall. Consistent with the observation of intermittency, the maximum probability of observing the flame at a point in the outer region, at this operating point, never exceeds 25%, or about half of the value that we see in the conical region.

The flame angle, which we show in figure 4-24(b), exhibits the same pattern in the conical and downstream regions that we observed in flame III, however, we see a slightly different structure in the outer flame. The outer flame is divided into two parts, a flame that propagates along the outer shear layer, nearly parallel to the centerline of the jet, and a flame that appears near the combustor wall, upstream of the jet. The portion of the outer flame in the shear layer is oriented into the jet, nearly 180° to the conical flame, while the portion of the flame near the combustor wall is oriented at nearly 90° and -90° in the upper and lower branches of the flame, respectively. This latter portion of the flame propagates toward the wall, consuming reactants as they enter the recirculation zone, and is effectively a continuation of the downstream portion of the flame.

As in the previous section, figure 4-24(c) maps the most probable component of the flow velocity normal to the flame. If we compare the flame probability distributions of the flame III and the transitional flame, we see that the conical section of the flame
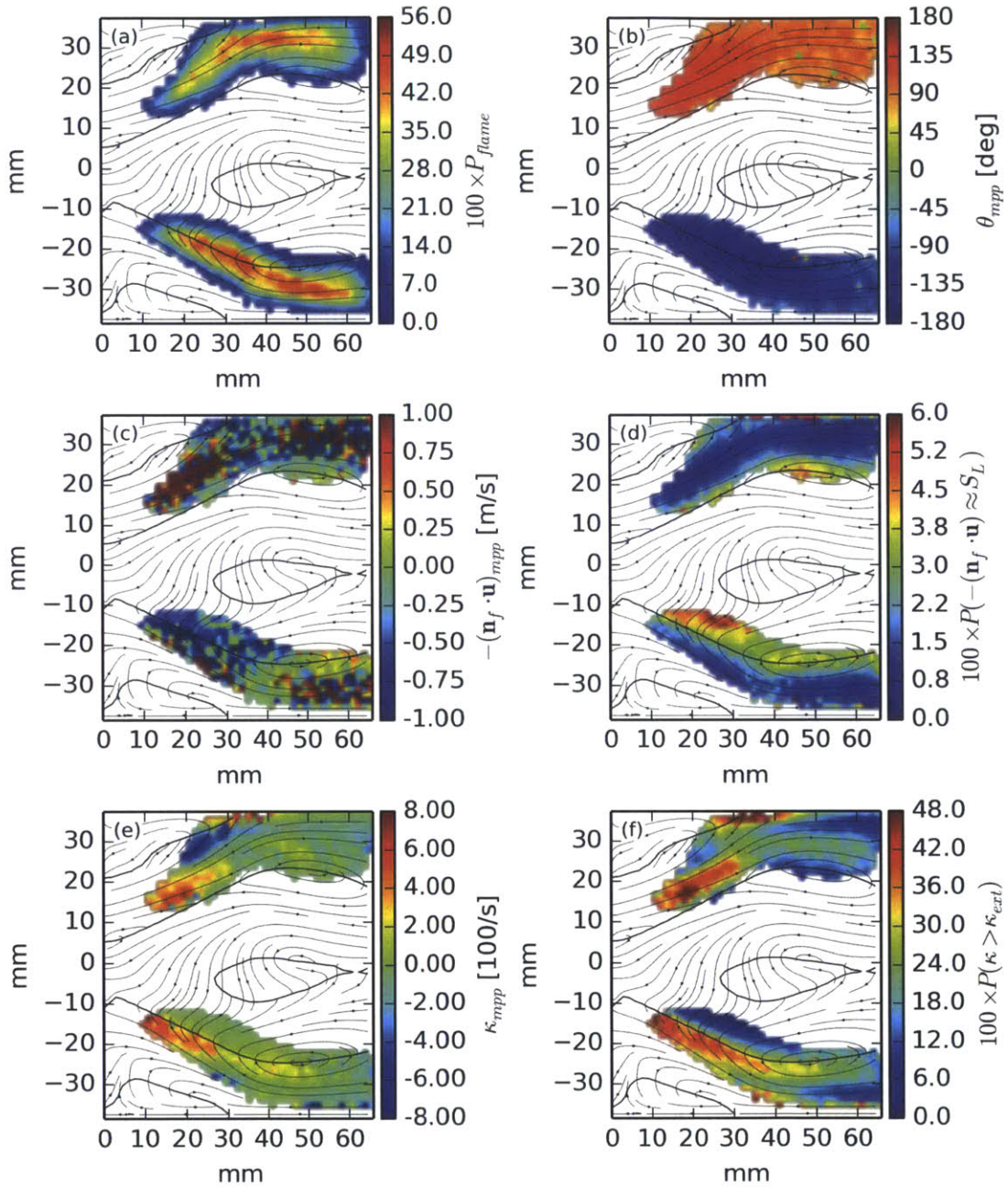
125
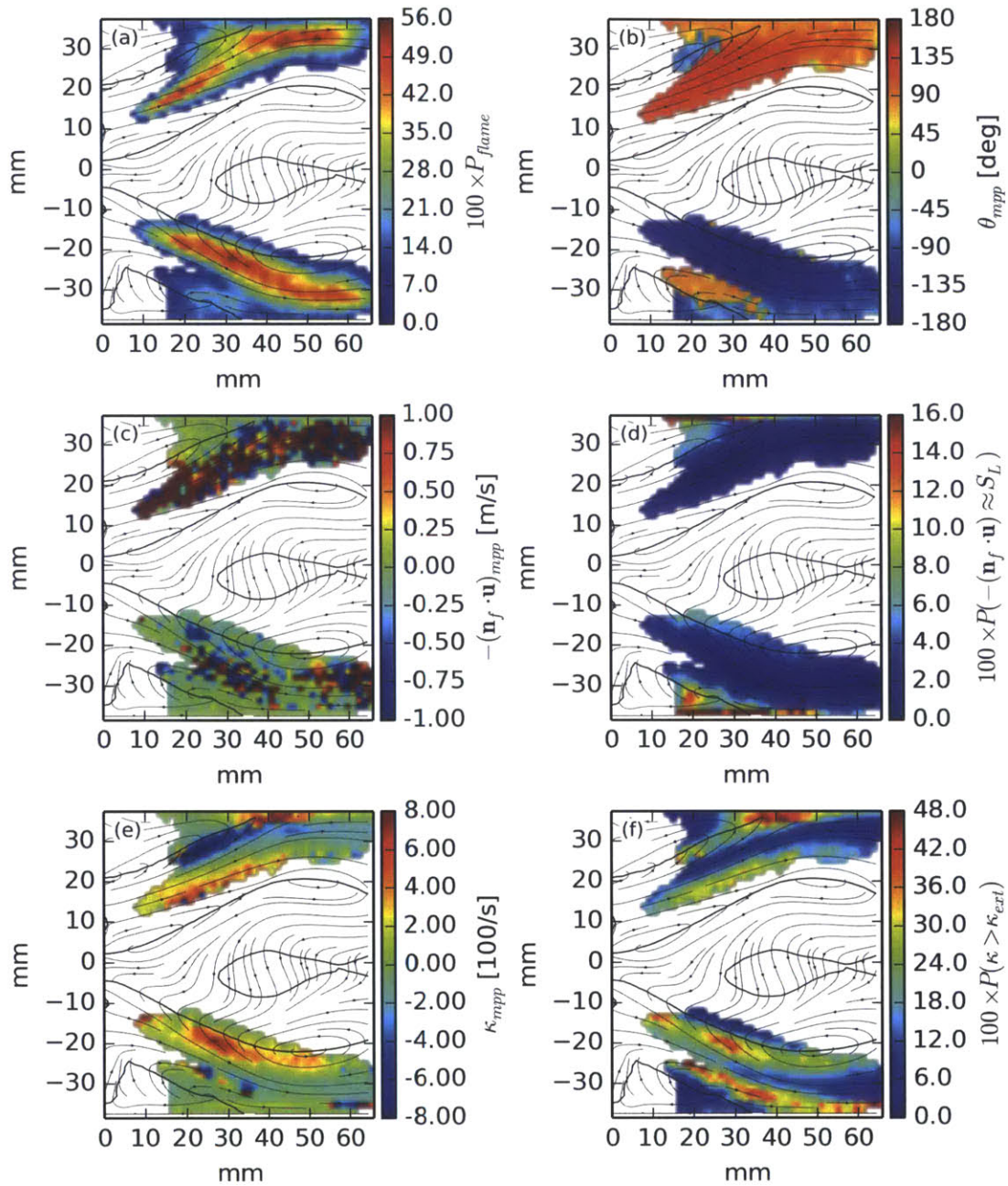
Figure 4-24: Spatially resolved maps show statistical flow-flame interactions for the trarnsitional flame at $\phi = 0.625$ in pure CH_4. The point-by-point probability of detecting a flame is shown in (a), and the most probable flame angle is shown in (b). The most probable velocity of the flow into the flame is shown in (c), and the probability of normal flow velocity being within 10 cm/s of the laminar flame speed (d). The most probable strain rate is shown in (e), and the probability of the strain rate exceeding the extinction limit is shown in (f).

126
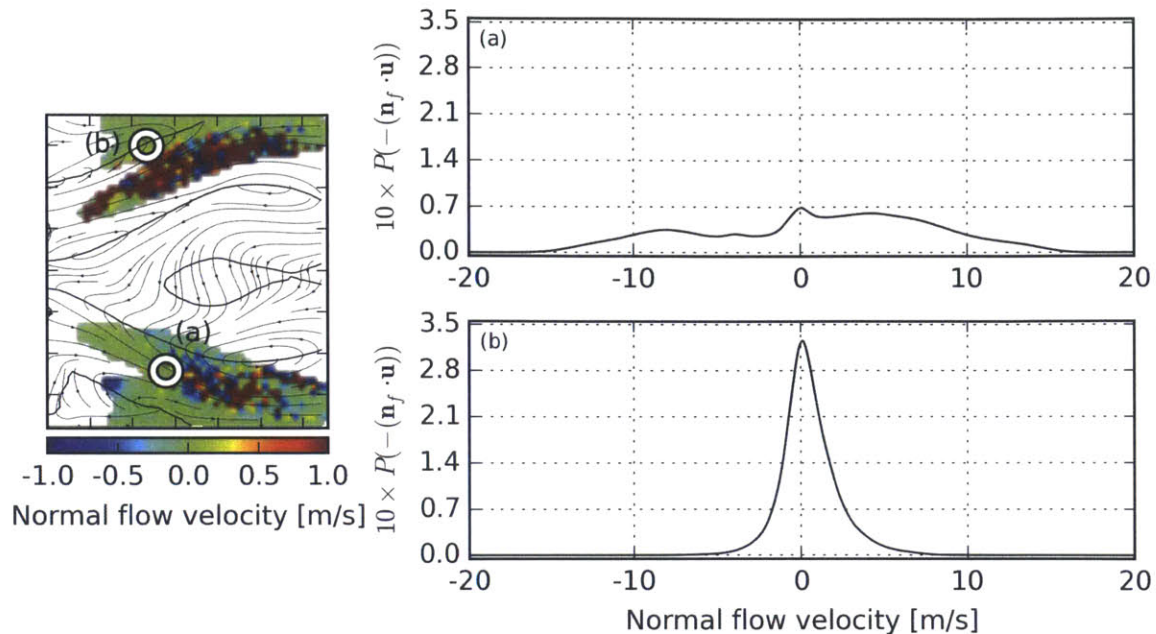
Figure 4-25: The distribution of the flow component normal to the flame is shown at two locations for the transitional flame. In (a) we have selected a point in the conical region of the flame showing a wide, flat distribution, and in (b) we have selected a point in the outer zone, showing strong clustering at low values.

has shifted toward the jet centerline. Consequently, we see that there is a lot of scatter in the spatial distribution of the most probable value of the normal flow velocity, in both branches of the conical flame, with neighboring values spanning the range from much less than -1.0 m/s, on the order of 10 cm/s, to much greater than 1.0 m/s. We can interpret this to mean that the distributions of the normal velocity component are very flat, which we show in figure 4-25(a). The wide distributions in the conical region suggest that there is very low probability of a flame properly stabilizing in this region, and that the presence of this conical flame must rely on continuous ignition from products in the inner recirculation zone. In the outer recirculation zone, however, we see that the most probable normal flow velocity is consistently on the order of the laminar flame speed.

This story becomes more clear when we look at the fraction of time that the normal flow velocity is observed within 10 cm/s of the laminar flame speed, which we

127

show in figure 4-24(d). The probability of observing a nearly stationary flame within the conical zone or downstream of the centerline of the cone is nearly uniformly zero, with only a very small probability being observed on the inner edge on the upstream side of the lower branch of the flame. In the outer zone, however, we see particularly high probabilities for normal flow velocities being near the laminar flame speed, a fact that is confirmed by the sample distribution that we examine in figure 4-25(b). The distribution shows a large peak at zero, and the decreases nearly symmetrically on both sides. Over 90% of the distribution is contained within ± 3 m/s, whereas the similar 90% of the distribution in 4-25(a) is contained between -10 m/s and 12 m/s. In the outer zone, the probability of the normal flow velocity being within 10 cm/s of the laminar flame speed approaches, and at a few points, exceeds 10%, suggesting that the conditions in this outer zone are particularly suitable for a flame to stabilize. This observation, however, is at odds with the fact that there is only a moderate to low probability of actually observing a flame in the outer zone in any particular realization of the flame at this operating point. To understand why this might be, we look to the flame strain statistics.

We show the most probable flame strain in figure 4-24(e), and note that throughout most of the observed flame, the most probable flame strain is very nearly zero, however we see there there are large excursions at the edges of the conical flame, on both the inner and outer side, which appear nearly symmetric with respect to the axis of symmetry. On the inside of the conical flame, we see small pockets where the most probable flame strain lies between 600 s^{-1} and 750 s^{-1}, although this is comparable to the stationary extinction strain rate of 720 s^{-1}. On the outside of the conical flame, separating the conical flame from the outer flame, most probable flame strain is actually strongly compressive, which we would not expect to hinder the propagation of the flame, and within the outer zone itself, the most probable flame strain is nearly zero, once more, suggesting that this should be a very likely place to find a flame.

It is when we observe the probability of observing strains in excess of the static extinction limit in figure 4-24 that we begin to understand the extinction mechanism that might be occurring in the outer flame. Near the centerline of the jet and in the

outer flame, the probability of the strain rate exceeding the extinction limit is very low, however both on the interior border of the conical flame and its continuation downstream, and on the exterior boundary of the conical flame, which separates it from outer flame, the probability of exceeding the extinction strain reach 30% to 40%. On the interior side, this suggests that the shift in the conical flame toward the center of the jet is principally driven by the reduced strains in this region. On the outer side, this suggests that there is a high probability of the flames in the cone and in the outer region either being or becoming disconnected.

The disconnection of the outer flame from the conical flame does not in itself explain why we observe flickering. As we have just noted, the flow velocities and strain rates in the outer zone are such that this is actually a very favorable region for observing a flame. The answer is probably very similar to that for the question as to why we do not see a flame become established in the outer zone, and persist there, at lower equivalence ratios, even though the flow statistics of the outer zone change little across equivalence ratios. The answer to this most likely lies in heat loss from the outer flame to the combustor wall. When the flame becomes detached from the conical region, there is too much energy lost to the walls to maintain a reaction, and so the flame extinguishes. At lower equivalence ratios, the lower extinction limit means that the likelihood of a flame connecting to the outer zone is extremely low, and it is only when the probability of connecting is comparable to the probability of not connecting do we see flickering occur. This hypothesis does predict that if we could construct a combustor with perfectly adiabatic walls, we should see an outer flame become established, even for very lean equivalence ratios, below the values where we even observe the conical flame.

4.3.5   Flame IV: Inner and outer shear layer stabilization

The final flame geometry that we consider is flame IV. Flame IV is characterized by a conical flame, extending downstream along the shear layer as the jet flows along the wall, as we saw with flame III, but it is joined by a flame in the outer recirculation zone, specifically, as we shall see, extending along the outer shear layer and parallel to

the combustor wall. This is similar to the transitional flame that we analyzed in the preceding section, except that we observe a fairly persistent flame in the outer zone rather than the intermittent flickering that appeared previously. In this configuration, we have also lost the concomitant transition of the inner recirculation zone between two-cell and one-cell configurations, and it stabilizes in a one-cell configuration, albeit with a free stagnation point approximately 9 mm downstream of the expansion plane.

When we examine the flame probability in figure 4-26(a), we see confirmation that the flickering has stopped and been replaced with a persistent flame in the outer zone. Within this region, we now see the flame probability reaching 40% to 45% at individual points, which is on the same order as the flame probability in the conical region. In between the conical region and the outer zone, where we have observed the flame bridging between the two regions, the probability of finding a flame drops to between 25% and 30%, although this is significantly higher than the values that we observed in the transitional flame.

The flame angle distribution in figure 4-26(b) shows a similar pattern to the transitional flame. In the conical region, the flow is angled nearly parallel to the incoming reactants, while in the outer zone, we observe two very distinct parts of the flame. The first part is angled into the jet from the outer shear layer, opposite the conical region, while the side part of the outer flame lies parallel to the combustor wall, propagating into it and consuming reactants as they are diverted backward into the outer recirculation zone. There is one discernible different between flame IV and the transitional flame, however. The angle of the cone with respect to the axis of the combustor has decreased in our transition to flame IV, and the mean angle in the conical flame is now closer to 125° and -125°. This change clearly accompanies the shift in the mean flow structure, but one way to account for it is that we now have a persistent flame in the outer zone, and so we should be expecting the outer recirculation zone to be filling with low density combustion product now, rather than relatively high density reactants that we would see in flame III, for example, and intermittently in the transitional flame.

As we shall see, flame IV is a progression of the three flame geometries that
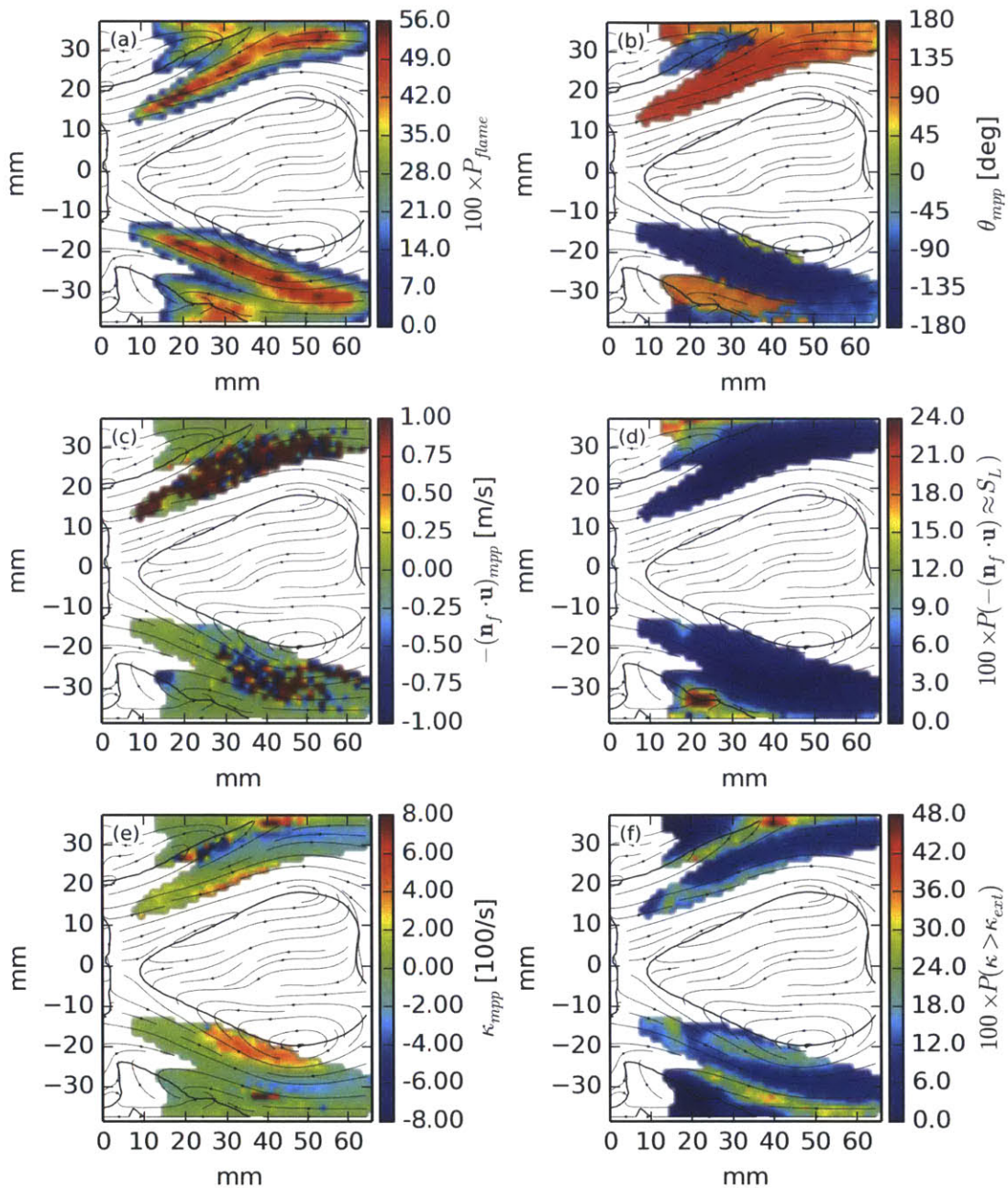
Figure 4-26: Spatially resolved maps show statistical flow-flame interactions for flame IV at $\phi = 0.650$ in pure CH_4. The point-by-point probability of detecting a flame is shown in (a), and the most probable flame angle is shown in (b). The most probable velocity of the flow into the flame is shown in (c), and the probability of normal flow velocity being within 10 cm/s of the laminar flame speed (d). The most probable strain rate is shown in (e), and the probability of the strain rate exceeding the extinction limit is shown in (f).

131
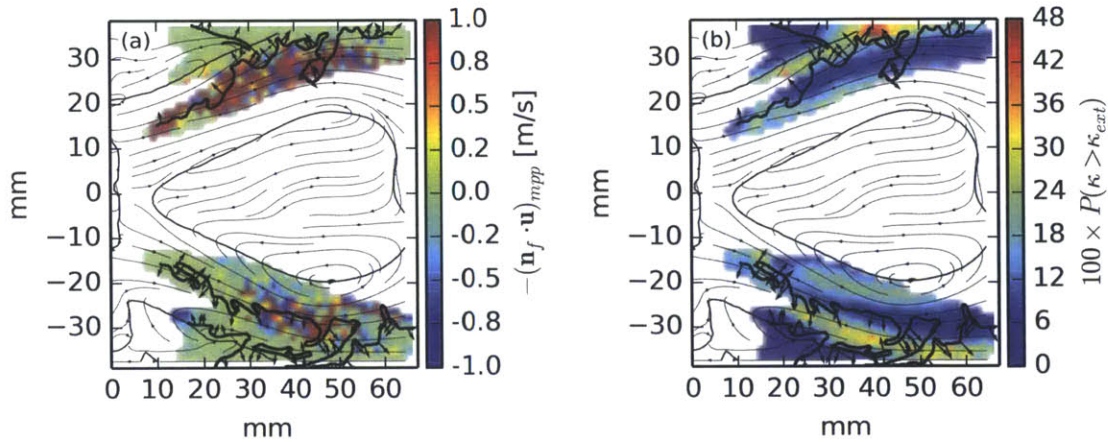
Figure 4-27: An instantaneous flame edge is overlaid on the most probable normal flow velocity (a) and the probability of exceeding the extinction strain rate (b) for flame IV. Red arrows indicate the direction of flame propagation.

we have already examined beyond the point where the flame stabilization is strain limited. We start be examining the characteristics of the most probable value of the normal component of the flow in figure 4-26(c), where our first observation is that, as we have been seeing with the progression from flame II to the transitional flame, the conical zone has propagated farther and farther into the jet. Despite the relatively large angle between the flame and the jet, we still see that the most probable normal flow velocity is exceedingly high in this region, surpassing the laminar flame speed by an order of magnitude. Even where the most probable value is low, the full distribution is skewed toward very high normal flow velocities, as is shown in figure 4-26(d), which plots the fraction of the distribution that is greater than the laminar flame speed. Almost nowhere in the conical region is there any significant probability of the flow allowing a stationary flame. In the outer zone in contrast, the most probable flow velocities are accompanied by a distribution that has a high probability of being near the laminar flame speed, reaching values between 10% and 30%. While there is a decent chance of properly stabilizing a flame for a short period of time in the outer zone, the conical flame is completely unsteady, and most likely owes its persistence to continuous ignition from the inner recirculation zone.

The flame strain presents a very different qualitative picture than we have previously seen. The magnitude and the location of the high strain and compression, which we show in figure 4-26(e) is very similar to what we saw in the transitional flame. We see some high positive strains on the interior of the conical flame, and some high compressive strains between the conical flame and the outer flame, but the flame has overwhelmingly confined itself to the interior of the jet where the strains are very low, despite not being able to stabilize in this region. The major qualitative difference comes when we look at the fraction of the strain rate distribution that lies above the extinction limit in figure 4-26(f), however. In going from the transitional flame to flame IV, the static extinction strain rate has gone from 720 s^{-1} to 870 s^{-1}, and while the large scale structures of the flow have changed, zones that the flame occupies have not, and the pointwise statistics of the flow in those regions is also very similar. As a result, the picture in 4-26(f) shows us that the strain rate rarely exceeds the extinction limit in either the conical or outer zones, and in the bridge between the two, it only exceeds the extinction limit 25% of the time.

Between flame IV and the transitional flame, we see a definite correlation between the probability of a flame being able to bridge between the conical region and the outer zone and the probability of observing a flame in that zone. In the transitional flame, where we often exceed the extinction limit in this band, we observe flickering. In contrast, when the extinction limit increases substantially, we see the flame bridging this gap more frequently, and the flame persists in the outer region. Consequently, this bridge appears to be critical to maintaining a flame in this outer zone, which lends credence to the theory that this outer flame is subject to extinction due to heat loss to the combustor walls.

In figure 4-27, we overlay an instantaneous flame edge showing the outer and inner flames in very close proximity to each other on two of the flame statistics: the most probable normal flow velocity, and the fraction of the strain rate distribution that exceeds the extinction limit. In the upper branch, these two pieces of the flame are disjoint and the outer flame is minimal, however in the lower branch, we see the flames actually connect through the reactant jet, and the outer flame extends upstream along

the outer shear layer. Although the normal flow velocity is high in this bridge (while remaining on the order of the laminar flame speed in the outer zone), this bridge could be maintained if flames could continuously make this connection. The flame strain gives us a bigger clue, however. The inner conical flame and outer shear layer flame are separated by a region of relatively high strain compared to the static extinction limit, something which is true to a greater degree in the transitional flame as well. Only as the equivalence ratio, and hence, the static extinction limit, increases do we see this bridge being made sufficiently frequently to maintain a flame in the outer zone. We must keep in mind that even if the outer flame is isolated, there is a timescale on which extinction due to heat loss occurs. If the bridge between the two regions is made sufficiently frequently, then we would expect not to see extinction occurring in this zone, which is the case with flame IV.

In order to understand the upstream propagation in this case, we need not look at the statistics of the flow-flame interactions, but at the mean streamlines of the flow field. The upstream edge of the conical flame extends just past the free stagnation point of the inner recirculation zone. The flow immediately upstream of the stagnation point is on the order of 10 m/s, the same as the jet centerline. Since the conical flame is not a stationary flame, it relies on continuous ignition provided by the inner recirculation zone, which therefore limits the propagation of the flame upstream. The previous flame geometries had all been limited by the extinction strain rate. The flame preferentially propagates into the reactants, but due to the strong shear in the flow, the propagation was limited. Flame IV is the first flame we observe that is effectively past that limit, and its stabilization is now only a function of the large scale flow features. This accounts for the relatively little variation in the flame geometry that we observe as we move to higher and higher equivalence ratios after we begin to observe flame IV.

4.3.6   Global flow-flame correlations

Over the preceding sections, we have taken a look at the spatially resolved statistics of three different flame geometries at four different operating points. We have focused on

two aspects of the flow-flame interactions–the component of the flow velocity normal to the flame, and the flame strain–and their spatial relationship to the probability of finding a flame in a given location. Our analysis has generally observed an expected relationship from basic flame kinematics between the normal flow velocity and the probability, where we note that the more likely the flow is to exceed the laminar burning speed, the more the flow will push the flame downstream outside of the region we are investigating, and the lower the probability is that we will find a flame in that location. While this mechanism clearly plays a role in the flame stabilization, in the statistical sense, it does not fully account for why the flame does not propagate any farther than it does. To account for the slow progression of the flame, we look to the flame strain, and in particular, relationship between the statistics of the flame strain and the extinction strain rate. In this section, we look at global statistics of both the strain rate and the flow velocity normal to the flame. We consider properties of the spatially resolved distributions and weight them by the probability of observing a flame in their respective locations to obtain distributions of these statistics that pertain to the entire interrogation region.

We begin by looking at the statistics of the flow velocity normal to the flame distributions. Starting with figure 4-28, we look at the most probable normal flow velocity. Although the distribution peaks at or just below the laminar flame speed, the distributions are all skewed toward negative values, or flows that advect the flame in the direction of flame propagation, and the distribution tapers off very rapidly for positive values above the laminar flame speed, a fact that is most readily observed in the cumulative distribution function. In figure 4-29, we show the fraction of the distribution that lies within 10 cm/s of the laminar flame speed. As the equivalence ratio increases, we observe that the peaks shifts toward lower relative values, but that the distributions becomes wider, and the result is that the higher the equivalence ratio, the lower the probability of observing a stationary flame, which is in agreement with our previous observation of the flame moving into higher speed flow as the equivalence ratio increases.

In figure 4-30, we show the distribution of the most probable flame strain, ob-
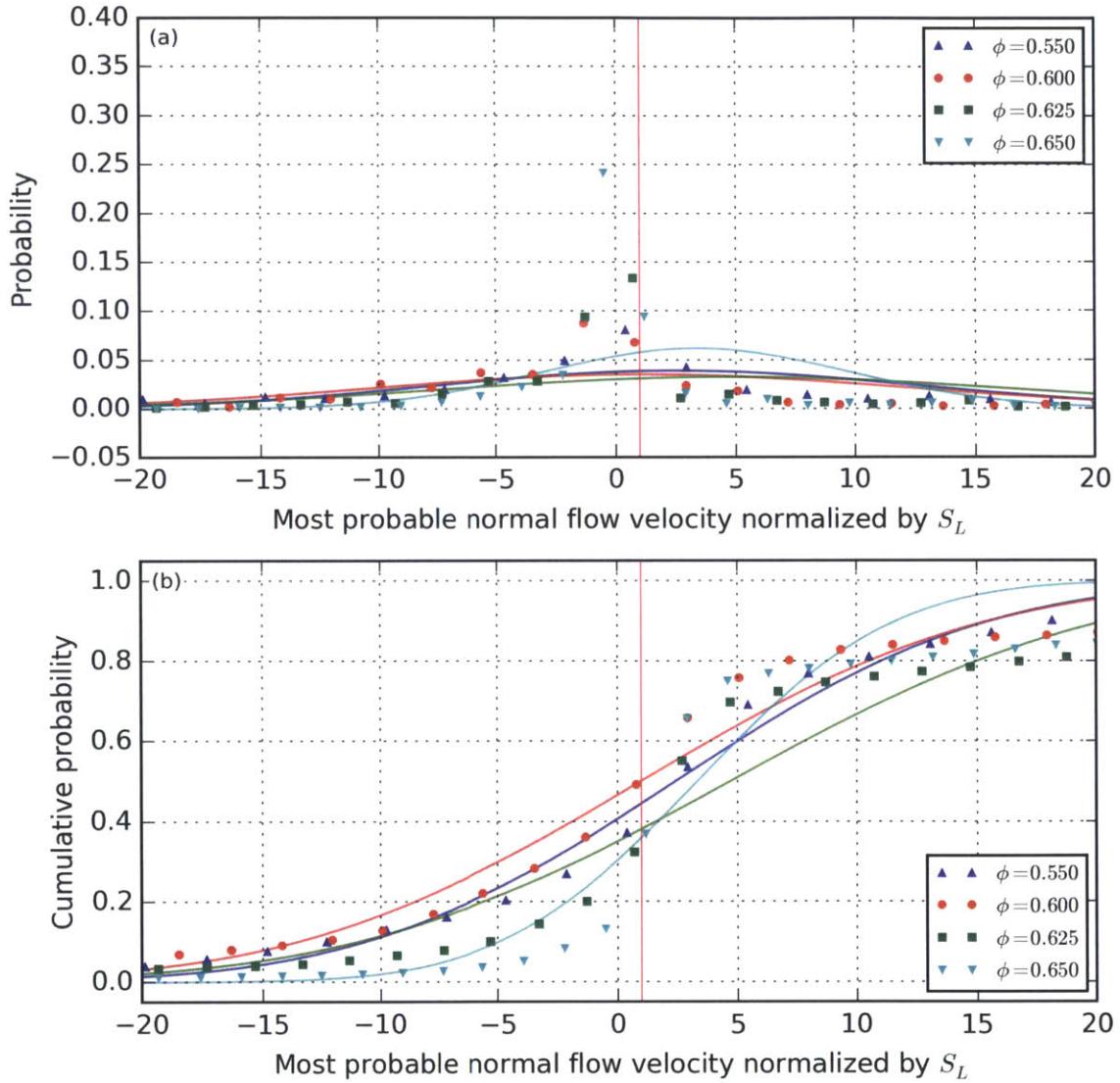
Figure 4-28: The probability density function (a) and cumulative density function (b) are shown for the pointwise value of the flow velocity component normal to the flame normalized by the laminar flame speed for each operating point. A red, vertical line marks the laminar flame speed.
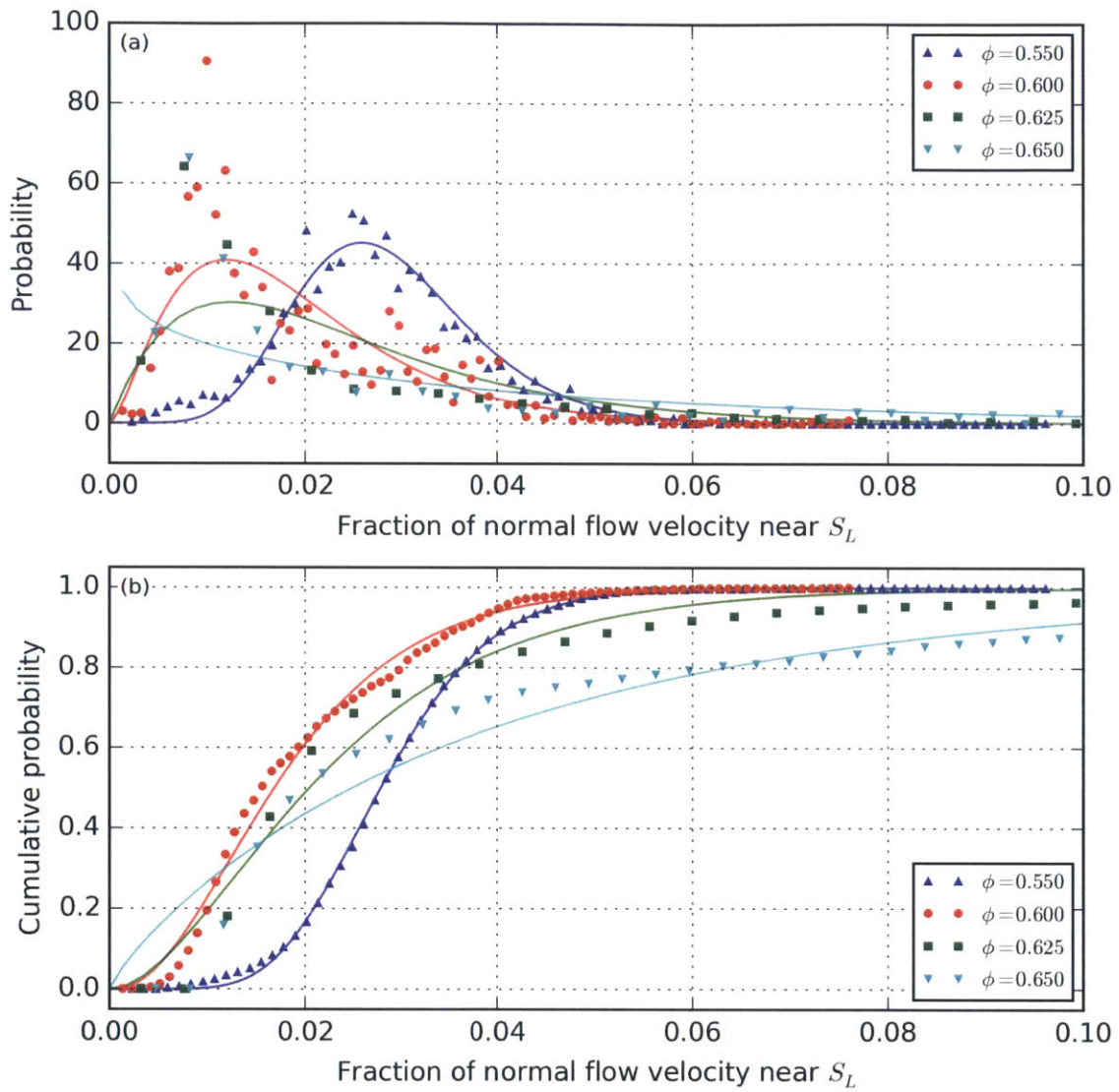
Figure 4-29: The probability density function (a) and cumulative density function (b) are shown for the pointwise fraction of the flow velocity component normal to the flame that lies within 10 cm/s of the laminar flame speed.

serving that the distributions peak near zero and gradually taper to either side, with nearly (but not quite) all observations of the most probable strain rate lying below the extinction limit. In figure 4-31, we see that the peak fraction of observations that lie above the extinction limit falls between 5% and 20%, depending on the case, but in all cases, a substantial fraction of the distributions exceed the extinction limit by up to 50%. The three lean cases all have distributions that lie close to each other, and we have already noted that these three appear to be primarily strain limited, while the fourth case, $\phi = 0.650$ appears to be limited primarily by the dominant flow features. As such, the fact that the distribution for this flame lies toward lower *relative* strains is consistent with this observation.

It is reasonable to attempt to find distributions with analytical expressions that closely match the experimental distributions. Doing so could shed some additional light on how these distributions vary with the combustor operating point, as well as provide usable statistics for use in conjunction with numerical modeling efforts.

We begin by looking at the distributions of the most probable strain rate and most probable normal flow speed. These distributions are nearly symmetric, with maxima near the center of the domain. Additionally, both distributions have exponentially decaying tails on either side of the most probable point. The best candidate distribution is a Gaussian distribution. We denote the probability density function of the most probable strain rate as g_κ and that of the most probable normal flow velocity as g_u. The general form for these probability density functions is given by:

$$g(x) = \frac{1}{\sigma\sqrt{2}} e^{-\frac{(x-\mu)^2}{2\sigma^2}} \tag{4.8}$$

where the parameter μ is the mean and the parameter σ is the standard deviation. The cumulative density functions are denoted by G_κ and G_u, respectively, and take on the following general form:

$$G(x) = \frac{1}{2}\left(1 + \mathrm{erf}\left[\frac{x-\mu}{\sigma\sqrt{2}}\right]\right) \tag{4.9}$$

138
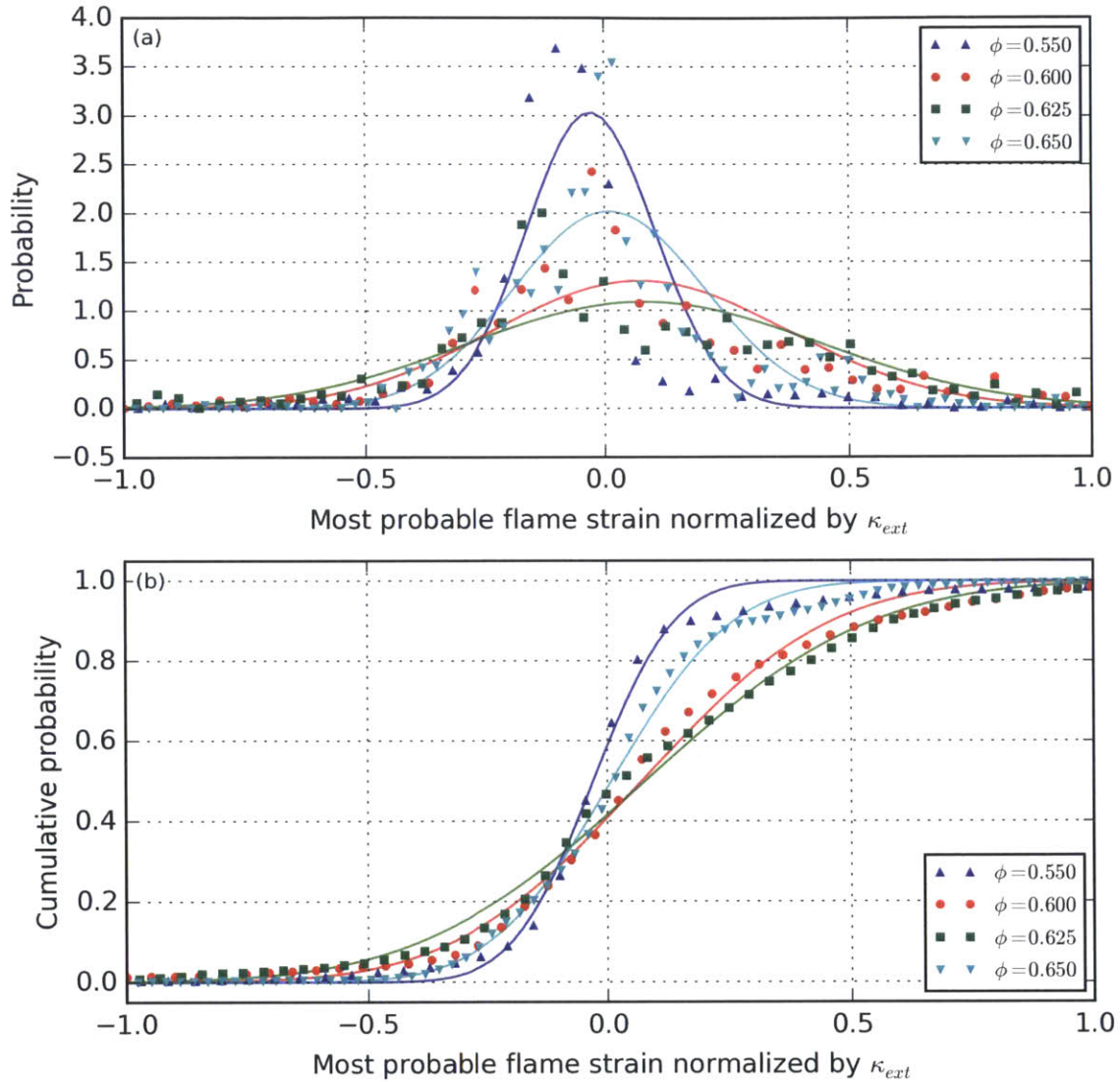
Figure 4-30: The probability density function (a) and cumulative density function (b) are shown for the pointwise value of of the flame strain normalized by the extinction strain rate for each operating point. A red, vertical line marks the extinction strain rate.
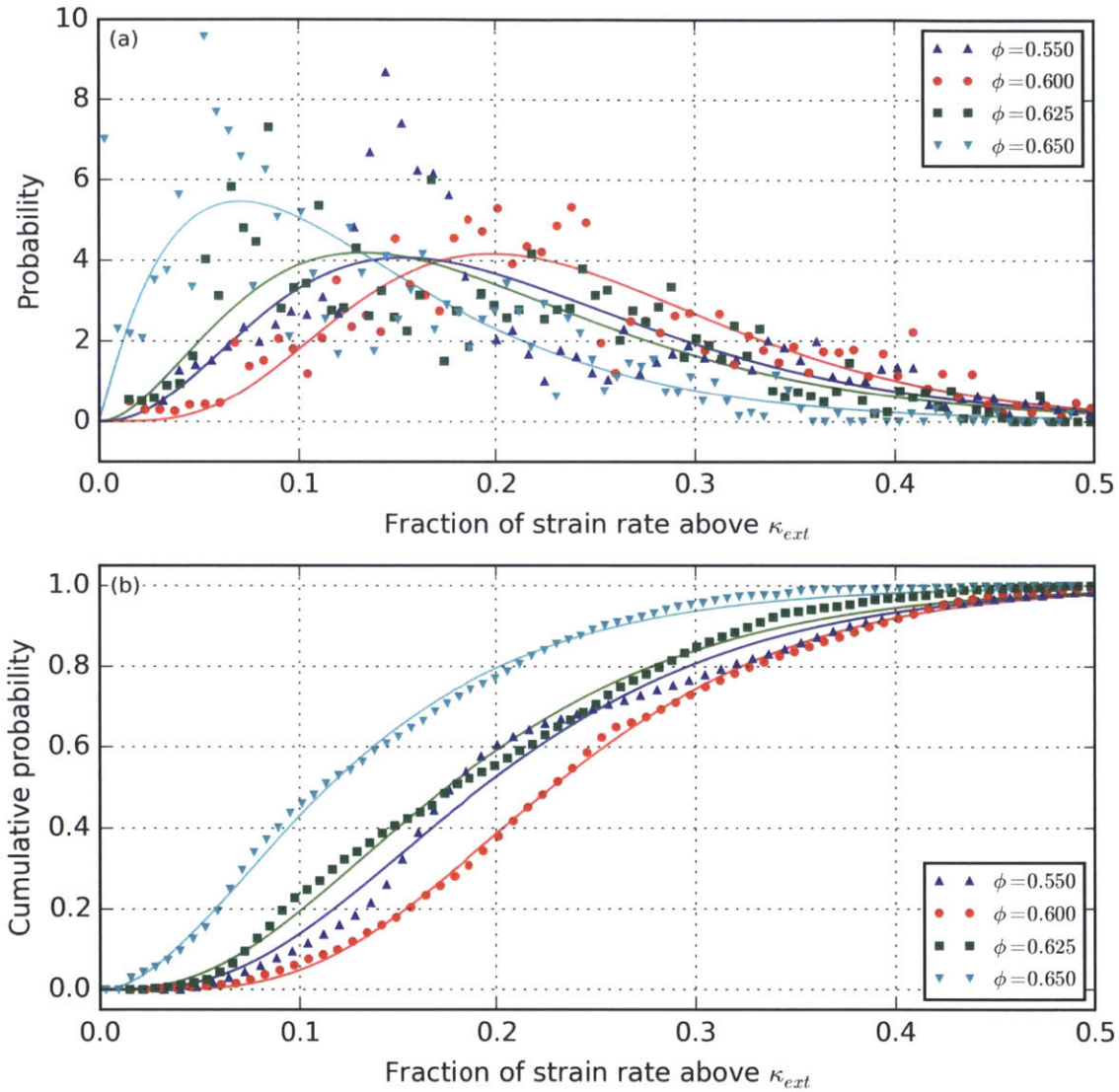
Figure 4-31: The probability density function (a) and cumulative density function (b) are shown for the pointwise fraction of the strain rate distribution that exceeds the extinction limit.

Table 4.1: Curve fit parameters are presented for analytical probability distributions based on a least squares fit to the experimental distributions. The most probable normal flow velocity ($u_n = -\mathbf{n}_f \cdot \mathbf{u}$) and the most probable flame strain (κ) are fit to Gaussian distributions, while the fraction of the normal flow velocity distribution above the laminar flame speed and the strain rate distribution over the extinction limit are fit to a gamma distribution. Speeds are normalized by the laminar flame speed for each case, and strain rates are normalized by the extinction strain rate for each case.

	$u_{n,mpp}$		$P(u_n > S_L)$		κ_{mpp}		$P(\kappa > \kappa_{ext})$	
ϕ	μ	σ	α	λ	μ	σ	α	λ
0.550	2.44	10.22	9.71	337.2	-0.03	0.14	3.61	17.0
0.600	0.99	11.32	2.62	136.9	0.07	0.31	5.46	22.5
0.625	4.73	12.24	2.02	83.4	0.08	0.37	3.09	15.8
0.650	3.34	6.47	0.84	21.5	0.01	0.20	2.08	15.3

where $\mathrm{erf}(y)$ is the error function, defined by:

$$\mathrm{erf}(y) = \frac{2}{\pi} \int_0^y e^{-t^2} \, dt \tag{4.10}$$

For each case, the parameters were calculated by fitting the analytical cumulative density function to that of the experimentally measured distribution. The fitted curves are shown in figures 4-28 and 4-30 in colors which correspond to the points representing the experimental distributions. The parameters, based off of a least squares fit to the experimental distributions are presented in table 4.1. Upon inspection, the Gaussian approximation to the most probable normal flow velocity fails to account for the extremity of the peak near zero, which we see in figure 4-28(a). There is an asymmetry in the distribution that is not well captured by the Gaussian model, which is best seen in 4-28(b), and is more pronounced at higher equivalence ratios. While the exponential tail of the Gaussian model captures the distribution of the negative normal flow velocities well (that is, flow which push the flame in the direction of propagation), the model greatly over predicts the normal velocities into the flame that are ten times the laminar flame speed or higher.

The Gaussian approximation to the most probable flame strain is shown in figure 4-30. The Gaussian model does a much better job predicting the extent of the peaks,

141

Table 4.2: A comparison of the means and standard deviations of the analytical (denoted by a subscript m) and experimental distributions (denoted by a subscript e) are presented for the most probable normal flow velocity ($u_n = -\mathbf{n}_f \cdot \mathbf{u}$) and the most probable flame strain (κ).

	$u_{n,mpp}$				κ_{mpp}			
ϕ	μ_e	μ_m	σ_e	σ_m	μ_e	μ_m	σ_e	σ_m
0.550	2.04	2.44	13.69	10.22	-0.06	-0.03	0.11	0.14
0.600	1.00	0.99	21.09	11.32	0.04	0.07	0.37	0.31
0.625	5.56	4.73	20.28	12.24	0.05	0.08	0.40	0.37
0.650	5.87	3.34	16.31	6.47	-0.01	0.01	0.23	0.20

and the experimental distribution shows greater symmetry in the exponential tails than the distribution of the most probable normal flow velocity did. There is a slight over prediction for strain rates between zero and the extinction strain rate, but by less than 10% in the worst case. For both variables, however, the analytical models do reasonably duplicate basic statistical properties of the experimental distribution such as the mean and standard deviation, as we show in table 4.2.

In contrast to the sharply peaked distributions of the most probable normal flow speed and most probable strain rate, the statistics for the fractional distribution of the strain rate above the extinction limit and the normal flow speed near the laminar flame speed are constrained to the interval from zero to one. The distributions show a peak at low values, and a decaying tail. If we relax the restriction on the domain, and let the probability density function take on non-zero values from zero to infinity, under the condition that the integral from one to infinity is negligible, we can approximate these distributions as gamma distributions, and we will see, there is much better agreement between the model and the data than we saw with the most probable flow-flame interactions.

We let f_κ denote the probability density function for the fraction of the flame strain distribution above the extinction limit and f_u denote the probability density function for the fraction of the normal flow component near the laminar flame speed. For each of the four flame geometries, both of these functions satisfy a parameterized

gamma distribution, given by:

$$f(x) = \frac{\lambda^\alpha x^{\alpha-1}}{\Gamma(\alpha)} e^{-\lambda x} \qquad (4.11)$$

where $\Gamma(y)$ is the gamma function, and α and λ are constants. The cumulative distribution functions for the distributions, F_κ and F_u, can then be expressed as:

$$F(x) = \frac{\gamma(\alpha, \lambda x)}{\Gamma(\alpha)} \qquad (4.12)$$

where the incomplete gamma function, $\gamma(s, y)$ is defined by:

$$\gamma(s, y) = \int_0^y t^{s-1} e^{-t} \, dt \qquad (4.13)$$

Again, we calculate the parameters by fitting the model cumulative density function to that of the experimental distribution, and the fitted curves are overlaid on their respective experimental distributions in figures 4-29 and 4-31. In general, we see much better agreement between the analytical and experimental distributions for this metric than we did with the spatially resolved most probable values of the normal flow velocity and the strain rate. We first consider the fraction of the normal flow velocity distribution that lies within 10 cm/s of the laminar flame speed, shown in 4-29. As the equivalence ratio increases the peak of this distribution shifts to lower values, but at the same time becoming broader. At the highest equivalence ratio, $\phi = 0.650$, the distribution has no local maxima within the domain, having the same characteristics as an exponential probability distribution (which would be exactly the case for $\alpha = 1$). The pattern we see from the cumulative density functions is that the flame is more likely to be observed in high speed flow more often in at higher equivalence ratios, which is consistent with the previous section in which we observed that the flame preferentially situates itself in the center of the reactant jet.

Next we look at the fraction of the strain rate distributions that lie above the extinction limit in figure 4-31. This function is approximated very well by the gamma distribution. The fraction of flame strain observations above the extinction limit

143

Table 4.3: A comparison of the means and standard deviations of the analytical (denoted by a subscript m) and experimental distributions (denoted by a subscript e) are presented for the fraction of the normal flow velocity distribution ($u_n = -\mathbf{n}_f \cdot \mathbf{u}$) within 10 cm/s of the laminar flame speed and the fraction of the flame strain distribution (κ) above the extinction limit.

	$P(u_n \approx S_L)$				$P(\kappa > \kappa_{ext})$			
ϕ	μ_e	μ_m	σ_e	σ_m	μ_e	μ_m	σ_e	σ_m
0.550	0.027	0.029	0.009	0.009	0.206	0.212	0.109	0.112
0.600	0.018	0.019	0.011	0.012	0.232	0.243	0.100	0.104
0.625	0.024	0.024	0.034	0.017	0.185	0.196	0.099	0.111
0.650	0.037	0.039	0.048	0.043	0.124	0.136	0.085	0.094

increase as we go from flame II to flame III, which is consistent with the observation that the flame moves from inside the inner recirculation zone at very low strain rate to the inner shear layer where the strain rates are much higher. As the extinction strain rate of the flame approaches the strain rates in of a particular region from below, flames will survive longer since the amount by which the extinction limit is exceeded goes down, and hence, we have more observations of flames above the extinction limit. As we move to the transitional flame and then flame IV, the flame spends more time in the center of the jet and in the outer recirculation zone where the strains are low, increasing the likelihood of observing flames at low strain rate, hence the shift in the peak toward lower fractions above the extinction limit as me move to $\phi = 0.600$ to $\phi = 0.625$, and finally to $\phi = 0.650$.

4.3.7 Summary of statistical flow-flame interactions

Over the preceding sections, we have examined statistics of the flow-flame interactions for four different equivalence ratios, corresponding to three distinct flame geometries. We have focused on the statistics surrounding the strain rate on the flame and the flow speed normal to the flame in order to develop and build support for hypothesis that would describe the progression of the flame geometry, particularly in relation to the shear layers that exist between the jet and the two primary recirculation zones.

In the absence of simultaneous or correlated PIV and PLIF data, we combined a

pair of datasets at each operating condition which gave us information about the flame location and orientation (PLIF) and about the flow velocities and velocity derivatives (PIV), in what amounts to a spatially resolved convolution of the two datasets, which provide a distribution of the flame angle and a distribution of the flow variables. The details of this method are provided in greater detail in chapter 2. In performing this convolution, we have made an underlying assumption that the point-wise flow statistics *at a given operating point* are not affected by the presence (or lack thereof) of the flame. The observation that the presence of a flame at a particular location is the result of non-local effects (such as the interaction of the flame with large scale vortices) allows us to conclude that this convolution does provide a reasonable estimate of the distributions of the flame strain and normal flow velocity.

We first examined each of the four operating points in a spatially resolved manner. We compared the point-wise probability of finding a flame in a given location to properties of the normal flow speed and flame strain distributions at each corresponding point. The most fruitful metrics came from examine the fraction of the point-wise flame strain distributions that exceeded the extinction strain rate, and the fraction of the point-wise normal flow speed distributions that were near the laminar flame speed. We chose to bound the laminar flame speed by 10 cm/s, which is on the order of the laminar flame speed for all four operating points.

At the lowest equivalence ratio, $\phi = 0.550$ corresponding to flame II, we found that the flame was confined primarily to the inner recirculation zone, where it could exists in a low strain environment in flows that nearly matched the laminar flame speed. Although flames propagated beyond the end of the recirculation zone, where they were advected downstream, they were unable to propagate far into the conical region of the jet, and when they are observed there, the strain rates greatly exceeded the static extinction limit. We saw that the recirculation pushed the flame upstream into the shear layer, provided mixing that is critical for ignition, but in the presence of such high relative strains, these flames we not able to penetrate far into the jet before extinguishing.

We examine flame III at $\phi = 0.600$, which is a conical flame that we typically

observe within the jet. Where we most often see this flame, the flow speed normal to the flame is so much higher than the laminar flame speed, that flames cannot be held stationary in this region. However, the increase in the equivalence ratio leads to an increase in the extinction strain rate, and we see that although the point-wise flow derivative distributions did not change substantially in the jet and shear layer, save for the upstream section of the cone, the fraction of the flame strain distributions in the conical region, and the downstream region of the jet that exceed the static extinction limit are much lower, with a correspondingly higher probability of finding flames here. Put another way, even though the flames are not stationary in this region, there ability to survive higher strain rates means that they can penetrate farther into the jet. With the recirculation zone providing a constant influx of hot products and radicals into the upstream region of the cone, the reaction is maintained in this region, even though the individual flames are convected downstream.

Only in the transitional flame, or the "flickering" flame that we examine at $\phi = 0.625$ do we begin to understand the relationship between the conical flame and the outer flame. The outer zone itself is a very low strain environment with low normal flow speeds that should be favorable for the existence of a flame, but we only observe it intermittently. In many of the PLIF snapshots in which we do observe this outer flame, it is connected to a conical flame that bridges through the jet, suggesting that this link is critical to the persistence of the outer flame, and that there is another extinction mechanism in play in the outer recirculation zone. A very likely candidate is heat loss to the combustor walls. The connection to the conical flame provides a pool of radicals to feed the reaction, but in the absence of this ignition source, the flame is quickly extinguished as energy is lost to the walls. The intermittency arises from the high strain rates in the outer shear layer, which sits between the conical flame and the outer flame. At $\phi = 0.625$, the relative fraction of the strain rate distributions in excess of the extinction limit in between these two flame regions sits near 50%, depriving the outer flame of an ignition source. As the equivalence ratio increases to $\phi = 0.650$, and we reach flame IV, the flame in the outer zone becomes persistent. The increase in the static extinction strain rate results in the more frequent bridging

of these two regions by the flame, providing a more consistent source of energy.

We take one final look at the spatially resolved statistics. In figure 4-32, we have created plots for flames II, III, and the transitional flame, at the particular operating conditions that we examined above. As before, we are looking at integrals of the flame strain distribution, however, in this case, we are looking at the probability of the flame strain exceeding the critical values that we found in figure 4-13 necessary to transition to the *current* flame geometry in the left column, and to the *next* flame geometry in the right column.

This figure provides additional evidence about the claim we have been making, namely as the flame encroaches on new regions, we find that the probability that flame strain in these regions (or in the bridging zone in the case of the outer flame) exceeds the extinction limit of weaker flames is very high, while we only observe relatively high fractions of the distribution exceeding the limit in the new critical regions, correlated with the next transition of the flame.

4.4   Summary

In this chapter, we have examined the evolution of flame geometry as a function of increasing equivalence ratio for several different CH_4/H_2 fuel blends. We began by showing in figure 4-1 that we obtain the same flame shapes, albeit at different equivalence ratios, as hydrogen is added, giving us some confidence that the complexity of the flame geometry can be reduced to a simpler parameter or set of parameters.

Next, we showed that the flame geometry is a function of the combustion parameters and flow properties, and that we can obtain the same flame geometries at the same equivalence ratios with different acoustic boundary conditions. Critically, this has allowed us to explore the fundamental properties of these flames by studying them in isolation from dynamic oscillations, and in chapter 5, will allow us to determine the forced acoustic behavior of the flames as a function of their geometry. Furthermore, we found evidence that the geometry is a critical factor in determining self-excited behavior of the flame by overlaying the transitions on the sound pres-
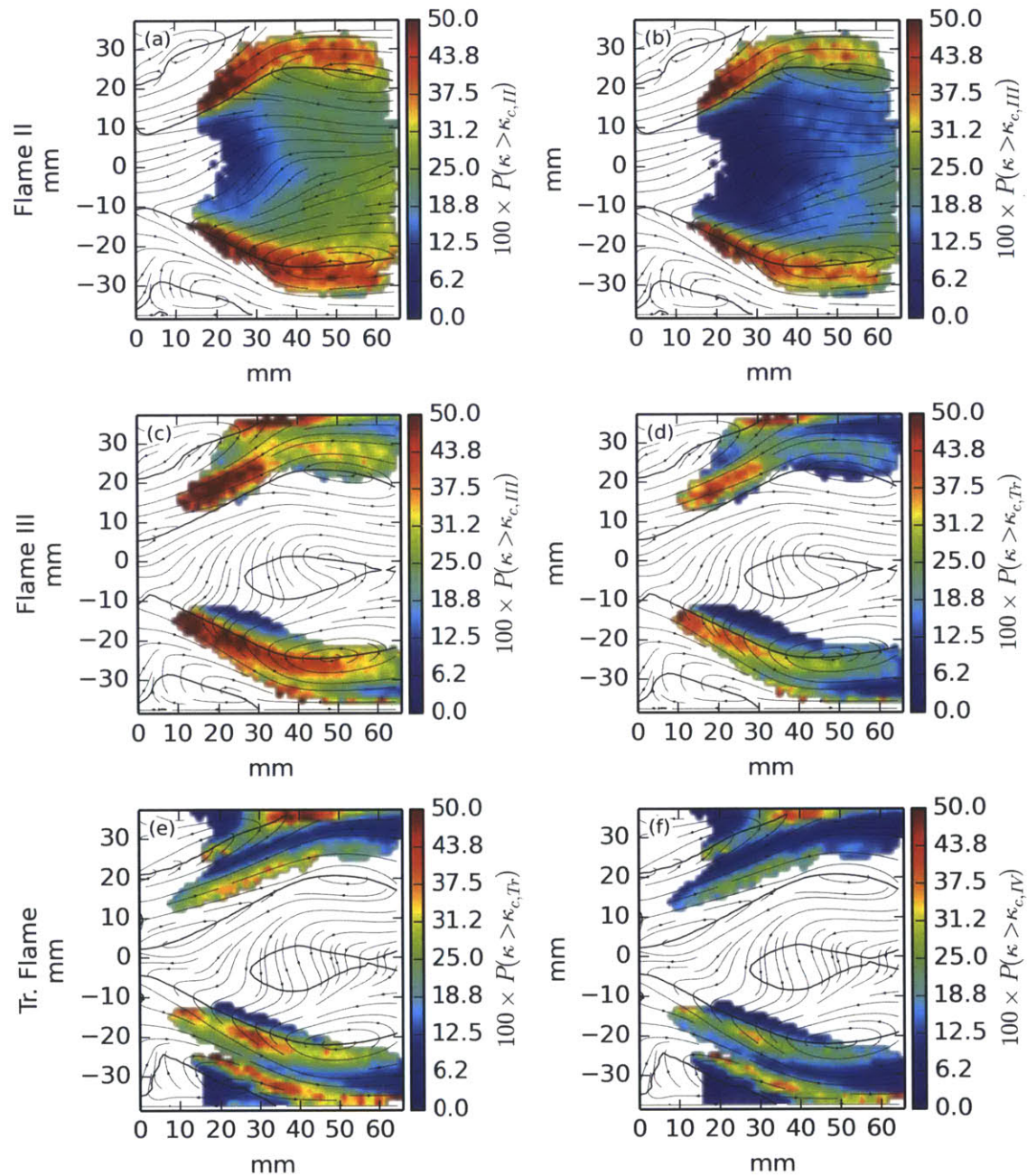
Figure 4-32: For three flame geometries–flame II (top), flame III (middle), and the transitional flame (bottom)–spatially resolved maps show the probability of each flame geometry exceeding the critical strain value necessary to transition to the current geometry (left) and the next higher flame geometry (right).

sure level spectra in figure 4-3. We found that the long, lazy flames that we find at low equivalence ratio did not have any self-excited dynamics associated with them, with weak oscillations appearing at the first discrete transition to a compact flame. Instability, however, set in when a conical flame was joined by the an intermittent outer flame. These observations held for the three fuel blends that we examined, and showing a connection between the geometry, which we know is independent of the acoustic boundary conditions, and the self-excited dynamics. And furthermore, it suggests that these processes of flame stabilization and dynamic behavior are tied together through a single governing parameter. This series of observations motivated the rest of the chapter.

We went on to examine each of the three flame geometries of interest within the context of the dynamic instability. These flames were labeled II, III, and IV. Additionally, we examined an intermediate regime in which the flame intermittently transitioned between the configurations corresponding to flames III and IV. We found that as the equivalence ratio increase, the downstream extent of the inner recirculation zone contracted, closing farther and farther upstream. The expansion of the jet in the wake of the recirculation zone also differed across cases. For low equivalence ratios, in which the relatively long recirculation bubble gradually contracted, the expansion of the jet was relatively slow. At the highest equivalence ratios, however, rapid expansion lead to a high level of turbulence in the wake. As the recirculation bubble contracted axially, it began to pinch off from the centerbody wake, which we finally observed at $\phi = 0.650$ where the mean recirculation bubble had a free stagnation point.

We then moved on to the examination of the flow field associated with the intermediate flame regime, in which we observe intermittent transitions between a conical flame (flame III) and a conical flame coupled with an outer flame (flame IV). In addition to a discernible frequency of rotation, we were able to detect a low frequency signal and its harmonic at 4 Hz and 8 Hz, which we correlated with the frequency of the transition itself. Using dynamic mode decomposition to study temporally coherent flow structures, we were able to identify corresponding modes in the PIV measurements of the flow field. These modes corresponded to non-convective vortex

149

events located in the annular jet where it impinges on the combustor wall. This is a critical region, through which the conical flame bridges, providing an ignition source of the outer flame. The superposition of these modes on the stationary mode showed an apparent low frequency "breathing" of the inner recirculation bubble. The frequencies at which we observe this phenomenon closely matches with the expected frequency of fluid dynamic instabilities associated with the filling and emptying of the vortex breakdown bubble. We go on to show that the strain on the flame in the boundary between the jet and outer recirculation zone, relative to the extinction strain rate is a critical factor in the establishment and persistence of the outer flame, and by linking the breathing of the inner recirculation zone to this region, our data suggests that this intermittency is the result of this particular fluid dynamic instability influencing the strain in a critical region. The reconstruction of the dynamic modes, however, shows that the the velocities are relatively weak compared to the mean, and consequently, these mods have insufficient influence on the strain to change the flame stabilization save for within this very narrow regime.

In the remainder of the chapter, we explored the relationship between the flow, as measured with PIV, and the flame, as measured with PLIF, using a statistical analysis to reconstruct some measure of the correlation between these two processes. We examined both flame strain and the component of the flow field normal to the direction of flame propagation. Our investigation of that latter revealed that the flame exists predominantly within flows where the instantaneous velocities normal to the flame are much greater than the laminar flame speed, placing the system in the corrugated flamelet regime. These flames are strongly advected by the flow, and, and so the global behavior of the flame must be established by a continuous reignition process arising from the interaction of the hot combustion products and the incoming reactants. Since the flame stabilization is nothing like a laminar flame, this gives us little clue to the transitions between the different flame geometries.

We gain a clue to these transitions, however, by looking the transitions points in relation to the extinction strain rate, as we have shown for a variety of fuel compositions in figure 4-13. Across the various fuel compositions, we see that the discrete

150

transitions tend to happen at certain critical values of the extinction strain rate, suggesting that the geometry can be parameterized by the extinction strain rate of the given fuel. In our statistical analysis, we compared the spatially resolved distribution of the probability that the flame strain exceeded the extinction limit with the spatially resolved probability of finding a flame, then we see a negative correlation between these quantitates. Several critical areas arise from this analysis, depending in the particular flame geometry. We see that flame II, which is contained within the interior of the inner recirculation zone is well bounded by the inner shear layer, where the probability of exceeding the extinction strain rate is particularly high. While flame III is able to propagate into the jet of reactants, higher strain rates in the outer shear layer keep it from propagating any farther. The distinction between the transitional flame (in which we observe the intermittency) and flame IV lies not in the outer recirculation zone, where we observe statistical very low relative strain rates, but in the decreasing probability that the strain in the outer shear layer exceeds the extinction limit. The persistence of the outer flame appears to be critically linked to the ability of the conical flame to bridge into the outer recirculation zone, which in turn suggests that the outer flame is extinguished by heat loss in the absence of a continuous or near continuous ignition source.

Chapter 5

Forced Acoustic Response

In this chapter, we go back to the questions surrounding combustion dynamics. In particular, we are interested in discovering the origin of self-excited acoustic instabilities. We proceed forward under the hypothesis that these instabilities arise due to the amplification of the unsteadiness that is already present in the system at low levels, and that particular frequencies are selected for amplification by the combined effect of the flame geometry and chamber acoustics.

The turbulent combustion environment is an inherently noisy one, with many pathway through which the chemical energy of the combustion process. Turbulent combustion noise arises in the form of traveling pressure waves with widely distributed wavelengths, and may be transferred into the acoustic field by various mean, stochastic, and periodic processes [85].

Acoustic forcing has been used as a tool to understand both the large scale and small scale responses of both laminar and turbulent flames to sinusoidal acoustic inputs. On the small scale, acoustic forcing has a direct impact on the wrinkling of the flame, inducing sinusoidal oscillations in the flame front, effectively increasing the flame surface area. While this effect is seen in laminar flames as well, the presence of turbulence fundamentally alters the response of the flame front, destroying the coherent, acoustically-induced flame wrinkles, tending to dampen the response [86]. The response of the flame to both turbulent fluctuations and acoustic forcing has been shown to be a coupled phenomenon, even at low forcing amplitudes [87]. The

result is an effective modulation of both the displacement speed and the consumption speed over the acoustic cycle, and intrinsically links the small scale flame response not only to the presence of turbulence, but to the nature of the turbulent flow field as well.

In this chapter, we calculate the flame transfer function over a range of fuel CH_4/H_2 blends from 0-20% H_2, for a range of equivalence ratios defined by the mapping of macrostructures shown in chapter 4 for macrostructures I, II, III, the transitional flame, and IV. Flame I proved to be very susceptible to blowoff, even under very low amplitude forcing, and therefore, defined the lean limit of the test matrix. The upper limit of the test matrix was bounded by self-excited instability of flame IV in the short-wave combustor configuration. The bulk flow velocity, calculated from the measured mass flow rates and measured gas properties upstream of the choke plate, was approximately 8.5 m/s for all cases, and the acoustic forcing amplitude was set at 1% of the bulk flow velocity, calculated using the two-microphone method, as outlined in §2.1.1.

5.1   Flame transfer functions

We quantify the forced acoustic response of a flame by means of the *flame transfer function* over a variety of equivalence ratios and fuel compositions covering the limits of the first unstable mode of the long combustor and the flame geometries that we described in chapter 4. We examine the acoustic response at frequencies from 32 Hz to 80 Hz in steps of 2 Hz, creating a detailed map of the acoustic response just below and just above the onset of the first unstable mode of the system. In this section, we will show the measurements and demonstrate a strong correlation between the acoustic response, and in particular the phase difference between the pressure and heat release, and the flame geometry. In the following sections, we will explore this correlation in greater depth, uncovering a quantity that parameterizes the flame geometry, developing approximate analytical expressions for the gain and phase, as a function of the combustion parameters, and finally coupling these equations to the

quasi one-dimensional acoustic model to present a framework for predicting the onset of instability.

The flame transfer function (FTF) is a mathematical tool used to describe the global response of a flame to harmonic acoustic forcing with the linear regime. The is derived from the frequency content of the pressure and heat release rate spectra, and is expressed as:

$$\mathcal{G}(f) = \frac{q'(f)/\overline{q}}{u'(f)/\overline{u}} \tag{5.1}$$

where f is the frequency of forcing, $q'(f)$ and $\overline{q}$ are the peak-to-peak and mean volumetric heat release rates, $u'(f)$ is the peak-to-peak acoustic particle velocity, and $\overline{u}$ is the bulk flow velocity. Pressure is directly measured in the upstream region of the flow, just prior to the sudden expansion into the combustion chamber. Heat release rate, however, is not directly measured. We measure the intensity of light emitted by the flame using a photomultiplier tube, using an optical notch filter for OH^* radicals, and operate under the assumption that this intensity signal, I, is proportional to the heat release rate such that we can use the following expression:

$$\mathcal{G}(f) = \frac{I'(f)/\overline{I}}{u'(f)/\overline{u}} \tag{5.2}$$

In figure 5-1, we present the flame transfer function for pure CH_4 at an equivalence ratio of $\phi = 0.620$ as a solitary example of an FTF measurement. We plot the gain as a function of forcing frequency in 5-1(a) and the phase difference between the pressure and flame intensity signals in 5-1(b). The gain represents the relative response of the flame to the

In the next several figures we have grouped the transfer functions coarsely into bins corresponding to the flame geometry that was exhibited at the particular operating point. That is, based on the observed flame geometry at each particular operating point (measured separately with spatially resolved CH^* chemiluminescence images, and verified during the measurement of the flame transfer functions), we categorize flames as: flame II, flame III, transitional flame, or flame IV. This qualitative binning is completely for all three fuel compositions across the tested range of equivalence

155
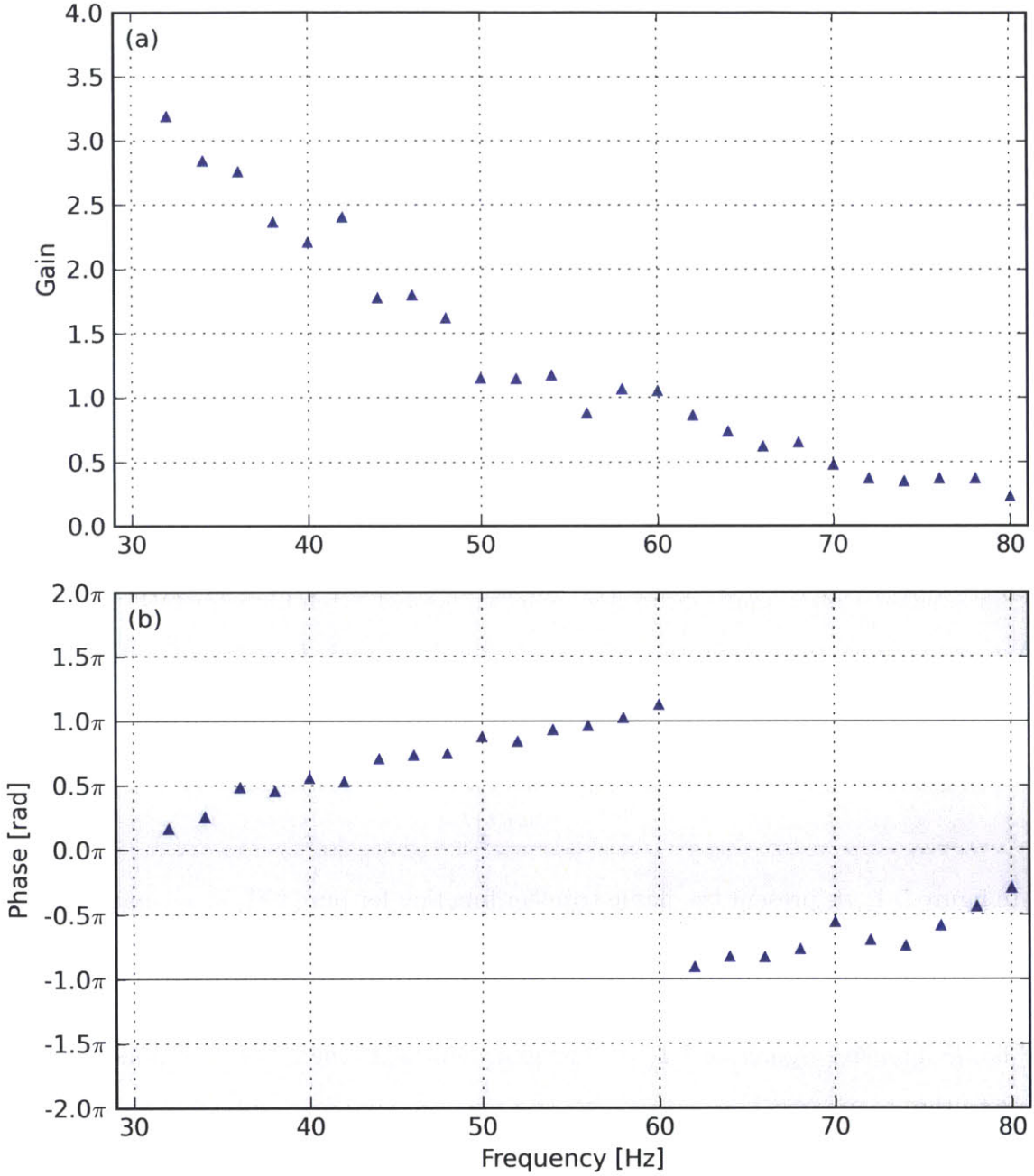
Figure 5-1: The gain (a) and phase (b) of the flame transfer function for pure CH_4 at $\phi = 0.620$ is plotted as a function of the forcing frequency. The gray shading in the phase plot indicates those regions within which pressure and phase are within $\pi/2$ radians of each other, and the solid black lines at $\pm\pi$ denote mark the edge of the periodic boundary.
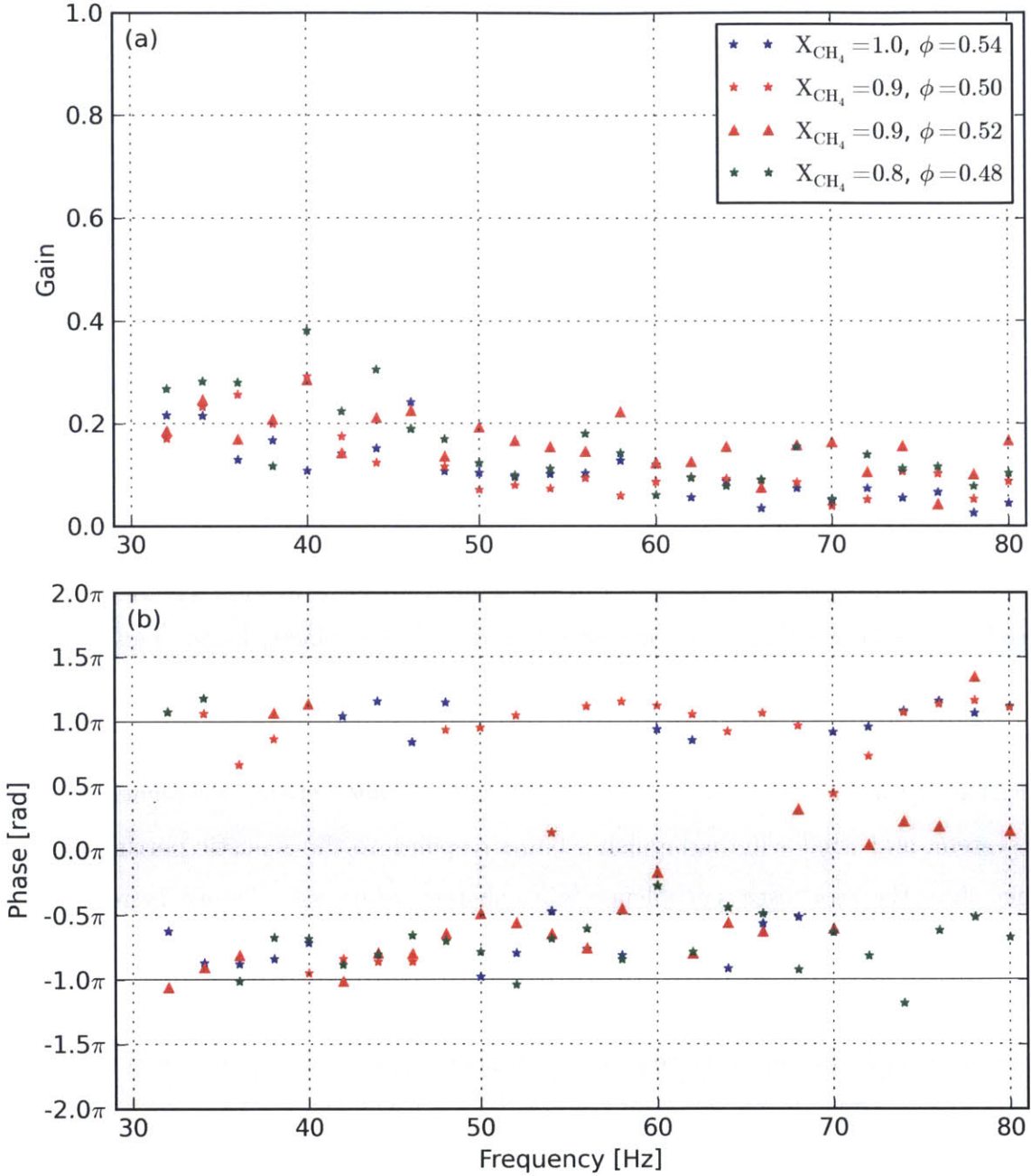
Figure 5-2: The gain (a) and phase (b) of the flame transfer functions for flames corresponding to the flame II geometry are plotted as a function of the forcing frequency. The gray shading in the phase plot indicates those regions within which pressure and phase are within $\pi/2$ radians of each other, and the solid black lines at $\pm\pi$ denote mark the edge of the periodic boundary.

ratios. Within each figure, we group transfer functions of the same fuel composition by color, and differentiate the various equivalence ratios with different symbols. In all cases except that corresponding to flame II, we have connected the data points for each case for easy visual identification. While we compare the acoustic response of the flame to the self-excited behavior of the combustion process in the long combustor configuration, the flame transfer functions are measured in the short combustor in order to isolate each particular flame geometry from the self-excited oscillations.

We start with flame II, for which we show the flame transfer function in 5-2. We recall that we saw no self-excited acoustics in the long combustor in conjunction with this flame. Based on our hypothesis that self-excited acoustics are the result of the amplification of perturbations that are already present, the lack of self-excited behavior leads us to expect very little response from this particular flame geometry. Indeed, this expectation is borne out in the flame transfer function. The gain never exceeds 0.4, indicating that a 1% perturbation in the inlet velocity leads to less than a 0.4% in the heat release rate over the entire experimental domain, which is sufficiently low that can consider this to be no response. We recall that the the acoustic velocity perturbations are on the same order of magnitude as much of the turbulence within the system, and what will distinguish a flame response to the acoustic perturbations rather than the stochastic turbulence is a coherent relationship as we increase the forcing frequency.

Moreover, examining the phase response, we see that the phase difference between the pressure and the heat release rate as a function of the forcing frequency is effectively random, showing no discernible pattern, much less the near linear increase in phase with frequency that we are lead to expect from theoretical arguments (and in figure 5-2, we have therefore refrained from connecting discrete data points, since they have no relationship to each other). Recalling the investigation of flame II in chapter 4, we can begin to understand why the acoustically forced flame response is not coherent: the spatial distribution of the flame varies substantially from instant to instant. As the flame is unable to propagate into the inner shear layer, it remains laterally confined by the inner recirculation zone, and due to the presence of unburned

Figure 5-3: The gain (a) and phase (b) of the flame transfer functions for flames corresponding to the flame III geometry are plotted as a function of the forcing frequency. The gray shading in the phase plot indicates those regions within which pressure and phase are within $\pi/2$ radians of each other, and the solid black lines at $\pm\pi$ denote mark the edge of the periodic boundary.

reactants that bypass the recirculation bubble, there is no downstream bound within the the combustion chamber. The poor spatial localization means that the time delay between a pressure wave entering the combustion chamber and interacting with the flame, even under an unsupported assumption that the pressure waves will interact with the flame in the same manner regardless of where they are encountered, means that we should not expect a coherent response, and furthermore, this explains the lack of any detectable self-excited acoustic behavior at the conditions that lead to this flame geometry.

As previously noted, we first begin to see a discernible self-excited acoustic band in the long combustor when the flame geometry transitions to flame III from flame II. While we do not consider this to be unstable, it does at least suggest that within this operating regime, the flame is responsive to acoustic oscillations. The flame transfer functions for those conditions corresponding to flame III are shown in figure 5-3. In contrast to the flame transfer functions corresponding to flame II, we begin to see a substantial response to the acoustic forcing. Two of the cases, pure CH_4 at $\phi = 0.56$ and 20% H_2 at $\phi = 0.50$ lie very close to the transition point between flame II and III. In these two cases, we see only a moderate response to acoustic forcing in 5-3(a), but in the remaining cases, we see a very strong flame response that tapers off as the forcing frequency increases. Near the upper boundary of the equivalence ratio for this particular flame geometry, we see the gain reach as high as 2.8 at low frequencies, indicating a very strong oscillation in the flame correlated with the velocity perturbations.

A much more striking picture is painted in figure 5-3(b), where we look at the phase angle between the acoustic pressure in the combustion chamber and the instantaneous heat release rate. First, we observe the the phase follows an apparently linear relationship, increasing with the forcing frequency for each case. We note that the phase is 2π-periodic, where phase difference of π and $-\pi$ are identical. In each case, the phase starts between $\pi/2$ and π at 32 Hz, increasing steadily, and crossing over between 42 Hz and 50 Hz, steadily increasing from $-\pi$ thereafter. Within a given fuel composition, we see that the phase decreases with increasing equivalence ratio.

160
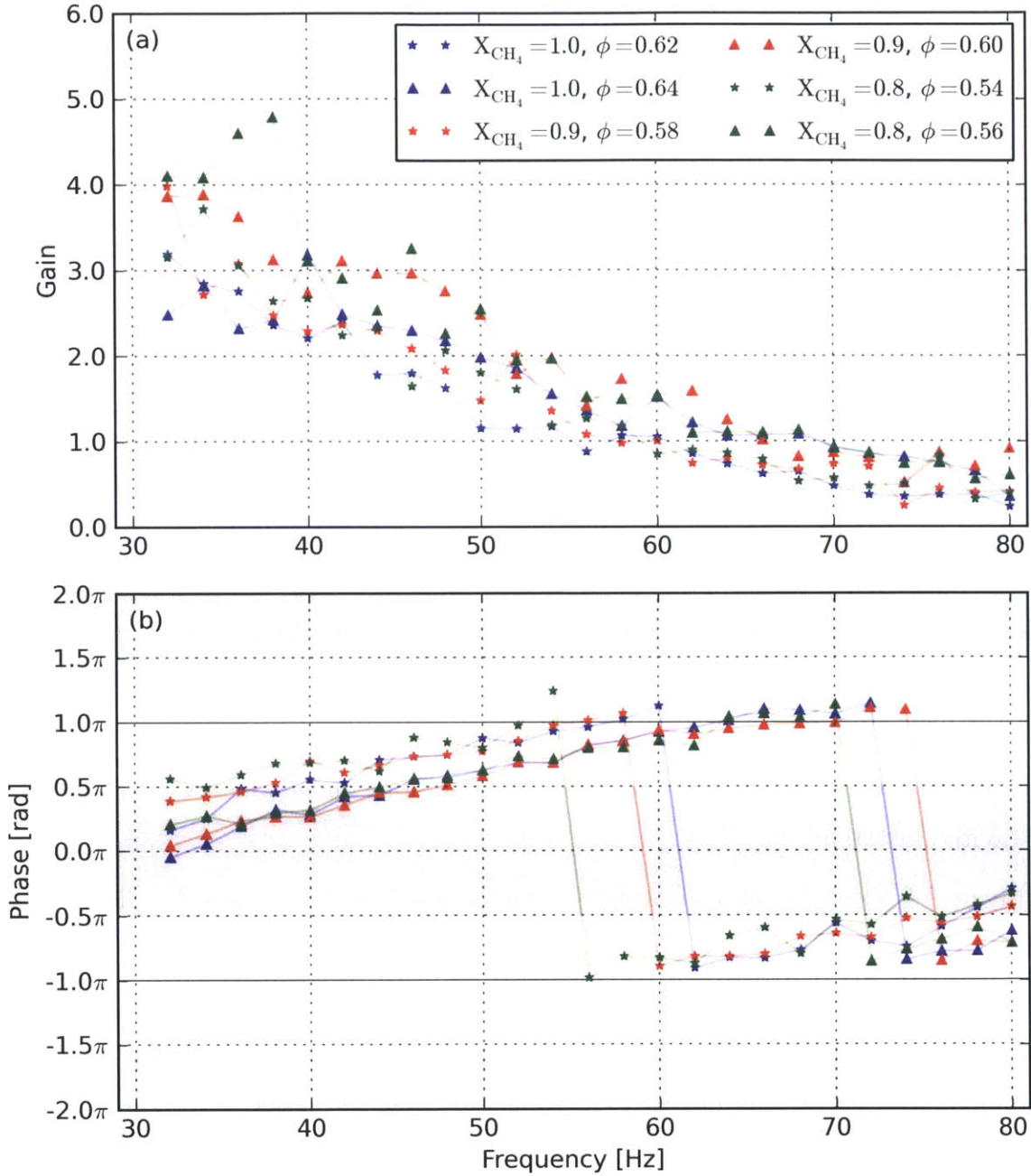
Figure 5-4: The gain (a) and phase (b) of the flame transfer functions for flames corresponding to the transitional flame geometry are plotted as a function of the forcing frequency. The gray shading in the phase plot indicates those regions within which pressure and phase are within $\pi/2$ radians of each other, and the solid black lines at $\pm\pi$ denote mark the edge of the periodic boundary.

With our eye toward dynamic instability, we shaded those regions of the phase plot in which the pressure and heat release are within $\pi/2$ radians of each other. Although any phase is possible since the forcing is external, these regions mark which frequencies in which the Rayleigh criterion is satisfied, and therefore the frequencies at which we *could* observe self-excited acoustic oscillations at the given operating conditions. For flame III, the Rayleigh criterion is satisfied only for frequencies above 45 Hz to 55 Hz, depending on the particular operating point.

We examine the transitional flame in figure 5-4. We see the same trends in the data as we saw with flame III. The gain continues to increase, particularly for the lower end of the frequency range, and the phase between pressure and heat release follows the same trends. We see that for each case, the phase increases with forcing frequency, and the phase decreases with increasing equivalence ratio. At the higher equivalence ratios shown in this figure, we also see that the phase between chamber pressure and heat release lies within $\pi/2$ radians at 40 Hz. This suggests that the flames under these operating conditions would satisfy the Rayleigh condition for thermoacoustic instability, and in the long combustor, where 40 Hz is a natural mode of the combustion chamber, these are operating conditions under which we do observe self-excited instability.

Figure 5-5 shows the flame transfer functions that loosely correspond to flame IV. As the equivalence ratio continues to increase, so too does the gain, particularly at low frequencies. The phase continues to follow the same trend, following an apparently linear increase with forcing frequency, but decreasing monotonically as the equivalence ratio increases. We do run into a case here where the forced acoustic response in the short combustor predicts operating conditions where the phase relationship satisfies the Rayleigh criterion, but we do not observe the 40 Hz mode in the long combustor configuration. In a subsequent section, we will attempt to explain this observation by noting that the natural acoustic frequencies of the chamber vary in response to changes in the flame response.

In this section, we have presented the flame transfer functions for three different fuel compositions, across a range of equivalence ratios that span the flames II, III,
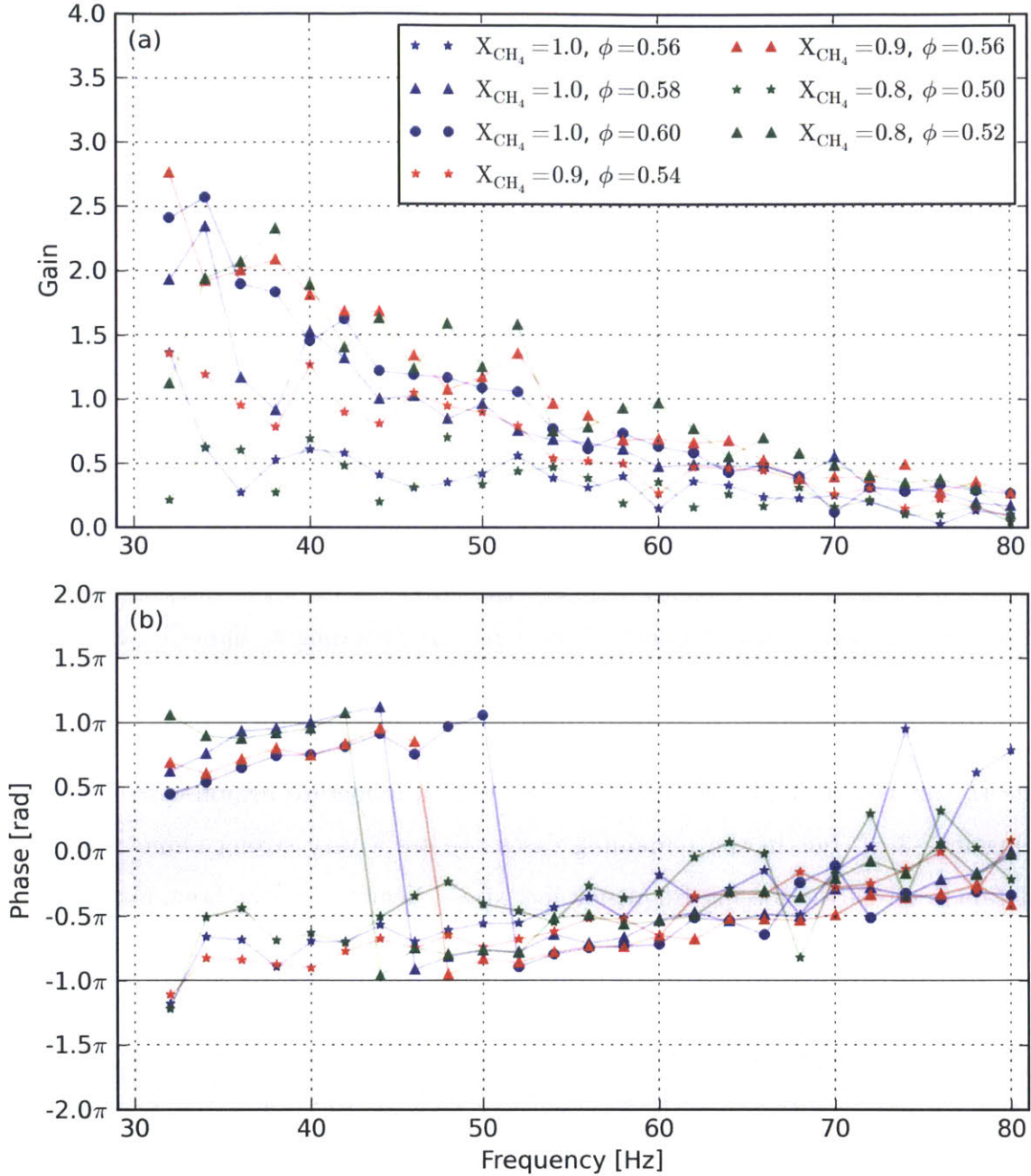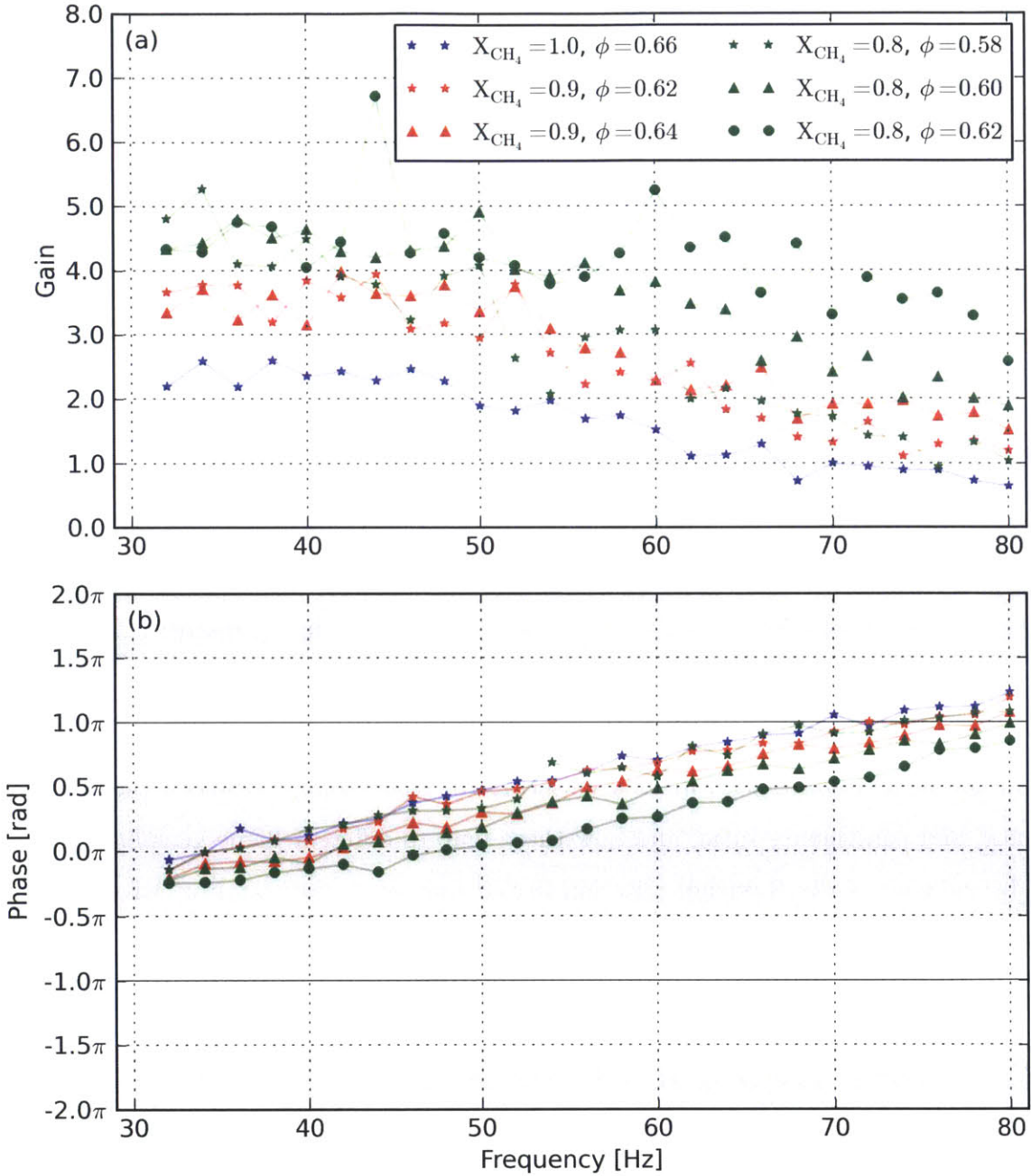
Figure 5-5: The gain (a) and phase (b) of the flame transfer functions for flames corresponding to the flame IV geometry are plotted as a function of the forcing frequency. The gray shading in the phase plot indicates those regions within which pressure and phase are within $\pi/2$ radians of each other, and the solid black lines at $\pm\pi$ denote mark the edge of the periodic boundary.

the transitional flame, and flame IV. We chose the limits of the test range to avoid lean blow off and avoid coupling in the short combustor at the rich end of the test domain. We showed that while flame II is effectively unresponsive to acoustic forcing, once we hit equivalence ratios corresponding to flame III and higher, we see a coherent response, particularly in the phase response. The phase between the chamber pressure and heat release rate increases nearly linearly as a function of the forcing frequency, and decreases as a function of equivalence ratio. By overlaying the boundaries of the Rayleigh criterion on the phase plots, we showed that the frequency of the lowest acoustic mode in the long combustor, 40 Hz, satisfies the Rayleigh criterion within those cases that we have classified as belonging to the transitional flame. Our coarse categorization of the flame transfer functions by their corresponding flame geometry suggest that, just as we saw with the transitions themselves, there is a more fundamental combustion parameter that governs the phase response to acoustic forcing (and perhaps less apparently, the gain response). In a subsequent section, we will show that the changes in the acoustic response are well correlated with the thermoacoustic transitions, and find a parameter that collapses both sets of data.

In the next section, we will look closer at the relationships between phase, frequency, and equivalence ratio, and how these map to different flame geometries and the boundaries of the Rayleigh criterion in the context of the standing wave modes in the long combustor configuration.

5.2 Phase response of the flame

In the preceding section, we observed what appeared to be a linear relationship between the forcing frequency and the phase difference between the combustion chamber pressure and the heat release over the range of tested frequencies. In figure 5-6, we remap the phase-frequency relationship using the 2π-periodicity for each fuel composition, and each equivalence ratio corresponding to flame III, the transitional flame, or flame IV. And, in addition, we overlay best fit lines for each fuel composition and equivalence ratio.

164

The linear relationship that we observe with this flame has theoretical backing.

Duchaine *et al* [88] further showed a linear relationship between the forcing frequency and phase in laminar flames. As the exit velocity increased, so did the slope of the phase changes, suggesting that the phase scales as a convective time delay. Such a scaling is not available here, as we have chosen to focus exclusively on the functional dependence of the transfer function and dynamics on the fuel composition and equivalence ratio, at a constant inlet Reynolds number (and very nearly constant mean inlet velocity), however, this suggests that the scaling parameter, α between frequency and phase, which we shall introduce next, is itself dependent on the inlet velocity.

Returning to the data that we obtained, we can approximately express the relationship between phase and forcing frequency as:

$$\theta_{pq}(f)|_{\mathrm{X},\phi} = \alpha f + \theta_0 \qquad (5.3)$$

where X represents the molar fraction of CH_4 and ϕ is the equivalence ratio. The two constants, α and θ_0 may be empirically determined by a least-squares fit, and the resulting lines are overlaid on the measured phase in figure 5-6.

The fitting parameters corresponding to figure 5-6 are shown in table 5.1. The mean value for α for the pure CH_4 case is 0.084, dropping to 0.076 for both 10% H_2 and 20% H_2. In each case, we see the offset, θ_0, decrease as a function of increasing equivalence ratio, however in all cases, we see that the rate at which it decreases tapers off. In figure 5-7, we show the dependence of θ_0 on the equivalence ratio for each of the three fuel compositions. The curves all follow an apparently asymptotic decay, save for those points at the lowest equivalence ratios for pure CH_4 and 10% H_2, which we taken on the border of flames II and III, at which the coherent response of the flame to acoustic forcing is weak. Although the particular form suggests an inverse relationship between the offset angle and the equivalence ratio, we will avoid attempting to fit these curves to an analytical function until we map these results onto a more fundamental combustion parameter, the flame consumption speed. We already
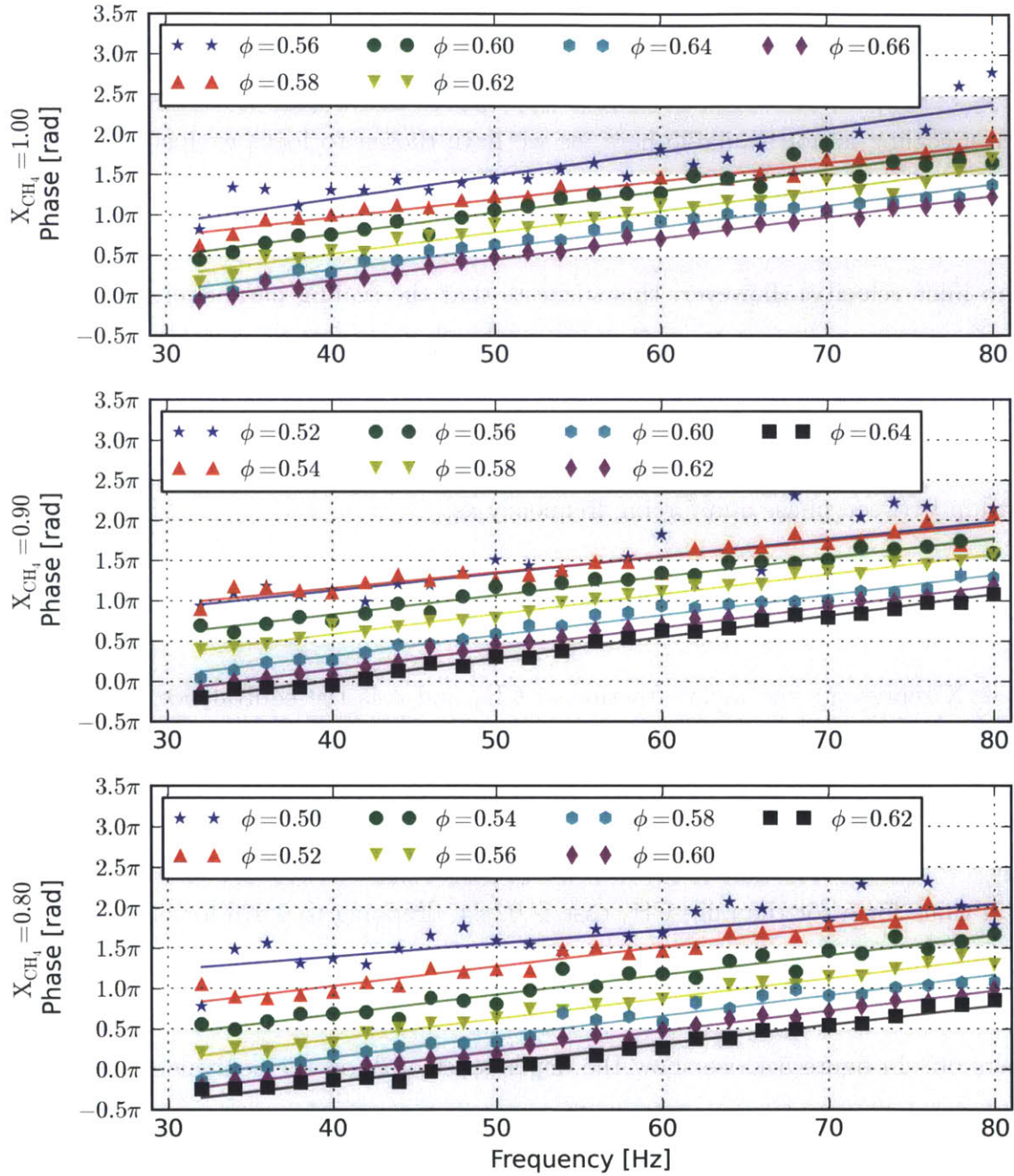
Figure 5-6: Linear curve fits for the relationship between forcing frequency and the phase difference between combustion chamber pressure and global heat release rate are shown for pure CH_4 (a), 10% H_2 (b), and 20% H_2 (c).

Table 5.1: Linear curve fit parameters describing the relationship between forcing frequency and the phase difference between combustion chamber pressure and global heat release rate are presented for all fuel compositions and equivalence ratios.

ϕ	$X_{CH_4} = 1.00$		$X_{CH_4} = 0.90$		$X_{CH_4} = 0.80$	
	α (rad/Hz)	θ_0 (rad)	α (rad/Hz)	θ_0 (rad)	α (rad/Hz)	θ_0 (rad)
0.500					0.066	1.44
0.520			0.071	0.90	0.076	0.21
0.540			0.064	1.05	0.077	-0.94
0.560	0.093	0.03	0.075	-0.40	0.079	-1.96
0.580	0.072	0.13	0.078	-1.29	0.080	-2.73
0.600	0.085	-1.02	0.079	-2.17	0.078	-3.18
0.620	0.085	-1.77	0.082	-2.80	0.074	-3.47
0.640	0.084	-2.34	0.083	-3.27		
0.660	0.083	-2.74				

expect that such a model would break down as we approach and pass stoichiometry, so we will hold off on generalizing until we have some confidence that we have chosen a parameterization that allows us to extrapolate our domain to values our test matrix. The leftmost data points for the 10% and 20% H_2 cases lie off the curve. We note that these correspond to flame II, however, where the coherent response to acoustic forcing is weak, so we should not be too surprises that these values do not fall on the same curve as the remaining data points.

While we see that θ_0 is a function of the equivalence ratio (and will later show it to be a function of the consumption speed), table 5.1 suggests that α is a constant, or nearly so. Across the range of equivalence ratios that we tested for each case, the mean values within each case range from 0.076 to 0.083 depending on the fuel composition, and this range becomes tighter if we exclude flame II, which has a very poor response to acoustic forcing. This does suggest that within the context of the experiment, α is likely a constant, or nearly so. We do not, however, expect that α is a true constant, but likely relies on parameters outside of the scope of this study. Since we can interpret the phase as the result of a time delay related to the acoustic pressure field, we might expect α to be dependent upon the inlet temperature.

Although the entirety of the flame transfer function has implications for combustion stability, we are particularly interested in the phase response for the purposes of developing simple criterion for mapping the forced acoustic response onto the self-

Figure 5-7: The angular offset of the phase difference between the chamber pressure and heat release rate for pure CH_4 (blue), 10% H_2 (red), and 20% H_2 (green) is plotted as a function the equivalence ratio.

excited behavior of the long combustor configuration. In particular, we are interested in how the forced phase between the chamber pressure and heat release rate compares to the Rayleigh criterion for instability at the frequencies that are natural acoustic frequencies of the long configuration.

In figure 5-8, we map out those regions in the space defined by the forcing frequency and the equivalence ratio that satisfy the Rayeligh criterion. These regions are shaded in the plot for each fuel composition. Going back to our discussion about the flame transfer functions, we do see that as the equivalence ratio increases, the shaded region eventually crosses 40 Hz, and the values at which this threshold is crossed correlate well with the onset of instability in the long combustor, suggesting that this mode arises as an amplification of 40 Hz turbulent noise when that mode is able to couple with the flame. Commensurate with our observation in figure 5-7
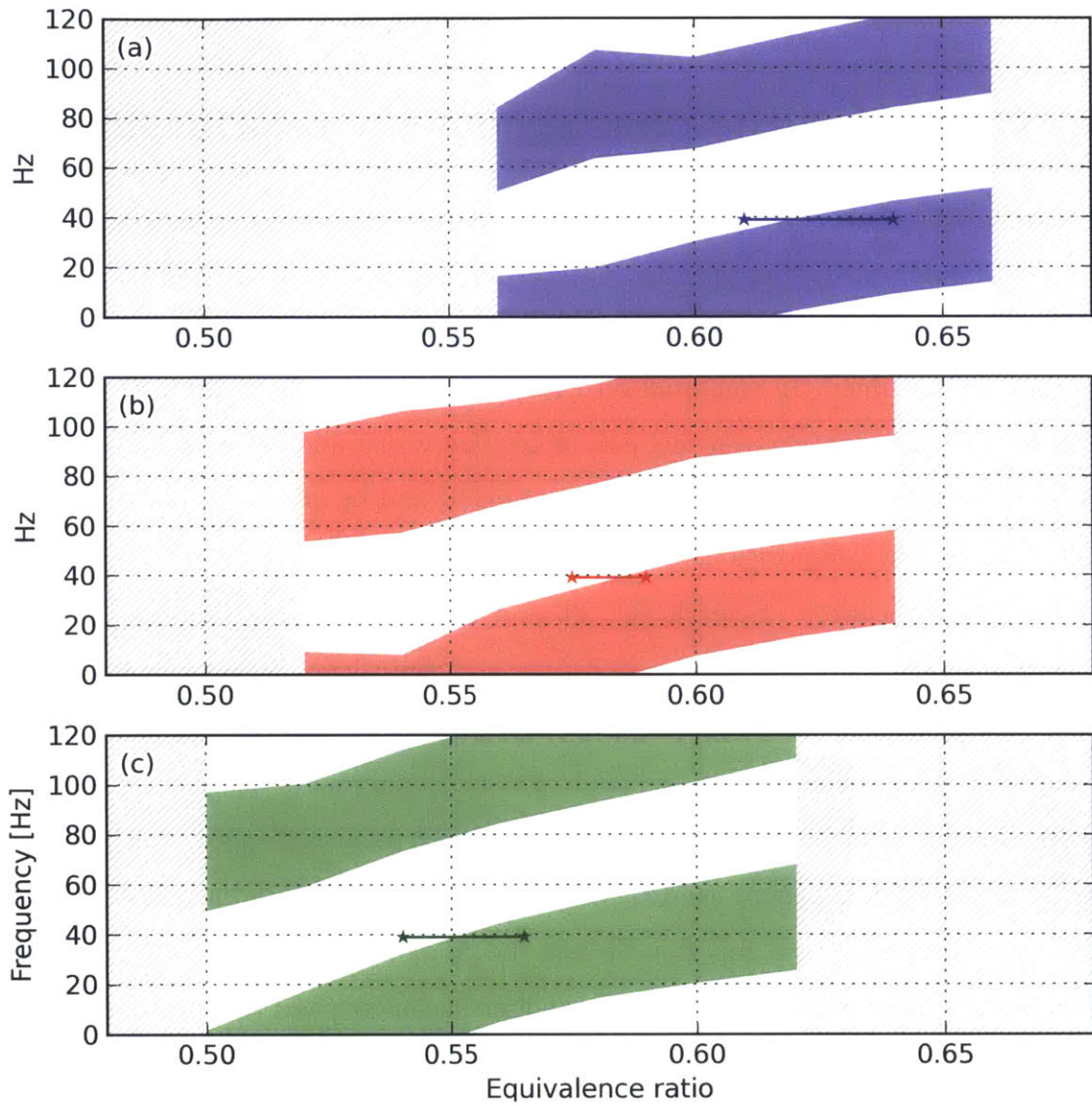
Figure 5-8: The upper and lower boundaries of the region, defined by the equivalence ratio and the forcing frequency, that satisfies the Rayleigh criterion are shaded for pure CH_4 (blue), 10% H_2 (red), and 20% H_2 (green). The operating points at which the 40 Hz mode is observed in the long combustor configuration are marked with a line in each plot with the endpoints denoting the onset and disappearance of the mode.

that the rate at which the phase decreases with equivalence ratio, we see that the boundaries of the Rayleigh-unstable region begin to become more horizontal with increasing equivalence ratio.

5.3   Collapsing the phase-geometry relationship

In the preceding sections, we have shown that in addition to the linear relationship the phase of the flame transfer function has with the forcing frequency, we have also shown that there was a particular inverse relationship with the equivalence ratio within the range that we examined. In combination with chapter 4, there is mounting evidence that there is a fundamental governing parameter that would allow us to collapse these transitions–forced acoustic response, flame geometry, and by association, self-excited behavior–across fuel compositions.

Following on the work of Speth [89, 39] and Hong [90, 91], we propose that we can capture the effects of both fuel composition and equivalence ratio by looking at a flame speed. Flame speed, the precise meaning of which, we will hold off on defining for a moment, is an obvious choice to look to for such a parameter based on the previous work. Insofar as we accept that the geometry of the flame is primarily responsible for its forced acoustic response (and therefore, we claim, self-excited acoustic behavior), the geometry itself is a function of how the flame propagates into the flow. In §5.1, we show a loose correlation between the flame geometry and the forced acoustic response. Confirmation will come from finding an appropriate parameter that captures/collapses the forced acoustic response that is either identical to the parameter we found previously, or at least scales in the same manner.

While the work of Speth and Hong established the strained flame consumption speed as such a parameter that collapses the data in a very similar experiment (in the case of Speth and Ghoniem, for calculated extinction strain rates), and in a backward facing step combustor (in the case of Hong *et al*, using strain rates calculated near the flame tip), this work focused on mapping the transitions between modes in the combustor, rather than predicting the onset of instability in a nominally stable
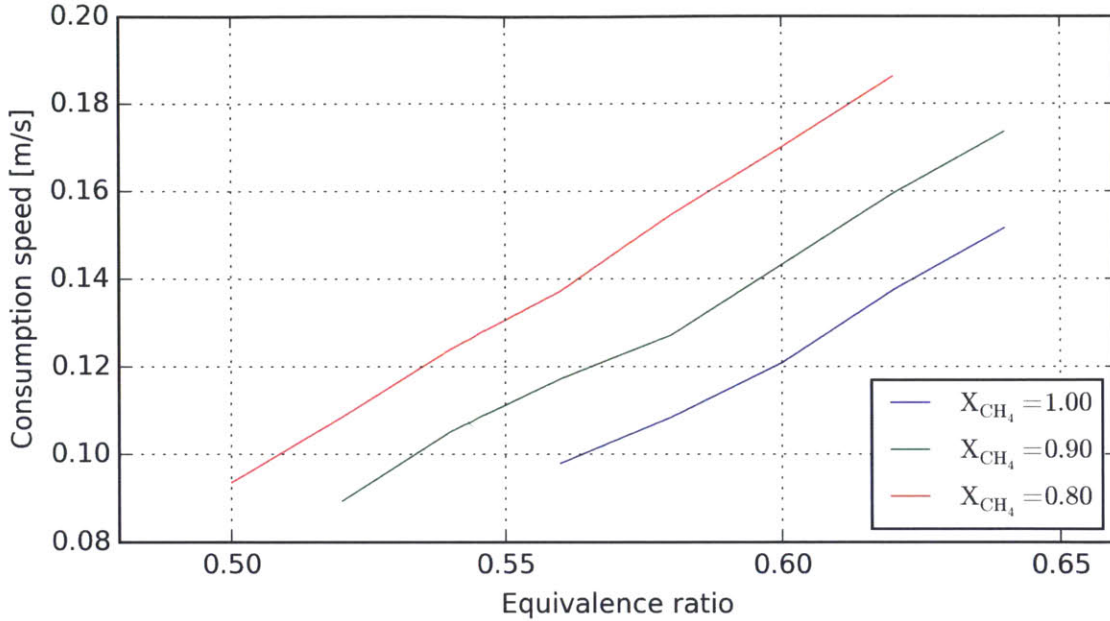
Figure 5-9: We plot the laminar flame speed (dashed lines) along with the strained flame consumption speed (solid lines) taken at the limit of the extinction strain rate, showing the relationship between these two quantities as a function of equivalence ratio.

system. Furthermore, for the consumption speed, the question still arises as to what characteristic strain rate to use. In Speth's work, the strain rate was empirically derived from in order to collapse the data, while the Hong identified a flame tip in the backward-facing step comustor, hypothesizing that this was the most critical region of the flame from a dynamics standpoint. In figure 5-9, we show both the laminar flame speed and the strained flame consumption speed at the extinction strain rate for the three fuel compositions as a function of equivalence ratio. The conclusion to draw from this is that not all choices of consumption speed are equal, and the particular functional relationship with equivalence ratio and composition will change depending on our choice.

While our goal is to be able to identify a particular strain rate to use, the dynamics and geometry of the swirl-stabilized flame do not readily lend themselves to the same interpretation as those of the backward facing step combustor. The flame tip, as we have shown, exists well upstream of the expansion plane, but even so, it is not clear

that it undergoes sufficient change across different operating points to drive the global changes that we see in the system. Furthermore, the flame geometries that are under consideration do not lend themselves to being described as a simple progression of the flame or any particular, identifiable section of the flame. Chapter 4 was dedicated to showing that certain geometric patterns appear consistently across fuel compositions, as a function of the equivalence ratio. In that chapter, we correlated these transitions with regions of high strain in the flow, reaching or exceeding the extinction limit, in the shear layers. The transition from flame III to flame IV showed a particularly nuanced dependence on the extinction properties. The strains in the outer recirculation zone itself were insufficient to cause flame extinction, but due to heat loss to the combustor walls, the presence of a flame in the outer region was dependent on the strain rate in the outer edge of the jet, where flames would cross from the conical region into the outer zone. The laminar flame speed does not adequately collapse the combustor data, but the next logical choice, given the critical role of the extinction strain rate, is the strained flame consumption speed taken at the limit of the extinction strain rate, $\tilde{S}_c$, for each operating condition. This quantity is defined as:

$$\tilde{S}_c = \lim_{\kappa \to \kappa_{ext}} \frac{\int_{-\infty}^{\infty} q''' / c_p \, dy}{\rho_u (T_b - T_u)} \tag{5.4}$$

where κ_{ext} is the extinction strain rate, q is the volumetric heat release rate which, c_p is the specific heat, ρ_u is the unburned gas density, T_b is the burned gas temperature, T_b is the burned gas temperature, and y is the coordinate normal to the flame. We find that this parameter collapses both the forced acoustic response and self-excited acoustic behavior very well, thereby linking the forced response, the self-excited behavior, and the flame geometry.

In order to demonstrate this collapse, we first show how the angular offset of the phase relationship, shown as a function of equivalence ratio in figure 5-7, maps onto the new parameter. This new curve is shown in figure 5-10, in which we see that all three curves collapse onto each other. Knowing that the phase scales with forcing frequency in nearly the same manner across fuel compositions, this lends itself to pro-
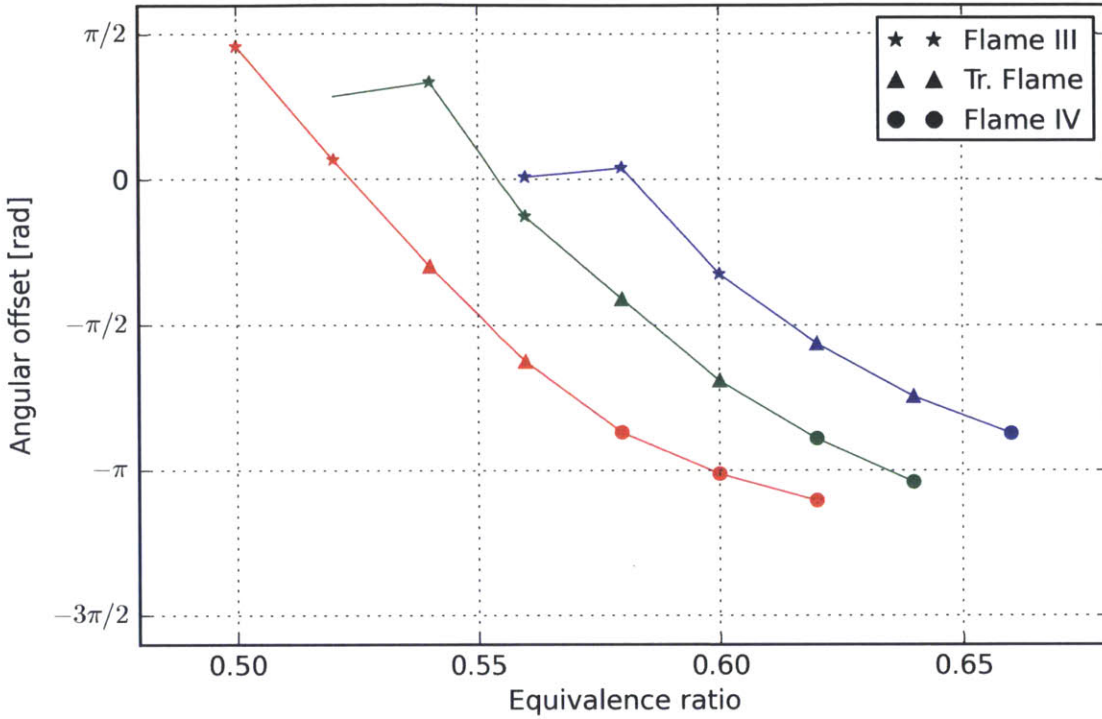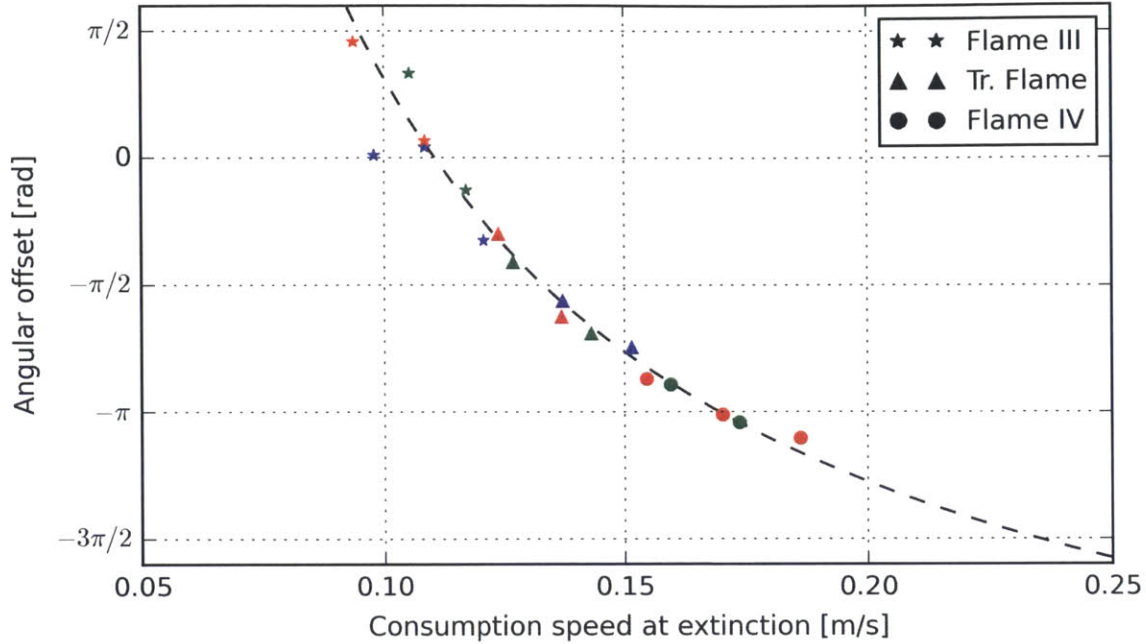
Figure 5-10: The angular offset of the phase difference between the chamber pressure and heat release rate for pure CH_4 (blue), 10% H_2 (red), and 20% H_2 (green) is plotted as a function the strained flame consumption speed.

ducing a universal function defining the phase response of the combustor. In figure 5-11, we mapped the boundaries of the region that satisfied the Rayleigh criterion for each fuel composition as a function of equivalence ratio and forcing frequency. In figure 5-13, we map the same boundaries as function of $\tilde{S}_c$ and the equivalence ratio, and as we predicted, we find that there boundaries lines up well for each case. In addition, we notice that the boundaries keep the characteristic curve that we previously saw, with the slope of the boundaries decreasing as a function of consumption speed. Furthermore, we also see that the transition points, corresponding to the onset of the 40 Hz mode in the long combustor configuration also line up.

More generally, in figure 5-12, we show that the self-excited behavior of the flame also scales with the strained flame consumption speed at the extinction limit. We see that the onset of both the 40 Hz and 110 Hz modes occurs at critical values of $\tilde{S}_c$, independent of the H_2 fraction. As we have already correlated the self-excited behavior with the flame geometry in chapter 4, we have now closed the loop, linking
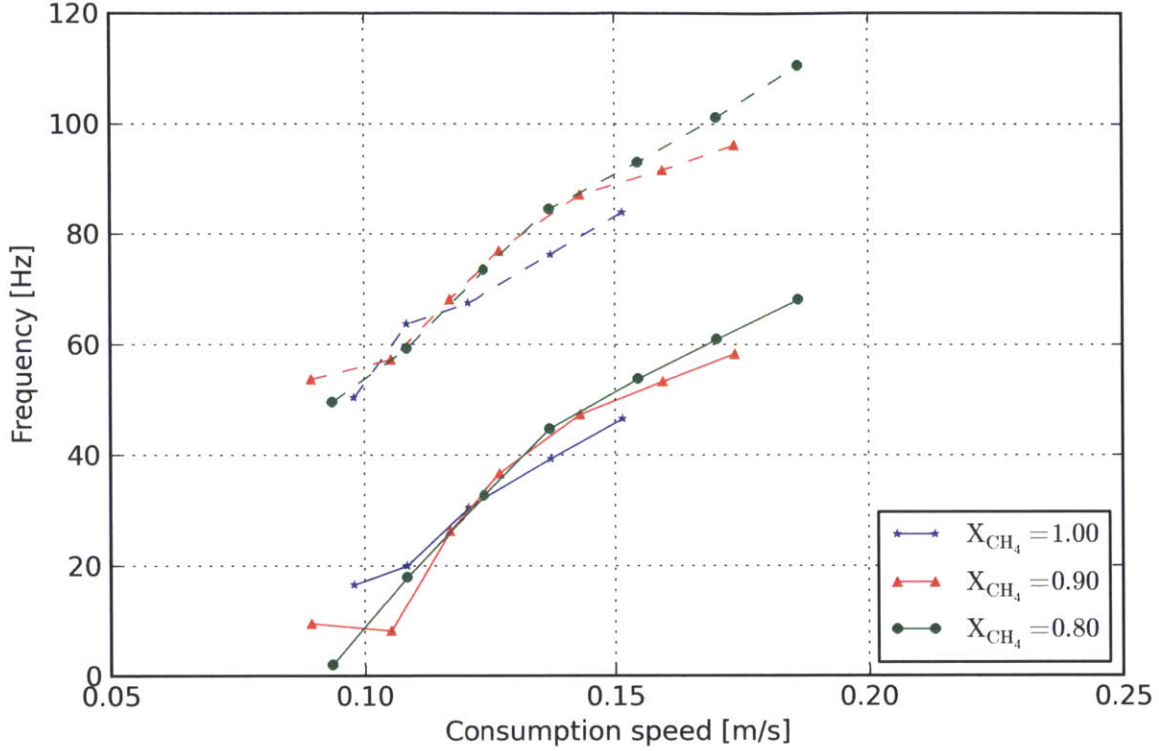
Figure 5-11: The upper and lower boundaries of the Rayleigh criterion are presented for the three fuel compositions as a function of consumption speed. The Rayleigh criterion is satisfied above the dashed curves and below the solid curves.

flame geometry, forced acoustic response of the short combustor configuration, and the self-excited behavior of the long combustor configuration. The disappearance of the 40 Hz mode will be discussed in connection with the gain of the flame transfer function in the next section. At present, however, we turn our attention to the finding a functional form for the phase collapse.

While we have already fit a linear curve to the phase response of each individual case, the angular offset, θ_0 shown in 5-10 suggests an inverse relationship with the consumption speed, such that we propose the following form for θ_{pq}:

$$\theta_{pq}(\tilde{S}_c, f) = \alpha f + \frac{\eta}{\tilde{S}_c + S_0} + \theta_1 \tag{5.5}$$

A curve representing the least-squares fit of the inverse function to θ_0 is shown as a dashed black line in figure 5-10. Fitting the ensemble of data to this expression, we
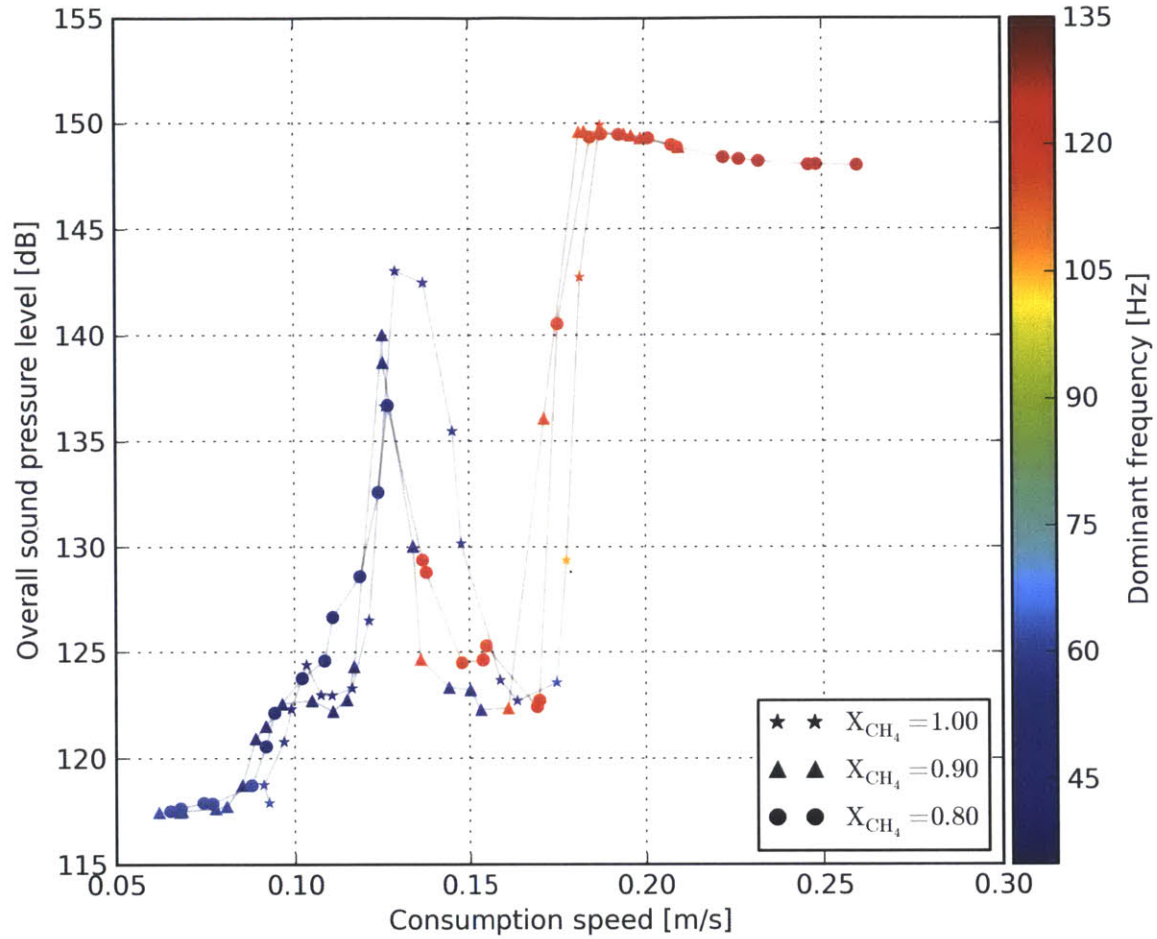
Figure 5-12: The overall sound pressure level is plotted as a function of the consumption speed at the limit of the composition-dependent extinction strain rate for fuel blends from pure CH_4 to 20% H_2.

arrive at the following equation:

$$\theta_{pq}(\tilde{S}_c, f) = 0.083\,\text{rad/Hz} \times f + \frac{0.876\,\text{rad} \cdot \text{m/s}}{\tilde{S}_c - 0.0086\,\text{m/s}} - 2.30\,\text{rad} \qquad (5.6)$$

To strengthen our case for correlating the forced acoustic response of the short combustor with the self-excited behavior of the long combustor, we can attempt to use this expression to predict the mode transitions within the combustor, based solely on the Rayleigh criterion, and our old map of natural frequencies derived from the two-parameter quasi one-dimensional acoustic model in chapter 2. In particular, we

175

wish to see if the relationship that we have derived can be extended to account for the 110 Hz mode. In figure 5-13, we have taken the expression in (5.6), and shaded in those regions for which $2\pi n - \pi/2 \leq \theta_{pq} \leq 2\pi n + \pi/2$ for any integer n, within which the Rayleigh criterion is satisfied. Along with it, we have plotted two lines corresponding to the maximum extent of the 40 Hz mode and 110 Hz modes as a function of consumption speed (noting that the 110 Hz mode does not disappear within the test domain). The onset of both unstable modes are well predicted by the Rayleigh criterion as bounded by equation (5.6), although the model does slightly over predict start of the 40 Hz mode and under predict the start of the 110 Hz mode.

In this section, we have not only shown that the flame geometry, forced acoustic response, and self-excited behavior of the flame are intrinsically linked through a particular value of the consumption speed (at extinction), but we have also shown how this information may be used to predict the onset of dynamic instability using a very simple model and examining the forced acoustic response in the context of the Rayleigh criterion.

5.4   Gain response of the flame

In the previous sections, we have shown that the phase difference between pressure and heat release under the action of acoustic forcing is correlated well with the geometry, and as the geometry is a function of the extinction limit and consumption speed, we were able to develop an analytical expression for the phase of the flame transfer function in terms of the frequency and the strained flame consumption speed. We went on to show how this could be used to create a map of those frequencies which satisfy the Rayleigh criterion in the presence of broad spectrum turbulence, showing that the boundaries of the Rayleigh-unstable regime, when compared to the natural modes of the combustor, predict the consumption speeds at which we see the onset of the first two modes of dynamic instability.

In the previous section, we noted that the phase response does not in itself predict the disappearance of the lowest dynamic mode at 40 Hz, but posited that this
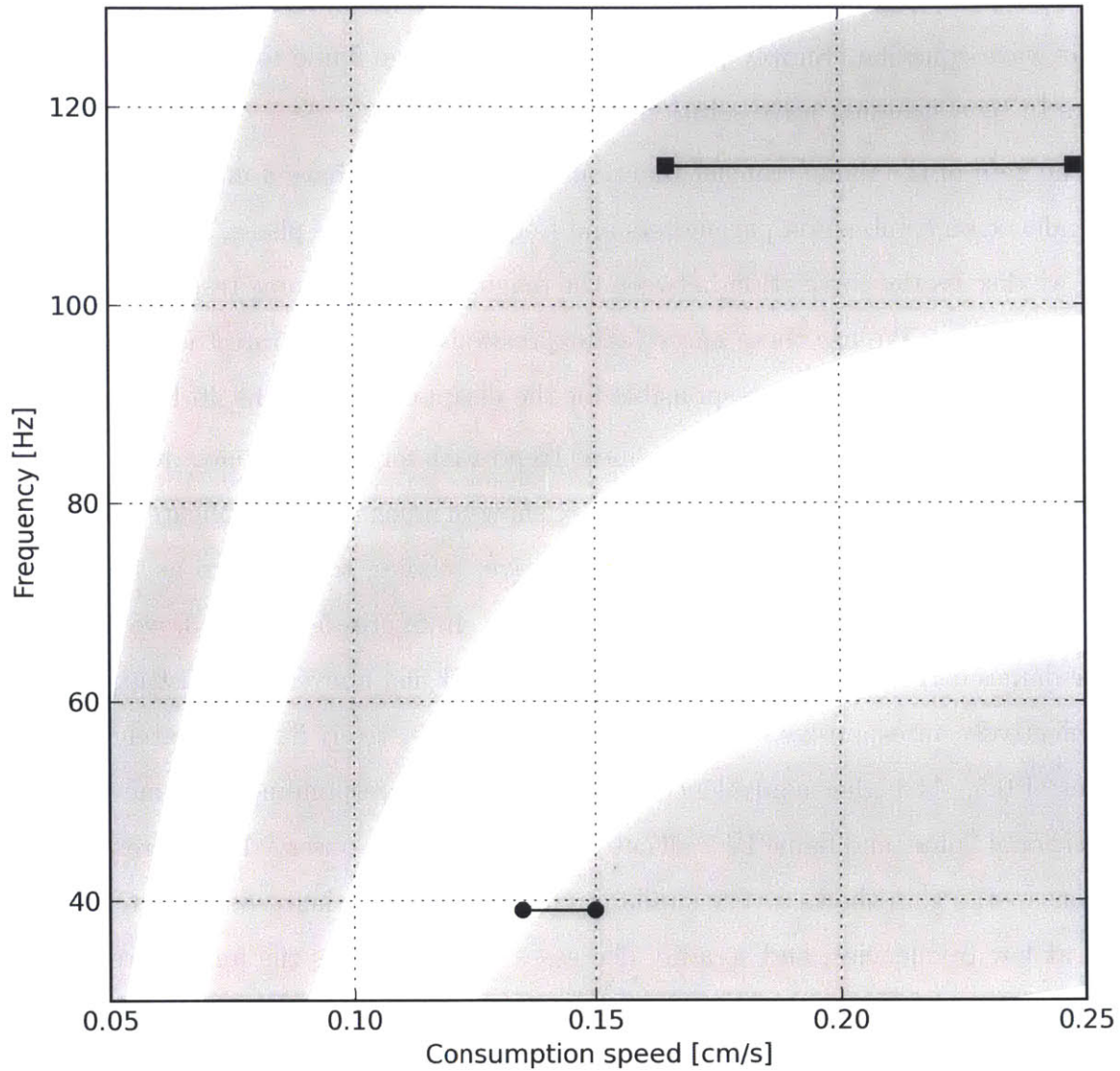
Figure 5-13: The regions in the frequency-consumption speed space that satisfy the Rayleigh criterion, under acoustic forcing in the short combustor configuration, are shaded in gray. The two unstable modes of the long combustor are overlaid, at the operating points at which they are observed.

phenomenon might be explained by the increasing magnitude of the forced acoustic response at higher consumption speeds (or equivalently, higher equivalence ratios for a given fuel composition). The quasi one-dimensional acoustics model predicts that for a sufficiently strong flame response the 40 Hz mode would no longer be a solution to the wave equation. Simply put, for a sufficiently large flame response, the lowest ceases to be a standing wave solution.

The gain of the flame transfer functions have proven to have a more complicated dependence on combustion parameters and frequency than the phase, but in this section, we discuss the correlation between the magnitude of the flame response and the flame geometry. We use these analytical expressions to demonstrate the plausibility of the increasing gain being responsible for the disappearance of the 40 Hz mode.

While the phase clearly showed a linear trend with forcing frequency over the test domain, the magnitude of the flame response shows a much more complicated pattern. By definition, the gain must be strictly positive, tending toward zero as the flame becomes unresponsive under the given conditions. In figures 5-2 and 5-3, we see that those flames corresponding to flame II (and flame III just above the transition point) are effectively unresponsive with gain curves that are relatively flat, and rarely exceed values of 0.5. At higher equivalence ratios, however, corresponding to flame III, the transitional flame, and flame IV—all cases in which we have observed a coherent phase response—the gain shows a very similar trend. The gain of the response is relatively high at low frequencies, and steadily decreases toward zero as the forcing frequency increases. Qualitatively, we see (particularly in figures 5-4 and 5-5, corresponding to the transitional flame and flame IV) that the slope at low frequency appears to have a flat top, rather than an increasing peak, however, experimental limitations on the lower bound of the forcing frequency hinder our ability to explore this aspect of the flame response. There are several functional forms that fit the experimental data, with dramatic differences in their behavior as the forcing frequency goes to zero, and so we must be careful when choosing a functional form (which we will need to do in order to explore the dependence on fuel composition and equivalence ratio).

Numerous experimental, analytical, and numerical studies have shown that geo-

metrical parameters of the flame affect its response to acoustic forcing. Various classes of flames (often designated as 'V'-flames, similar to flame III, and 'M'-flames, similar to flame IV) have different characteristic curves (with M-flames even exhibiting distinct peaks in the magnitude of the flame response at non-zero frequencies, as shown by Preetham *et al* [92]). One study, which is particularly useful for our purposes, was carried out by You *et al* [93], who developed analytical models of the forced acoustic response for different classes of swirl-stabilized flames (roughly corresponding to the flames III and IV).

The non-dimensionalizations in the model assume a relationship between the flame speed and the flow velocity that allows the flame to properly stabilize. As we have shown in chapter 4, the mean flame sits well within the incoming jet, and cannot properly stabilize. As such, it bears more relation to a flame in a high-speed crossflow than a laminar, stabilized flame, and so such clear relationships do not exist, and we are not able to make use of the same non-dimensionalizations. However, we can still gain useful insight into the basic functional form of the flame response that is associated with these flame geometries.

The model demonstrated by You *et al* shows that the acoustic waves perturb the flame front. If, in the absence of acoustic forcing, we were to observe a simple conical flame, for example, then the harmonic waves would form as perturbations in the normal direction to the mean flame front, increasing the effective flame surface area. Again, we cannot make use of the same non-dimensionalizations as You *et al* did, but operating under the hypothesis that the flames in the high-speed flow are subject to similar small perturbations normal to the flame surface, the argument can be made that the magnitude of the turbulent flame transfer function decreases asymptotically as the inverse square as well, such that:

$$\lim_{f \to \infty} ||\mathcal{G}(f)|| \propto \frac{1}{f^2} \tag{5.7}$$

The low frequency limit is more complicated. Neither our data nor the model produced by You *et al* (nor others) project an infinite (or very high) gain at the

179

limit of zero forcing. Physically, as the forcing frequency declines to zero, in the limiting case, the flame is effectively responding to quasi-steady changes in the mean velocity. That is, the change in pressure at a given point, due to the forcing becomes extremely slow compared to the flow time scales. This means that the magnitude of the flame response as we approach this limit represents the change in heat release rate to changes in the mean bulk flow velocity, which cannot be infinite. Rather, under the assumption of complete combustion, which we assert is a good assumption for equivalence ratios corresponding to flame III and above, then as we approach the limit, there should be a direct proportionality between the change in heat release rate and the pressure amplitude related to the quasi-steady increase and decrease in the incoming volume of reactants. Therefore, the gain, in this limit, should approach unity.

The experimental data that we have obtained shows the magnitude of the flame response overshooting unity for frequencies in the vicinity of 30 Hz to 40 Hz and slightly above. This behavior is not unprecedented, however, particularly for conical flames (flame III, although some authors consider this an "inverted conical" flame), and was predicted by Schuller et al [94] for laminar flames. Bellows et al [95] examined the forced acoustic response of a turbulent, swirl-stabilized flame. In addition to noting the linear phase relationship, their data showed multiple peaks in the amplitude of the forced response. Although gaps in the data leave some ambiguity in the domain between 50 Hz and 100 Hz, the authors noted peaks at 90 Hz and 240 Hz at an equivalence ratio of $\phi = 0.95$, with the magnitude of the transfer function exceeding 2.0 in both instance, before monotonically decaying as the forcing frequency was further increased.

Preetham et al [92] conducted a study on laminar flames, examining two configurations, corresponding to the two possible orientations of a cone. Notably, the behavior of the "wedge" shape flames (similar to flame III) that they examined, which are qualitatively similar to flame III, starts at unity in the limit of zero forcing frequency, and then peaks, prior to decaying at high frequencies, in contrast to the "conical" flame, wherein the envelope of the magnitude decays monotonically from

unity toward zero. The modeling approach was similar to Fleifil *et al* [35], wherein a laminar flame was assumed to anchor in a non-turbulent flow. An analytical expression was derived using these basic assumptions, showing this result falling readily out of the governing equations.

Although our data qualitatively agrees, there is no clear analytical solution of this form for the data for the turbulent, swirl-stabilized combustor that we have investigated. As the turbulent flame brush does not transform in the presence of the incoming flow in the same manner, we cannot extend the results of the analytical solutions directly, but we can argue that we should expect to see similar behavior wherein the gain at low frequency peaks at some non-zero value, and that increases in consumption speed (via equivalence ratio or hydrogen-enrichment) should increase the gain across all non-zero frequencies.

5.5 Predictive framework for dynamic instability

The previous sections have been devoted to showing that the self-excited behavior of the long combustor can be reasonably predicted from the acoustically forced behavior of the short combustor by correlating the phase response, which we have shown is a function of the flame geometry, with the boundaries set by the Rayleigh criterion. This showed the potential for very small amplitude acoustic perturbations, the likes of which are inherently present within any turbulent combustion system, within the system to force the flame in a manner that could result in amplification. If the pressure perturbation wave is not a standing wave, however, there is no possibility of instability.

Linking the measured flame response to the instability through the predicted spectrum of resonant acoustic modes suggests that we can directly couple the flame response to the linear wave equation. Doing so will result in a strongly non-linear set of equations which should produce a map of standing wave modes along with phase between pressure and heat release as a function of the consumption speed. Before presenting these equations, however, we should briefly revisit one of our main

181

assumptions. In our acoustic modeling, we have assumed that the flame was flat, or rather, acoustically compact.

5.5.1 Nonlinear phase model

Recognizing the central role that the Rayleigh criterion plays in the self-sustaining combustion oscillations, we begin our model development by accounting only for the functional dependence of the phase difference between pressure and heat release on the resonant acoustic modes of the system. In order to assemble an integrated model, we begin by revisiting the quasi one-dimensional acoustics model that we developed in §2.2. We will adopt the same simplified geometry, and same fundamental assumptions, the most important of which are enumerated below:

1. The mean Mach number is small and therefore, the mean flow does not substantially alter the propagation of acoustic waves.

2. The reactants and products are each perfect gases with their own uniform fluid properties.

3. The bulk of the heat release takes place in a region whose axial extent that is substantially shorter than the wavelength of the resonant acoustic waves.

As before, we wish to express the pressure and acoustic velocity as the sum of forward and reflected waves. General expressions for the pressure and acoustic velocity waves in terms of the acoustic frequency, f, instead of the angular frequency, ω, are given by:

$$\hat{p}(x) = \hat{g}e^{-2\pi i f x/c} + \hat{h}e^{2\pi i f x/c} \tag{5.8}$$

$$\hat{u}(x) = \frac{1}{\rho c}\left[\hat{g}e^{-2\pi i f x/c} - \hat{h}e^{2\pi i f x/c}\right] \tag{5.9}$$

We refer the reader back to figure 2-3 for a schematic of the simplified combustor geometry that we use for the acoustic model, but will review the boundary and matching conditions here. At the upstream boundary, $x = 0$, the flow is choked,

resulting is no velocity perturbations, expressed as:

$$\hat{u}_1(0) = 0 \tag{5.10}$$

At the downstream boundary at $x = L$, the duct opens into an infinite plenum at constant pressure, yielding:

$$\hat{p}_3(L) = 0 \tag{5.11}$$

At the expansion from the inlet duct into the combustion chamber at $x = x_1$, mass is conserved and the pressure is continuous, which we expressed with:

$$\hat{u}_2(x_1) = \frac{A_1}{A_2}\hat{u}_1(x_1) \tag{5.12}$$

$$\hat{p}_2(x_1) = \hat{p}_1(x_1) \tag{5.13}$$

The pressure across the flame at $x = x_f$ is constant, giving us:

$$\hat{p}_3(x_f) = \hat{p}_2(x_f) \tag{5.14}$$

Earlier, we expressed the velocity jump across the flame as:

$$\hat{u}_3(x_f) = \hat{u}_2(x_f) + \frac{\beta e^{-i\theta_{pq}}}{\rho c}\hat{p}_2(x_f) \tag{5.15}$$

where the flame response is represented by $\beta e^{-i\theta_{pq}}$. While previously, we had treated both β and θ_{pq} as independent variables, however, having shown that there is a functional dependence of these variables on both the extinction-limited strained flame consumption speed, $\tilde{S}_c$, and the acoustic frequency, f, we note that these variables are not independent.

In this section, we continue to treat β as an independent variable, but we substitute in the functional form of θ_{pq}, given by equation (5.6). The consumption speed is an independent variable, but the linear relationship between the phase difference and the acoustic frequency creates and implicit relationship between this two parameters,

yielding a strongly nonlinear equation.

In particular, if we expand equation (5.15) in terms of $\hat{g}_2$, $\hat{h}_2$, $\hat{g}_3$, and $\hat{h}_3$ at a fixed consumption speed, we obtain:

$$
\begin{aligned}
\hat{g}_3 e^{-2\pi i f x_f/c} - \hat{h}_3 e^{2\pi i f x_f/c} = \hat{g}_2 e^{-2\pi i f x_f/c} \left[1 + \beta e^{-i(\alpha f - \theta_1)}\right] \\
-\hat{h}_2 e^{2\pi i f x_f/c} \left[1 - \beta e^{-i(\alpha f - \theta_1)}\right]
\end{aligned}
\tag{5.16}
$$

where θ_1 accounts for the effect of consumption speed.

Again, we have a nonlinear set of six equations in seven unknowns. As we are primarily interested in the frequency, we may assume that $\hat{g}_1 = 1$, thereby reducing the number of unknowns to six, and solve the resulting equations numerically. We have shown the results in figure 5-14, where we have selected two values of $\tilde{S}_c$: 0.13 m/s, corresponding to the 40 Hz mode of instability, and 0.18 m/s, corresponding to the 110 Hz mode of instability.

These results show that at low consumption speed, the frequency of the modes remains relatively constant. At the higher consumption speed, however, the lowest mode drops from 45 Hz to 30 Hz, below the minimum frequency that satisfies the Rayleigh criterion for large values of β, even though the mode does not completely disappear. Whereas we have already shown that the phase can be used to predict the onset of the different modes, this gives us strong evidence that the disappearance of the 40 Hz mode is due to a change in the chamber acoustics. This is further reinforced by figure 5-15, in which we have overlaid the lowest modeled frequency on the bands of frequency and consumption speed that satisfy the Rayleigh criterion based on our empirical model. We see that as the frequency of the lowest mode decreases, it exits the region in which the Rayleigh criterion is satisfied, suggesting that this *is* a valid mechanism by which a thermoacoustic mode may cease to exist.

5.6   Summary

The primary challenge that combustion instability research focuses on is the prediction of *a priori* prediction of instabilities through a generalizable framework linking

184
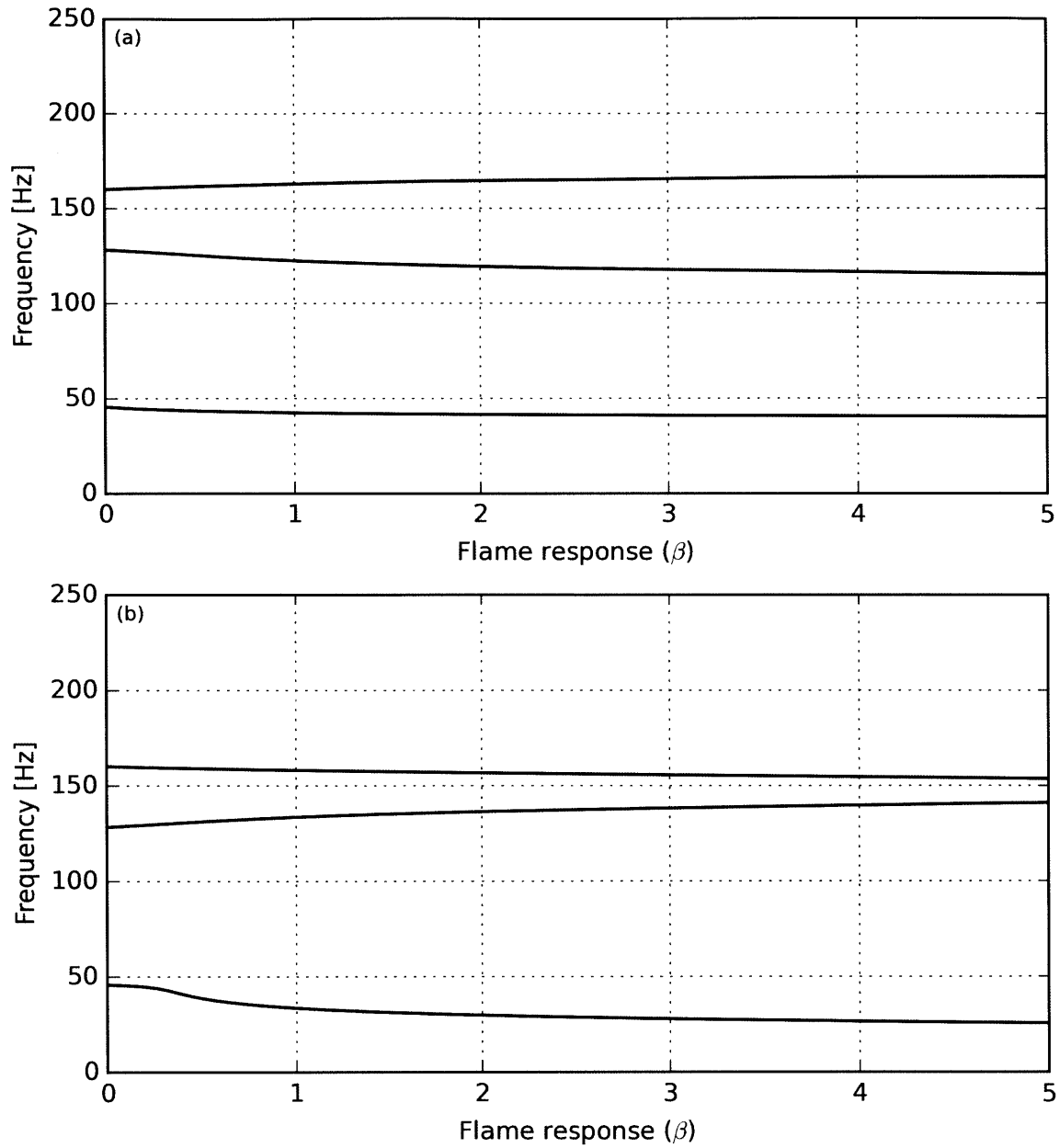
Figure 5-14: The natural modes of the long combustor are shown with the integrated phase-frequency relationship at consumption speeds of 0.13 m/s (a) and 0.18 m/s (b). We note that at the higher consumption speed, the frequency of the lowest natural mode drops to 30 Hz for large values of β.
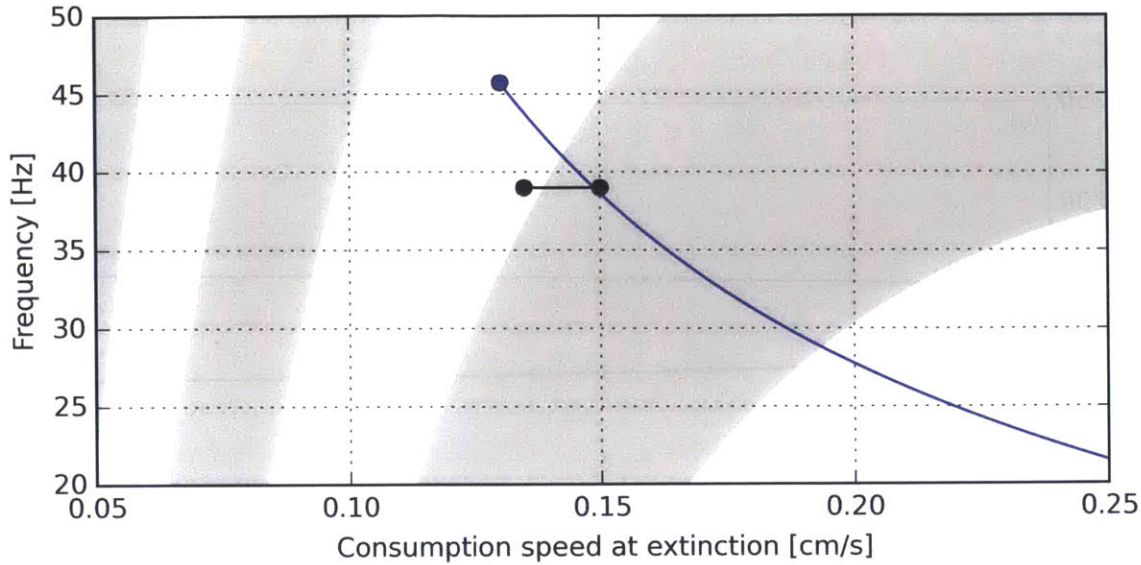
Figure 5-15: The lowest observed unstable frequency (black) and the lowest predicted unstable frequency (blue) are overlaid on the frequency bands that satisfy the Rayleigh criterion based on the empirical $p-q$ phase relationship as a function of frequency and consumption speed at the extinction limit. The regions in grey satisfy the Rayleigh criterion.

flow properties, chamber geometry, and flow properties. Any such framework must take into consideration the nonlinearities that result from the interaction of the various processes, however, these interactions necessarily complicate the framework. By including only those nonlinearities that are necessary, the hope is that a sufficiently simple model can be built while maintaining accuracy.

Particularly notably, Noiray *et al* present a comprehensive, generalized framework based on the flame defining function, an amplitude-dependent version of the flame transfer function [96]. With this model, they were able to compute limit cycles of the system, and find bifurcations, but such a complex model required much more knowledge of the system to be of practical use than the model presented here. Like Noiray *et al*, the model that we are presenting in this thesis recognizes the flame, and particular its response to acoustic perturbations, as the primary source of nonlinearity in the system, however rather than focusing on the limit cycle amplitudes, we focus on a more fundamental physical change due to the nonlinearity, and introduce it into the wave equation in the form of the flame response.

186

The primary result of this chapter is that the acoustic response of a flame, at least in the linear regime, which was considered here, is a primarily a function of the geometric properties of the flame and flow, that is, the macrostructure. While we know from the literature that the effects of acoustic forcing on a flame are also responsible for unsteady flame wrinkling, which will be more influenced by the details of the chemistry, particularly the Lewis number, this is a secondary effect compared to larger scale effects that are dependent on the particular flame macrostructure.

We observed that at each composition and equivalence ratio, there exists two regimes in the test domain in which the Rayleigh criterion is satisfied, and the frequency limits of these regimes (bounded above at lower frequencies and bounded below at higher frequencies) increase with both equivalence ratio and H_2 mass fraction. This shift in frequencies at least partially accounts for the absence of instability at very lean equivalence ratios, followed by the sudden onset at a critical value. The observed transition back to a stable combustion mode, however, is not accounted for by the shift in the pressure-heat release phase difference. Rather, our data suggest that the amplified response of the flame at these higher equivalence ratios may modify the combustion acoustics, and eliminate the natural frequency with which the flame oscillations are attempting to couple from the set of frequencies that satisfy the Rayleigh criterion.

Chapter 6

Conclusion

In this thesis, we have put forward a model for the onset of thermoacoustic instability in a premixed, swirl-stabilized combustor. The goal was to develop a consistent framework that would explain how combustion instability arises in such systems in the absence of any obvious destabilizing source, such as a coupling between the pressure and injector leading directly to equivalence ratio oscillations. The framework that we put forward is predicated on the assumption that instability arises from the selective amplification of preexisting turbulent noise within the combustion chamber, when the conditions are such that the natural frequencies of the combustor overlap with the set of frequencies that satisfy the Rayleigh criterion, based on the acoustic response of the particular flame geometry, and the magnitude of the flame response is sufficient to overcome boundary losses.

In order to understand how instability arises from the coincidence of these parameters, we first need to understand what drives these parameters. First, we showed that the self-excited acoustic properties for two configurations of the combustor: one admitting a low frequency oscillation at 40 Hz, and the second configuration admitting a 140 Hz instability as the lowest frequency instability. In this latter configuration, the 140 Hz instability first appeared at much higher equivalence ratio than the 40 Hz mode in the long combustor. We used a simple, quasi one-dimensional acoustics model with a combustion delay parameter, comparable to an n-τ model, to show how the acoustic response of the flame can alter the fundamental acoustic modes of

the combustor. Using a simplified flat-flame model, we saw that both the phase and amplitude of the flame response modified the frequency of the natural modes, and in the case of the 40 Hz mode in the long-wave combustor configuration, the existence of the acoustic mode is dependent on the flame response. In particular, we see the mode completely vanish as a solution for if the pressure leads the heat release for a sufficiently strong flame response. Along with this behavior, we also observed that the dynamic behavior of the flame was very similar across several different fuel compositions. We were able to obtain similar transitions and nearly identical modes with different hydrogen-enrichment fractions, however, the transition points shifted to lower equivalence ratios.

We were able to show that the same flame geometry appears in the presence of acoustic oscillations and in their absence by modifying the boundary conditions. In this way, we were able to use the short combustor configuration as an acoustically uncoupled model of the long combustor configuration for equivalence ratios that correspond to the onset of the first mode of instability, the 40 Hz mode. By doing this, we were able to show that the transitions in the dynamic behavior that we had previously observed in the combustor acoustics correlated with the changing flame geometry, and furthermore, we observed that these changes occurred in across the various fuel compositions, all in conjunction with the the same dynamic transitions. The implication of this observation is that the flame geometry is largely responsible for the determining the dynamic behavior of the combustor. Furthermore, the fact that we obtained the same progression of flame geometries is indicative of some more universal governing property of the combustion process that determines how the flame interacts with the flow.

Through the use of particle image velocimetry and planar laser-induced fluorescence measurements, and the combination of these datasets to derive a statistical look at the small-scale flow-flame interactions, we were able to correlate the transitions in the flame behavior with the flame strain in zones with the highest shear rates. The most critical observation from this study was that the propagation of the flame into the fresh reactants was bounded by high strain regions that matched or

slightly exceeded the extinction strain rate of the flame at that operating point. As the equivalence ratio increased, and the flame became more resistant to extinction, it was able to persist in higher strain environments, and gradually moved forward into new regions of the flow. At the very leanest equivalence ratios, just above the lean blow off limit, the flame is tubular in nature and confined to a region very near the symmetry axis. Rotation, consistent with a precessing vortex core is observed, but this was generally a very weak flame, and the reaction extended well into the combustor exhaust. As the equivalence ratio increased, the flame became more compact, but remained confined to the interior of the inner recirculation zone. Unable to propagate into the inner shear layer due to the high shear rates in the flow relative to the extinction strain rate, the flame propagates outward from the near the leading edge of the inner recirculation zone. As the equivalence ratio was further increased, the the flame was able to persist in the inner shear layer, and remained confined to the thin conical region of space where the incoming jet of reactants meets the inner recirculation zone, and follows this shear layer downstream along the combustor wall. We next observed a finite bifurcation regime in which the flame and flow structures intermittently jumped between the conical flame and the subsequent flame geometry, which was characterized by the advancement of the flame through the jet where it turns parallel to the wall, and up into the outer shear layer. Observing the strain rate in the two shear layers, as well as examining the individual PLIF snapshots, we concluded that the outer flame is continuously ignited by the conical flame bridging through the reactant jet. The intermittent geometry is a result of intermittent ignition, but as the flame is able to overcome the strain rates of the outer shear layer more frequently, it can provide a more continuous or regular ignition source. At lower equivalence ratios, the flames would not be able to cross into the outer recirculation zone and maintain a persistent connection with the conical region of the flame.

One of the fundamental properties of combustion instability, and one of the properties that makes it most difficult to study, is that it is self-excited. Even in the absence of any obvious unsteady perturbations to the system, a combustor will transition from either a stable state to an unstable state or vice-versa in response to

very small, quasi-steady changes to the combustion parameters. In the context of this experiment, this is seen as a response to small changes in the equivalence ratio. Seeing as the instability is self-excited, and thus we posit that it is the result of some unsteadiness already in the system, we put forward the hypothesis that the broad spectrum noise that is present in any turbulent combustion system is selectively amplified at certain frequencies through a direct feedback with the flame when these frequencies match natural acoustic frequencies of the combustor. To test this, we examined the response of the uncoupled flame to acoustic forcing at a range of frequencies from just below to above the frequency of the first mode at 40 Hz across several different fuel compositions. What we observed is that the low frequency gain increased with equivalence ratio, with the outer recirculation zone flames, both the intermittent flame and the persistent outer shear layer flame, showing a particularly high gain. Critically, the phase difference between the pressure and the heat release rate varied in a manner such that the Rayleigh criterion was first satisfied for 40 Hz forcing at the equivalence ratios at which we first observed the onset of the 40 Hz instability, a relationship that held across fuel compositions. What we can take from this is that at the point of onset, 40 Hz forcing provided by the broad spectrum noise will create an amplified response from the flame. This amplified flame response will in turn pump energy into the acoustic field at 40 Hz, and since this happens to be a natural frequency of the combustion chamber, we get an amplified pressure response, completing the feedback loop. Eventually, the total amplification is limited by energy loss through the boundaries. In this system, we eventually see the 40 Hz mode disappearing as the equivalence ratio increases. Although we cannot explain this in terms of the Rayleigh criterion, we can explain it in terms of the combustor acoustics. At these higher equivalence ratios, the magnitude of the flame response, that is, the gain of the flame transfer function, increases. When we go back to our combustion delay model, we see that for a sufficiently strong flame response, with a phase lead, the 40 Hz mode is no longer a natural frequency of the system. That is, the 40 Hz noise drives a sufficiently large flame response to eliminate itself as a natural mode, preventing further amplification of the pressure.

Building on previous work carried out by Speth [89] and Hong [90], we sought to find a parameter than encapsulated the fuel-dependence of the thermoacoustic behavior. The strained flame consumption speed has been shown to be an effective governing parameter, and in Hong's work, the the strained flame consumption speed was calculated based directly on measured stretch rates in a critical region for the flame. In the swirl combustor, choosing an appropriate, physically meaningful flame speed has been difficult. However, we made use of our observations that the acoustic response is well correlated with the macrostructure, and that changes in the macrostructure are well correlated with changes in the extinction strain rate to propose a correlation between the acoustic behavior and the strained flame consumption speed taken in the limit as the strain approaches the extinction strain rate. By doing this, we see that the mappings of the self-excited and forced acoustic behavior collapse across fuel compositions, and that the various transitions correlate well with specific consumption speeds, regardless of the composition and equivalence ratio combinations used to achieve those speeds. Furthermore, by taking the consumption speed at the extinction limit, we have found a governing parameter that is a function of the mixture, rather than relying on the precise identification of a critical location, which may vary with equivalence ratio, and measurements of the strain rate at that location, making this particularly choice of parameter very general.

The practical goal of combustion dynamics research is to develop the capability to predict instability at design time, and furthermore, to guide changes that will bypass instability without the need for either active control or passive solutions that in some way compromise the performance of the system. To this end, the model that we have put forward here provides some basic motivation for a framework with which it would be possible to estimate the dynamic performance of a combustor with acoustically-uncoupled computational tools. With the computational tools to calculate the flame transfer function and with a network acoustics model based on the flame response, it would in principle be possible to map out those conditions under which the Rayleigh criterion would be satisfied at an eigenfrequency of the combustion chamber. Furthermore, the understanding how the different fuel compositions effect

the acoustic behavior would allow designers and operators to consider alternate fuels or map out the tolerable limits of uncertainty in fuel compositions.

From a fundamental perspective, this work begins to create a picture of one particular mechanism. There are clear limits to the scope of this model, and its scalability to varying inlet conditions such as temperature and pressure would need to be further explored. Inlet temperature is one known weakness of this work. The preceding work by Speth found that consumption speed proved to be a valuable parameter to collapse the data at a particular inlet temperature, but to apply the collapse across temperatures, the density ratio needed to be accounted for as well as the consumption speed [39]. Nonetheless, we are beginning to understand which interactions are important, and refine the set of parameters we consider important to combustion dynamics. The fundamental relationship we found between the flame geometry and the phase, allows us to restrict our view to those parameters that affect flame geometry and interpret their effect by analyzing the manner in which they affect the geometry.

6.1 A look back at microjets

It is worthwhile to take a brief look back at the project that lead to the several of the initial key insights for this thesis. In an attempt to address combustion stability from an engineering perspective, a device, which is now known as a "swirl-counter-swirl" microjet was developed as a means of passively mitigating combustion instability [36]. Using the same combustor that was used throughout this thesis work, a series of injector ports were placed radially inward just upstream of the expansion plane. These injectors were angled so as to produce fluid rotation in the opposite direction.

When actuated with a premixed mixture to prevent dilution, the effect of these microjets was to completely suppress the lowest frequency acoustic instability, the 40 Hz mode. In order to see this effect, 15% of the total mass flow was pushed through the microjets, which accounted for approximately 0.5% of the total inlet area. The injection of so much counter-rotating momentum resulted in a complete reversal of the flow, creating a very strong shear layer, sufficient to substantially delay

the encroachment of the flame into the outer shear layer.

From our previous discussion, we can deduce that the effect of the microjets was to alter the geometry of the flame, thus altering the acoustic response. The increased shear rates due to the counter-flowing jets require a stronger flame to cross into the outer shear layer without being extinguished. We have noted that this outer flame is particularly active, and in its absence, this likely means that he Rayleigh criterion cannot be satisfied at 40 Hz, thus suppressing that thermoacoustic mode.

Appendix A

Statistical Analysis of Flames Near the Expansion Plane

In chapter 4, we focused our analysis on three flame geometries (flames II, III, and IV), and a intermediate regime in which the flame intermittently transitions between configurations III and IV. These transitions are primarily characterized by the relationship between the most probable flame position and the inner and outer recirculation zones and the outer recirculation zone. As this was the critical region, we focused on PLIF that captured this region well, however, due to the diminishing thickness of the Gaussian beam profile, the PLIF data was poorly resolved over the first 20 mm downstream of the expansion plane. In this appendix, we will briefly present the same statistical analyses performed with PLIF datasets that do capture this region. The PIV datasets with which they are combined are the same datasets that were used in the analyses of chapter 4.

Before we move on to the statistical analyses, we briefly look at instantaneous snapshots of the PLIF data, post-processed to reveal flame location and direction of propagation, in figures A-1 through A-4. Starting with flame II, shown in figure A-1, we see the upstream continuation of the flame that is confined to the interior of the inner recirculation zone. In A-1(a), we see the mean PLIF signal. The greatest intensity is concentrated just inside the inner shear layer between the expansion and 20 mm downstream of the expansion, however, we do see a PLIF signal within the

Figure A-1: The mean PLIF signal is shown (a) alongside several instantaneous PLIF snapshots showing the flame edge and direction of propagation (b-f) for flame II. PIV data were captured in pure CH_4 at $\phi = 0.550$ and PLIF data at $\phi = 0.560$.

Figure A-2: The mean PLIF signal is shown (a) alongside several instantaneous PLIF snapshots showing the flame edge and direction of propagation (b-f) for flame III. PIV and PLIF data were captured in pure CH_4 at $\phi = 0.600$.

interior of the recirculation zone as well. The instantaneous snapshots, shown in A-1(b-f) show that the flame within these first 20 mm of the expansion typically follows along parallel to the jet, and we observe wrinkling that is characteristic of shear layer instabilities [97]. As it progresses farther downstream, however, it wraps into the interior region, particularly near the primary eddy of the recirculation zone. The upper branch of A-1(b) and lower branch of A-1(f) are good examples of this observation. As we move farther downstream, like we do in chapter 4, we see that the flame is pushed farther in toward the center of the inner recirculation zone by these eddies.

Next, we take a look at flame III, which is shown in figure A-2. The mean PLIF signal, shown in A-2(a) shows an increased and radially narrower concentration of OH in the shear layer, when compared to flame II. Again, the signal is strongest within the first 20 mm of the expansion, gradually expanding, however, we do not observe the same extent of inward expansion of the PLIF signal, which is consistent with our previous observations in which we stated that the flame brush of this geometry is conical, sitting along the inner shear layer. In the instantaneous snapshots, shown in A-2(b-f), we see the flame fronts extend along the inner shear layer. The upper branches of A-2(d) and A-2(e), for example, show the flame being pushed into the interior by the primary eddy, but not to the same extent, either axially or radially, as we see with flame II.

Now we turn our attention to the transitional flame shown in figure A-3. This is the "flickering" flame that is characterized by a persistent conical flame in the inner recirculation zone, which is intermittently accompanied by a flame that propagates upstream along the outer shear layer. This is manifested in the mean PLIF, shown in A-3(a), by a conical signal, similar to that of flame III. The upstream region of the outer recirculation zone contains very little OH, such that the mean signal is not significantly larger than the noise. Nonetheless, we see from the instantaneous snapshots in A-3(b-f) that a flame in the outer shear layer does intermittently accompany the conical flame. The instantaneous data shows us that this outer flame propagates up from the near the wall where the reactant jet impinges. This helps confirm our
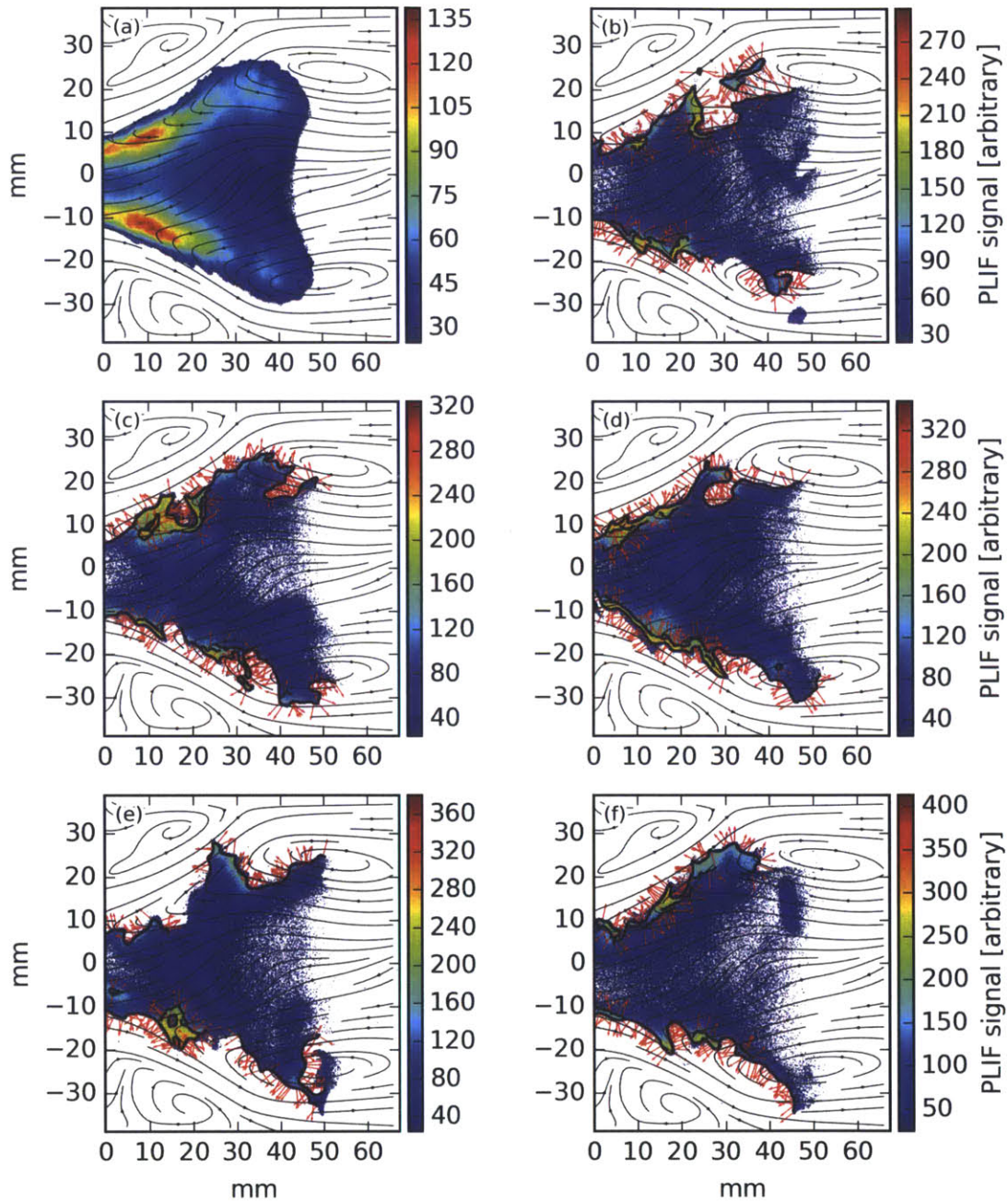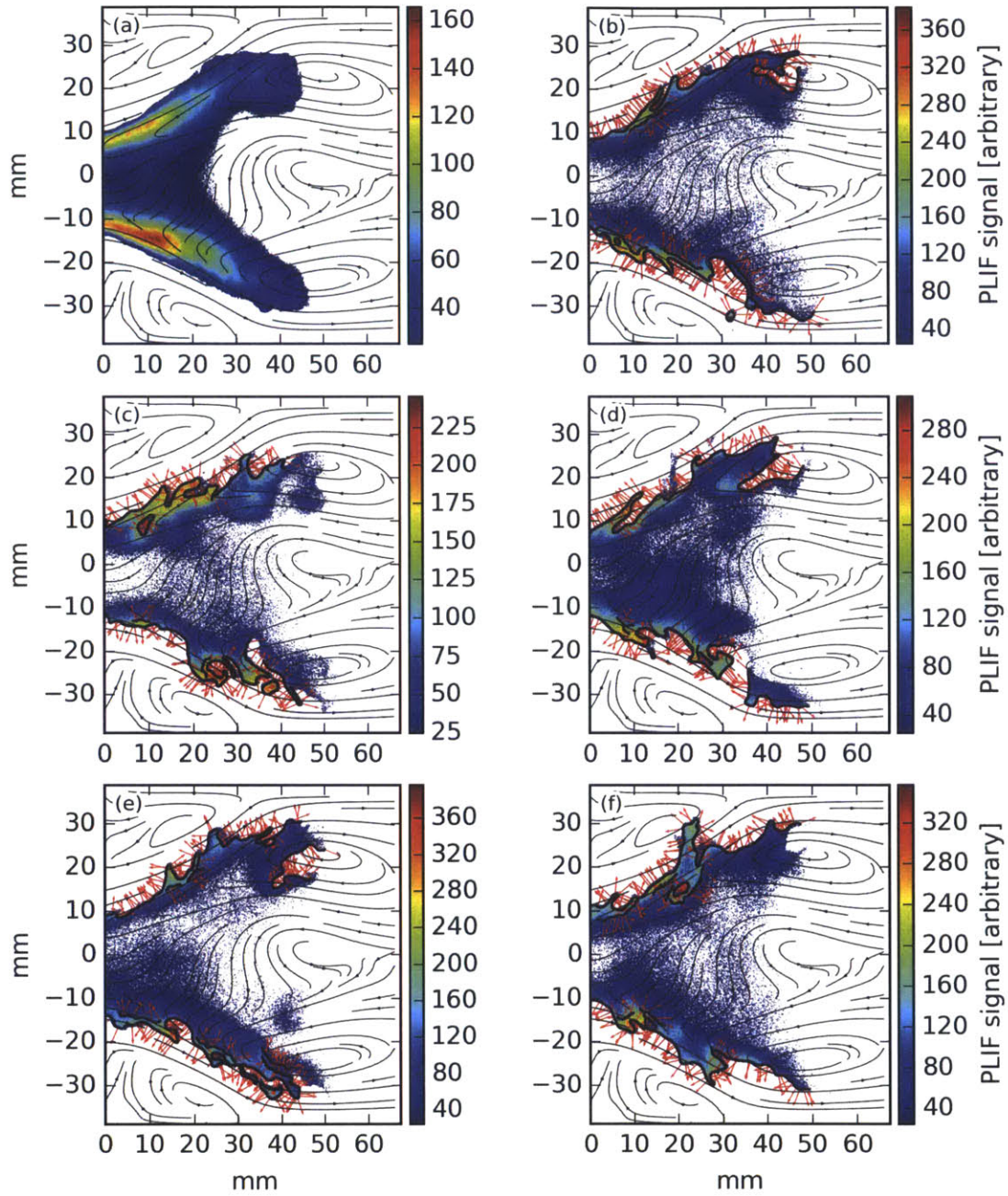
Figure A-3: The mean PLIF signal is shown (a) alongside several instantaneous PLIF snapshots showing the flame edge and direction of propagation (b-f) for the transitional flame. PIV data were captured in pure CH_4 at $\phi = 0.625$ and PLIF data at $\phi = 0.620$.
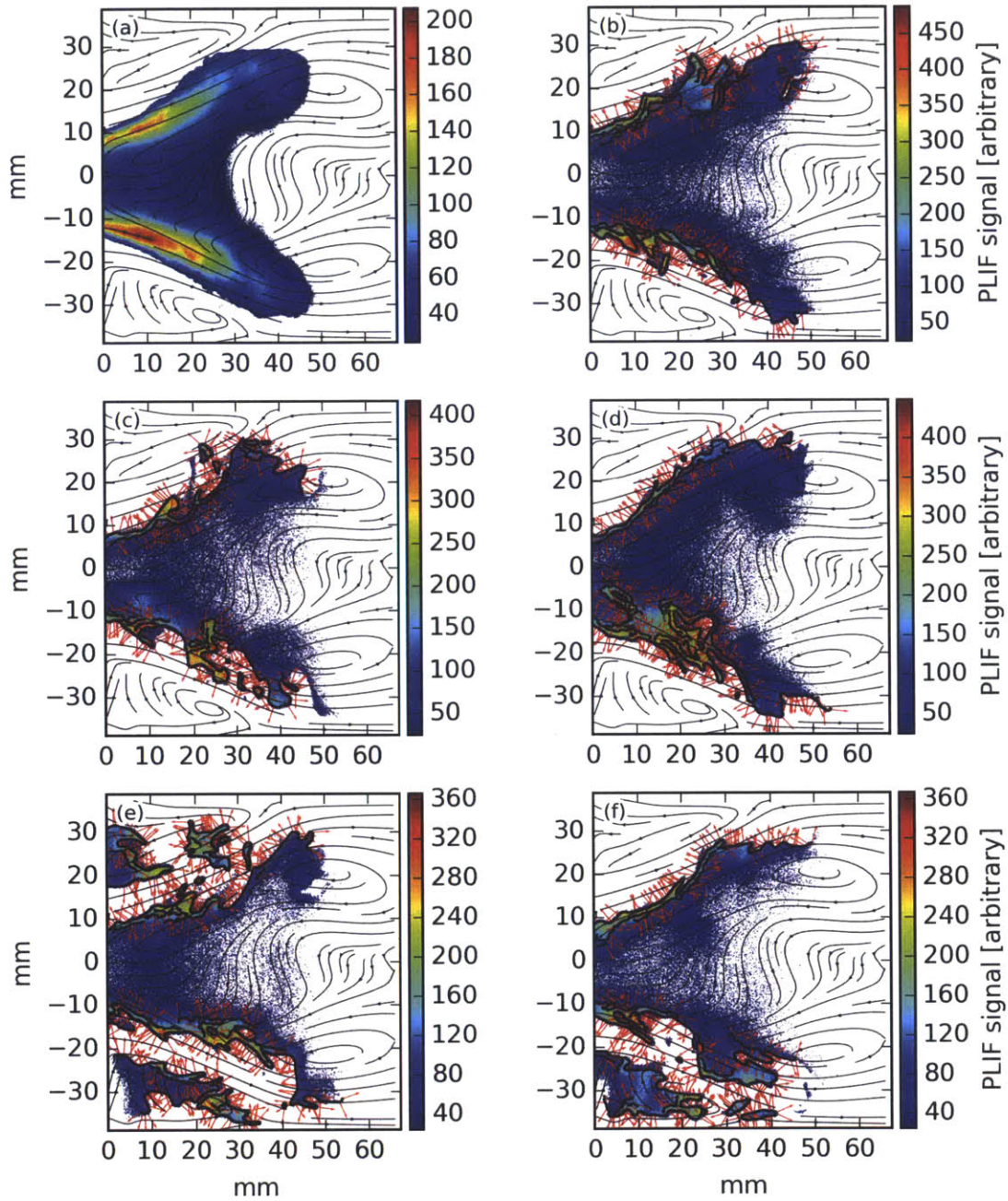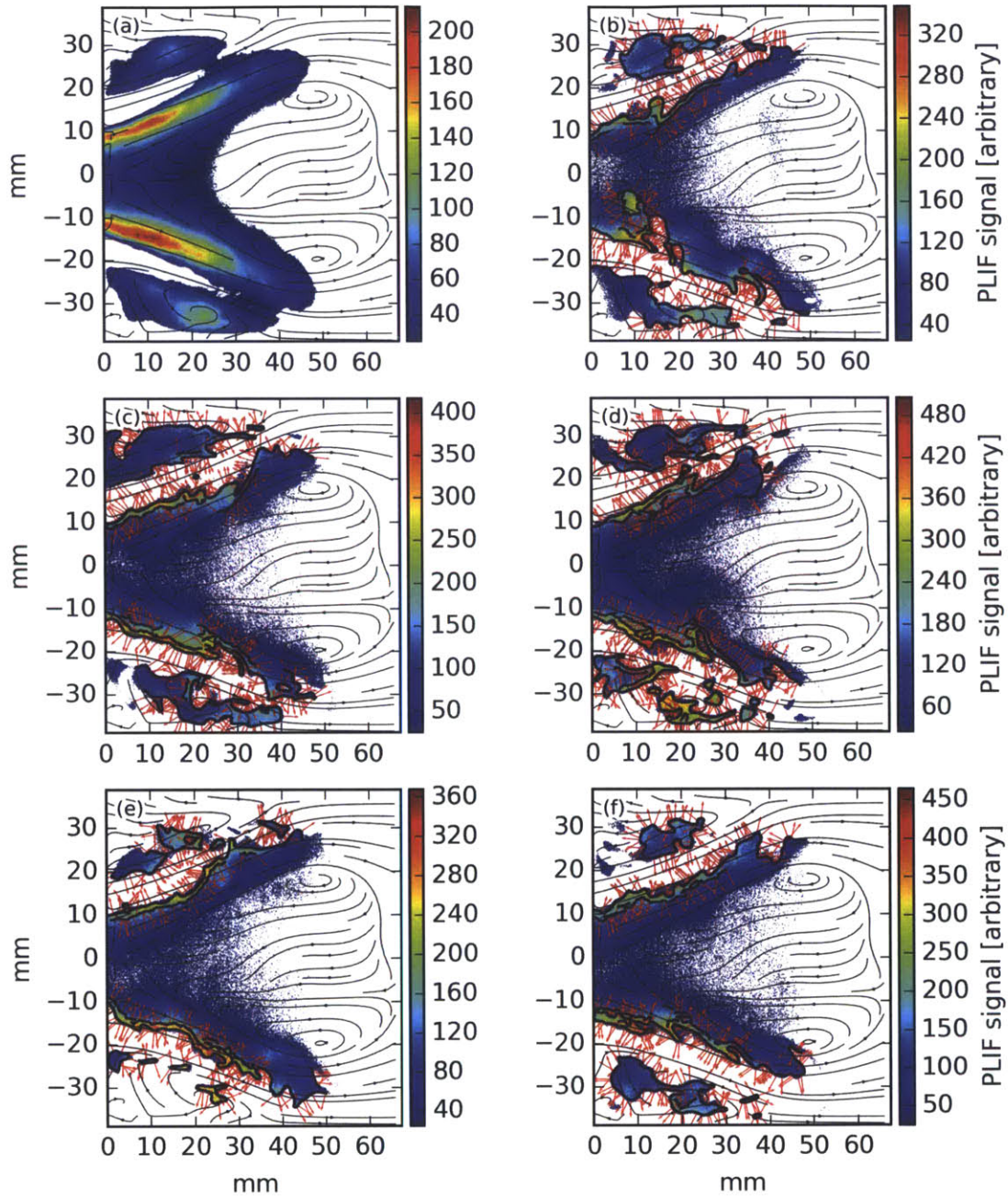
Figure A-4: The mean PLIF signal is shown (a) alongside several instantaneous PLIF snapshots showing the flame edge and direction of propagation (b-f) for flame IV. PIV and PLIF data were captured in pure CH_4 at $\phi = 0.650$.

statements in chapter 4 where we suggested that the link between the conical flame in the inner shear layer and the outer shear layer was critical for igniting and maintaining this flame, which again leads us to the conclusion that the extinction of the outer flame (or rather, its outright absence) at lower equivalence ratios is the result of heat loss to the combustor walls, which requires a continuous (or nearly so) ignition source to maintain a flame. In A-3(b-d), we see what appears to be a highly wrinkled conical flame, qualitatively similar in nature to flame III. The additional wrinkling can be accounted for by noting that the flame is embedded closer to the centerline of the jet in the transitional flame than in flame III. In A-3(e), we see the outer flame in both upper and lower branches, propagating upstream from the wall, however in the upper branch, this flame is broken, whereas in A-3(f), we see that the outer flame in the lower branch extends both along the outer shear layer and parallel to the combustor wall, near the boundary layer.

We should address one aspect of this dataset, which also pertains to the dataset corresponding to flame IV. Particularly in the upstream conical section of the flame, we see a very strong gradient in the PLIF signal on either side of the flame. While we have previously discussed the relatively slow decay of the OH in the post-combustion region (most notably when we looked at the flame profiles in chapter 3), these flames are embedded within the center of the jet, where the mean flow speeds exceed 10 m/s. Consequently, although the OH persists, it is very rapidly advected away, and we are left with an artificially large gradient on the back side of the flame. As the instantaneous snapshots show, the gradients are so similar that the edge detection algorithm cannot reliably distinguish the real flame from the false flame, and we are left with this false "conjugate flame" in the data. In the statistical analyses later in this appendix, we will see that this manifests itself in a slightly enlarged region with non-zero probability and a false flame in the first 20 mm to 30 mm of the inner conical flame, which is most apparent in the spatially resolved flame angle. This artifact will not alter our interpretation of the data, but should be noted.

Finally, we look at figure A-4 where we examine flame IV, which is characterized by an inner conical flame that is accompanied by a persistent outer flame. Consistent

with this characterization, the mean PLIF signal, shown in A-4(a), features a strong signal in the outer recirculation zone, concentrated along the outer shear layer, and extending downstream to the wall where the reactant jet impinges upon it. The instantaneous snapshots in A-4(b-f) reveal a persistent outer flame, although very occasional extinction or partial extinction may occur as in A-4(e). We see the outer flame propagating up the outer shear layer and into the reactant jet, as well as parallel to the combustor wall, propagating radially outward into reactants that are being recirculated from the jet along the wall. As previously noted, we see the inner and outer flames coming in close proximity to one another near the impingement point, again suggesting the the flames originate from this region and propagate up along the shear layer and the boundary layer. Furthermore, with the flame consuming reactants along both sides of the shear layer, extending up into the inlet, and along the wall, we would not predict further changes in the flame geometry unless there was a significant, externally-driven change in the flow structure.

Next, we look at the statistics of the flow-flame interaction. In figures A-5 through A-8, we have plotted spatially resolved statistics for all four conditions, analogous to those plots in chapter 4. Beginning with flame II, shown in A-5, we see that in the upstream region, the flame remains confined to the inner recirculation zone, which extends upstream past the expansion to the swirler centerbody. The highest localized probability of finding a flame, shown in A-5(a), is within the interior of the inner recirculation zone where there is a very low chance of observing strain rates, shown in A-5(f), that exceed the (relatively) low extinction strain rate. At the boundaries of the inner recirculation zone, there is a sharp gradient in both the flame probability and the probability of exceeding the extinction limit. Moving radially outward, the probability of exceeding the extinction limit jumps sharply, and the probability of observing a flame rapidly drops to zero. This is consistent with the observations that we made in chapter 4, which suggesting that high strains in the inner shear layer are primarily responsible for keeping the flame contained in the interior.

The flames propagate outward toward the shear layer, which we can see from the most probable flame angle, shown in A-5(b), but are rapidly extinguished as they

Figure A-5: Spatially resolved maps show statistical flow-flame interactions for flame II in pure CH4. PIV data were captured at $\phi = 0.550$ and PLIF data at $\phi = 0.560$. The point-by-point probability of detecting a flame is shown in (a), and the most probable flame angle is shown in (b). The most probable velocity of the flow into the flame is shown in (c), and the probability of normal flow velocity being within 10 cm/s of the laminar flame speed (d). The most probable strain rate is shown in (e), and the probability of the strain rate exceeding the extinction limit is shown in (f).

attempt to propagate into the jet through the shear layer. In the interior, upstream region, we see conjugate flame angles–flame angles near the shear layer reaching 135° and -45° immediately inside, for example. We previously mentioned the issue in regard to the transitional flame and flame IV in which the edge detection algorithm is unable to correct for the rapid advection of the products near the centerline of the jet. While this effect does artificially produce this same pattern, in the case of flame II, we are observing the conjugate flames in the low speed region of the inner recirculation zone. This is a result of the substantial large-scale flame wrinkling that we observe for this flame geometry, and is a real effect, not an artifact of the post-processing algorithms.

The probability that the normal component of the velocity lies within 10 cm/s of the laminar flame speed, shown in figure A-5(d), shows the expected pattern. In the jet, we see that the probability of observing this particular flame is low, the probability of the normal flow velocity being near S_L is low, and the most probable normal flow speed, shown in A-5(c), is high. Within the interior, however, flow in the recirculation zone is very slow, with a relatively high (although still low in absolute terms) probability of being near the laminar flame speed. We are still dealing with unsteady, turbulent flames, however the greater residence times afforded by this low speed flow is likely to be responsible for the greater large-scale wrinkling that we observe in the instantaneous snapshots of flame II compared to the other geometries.

In figure A-6, we look at the spatially resolved statistics corresponding to flame III. As we saw in chapter 4, the flame is confined to a narrow zone of the inner shear layer, having propagated out of the interior of the inner recirculation zone. The flame probability, shown in A-6(a) is high inside of a narrow, conical band, and nearly identically zero everywhere else in the interrogation domain. The flame angle shown in A-6(b) is consistent with this description. The flame overwhelmingly propagates into the jet of reactants nearly perpendicularly (on average) due to the discrepancy between the flow velocity and the laminar flame speed. We do observe conjugate flames (artifacts of the post-processing) immediately downstream of the expansion plane. As the flame has moved into the shear layer, the normal component of the flow velocity where the flame probability is high is well in excess of the laminar flame
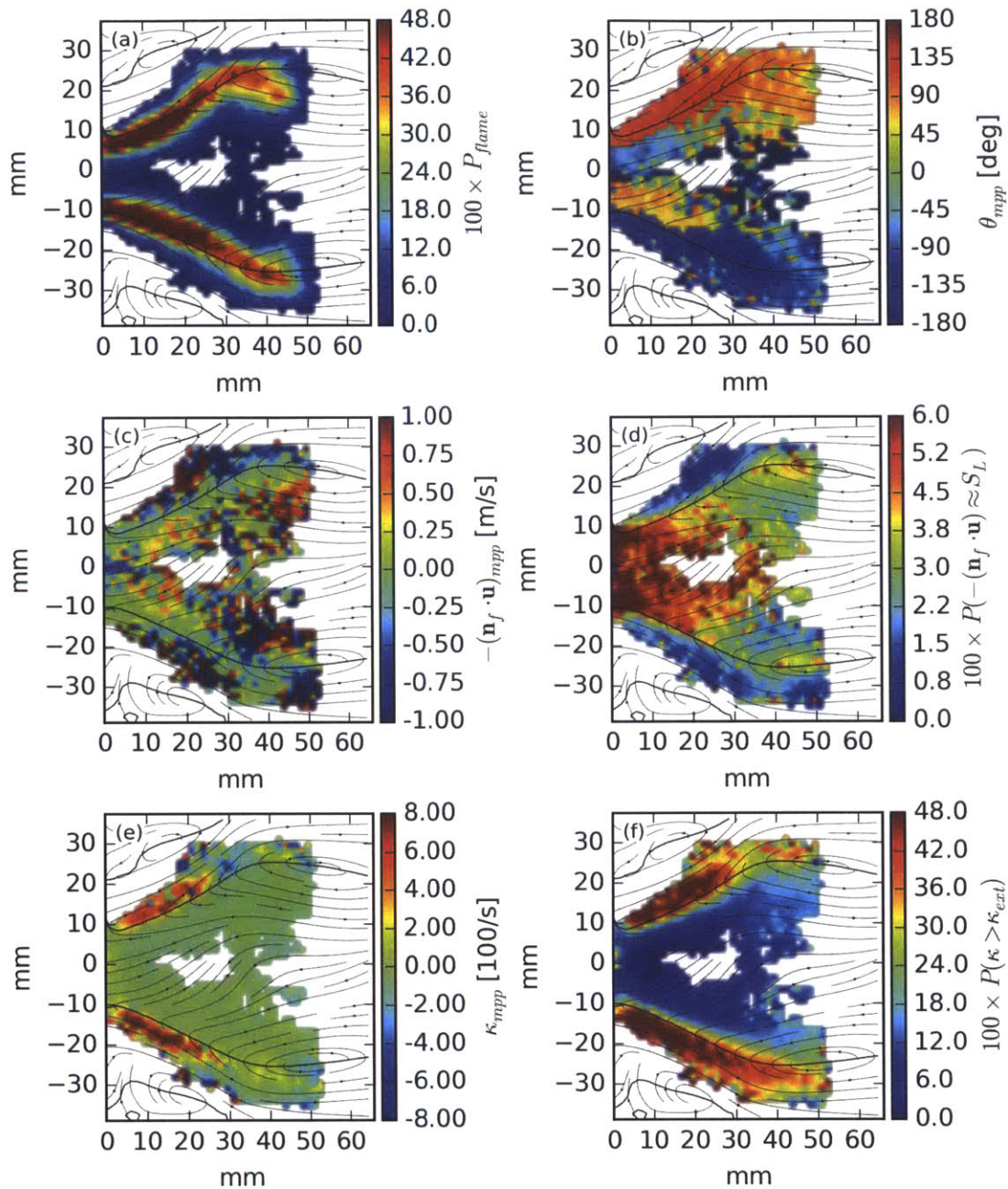
Figure A-6: Spatially resolved maps show statistical flow-flame interactions for flame III in pure CH4. PIV and PLIF data were captured at $\phi = 0.600$. The point-by-point probability of detecting a flame is shown in (a), and the most probable flame angle is shown in (b). The most probable velocity of the flow into the flame is shown in (c), and the probability of normal flow velocity being within 10 cm/s of the laminar flame speed (d). The most probable strain rate is shown in (e), and the probability of the strain rate exceeding the extinction limit is shown in (f).

speed.

The critical figure for the strain rate is A-6(f), which plots the probability of the strain rate exceeding the extinction limit. Along the outer edge of the conical flame, the probability of exceeding the extinction strain rate sits above 30%, and this follows the flame into the inlet pipe. For the flame to move radially outward beyond this point, not only would it be subject to higher speed flow, but as we have seen in chapter 4, it would be subject to higher strain rates more often, and consequently, the flame remains contained to this narrow region.

Figure A-7 shows the statistical flow-flame interactions for the transitional flame, and more prominently illustrates the limitations of this particular dataset, which focuses on the upstream region of flame rather than near the impingement point, for the purposes of analyzing the transition. The flame probability in A-7(a) shows a low, but finite probability of observing the flame in the outer zone, particularly in the lower branch (the upper branch was not captured as well). Nonetheless, this presents us with a consistent picture with what we described in chapter 4. There is a very persistent flame in the inner shear layer, propagating into the jet, shown in A-7(b), which is accompanied, with relatively low probability, a flame in the outer recirculation zone that both propagates along the outer shear layer into the jet of reactants, and into the wall boundary layer where reactants recirculate as they are deflected from the wall (the conjugate flame angles inside the cone are artifacts, and artificially thicken the flame brush in this region).

As the conical flame is embedded well within the inner shear layer by this point, the probability of the normal component of the flow velocity being near the laminar flame speed is vanishingly small as shown in A-7(c-d), consistent with our prior statements that these conical flame brushes must be the product of continuous ignition from the hot recirculated products in the inner recirculation zone. Although the most probable flame strain, shown in A-7(e) is often relatively low, which we have previously shown is due to relatively broad and flat distributions, the most critical piece with respect to flame stabilization is the probability that the flame strain exceeds the extinction limit, which is shown in A-7(f). The data in this particular dataset is a bit more
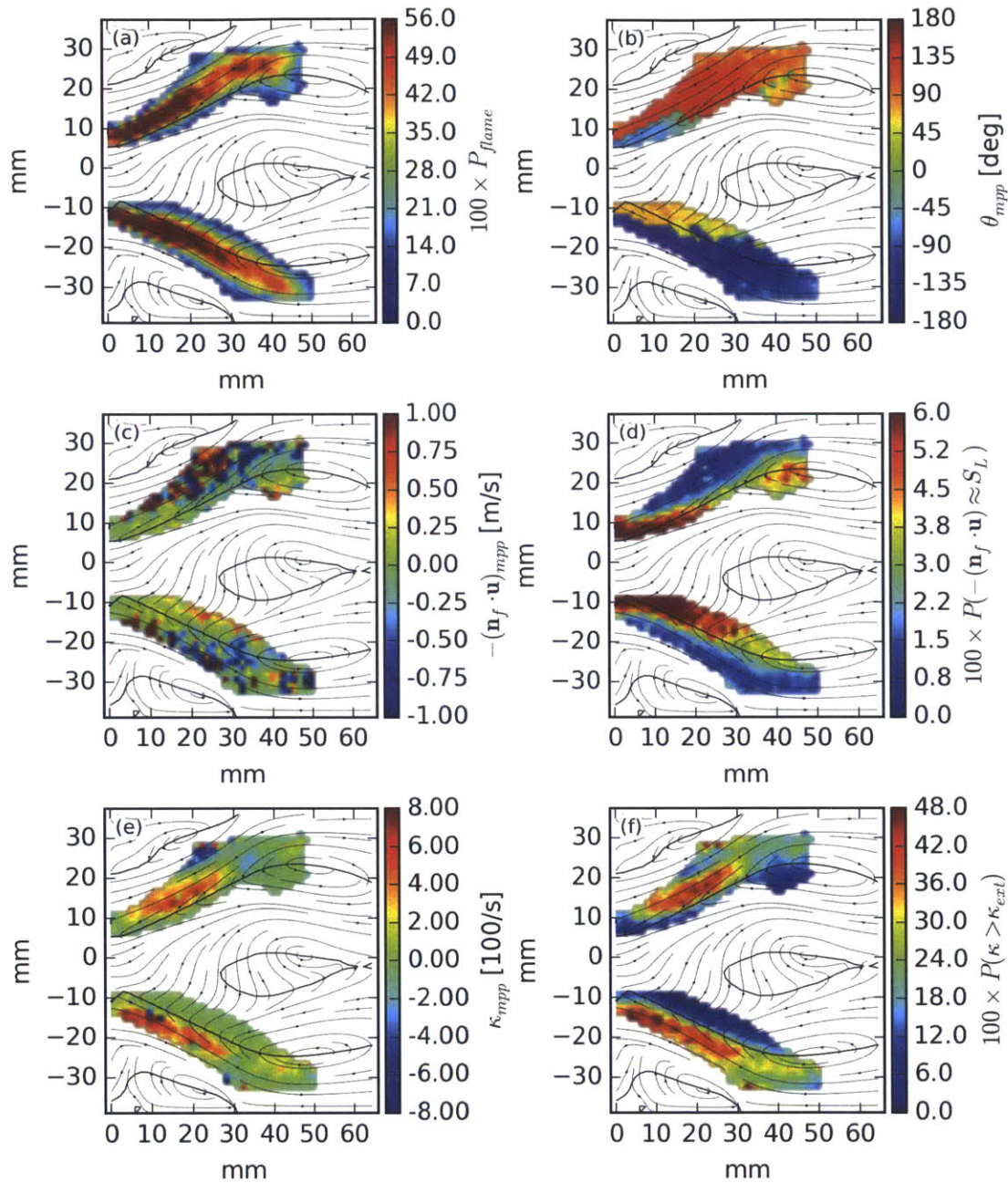
Figure A-7: Spatially resolved maps show statistical flow-flame interactions for the transitional flame in pure CH4. PIV data were captured at $\phi = 0.625$ and PLIF data at $\phi = 0.620$. The point-by-point probability of detecting a flame is shown in (a), and the most probable flame angle is shown in (b). The most probable velocity of the flow into the flame is shown in (c), and the probability of normal flow velocity being within 10 cm/s of the laminar flame speed (d). The most probable strain rate is shown in (e), and the probability of the strain rate exceeding the extinction limit is shown in (f).

sparse than in the dataset we used in chapter 4, but we can examine the lower branch to see that our previous conclusions are confirmed in light of this new data. The probability of exceeding the extinction limit is relatively high in both the inner and outer shear layer, however, it is higher in the outer shear layer. This is one of the key observations relating back to flame III–the outer shear layer is subject to high strains more frequently that the inner shear layer. With respect to the transitional flame, however, this means that there is a hydrodynamic barrier between the inner conical and outer flames. There is one important clue that this dataset provides, which the dataset used in chapter 4 did not, and which this set of figures hints at. The probability of observing the outer flame is highest near the impingement point than at the expansion (accounting for the number of cells as a function of axial position in which the flame is observed, even though the value of the probabilities are consistently low). This bolsters the argument that the flame originates from the impingement point and travels upward, and thus the ability of the inner flame to bridge across the jet is critical. We will see stronger evidence of this when we examine flame IV.

Finally, in figure A-8, we look at flame IV, characterized by an inner conical flame joined by a persistent outer flame, confirmed by comparable flame probabilities in both regions, shown in A-8(a). From the instantaneous snapshots in A-4 and by the flame angle in A-8(b), we see that the outer flame consists of two distinct (although potentially joined) flame fronts: one that propagates along the outer shear layer nearly normal to the jet of reactants and opposite the inner flame, and one that propagates toward the wall, but remains lifted, consuming the reactants that are recirculated along the wall boundary layer. (We do note that A-8(b) shows artificial conjugate flames in the first 30 mm to 40 mm of the inner conical flame, which artificially thickens the flame brush as it did with the transitional flame.) The flame probabilities in A-8(a) are critical. The highest probability of finding a flame in the outer recirculation zone as a function of axial position, accounting both for the magnitude of the spatially resolved probabilities and the distribution of cells in which the flame is observed, is highest near the impingement point. While the outer flame
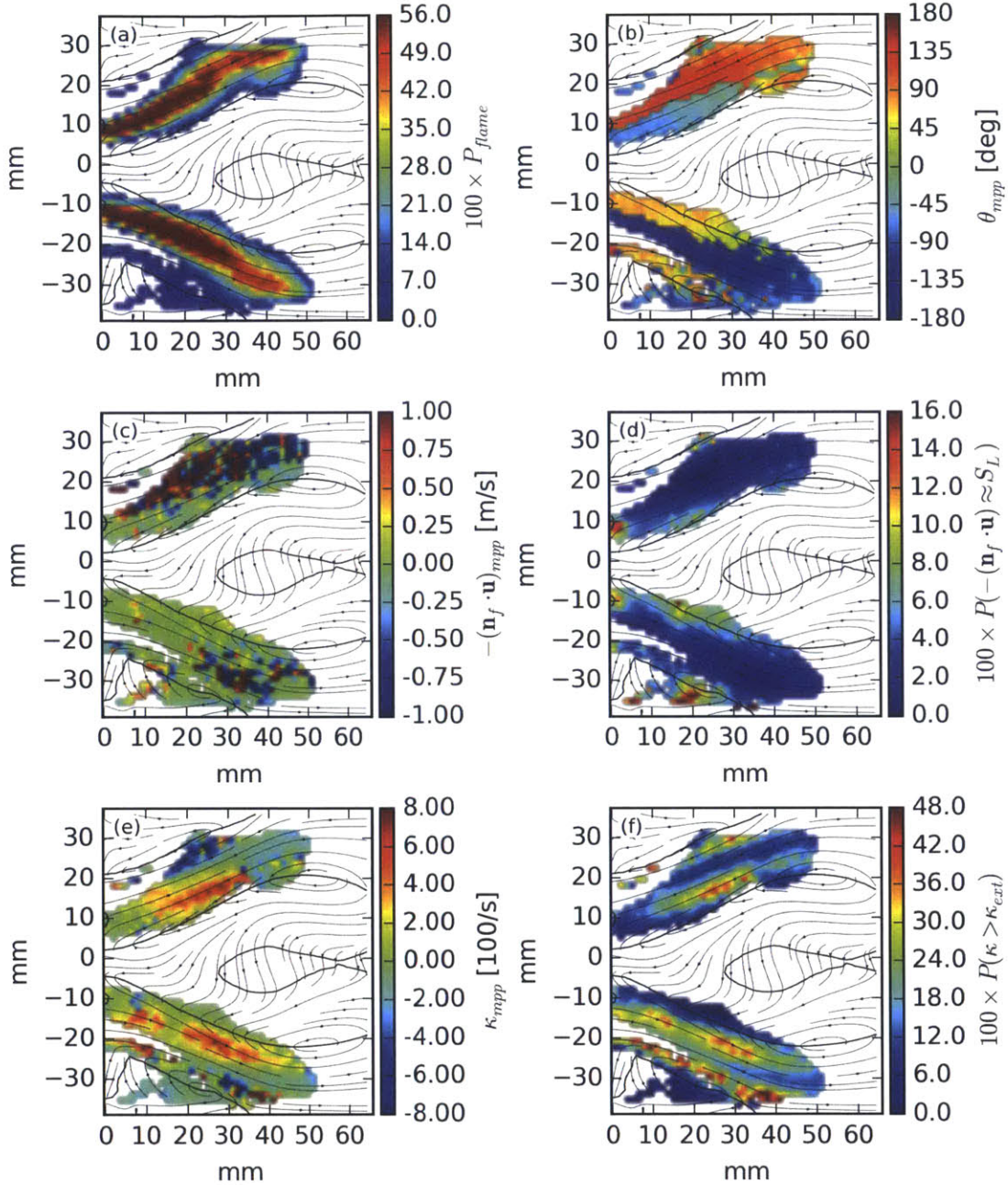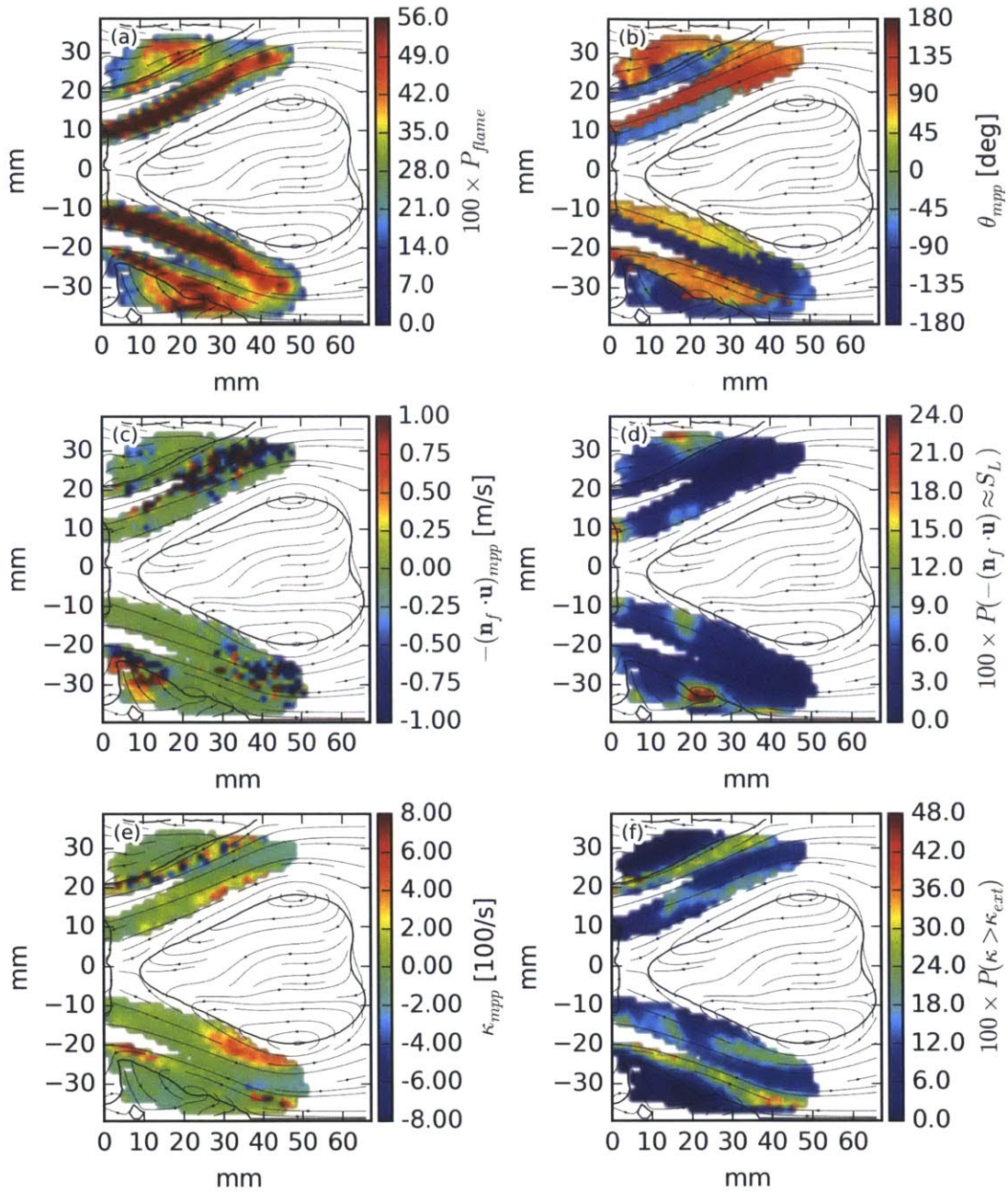
Figure A-8: Spatially resolved maps show statistical flow-flame interactions for flame IV in pure CH4. PIV and PLIF data were captured at $\phi = 0.650$. The point-by-point probability of detecting a flame is shown in (a), and the most probable flame angle is shown in (b). The most probable velocity of the flow into the flame is shown in (c), and the probability of normal flow velocity being within 10 cm/s of the laminar flame speed (d). The most probable strain rate is shown in (e), and the probability of the strain rate exceeding the extinction limit is shown in (f).

does propagate along the outer shear layer up to the expansion plane, this provides much stronger evidence that it originates from the impingement point where the inner flame can act as an ignition source.

As with the transitional flame, A-8(c-d) shows that the inner conical flame exists in an almost exclusively high-speed flow domain, and while there are some small pockets of slower flow captured in the outer recirculation zone, the flame by and large is not stabilized in the laminar sense. The most probable strain rate, shown in A-8(e) remains close to zero, and critically, we observe that the fraction of observations exceeding the extinction limit, shown in A-8(f), has dropped in both the inner and outer shear layers due to the increasing strength of the flame. This is consistent with our earlier analysis in which we claimed that the outer flame persists when the inner flame is strong enough to provide a consistent ignition source.

While the primary motivation of this appendix was to justify the use of one particular PLIF dataset that did not capture the most upstream extent of the flame that is optically accessible, it has also served to document some of the dynamics that take place as the flame propagates upstream into the inlet. By capturing more of the inner conical flame, we have been able to see the wrinkling consistent with a flame sitting in a shear layer, and very importantly, we have provided additional evidence to support the notion that the outer flame originates from the impingement point and not from the inlet.

Bibliography

[1] S. Candel, "Combustion Dynamics and Control: Progress and Challenges," in *Proceedings of the Combustion Institute*, pp. 1–28, 2002.

[2] Y. Huang and V. Yang, "Dynamics and Stability of Lean-Premixed Swirl-Stabilized Combustion," *Progress in Energy and Combustion Science*, vol. 35, pp. 293–364, 2009.

[3] H. C. Mongia, T. J. Held, G. C. Hsiao, and R. P. Pandali, "Challenges and Progress in Controlling Dynamics in Gas Turbine Combustors," *Journal of Propulsion and Power*, vol. 19, no. 5, pp. 822–829, 2003.

[4] C. T. Bowman, "Control of Combustion-Generated Nitrogen Oxide Emissions: Technology Driven by Regulation," *Proceedings of the ...*, 1992.

[5] S. M. Correa, "A Review of NOx Formation Under Gas-Turbine Combustion Conditions," *Combustion Science and Technology*, vol. 87, pp. 329–362, Jan. 1993.

[6] J. A. Miller and C. T. Bowman, "Mechanism and Modeling of Nitrogen Chemistry in Combustion," *Progress in Energy and Combustion Science*, vol. 15, pp. 287–338, Jan. 1989.

[7] J. J. Keller, "Thermoacoustic Oscillations in Combustion Chambers of Gas Turbines," *AIAA Journal*, vol. 33, no. 12, pp. 2280–2287, 1995.

[8] T. Lieuwen and K. McManus, "Combustion Dynamics in Lean-Premixed Prevaporized Gas Turbine," *Journal of Propulsion and Power*, vol. 19, p. 721, 2003.

[9] J. W. S. Rayleigh, "The Explanation of Certain Acoustical Phenomena," *Nature*, vol. 18, pp. 319–321, 1878.

[10] B.-T. Chu, "Stability of Systems Containing a Heat Source: The Rayleigh Criterion," Tech. Rep. RM 56D27, 1956.

[11] B.-T. Chu, "On the Energy Transfer to Small Disturbances in Fluid Flow (Part I)," *Acta Mechanica*, vol. 1, no. 3, pp. 215–234, 1965.

[12] F. Nicoud and T. Poinsot, "Fluctuation Energies and Stability Criteria for Thermoacoustic Instabilities: Is the Rayleigh Criterion Right?," *Combustion and Flame*, vol. 142, no. 1-2, pp. 153–159, 2005.

[13] J. C. Broda, S. Seo, R. J. Santoro, and G. Shirhattikar, "An Experimental Study of Combustion Dynamics of a Premixed Swirl Injector," *Proceedings of the ...*, 1998.

[14] J. H. Cho and T. Lieuwen, "Laminar Premixed Flame Response to Equivalence Ratio Oscillations," *Combustion and Flame*, 2005.

[15] K. T. Kim, J. G. Lee, B. D. Quay, and D. A. Santavicca, "Response of Partially Premixed Flames to Acoustic Velocity and Equivalence Ratio Perturbations," *Combustion and Flame*, 2010.

[16] T. Sattelmayer, "Influence of the Combustor Aerodynamics on Combustion Instabilities From Equivalence Ratio Fluctuations," *Journal of Engineering for Gas Turbines and Power*, 2003.

[17] A. M. Steinberg, I. Boxx, M. Stöhr, C. D. Carter, and W. Meier, "Flow–Flame Interactions Causing Acoustically Coupled Heat Release Fluctuations in a Thermo-Acoustically Unstable Gas Turbine Model Combustor," *Combustion and Flame*, vol. 157, pp. 2250–2266, Dec. 2010.

[18] J. Chen and H. G. Im, "Correlation of Flame Speed with Stretch in Turbulent Premixed Methane/Air Flames," *Proceedings of the Combustion Institute*, vol. 27, pp. 819–826, Jan. 1998.

[19] T. Echekki and J. H. Chen, "Unsteady Strain Rate and Curvature Effects in Turbulent Premixed Methane-Air Flames," *Combustion and Flame*, 1996.

[20] E. R. Hawkes and J. H. Chen, "Direct Numerical Simulation of Hydrogen-Enriched Lean Premixed Methane-Air Flames," *Combustion and Flame*, 2004.

[21] A. N. Lipatnikov and J. Chomiak, "Turbulent Flame Speed and Thickness: Phenomenology, Evaluation, and Application in Multi-Dimensional Simulations," *Progress in Energy and Combustion Science*, vol. 28, pp. 1–74, Jan. 2002.

[22] G. L. Brown and J. M. Lopez, "Axisymmetric Vortex Breakdown Part 2. Physical Mechanisms," *Journal of Fluid Mechanics*, vol. 221, pp. 553–576, 1990.

[23] M. Escudier, "Vortex Breakdown: Observations and Explanations," *Progress in Aerospace Sciences*, vol. 25, pp. 189–229, 1988.

[24] J. M. Lopez, "Axisymmetric Vortex Breakdown Part 1. Confined Swirling Flow," *Journal of Fluid Mechanics*, vol. 221, pp. 533–552, 1990.

[25] Z. Rusak, S. Wang, and C. H. Whiting, "The Evolution of a Perturbed Vortex in a Pipe to Axisymmetric Vortex Breakdown," *Journal of Fluid Mechanics*, 1998.

[26] F. Sotiropoulos and Y. Ventikos, "The Three-Dimensional Structure of Confined Swirling Flows with Vortex Breakdown," *Journal of Fluid Mechanics*, vol. 426, pp. 155–175, Jan. 2001.

[27] M. P. Escudier and J. J. Keller, "Recirculation in Swirling Flow - a Manifestation of Vortex Breakdown," *AIAA Journal*, vol. 23, no. 1, pp. 111–116, 1985.

[28] C. O. Paschereit, P. Flohr, and E. J. Gutmark, "Combustion Control by Vortex Breakdown Stabilization," *Journal of Turbomachinery*, vol. 128, no. 4, pp. 679–688, 2006.

[29] N. Syred and J. M. Beer, "Combustion in Swirling Flows: a Review," *Combustion and Flame*, 1974.

[30] C. O. Paschereit, E. Gutmark, and W. Weisenstein, "Structure and Control of Thermoacoustic Instabilities in a Gas-turbine Combustor," *Combustion Science and Technology*, vol. 138, pp. 213–232, Sept. 1998.

[31] C. O. Paschereit, E. Gutmark, and W. Weisenstein, "Excitation of Thermoacoustic Instabilities by Interaction of Acoustics and Unstable Swirling Flow," *AIAA Journal*, vol. 38, no. 6, pp. 1025–1034, 2000.

[32] N. Syred, "A Review of Oscillation Mechanisms and the Role of the Precessing Vortex Core (PVC) in Swirl Combustion Systems," *Progress in Energy and Combustion Science*, vol. 32, pp. 93–161, Jan. 2006.

[33] A. P. Dowling and S. Hubbard, "Instability in lean premixed combustors," *Proceedings of the Institution of Mechanical Engineers, Part A: Journal of Power and Energy*, vol. 214, pp. 317–332, Dec. 2005.

[34] A. P. Dowling and S. R. Stow, "Acoustic Analysis of Gas Turbine Combustors," *Journal of Propulsion and Power*, vol. 19, pp. 751–764, Sept. 2003.

[35] M. Fleifil, A. M. Annaswamy, Z. A. Ghoneim, and A. F. Ghoniem, "Response of a Laminar Premixed Flame to Flow Oscillations: A Kinematic Model and Thermoacoustic Instability Results," *Combustion and Flame*, vol. 106, pp. 487–510, 1996.

[36] Z. A. LaBry, "Suppression of Thermoacoustic Instabilities in a Swirl Combustor Through Microjet Air Injection," *SM Thesis, Massachusetts Institute of Technology*, 2010.

[37] M. G. Jones and P. E. Stiede, "Comparison of Methods for Determining Specific Acoustic Impedance," *Journal of the Acoustical Society of America*, vol. 101, no. 5, pp. 2694–2704, 1997.

[38] T. Schultz, M. Sheplak, and L. N. Cattafesta, III, "Uncertainty Analysis of the Two-Microphone Method," *Journal of sound and vibration*, vol. 304, pp. 91–109, 2007.

[39] R. L. Speth, *Fundamental Studies in Hydrogen-Rich Combustion: Instability Mechanisms and Dynamic Mode Selection*. PhD thesis, Massachusetts Institute of Technology, PhD Thesis, 2010.

215

[40] P. J. Schmid, "Dynamic Mode Decomposition of Numerical and Experimental Data," *Journal of Fluid Mechanics*, vol. 656, pp. 5–28, July 2010.

[41] P. J. Schmid, "Application of the Dynamic Mode Decomposition to Experimental Data," *Experiments in Fluids*, vol. 50, pp. 1123–1130, Feb. 2011.

[42] K. K. Chen, J. H. Tu, and C. W. Rowley, "Variants of Dynamic Mode Decomposition: Boundary Condition, Koopman, and Fourier Analyses," *Journal of Nonlinear Science*, vol. 22, pp. 887–915, Apr. 2012.

[43] L. Ding and A. Goshtasby, "On the Canny Edge Detector," *Pattern Recognition*, vol. 34, pp. 721–725, 2001.

[44] M. Matalon, C. Cui, and J. K. Bechtold, "Hydrodynamic Theory of Premixed Flames: Effects of Stoichiometry, Variable Transport Coefficients and Arbitrary Reaction Orders," *Journal of Fluid Mechanics*, vol. 487, pp. 179–210, June 2003.

[45] M. Matalon and B. J. Matkowsky, "Flames in Fluids: Their Interaction and Stability," *Combustion Science and Technology*, vol. 34, pp. 295–316, Oct. 1983.

[46] M. Matalon and B. J. Matkowsky, "On the Stability of Plane and Curved Flames," *Journal of Applied Mathematics*, vol. 44, pp. 327–343, Apr. 1984.

[47] S. M. Candel and T. J. Poinsot, "Flame Stretch and the Balance Equation for the Flame Area," *Combustion Science and Technology*, vol. 70, no. 1-3, pp. 1–15, 1990.

[48] C. K. Law, "Dynamics of Stretched Flames," *Proceedings of the Combustion Institute*, pp. 1381–1402, 1988.

[49] G. S. Jackson, R. Sai, J. M. Plaia, C. M. Boggs, and K. T. Kiger, "Influence of H_2 on the Response of Lean Premixed CH_4 Flames to High Strained Flows," *Combustion and Flame*, vol. 132, pp. 503–511, Feb. 2003.

[50] J. Sato, "Effects of Lewis Number on Extinction Behavior of Premixed Flames in a Stagnation Flow," *Proceedings of the Combustion Institute*, 1982.

[51] R. W. Schefer, D. M. Wicksall, and A. K. Agrawal, "Combustion of Hydrogen-Enriched Methane in a Lean Premixed Swirl-Stabilized Burner," *Proceedings of the Combustion Institute*, vol. 29, pp. 843–851, Jan. 2002.

[52] Y. M. Marzouk, A. F. Ghoniem, and H. N. Najm, "Dynamic Response of Strained Premixed Flames to Equivalence Ratio Gradients," *Proceedings of the Combustion Institute*, vol. 28, pp. 1859–1866, Jan. 2000.

[53] Y. M. Marzouk, A. F. Ghoniem, and H. N. Najm, "Toward a Flame Embedding Model for Turbulent Combustion Simulation," *AIAA Journal*, 2003.

[54] R. L. Speth, "Ember 1.3.0b1," *https://github.com/speth/ember*, June 2014.

[55] G. P. Smith, D. M. Golden, M. Frenklach, N. W. Moriarty, B. Eiteneer, M. Goldenberg, C. T. Bowman, R. K. Hanson, S. Song, W. C. Gardiner, Jr, V. V. Lissianski, and Z. Qin, "GRI-Mech 3.0," *http://www.me.berkeley.edu/gri_mech/*.

[56] R. J. Kee, J. A. Miller, G. H. Evans, and G. Dixon-Lewis, "A Computational Model of the Structure and Extinction of Strained, Opposed Flow, Premixed Methane-Air Flames," *Proceedings of the Combustion Institute*, vol. 22, pp. 1479–1494, Jan. 1989.

[57] R. L. Speth, Y. M. Marzouk, and A. F. Ghoniem, "Impact of Hydrogen Addition on Flame Response to Stretch and Curvature," *43rd AIAA Aerospace Sciences Conference*, 2005.

[58] F. Coppens, J. Deruyck, and A. Konnov, "The Effects of Composition on Burning Velocity and Nitric Oxide Formation in Laminar Premixed Flames of CH4 + H2 + O2 + N2," *Combustion and Flame*, vol. 149, pp. 409–417, June 2007.

[59] V. Disarli and A. Benedetto, "Laminar Burning Velocity of Hydrogen–Methane/Air Premixed Flames," *International Journal of Hydrogen Energy*, vol. 32, pp. 637–646, Apr. 2007.

[60] G. Yu, C. K. Law, and C. K. Wu, "Laminar Flame Speeds of Hydrocarbon + Air Mixtures with Hydrogen Addition," *Combustion and Flame*, vol. 63, pp. 339–347, Mar. 1986.

[61] V. Giovangigli and M. D. Smooke, "Extinction of Strained Premixed Laminar Flames With Complex Chemistry," *Combustion Science and Technology*, vol. 53, pp. 23–49, May 1987.

[62] H. N. Najm and P. S. Wyckoff, "Premixed Flame Response to Unsteady Strain Rate and Curvature," *Combustion and Flame*, vol. 110, pp. 92–112, July 1997.

[63] K. T. Kim, H. J. Lee, J. G. Lee, B. D. Quay, and D. Santavicca, "Flame Transfer Function Measurement and Instability Frequency Prediction Using a Thermoacoustic Model," in *ASME Turbo Expo 2009: Power for Land, Sea, and Air*, pp. 799–810, ASME, 2009.

[64] D. Kim, J. G. Lee, B. D. Quay, D. A. Santavicca, K. Kim, and S. Srinivasan, "Effect of Flame Structure on the Flame Transfer Function in a Premixed Gas Turbine Combustor," *Journal of Engineering for Gas Turbines and Power*, vol. 132, no. 2, p. 021502, 2010.

[65] T. Schuller, D. Durox, and S. Candel, "Self-Induced Combustion Oscillations of Laminar Premixed Flames Stabilized on Annular Burners," *Combustion and Flame*, vol. 135, pp. 525–537, Dec. 2003.

[66] P. Weigand, W. Meier, X. R. Duan, W. Stricker, and M. Aigner, "Investigations of Swirl Flames in a Gas Turbine Model Combustor I. Flow Field, Structures, Temperature, and Species Distributions," *Combustion and Flame*, vol. 144, pp. 205–224, Jan. 2006.

[67] W. Meier, X. R. Duan, and P. Weigand, "Investigations of Swirl Flames in a Gas Turbine Model Combustor: II. Turbulence–Chemistry Interactions," *Combustion and Flame*, 2006.

[68] W. Meier, P. Weigand, X. Duan, and R. Giezendanner-Thoben, "Detailed Characterization of the Dynamics of Thermoacoustic Pulsations in a Lean Premixed Swirl Flame," *Combustion and Flame*, vol. 150, pp. 2–26, July 2007.

[69] Z. A. LaBry, S. J. Shanbhogue, R. L. Speth, and A. F. Ghoniem, "Flow Structures in a Lean-Premixed Swirl-Stabilized Combustor with Microjet Air Injection," *Proceedings of the Combustion Institute*, vol. 33, no. 1, pp. 1575–1581, 2011.

[70] T. Sarpkaya, "Effect of the Adverse Pressure Gradient on Vortex Breakdown," *AIAA Journal*, vol. 12, May 1974.

[71] D. L. Darmofal, "Comparisons of Experimental and Numerical Results for Axisymmetric Vortex Breakdown in Pipes," *Computers & fluids*, vol. 25, no. 4, pp. 353–371, 1996.

[72] J. Saghbini and A. F. Ghoniem, "Numerical Simulation of the Dynamics and Mixing in a Swirling Flow," *35th AIAA Aerospace Sciences Conference*, 1997.

[73] O. Lucca-Negro and T. O'Doherty, "Vortex Breakdown: a Review," *Progress in Energy and Combustion Science*, vol. 27, pp. 431–481, Jan. 2001.

[74] S. Leibovich, "The Structure of Vortex Breakdown," *Annual Review of Fluid Mechanics*, vol. 10, pp. 221–246, 1978.

[75] J. H. Faler and S. Leibovich, "An Experimental Map of the Internal Structure of a Vortex Breakdown," *Journal of Fluid Mechanics*, vol. 86, no. 2, pp. 313–335, 1978.

[76] F. Novak and T. Sarpkaya, "Turbulent Vortex Breakdown at High Reynolds Numbers," *AIAA Journal*, 2000.

[77] P. Billant, J.-M. Chomaz, and P. Huerre, "Experimental Study of Vortex Breakdown in Swirling Jets," *Journal of Fluid Mechanics*, vol. 376, pp. 183–219, Dec. 1998.

[78] C. Brücker and W. Althaus, "Study of Vortex Breakdown by Particle Tracking Velocimetry (PTV)," *Experiments in Fluids*, vol. 13, pp. 339–349, Sept. 1992.

[79] T. Sarpkaya, "Vortex Breakdown in Swirling Conical Flows," *AIAA Journal,* vol. 9, pp. 1792–1799, Sept. 1971.

[80] J. H. Faler and S. Leibovich, "Disrupted States of Vortex Flow and Vortex Breakdown," *Physics of Fluids*, vol. 20, no. 9, pp. 1385–1400, 1977.

[81] J. H. Chen, T. Echekki, and W. Kollmann, "The Mechanism of Two-Dimensional Pocket Formation in Lean Premixed Methane-Air Flames with Implications to Turbulent Combustion," *Combustion and Flame*, vol. 116, pp. 15–48, Jan. 1999.

[82] K. Sardi, A. Taylor, and J. H. Whitelaw, "Extinction of Turbulent Counterflow Flames Under Periodic Strain," *Combustion and Flame*, 2000.

[83] F. N. Egolfopoulos, "Dynamics and Structure of Unsteady, Strained, Laminar Premixed Flames," *Proceedings of the Combustion Institute*, 1994.

[84] A. R. Masri, P. A. M. Kalt, and R. S. Barlow, "The Compositional Structure of Swirl-Stabilised Turbulent Nonpremixed Flames," *Combustion and Flame*, vol. 137, pp. 1–37, Apr. 2004.

[85] Y. Huang, S. Wang, and V. Yang, "Systematic Analysis of Lean-Premixed Swirl-Stabilized Combustion," *AIAA Journal*, 2006.

[86] S. H. Preetham and T. C. Lieuwen, "Response of Turbulent Premixed Flames to Harmonic Acoustic Forcing," *Proceedings of the Combustion Institute*, vol. 31, pp. 1427–1434, Jan. 2007.

[87] S. Hemchandra, N. Peters, and T. Lieuwen, "Heat Release Response of Acoustically Forced Turbulent Premixed Flames-Role of Kinematic Restoration," in *Proceedings of the Combustion Institute*, 2011.

[88] F. Duchaine, F. Boudy, D. Durox, and T. Poinsot, "Sensitivity Analysis of Transfer Functions of Laminar Flames," *Combustion and Flame*, vol. 158, pp. 2384–2394, Dec. 2011.

[89] R. L. Speth and A. F. Ghoniem, "Using a Strained Flame Model to Collapse Dynamic Mode Data in a Swirl-Stabilized Syngas Combustor," in *Proceedings of the Combustion Institute*, 2009.

[90] S. H. Hong, R. L. Speth, S. J. Shanbhogue, and A. F. Ghoniem, "Examining Flow-Flame Interaction and the Characteristic Stretch Rate in Vortex-Driven Combustion Dynamics Using PIV and Numerical Simulation," *Combustion and Flame*, vol. 160, pp. 1381–1397, Aug. 2013.

[91] S. H. Hong, *Towards Predicting Dynamics in Turbulent Premixed Combustion Using PIV-PLIF Measurement of Flow-Flame Microstructure*. PhD thesis, Massachusetts Institute of Technology, 2014.

[92] Preetham, H. Santosh, and T. Lieuwen, "Dynamics of Laminar Premixed Flames Forced by Harmonic Velocity Disturbances," *Journal of Propulsion and Power*, 2008.

[93] D. You, Y. Huang, and V. Yang, "A Generalized Model of Acoustic Response of Turbulent Premixed Flame and Its Application to Gas-Turbine Combustion Instability Analysis," *Combustion Science and Technology*, 2005.

[94] T. Schuller, D. Durox, and S. Candel, "A Unified Model for the Prediction of Laminar Flame Transfer Functions," *Combustion and Flame*, vol. 134, pp. 21–34, July 2003.

[95] B. D. Bellows, Y. Neumeier, and T. Lieuwen, "Forced Response of a Swirling, Premixed Flame to Flow Disturbances," *Journal of Propulsion and Power*, 2006.

[96] N. Noiray, D. Durox, and T. Schuller, "A Unified Framework for Nonlinear Combustion Instability Analysis Based on the Flame Describing Function," *Journal of Fluid Mechanics*, vol. 615, pp. 139–167, 2008.

[97] C. M. Ho and P. Huerre, "Perturbed Free Shear Layers," *Annual Review of Fluid Mechanics*, 1984.